Nanostructure and Reactivity of Soot Produced from Partially Premixed Charge Compression Ignition (PCCI) Combustion and Post Injection

by

Chenxi Sun

A dissertation submitted in partial fulfillment
of the requirements for the degree of
Doctor of Philosophy
(Mechanical Engineering)
in the University of Michigan
2017

Doctoral Committee:

Professor André L. Boehman, Chair
Associate Professor Christian M. Lastoskie
Professor Angela Violi
Professor Margaret S. Wooldridge

Chenxi Sun

suncx@umich.edu

ORCID iD: 0000-0003-0888-6945

© Chenxi Sun 2017

Acknowledgement

I want to express my deepest gratitude to my academic advisor Prof. André Boehman for all his support during my Ph. D study. He is the best teacher and advisor through my life. I want to thank him for his guidance, patience and encouragement all these years. He led me to a new research field which I have little knowledge before and guided me with great patience. His passion, kindness and optimism have always inspired me. I will always be grateful to him.

I also want to express great appreciation to my committee members Prof. Wooldridge, Prof. Violi, and Prof. Lastoskie for their valuable comments and suggestions for my research and thesis.

I am also sincerely grateful for Dr. Stani Bohac, Dr. Dongil Kang, and Jonathan Martin for working with me on different projects. Their advice and help during my Ph.D invaluable. This study could not be accomplished without them.

I also want to thank the visiting scholars in our group during my Ph. D study: Prof. Magin Lapuerta, Prof. John Agudelo, Prof. Xingcai Lu, and Prof. Wei Tian for working and sharing their great knowledge with me.

I want to thank previous group members: Dr. Yehliu Kuen, Dr. HeeJe Seong, Dr. Greg Lilik, Dr. Peng Ye, Dr. Bhaskar Prabhakar, and Dr. Vickey Kalaskar for their valuable guidance

or discussions. I also want to thank our current group members Shuqi Cheng, Jordan Easter, Yan Chang, Justin Koczac, Kwanghee Yoo, Taehoon Han and Taemin Kim for working and sharing their friendship with me. It is great pleasure for me to working with all of you.

I want to give my special gratitude to Dr. Kai Sun from MC2 for his guidance regarding TEM, EELS and XPS analysis. He is always very kind, patient and ready to help us students. He always assists me with instrument operation and provides me useful information. I also want to thank Prof. Matzger and his group members for Raman Spectroscopy and BET surface area analysis. Thanks Dr. Ying Qi from XMAL for XRD analysis. I also want to thank Trevor Clark and Vince Bojan from Penn State University for their help in learning materials characterization. I gained a lot of knowledge from them.

I want to express my special thank my parents, who always supported me unconditionally. I also want to thank my husband Xu Chen, who is always my best friend and supporter for so many years. Finally, thank my child Sunny Chen, who brings happiness to the family.

This work has been supported by the Department of Mechanical Engineering and the College of Engineering at the University of Michigan. Support was also received from Volvo Technology of America and the U.S. Department of Energy under DOE award number DEEE0004232.

Table of Contents

Acknowledgement ii
List of Figures viii
List of Tables xiv
List of Appendices xvi
Abstract xvii
Chapter 1. Introduction 1
1.1 Background 1
1.2 Motivating work 3
1.3 Hypothesis and objective 5
1.3.1 Hypothesis 5
1.3.2 Research objective 5
Chapter 2. Literature review 6
2.1 Diesel particulate matter and particulate emissions control 6
2.2 Partially-premixed charged compression ignition combustion 9
2.3 Impact of fuel on PCCI combustion mode 11
2.4 Post injection 14
2.5 Soot formation and nanostructure 16
2.5.1 Soot formation and oxidation 16
2.5.2 Soot nanostructure 17
2.6 Soot nanostructure and oxidative reactivity 18
2.6.1 The dependence of soot oxidative reactivity on its nanostructure 18

2.6.2 The dependence of soot nanostructure on synthesis condition 18
2.6.3 Soot nanostructure change during oxidation 19
Chapter 3. Experimental 21
3.1 Experimental Instruments 21
3.1.1 Testing Engines 21
3.1.2 Testing facilities 23
3.1.3 Fuel 24
3.1.4 Test Conditions 25
3.2 Soot characterization methods 30
3.2.1 Thermogravimetric analysis (TGA) 30
3.2.2 Surface area analysis 32
3.2.3 Raman spectroscopy 32
3.2.4 X-ray diffraction (XRD) 33
3.2.5 X-ray photoelectron spectroscopy (XPS) 35
3.2.6 Transmission electron microscopy (TEM) 36
3.2.7 Electron energy loss spectroscopy (EELS) 37
Chapter 4. Impact of fuel on PCCI combustion in single-cylinder engine 38
4.1 Apparent rate of heat release 39
4.2 NOx emissions 42
4.3 CO and THC emissions 47
4.4 Filter smoke number 54
4.5 PM emissions 56
4.6 Particle size distribution 59
4.7 Brake specific fuel consumption (BSFC) 62
4.8 THC-NOx trade-off 64
4.9 Comparison of PCCI combustion and conventional combustion 66
4.10 Conclusion 69
Chapter 5. PCCI combustion in a multi-cylinder engine and soot nanostructure and reactivity 71
5.1 Heat release rate 71

5.2 NOx emissions 74
5.3 CO and UHC emissions 75
5.4 Filter smoke number 78
5.5 PM emissions 79
5.6 Particle size distribution 80
5.7 BSFC and BTE 83
5.8 Soot reactivity analysis 84
5.9 Soot surface area analysis 90
5.10 X-ray diffraction 91
5.11 X-ray photoelectron spectroscopy 93
5.12 Raman spectroscopy 109
5.13 Transmission electron microscopy 118
5.14 Electron energy loss spectroscopy 133
5.15 Summary 135
Chapter 6. Effect of post injection on soot nanostructure and reactivity 137
6.1 Heat release rate 137
6.2 Brake specific fuel consumption 139
6.3 NOx emissions 140
6.4 CO and THC emissions 142
6.5 FSN and PM emissions 144
6.6 SMPS and surface area 148
6.7 Soot reactivity analysis 150
6.8 XRD analysis 155
6.9 X-ray photoelectron spectroscopy 157
6.10 Raman spectroscopy 169
6.11 Transmission electron microscopy 172
6.12 Summary 179
Chapter 7. Conclusions and future work 181
7.1 Conclusions 181

7.1.1 PCCI 181
7.1.2 Post injection 182
7.2 Future work 183
7.2.1 Investigation of soot oxidation behavior and mechanism 183
7.2.2 Improve technical approach 185
Appendices 188
Appendix A TEM images for soot from single cylinder Isuzu engine 188
Appendix B Post injection schedule, BSFC and emissions 195
References 198

List of Figures

Figure 2.1 Schematif of diesel particulate matter[3] 7

Figure 2.2 Schematic representation of wall flow DPF[6] 8

Figure 2.3 Soot formation process 16

Figure 4.1 Heat release rate for conventional and PCCI combustion modes for (a) ULSD, (b) LTFT, and (c) RD fuel 42

Figure 4.2 NOx emissions for conventional and PCCI combustion modes with (a) ULSD, (b) LTFT, and (c) RD fuel 44

Figure 4.3 NOx emissions versus timing ofmaximum cylinder temperature with ULSD, LTFT, and RD under PCCI and conventional combustion modes 46

Figure 4.4 NOx emissions versus CA50 with ULSD, LTFT, and RD under PCCI and conventional combustion modes 47

Figure 4.5 CO emissions for conventional and PCCI combustion modes with (a) ULSD, (b) LTFT, and (c) RD fuel 51

Figure 4.6 THC emissions for conventional and PCCI combustion modes with (a) ULSD, (b) LTFT, and (c) RD fuel 52

Figure 4.7 THC emissions versus timing ignition dwellwith ULSD, LTFT, and RD under PCCI and conventional combustion modes 53

Figure 4.8 Filter smoke number for conventional and PCCI combustion modes of (a) ULSD, (b) LTFT, and (c) RD fuel 56

Figure 4.9 PM emissions for conventional and PCCI combustion modes with (a) ULSD, (b) LTFT, and (c) RD fuel 59

Figure 4.10 Particle size distribution for conventional and PCCI combustion modes with (a) ULSD, (b) LTFT, and (c) RD fuel 62

Figure 4.12 NOx emissions versus total hydrocarbon emissions for ULSD, LTFT and RD under PCCI and conventional combustion modes 65

Figure 4.13 (a) NOx, (b) CO, (c)THC, (d) PM emissions, and (e) FSN for conventional and PCCI combustion modes when CA50 is 10^{o}aTDC 69

Figure 5.1 Heat release rate for conventional and PCCI combustion modes for (a) ULSD, (b) LTFT and (c) RD fuel 73

Figure 5.2 NOx emissions for conventional and PCCI combustion modes with ULSD, LTFT and RD fuel 75

Figure 5.3 CO emissions for conventional and PCCI combustion modes with ULSD, LTFT and RD fuel 76

Figure 5.4 THC emissions for conventional and PCCI combustion modes with ULSD, LTFT and RD fuel 77

Figure 5.5 NOx emissions versus total hydrocarbon emissions for ULSD, LTFT and RD under PCCI and conventional combustion modes 78

Figure 5.6 Filter smoke number for conventional and PCCI combustion modes of ULSD, LTFT and RD fuel 79

Figure 5.7 PM emissions for conventional and PCCI combustion modes with ULSD, LTFT and RD fuel 80

Figure 5.8 Particle size distribution for conventional and PCCI combustion modes with (a) ULSD, (b) LTFT and (c) RD fuel 82

Figure 5.9 BSFC for conventional and PCCI combustion modes with ULSD, LTFT and RD fuel 83

Figure 5.10 BTE for conventional and PCCI combustion modes with ULSD, LTFT and RD fuel 84

Figure 5.11 Thermogravimetric analyses for soot generated from conventional and late injection PCCI combustion modes with (a) ULSD, (b) LTFT and (c) RD fuel under isothermal oxidation at 525^{o}C 87

Figure 5.12 XRD patterns for soot collected from ULSD, LTFT and RD under both conventional and late injection PCCI conditions 92

Figure 5.13 Peak deconvolution of (a) C 1s and (b) O 1s spectra 96

Figure 5.14 C 1s peaks for soot produced from (a) ULSD, (b) LTFT and (c) RD fuels under conventional and late injection PCCI combustion mode 99

Figure 5.15 O 1s peaks for soot produced from (a) ULSD, (b) LTFT and (c) RD fuels under conventional and late injection PCCI combustion mode 101

Figure 5.16 Defect/graphitic carbon ratio versus oxidative rate constant for ULSD, LTFT and RD fuels for both conventional and late injection PCCI combustion mode 102

Figure 5.17 Oxygen functional content versus oxidative rate constant for ULSD, LTFT and RD fuels for both conventional and late injection PCCI combustion mode 103

Figure 5.18 Defect/graphitic carbon ratios of soot from (a) ULSD, (b) LTFT and (3) RD fuels of as received soot, and soot at 40% and 75% mass burned 107

Figure 5.19 Ratio of carbon bonded with oxygen functional groups of soot from (a) ULSD, (b) LTFT and (c) RD of as received soot, and soot at 40% and 75% mass burned 109

Figure 5.20 Raman spectroscopy peak fitting 110

Figure 5.21 FWHM of (a) D1 and (b) G band versus rate constant 112

Figure 5.22 Intensity of D1 peak and G peak ratio of soot from (a) ULSD, (b) LTFT and (3) RD of as received soot, and soot at 40% and 75% mass burned 114

Figure 5.23 Ratio FWHM of D1 band of soot from (a) ULSD, (b) LTFT and (3) RD of as received soot, and soot at 40% and 75% mass burned 116

Figure 5.24 Ratio FWHM of G band of soot from (a) ULSD, (b) LTFT and (3) RD of as received soot, and soot at 40% and 75% mass burned 117

Figure 5.25 TEM images for soot produced from ULSD under conventional combustion mode at (a) 40,000x (b) 400,000x, PCCI combustion mode at injection timing 4.5^{o}bTDC at (c) 40,000x (d) 400,000x, and PCCI combustion mode at injection timing 2.5obTDC at (e) 40,000x and (f) 400,000x 121

Figure 5.26 TEM images for soot produced from LTFT under conventional combustion mode at (a) 40,000x (b) 400,000x, PCCI combustion mode at injection timing -1.5^{o}bTDC at (c) 40,000x (d) 400,000x, and PCCI combustion mode at injection timing -3.5^{o}bTDC at (e) 40,000x and (f) 400,000x 122

Figure 5.27 TEM images for soot produced from RD under conventional combustion mode at (a) 40,000x (b) 400,000x, PCCI combustion mode at injection timing -1.5^{o}bTDC (c) 40,000x (d) 400,000x, and PCCI combustion mode at injection timing -3.5^{o}bTDC at (e) 40,000x (f) 400,000x 124

Figure 5.28 TEM images for soot produced from USLD conventional combustion mode after 40% mass burn at (a) 40,000x (b) 400,000x and 75% mass burn at (c) 40,000x (d) 400,000x 126

Figure 5.29 TEM images for soot produced from USLD PCCI combustion mode with injection timing 4.5^{o} bTDC after 40% mass burn at (a) 40,000x (b) 400,000x, and 75% mass burn at (c) 40,000x (d) 400,000x 127

Figure 5.30 TEM images for soot produced from USLD PCCI combustion mode with injection timing 2.5^{o} bTDC after 40% mass burn at (a) 40,000x (b) 400,000x, and 75% mass burn at (c) 40,000x (d) 400,000x 128

Figure 5.31 TEM images for soot produced from LTFT conventional combustion mode after 40% mass burn at (a) 40,000x (b) 400,000x, and 75% mass burn at (c) 40,000x (d) 400,000x 129

Figure 5.32 TEM images for soot produced from LTFT PCCI combustion mode with injection timing -3.5^{o} bTDC after 40% mass burn at (a) 40,000x (b) 400,000x, and 75% mass burn at (c) 40,000x (d) 400,000x 130

Figure 5.33 TEM images for soot produced from RD conventional combustion mode after 40% mass burn at (a) 40,000x (b) 400,000x, and 75% mass burn at (c) 40,000x (d) 400,000x 131

Figure 5.34 TEM images for soot produced from RD PCCI combustion mode with injection timing -3.5^{o} bTDC after 40% mass burn at (a) 40,000x (b) 400,000x, and 75% mass burn at (c) 40,000x (d) 400,000x 132

Figure 5.35 EELS spectra for initial and soot oxidized for 40% and 75% mass burn 135

Figure 6.1 Heat release rate for baseline, main injection only and 7.5% post injection with injection dwell 4^{o}CAD, 10^{o}CAD and 16^{o}CAD 138

Figure 6.2 BSFC for baseline, main injection only and post injection conditions 140

Figure 6.3 NOx emissions for baseline, main injection only and post injection conditions 141

Figure 6.4 CO emissions for baseline, main injection only and post injection conditions 143

Figure 6.5 THC emissions for baseline, main injection only and post injection conditions 144

Figure 6.6 FSN for baseline, main injection only and post injection conditions 145

Figure 6.7 PM emissions for baseline, main injection only and post injection conditions 146

Figure 6.8 Particle size distributions for baseline, main injection only and (a) 4.5 and (b) 7.5% post injection with injection dwell 4^{o}CAD, 10^{o}CAD and 16^{o}CAD 149

Figure 6.9 VOF of PM for baseline, main injection only and post injection conditions 151

Figure 6.10 Normalized mass from isothermal oxidation of PM from baseline and (a) 4.5 and (b) 7.5% post injection with injection dwell 4^{o}CAD and 16^{o}CAD at 500^{o}C 153

Figure 6.11 XRD patterns for soot collected from baseline, main injection only and post injection conditions 156

Figure 6.12 Defect/graphitic carbon ratios versus oxidation rate constant 160

Figure 6.13 Percentage of carbon atoms bonded with oxygen functional groups versus oxidation rate constant 161

Figure 6.14 C 1s core scan peaks for baseline, main injection only and (a) 4.5 and (b) 7.5% post injection with injection dwell 4°CAD, 10°CAD and 16°CAD 162

Figure 6.15 O 1s core scan peaks for baseline, main injection only and (a) 4.5 and (b) 7.5% post injection with injection dwell 4°CAD, 10°CAD and 16°CAD 163

Figure 6.16 Defect/graphitic carbon ratios for baseline, main injection only and (a) 4.5 and (b) 7.5% post injection conditions of initial, 40% and 75% mass burned soot 167

Figure 6.17 Percentage of carbon atoms bonded with oxygen functional groups for baseline, main injection only and (a) 4.5 and (b) 7.5% post injection conditions of initial, 40% and 75% mass burned soot 168

Figure 6.18 D1 band FWHM versus soot oxidation rate constant for soot from baseline, main injection only and 7.5% post injection conditions 170

Figure 6.19 (a) ID1/IG and (b) D1 band FWHM for initial soot, 40% and 75% mass burned soot from baseline and 7.5% post injection conditions 171

Figure 6.20 TEM images for soot produced from baseline condition at (a) 40,000x (b) 400,000x, and 7.5% post injection conditions with injection dwell 4°CAD at (c) 40,000x (d) 400,000x, 10°CAD at (e) 40,000x (f) 400,000x, and 16°CAD at (g) 40,000x (h) 400,000x 174

Figure 6.21 TEM images for soot produced from baseline condition at 40% mass burned with magnification (a) 40,000x (b) 400,000x, and 75% mass burned with magnification (c) 40,000x (d) 400,000x 176

Figure 6.22 TEM images for soot produced from 7.5% post injection condition with injection dwell 4°CAD at 40% mass burned with magnification (a) 40,000x (b) 400,000x, and 75% mass burned with magnification (c) 40,000x (d) 400,000x 177

Figure 6.23 TEM images for soot produced from 7.5% post injection condition with injection dwell 16°CAD at 40% mass burned with magnification (a) 40,000x (b) 400,000x, and 75% mass burned with magnification (c) 40,000x (d) 400,000x 178

Figure A. 1 Soot morphology of (a) ULSD conventional combustion, (b) ULSD PCCI combustion with injection timing -18°ATDC, (c) ULSD PCCI combustion with injection timing -8°ATDC, (d) LTFT conventional combustion, (e) LTFT PCCI combustion with injection timing -10°ATDC, (f) LTFT PCCI combustion with injection timing 0°ATDC, (g) RD conventional combustion, (h) RD PCCI combustion with injection timing -12°ATDC, (i) RD PCCI combustion with injection timing 0°ATDC at magnification of 40,000x 191

Figure A. 2 Soot nanostructure of (a) ULSD conventional combustion, (b) ULSD PCCI combustion with injection timing -18°ATDC, (c) ULSD PCCI combustion with injection timing -8°ATDC, (d) LTFT conventional combustion, (e) LTFT PCCI combustion with injection timing -10°ATDC, (f) LTFT PCCI combustion with injection timing 0°ATDC, (g) RD conventional combustion, (h) RD

PCCI combustion with injection timing -12°ATDC, (i) RD PCCI combustion with injection timing 0°ATDC at magnification of 400,000x 194

Figure B. 1 Example of injection schedules and injector current for (a) baseline condition, (b) 3% post injection with injection dwell 10°CAD, (c) 12% post injection with injection dwell 10°CAD (d) 7.5% post injection with injection dwell 4°CAD, and (e) 7.5% post injection with injection dwell 16°CAD[18] 195

Figure B. 2 Filter smoke number, varying post-injection schedule. Close-coupled regime highlighted in blue, long-dwell regime highlighted in violet[18] 196

Figure B. 3 CO emissions, varying post-injection schedule[18] 196

Figure B. 4 THC emissions, varying post-injection schedule[18] 196

Figure B. 5 NOx emissions, varying post-injection schedule[18] 197

Figure B. 6 Brake specific fuel consumption, varying post-injection schedule[18] 197

List of Tables

Table 3.1 Isuzu single cylinder engine specifications 22

Table 3.2 GM multi-cylinder engine specifications 23

Table 3.3 Fuel specifications 25

Table 3.4 Operating conditions for single-cylinder engine PCCI study 27

Table 3.5 Operating conditions for multi-cylinder engine PCCI study 28

Table 3.6 Operating conditions for post injection study 30

Table 3.7 Thermogravimetric analysis procedure 31

Table 3.8 Peak positions for interpretation of C 1s spectra 36

Table 4.1 Conditions for conventional and PCCI combustion modes when CA50 is 10^{o}aTDC 66

Table 5.1 Volatile organic fraction and time for 50% mass burn 85

Table 5.2 Overall apparent rate of constant and rate constant at different stages of oxidation at 525^{o}C 88

Table 5.3 BET surface area for soot generated from ULSD, LTFT and RD under conventional and late PCCI conditions 91

Table 5.4 Structure parameters from XRD spectra analysis 93

Table 5.5 Elemental composition for soot collected from conventional and PCCI conditions 95

Table 5.6 Element state analysis from C 1s and O 1s spectra of original soot 97

Table 5.7 Surface carbon and oxygen concentrations at 40% and 75% burn 104

Table 5.8 Element state analysis of C 1s and O 1s spectra of soot at 40% burn 105

Table 5.9 Element state analysis of C 1s and O 1s spectra of soot at 75% burn 106

Table 6.1 FSN for baseline, main injection and post injection conditions 145

Table 6.2 BET surface area of PM from baseline and post injection conditions 150

Table 6.3 Overall apparent rate of constant and rate constant at different stages of oxidation at 500^{o}C 152

Table 6.4 Interlayer spacing, stacking height, crystalline basal plane diameter and average number of layers from XRD pattern analysis 157

Table 6.5 Elemental compositions for soot from baseline main injection only and post injection conditions 158

Table 6.6 Element state analysis for C 1s and O 1s spectra of original soot 159

Table 6.7 Element composition of soot at 40% and 75% mass burned 164

Table 6.8 Elemental state analysis for C 1s and O 1s spectra of 40% mass burn soot 165

Table 6.9 Elemental state analysis for C 1s and O 1s spectra of 75% mass burned soot 166

List of Appendices

Appendix A TEM images for soot from single cylinder Isuzu engine 188

Appendix B Post injection schedule, BSFC and emissions 195

Abstract

Researchers have invested significant effort on optimizing the engine operation mode while cutting down the emissions due to increasingly strict emissions regulations. This study explores Partially-Premixed Charge Compression Ignition (PCCI) combustion and post injection in a light duty multicylinder turbodiesel engine to reduce particulate matter (PM) and NOx emissions without sacrificing the engine performance.

Three different fuels are tested in this PCCI combustion research: Ultra Low Sulfur Diesel (ULSD), diesel fuel produced via a low temperature Fischer-Tropsch process (LTFT) and a Renewable Diesel (RD). Late injection PCCI combustion can reduce NOx emissions by 76-78% and reduce soot emissions by 25-35%. High cetane number (CN), high ignition quality fuels LTFT and RD only increase CO emissions by 40-45% and THC emissions by 11-16% under late injection PCCI combustion compared to conventional combustion, while ULSD increases CO emissions by 78% and THC emissions by 24% under late injection PCCI combustion.

The reaction rate constants of soot produced from late injection PCCI combustion are 1.2-2.2 times higher than soot from the conventional combustion conditions. The reaction rate constants of soot from LTFT and RD fuels are 47-66% lower than soot produced from ULSD. Soots produced from PCCI combustion have smaller graphene layers, higher surface oxygen

concentration and higher portion of amorphous carbon. In addition, the primary particle and particle aggregate sizes are around 25nm and 400 nm for conventional combustion soot, while 10 nm and 150 nm for late injection PCCI combustion soot. Soots produced from LTFT and RD fuel under conventional combustion, show internal burning during oxidation. However, soots produced from late injection PCCI combustion and ULSD show shrinking core oxidation, likely because of their overall amorphous structure.

Post injection is another method to reduce engine-out soot emissions while maintaining efficiency, potentially to reduce or eliminate exhaust aftertreatment. Close-coupled post injections reduce soot emissions by 11-21%, THC emissions by 14-28%, and CO emissions by 7-8%. However, NOx emissions increase by 3-5%. For long-dwell post injection condition, soot emissions are reduced by 28-33% and NOx emissions are reduced by 7-8%. CO and THC emissions do not vary much under long dwell post injection conditions.

The reaction rate constants of soot from close-coupled post injection conditions increase by 10-13% compared to baseline condition, while the reaction rate constants of soot from long dwell post injection conditions decrease by 37-39% compared to baseline condition. Moreover, with the increase of injection dwell and post injection size, soot surface oxygen content and amorphous carbon content increase. This explains the change in reactivity of soot from different injection dwells. Primary soot particle and particle aggregate sizes do not vary much with post injection. Soot from post injection conditions all show shrinking core type oxidation without graphene layer rearrangement.

Chapter 1.

Introduction

1.1 Background

Diesel emissions reduction has drawn much attention from researchers due to the increasingly strict regulations. Since particulate matter (PM) emissions can elicit many adverse health effects such as respiratory and cardiovascular diseases,[1] particulate emissions from diesel engines have been mandated to dramatically be reduced over the last 20 years. Diesel particulate filters (DPFs) are the most effective and commercially viable device for controlling PM emissions, which attains a filtration efficiency of 90% or more.[2] However, the DPF should be regenerated intermittently to avoid soot accumulation on the DPF substrate, which increases engine back pressure. Thus, it is critical to reduce engine out PM emissions and raise PM reactivity via improving the combustion strategy or fuel properties.

Advanced combustion modes combine the advantages of traditional spark-ignition (SI) and compression-ignition (CI) engines, which control engine emissions while maintaining the efficiency. Homogenous charged compression ignition (HCCI) combustion can achieve high thermal efficiency while significantly reducing NOx and PM emissions.[3] However, HCCI combustion is limited to low loads, since it is very difficult to control the ignition timing and

combustion rate. Several other combustion modes are derived from the HCCI combustion concept: low-temperature combustion (LTC), partially-premixed charge compression ignition (PCCI), and reactivity controlled compression ignition (RCCI) combustion modes.

To utilize this advanced combustion concept at higher engine loads, a partially premixed charge compression ignition combustion (PCCI) process was developed.[4] PCCI combustion applies very early or late injection timing, low compression ratio and high EGR level to achieve a separation between the end of injection and the start of combustion, which can give enough time to create a premixed charge inside the cylinder. PCCI combustion can also use port injection and direct injection together.[5] Low cetane number fuel also provides an effective way to achieve ignition delay for PCCI combustion.[6] Soot and NOx emissions are much reduced compared to traditional CI engines. PCCI provides an effective way to reduce the soot and NOx emissions without sacrificing the engine load.

Alternative fuels are a topic with growing importance to reduce the dependence on traditional petroleum fuels and to reduce carbon footprint. Compared to traditional petroleum fuels, biofuels provide greater energy and economic security, as well as less environmental impact.[7] Thus, it is also very important to evaluate the performance and emissions from alternative fuels. Alternative fuels can also impact the properties of soot, which is essential for DPF regeneration. In this research, the performance of renewable diesel (RD) and low temperature Fischer-Tropsch diesel (LTFT) are investigated under PCCI combustion.

Post injections are widely used for the DPF regeneration process,[8] or the reduction of total hydrocarbon (THC) emissions during low temperature combustion conditions.[9] In addition, post injection is another method to reduce engine out PM emissions by altering the PM

formation and oxidation process. Post injection consists of altering the fuel injection schedule so that the main injection pulse is followed by a short post injection pulse, separated by a gap in which no fuel injection occurs. When the injection size and dwell between the main and post injections are properly adjusted, soot production is reduced.[10,11]

1.2 Motivating work

One problem for PCCI combustion is that it produces high levels of CO and THC emissions due to the reduced combustion temperature and over-lean charge.[12] Lilik et al.[13] shows that fuels with a lower critical equivalence ratio could effectively reduce the THC and CO emission from PCCI combustion. As a high n-alkane content, high CN fuel, LTFT can effectively reduce the CO and THC emissions from PCCI combustion, as well as increase the brake thermal efficiency. In addition, NOx and PM emissions could also be reduced by high n-alkane content fuels due to the reduced combustion temperature. The goal of this study is to investigate if RD can also provide the same benefit, because RD can become a practical and widespread fuel at much lower cost than FT fuels and has inherently low carbon footprint. This study also tests the hypothesis put forth by Lilik and Boehman[13] that high n-alkane content is required to realize the benefits of a low critical equivalence ratio fuel. The comparison of the emissions performance of the LTFT fuel and the RD fuel serves to explore how both the amount and composition of saturates in a fuel influence CO and THC emissions during PCCI combustion.

There are several mechanisms proposed for PM reduction by post injection. The momentum of the post injection jet could enhance the mixing of main injection flame and reduce the local equivalence ratio, thus reducing soot formation and enhance soot oxidation.[14] Post

injection also can increase the cylinder temperature later during the cycle and improve the soot oxidation.[15] Soot formation can also be suppressed because fuel is not replenished to the region where soot formation occurs.[16] However, the mechanisms for soot reduction by post injection are still under investigation.

There is a systematic lack of investigation into the properties of soot produced from PCCI combustion and post injection conditions, such as their formation and oxidative properties, and the dependence of soot nanostructure and reactivity on combustion parameters. In addition, there is still very little characterization work done for soot from PCCI and post injection conditions, especially high-resolution transmissions electron microscopy (HRTEM) study. This research will investigate the nanostructure and oxidation process of soot from PCCI and post injection conditions.

Yehliu et al.[17] found that soot produced from PCCI combustion has higher reactivity than soot produced from conventional diesel combustion mode. The reaction rate constant of PCCI combustion soot is 2-4 times higher than conventional combustion soot. In addition, soot from PCCI combustion also has less ordered nanostructure compared to soot from conventional combustion, which explains the higher reactivity of soot from PCCI combustion.

Previous work has already found that soot emissions are reduced by both close-coupled and long dwell post injection conditions.[18] However the reactivity and properties of soot from different injection dwells and sizes are not examined yet. This research will continue the previous work and investigate the properties of soot from various post injection conditions.

Soot structure change during oxidation also has a strong impact on the soot oxidation reactivity. Soot produced from different fuels or engine operating conditions could have different

structure change during oxidation. Song et al.[19] found that biodiesel soot goes through structural rearrangement and forms a ribbon-like structure during oxidation. Al-Quarshi et al.[20] found that soot produced under EGR conditions shows internal burning. The oxidation process for soot from PCCI combustion and post injection conditions have not been examined. In this research, the oxidation rate constant and structural change during oxidation of soot from PCCI and post injection conditions are investigated.

1.3 Hypothesis and objective

1.3.1 Hypothesis

By altering the environment in which soot formation occurs, PCCI combustion and other dilute advanced combustion strategies will profoundly affect the characteristics of the soot that is emitted, as evidenced by the nanostructure and reactivity of the soot.

Examination of soot nanostructure and morphology can determine the mechanism of soot suppression by post injection.

1.3.2 Research objective

Explore the impact of PCCI combustion and fuel on soot nanostructure, reactivity and other emissions.

Explore soot nanostructure or morphology change by post injection. Explore the mechanism of soot reduction by post injection.

Chapter 2.

Literature review

2.1 Diesel particulate matter and particulate emissions control

Particulate matter (PM) has many deleterious effects on human health. PM not only can causes respiratory diseases such as decreased lung function, aggravated asthma, coughing or difficulty breathing;[21] the fine particles (PM 2.5) can also translocate into the blood system and cause heart attacks, irregular heartbeats, increased blood pressure and even sudden death.[22] As a major contributor of PM emissions, the automotive industry is obliged to provide solutions to reduce transportation related environmental and health impacts.

As illustrated in Figure 2.1, PM usually contains hundreds of primarily spherical carbon primary particles, which is the solid and insoluble fraction of particle aggregates. A layer of condensed hydrocarbon is usually coated on the surface of the carbon particles, which is defined as volatile organic fraction (VOF) or soluble organic fraction (SOF).[23]

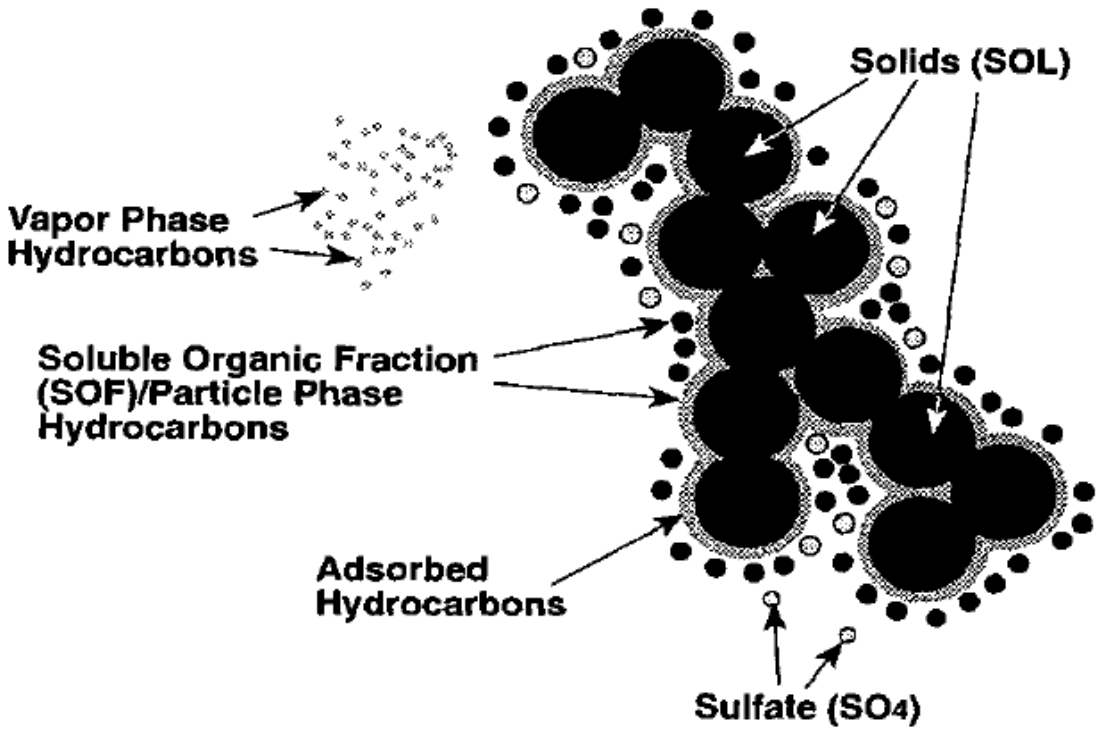

Figure 2.1 Schematicf of diesel particulate matter[23]

PM reduction is especially important for diesel engines due to their heterogeneous combustion. Diesel particulate filters (DPF) are generally used to reduce PM emissions from compression ignition engines. Wall-flow DPF is the most popular type, which is shown in Figure 2.2. Wall-flow DPF has open channels on one end and allows the exhaust gas to flow through the channel walls. To trap PM emissions, DPF filtration usually has four stages.[24] Stage one is a clean DPF, which has pores on the substrate walls. During stage two, soot deposits begin to build on the large surface pores of the substrate walls. The filtration efficiency is low during this stage because the pores on the channel walls are still open. Stage three includes pore bridging caused by the accumulation of PM deposit across the necks of surface pores. Stage four is reached when a layer of soot cake is developed on the channel

walls. PM filtration efficiency reaches a maximum when a thin layer of soot cake is developed. However, when this layer of soot cake continues to grow thicker, back pressure begins to increase and the filter needs to be regenerated.[25] Passive regeneration occurs simultaneously with the DPF deposition process. Catalytic filter coatings, which enhance the oxidation of PM via catalysts, and reactive species generation, which generally oxidizes PM via oxidants such as NOx, can trigger passive DPF regeneration. Active regeneration means DPFs are forced to regenerate when back pressure reaches a certain value. Active regeneration could be achieved by heating the DPF by throttling the intake air to increase the exhaust temperature or by introducing a post combustion process, which increases the exhaust temperature and oxidizes the PM collected on the filter walls[26].

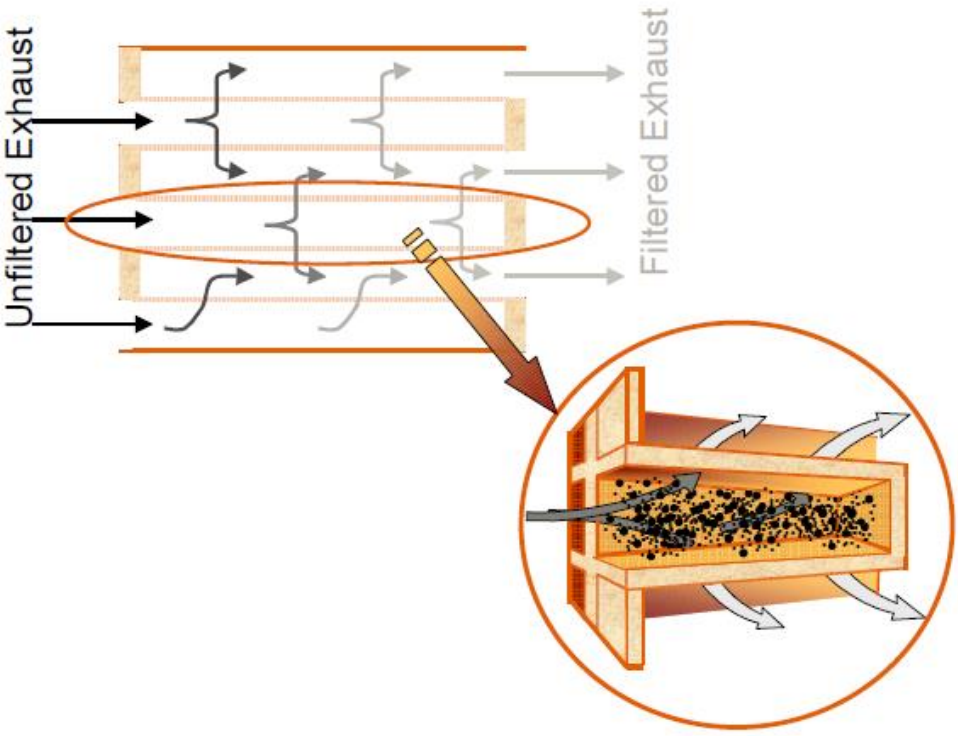

Figure 2.2 Schematic representation of wall flow DPF[26]

Although a DPF can reduce PM emissions by more than 90%, the installation of a DPF could cause a 3-5% loss in fuel economy.[27] The back pressure caused by the DPF increases with loading, which can reduce engine efficiency[28]. In addition, post combustion of fuel, the most common active DPF regeneration method, can also reduce fuel economy. However, due to its high effectiveness in reducing PM, DPFs are installed in all new diesel vehicles since 2007 in the United States, to reduce PM emissions to meet the US 2010 standard level.[29]

The regeneration of the DPF is strongly affected by PM reactivity, which is related to the physical and chemical properties of PM. Soot morphology, nanostructure, composition and surface functional groups could all impact the oxidative reactivity of PM and the regeneration of DPFs. As a consequence, researchers are trying to reduce PM emissions as well as increase the reactivity of soot particles.

2.2 Partially-premixed charged compression ignition combustion

Advanced combustion modes aim to reduce engine emissions while maintaining the thermal efficiency. HCCI is the first concept of advanced combustion. It applies a homogenous charge in the cylinder similar to spark ignition engines in order to reduce the PM and NOx emissions, and uses compression to ignite the charge to maintain the thermal efficiency.[30] However, there are still many limitations for this combustion mode,[31] such as 1) Difficulty to control combustion phasing; 2) High level of noise, unburned hydrocarbon (UHC) and CO emissions; 3) Limited operating range; 4) Difficulty to fire during cold start. 5) Difficulty to obtain a homogenous mixture in the cylinder.

PCCI combustion exploits the HCCI combustion concept from low to medium engine loads, which provides an effective way to reduce NOx and PM emissions at medium load. Its basic operating mechanism is to apply combinations of very early or late injection timing, high injection pressure, low compression ratio and high exhaust gas recirculation (EGR) levels to achieve a separation between the end of injection and the start of combustion, so that a premixed charge can be achieved before ignition occurs.[32] PCCI combustion mode can be considered as diesel combustion with a reduced fraction of mixing controlled combustion. Soot and NOx emissions from PCCI combustion can be higher than from HCCI combustion, but much less than emissions from the traditional CI combustion mode.

In early injection PCCI combustion mode, multiple early injections[33] or port injection can be used to achieve a partially premixed mixture. An additional direct injection near TDC can be used to control ignition timing and extend engine operation to higher load. Early port injection or pilot injection can provide an effective way to control the PM and NOx emissions. However, heat release during the compression stroke may increase specific fuel consumption. Early single direct injection can also be applied to achieve PCCI combustion. By using early direct injection during the compression stroke, higher in-cylinder temperature can help vaporize fuel and promote mixing. However, very early injection can cause wall wetting which consequently reduces thermal efficiency and increases THC emissions.[34,35] Late injection can also be used to achieve sufficient ignition delay for good mixing. The advantage of late injection is that it can provide better control over the combustion phasing.[36]

Increased injection pressure can enhance penetration depth of the fuel jet. Higher injection pressure is preferred to achieve a more premixed mixture, which can reduce PM

emissions but may cause slightly higher NOx emissions.[37] In addition, the engine efficiency may be negatively affected due to the extra work done by the injection pump.

High levels of EGR are used to achieve a longer ignition delay and reduce combustion temperature in order to reduce soot and NOx emissions.[38] However, very high levels of EGR can also increase THC and CO emissions, as well as reduce thermal efficiency.[39] Manente et al.[40] examined how EGR rate affects engine-out emissions during partially premixed combustion. They found that when EGR rate is increased, efficiency does not diminish, while low CO and HC emissions are achieved with EGR as high as 45%. NOx emissions decrease with the increasing levels of EGR, and soot emissions remain at a low level. Lewander et al.[41] found that increasing the EGR level and reducing the engine coolant temperature can extend the engine operating range.

2.3 Impact of fuel on PCCI combustion mode

With regard to fuel, cetane number, aromatic content and distillation temperature are the three primary factors that affect PCCI combustion.[42] Other parameters such as oxygen content, viscosity and density can also impact PCCI combustion. Generally, low cetane number, low distillation temperature and low viscosity fuels are preferred to achieve the ignition delay and reach a more homogenous mixture inside the cylinder before ignition occurs, which can effectively reduce soot emissions. Cetane number is considered to be the most significant factor.

Low cetane number (CN) fuel is applied to promote ignition delay, as well as to extend the load range.[43,44,45] However, low CN fuels still have problems at low load and high EGR conditions because of ignition difficulty, and result in higher fuel consumption. Higher pressure

oscillation ringing and enhanced heat transfer after combustion are also problems for low CN fuels.[46]

With the increasing of fuel aromatic content, the density and viscosity of the fuel would increase while the CN would decrease. Neill[47] showed that higher PM and NOx emissions will result from high aromatic content fuel. The high PM emissions for high aromatic content fuel is due to the high carbon content, and the ring structure of aromatics can strongly assist soot precursor formation. The higher adiabatic flame temperature can effectively advance the combustion phasing for high aromatic fuel, which can increase NOx emissions.[42]

Paraffinic fuels have shorter ignition delay compared to aromatic fuels, because the chain structure is much easier to decompose than aromatic rings. As a result, paraffinic fuel can keep the combustion efficiency high even with very late injection timings. The shorter ignition delay for paraffinic fuel can effectively increase the combustion duration and decrease the maximum rate of heat release, which can reduce the NOx emissions. CO and UHC emissions are also reduced by paraffinic fuels because aromatic fuels achieve a leaner mixture before ignition occurs.

Low distillation temperature fuel can improve the homogeneity of the mixture before ignition occurs. The reduced local equivalence ratio can highly suppress the PM formation, which could improve the soot-NOx trade-off.[48] In addition, thermal efficiency can also be improved by low distillation fuel.

Oxygenated fuels are used to reduce soot emissions. High oxygen content fuels can reduce local fuel/air ratio and reduce soot emissions as a consequence. Biodiesel is also known to

reduce CO, UHC and soot emissions simultaneously. However, NOx emissions usually increase with oxygenated fuels. [49,50,51]

Lilik and Boehman[13] found that during PCCI combustion, high ignition quality fuel can reduce incomplete combustion products arising from an over lean charge. They showed that LTFT fuel can reduce PM, NOx, CO and THC simultaneously with a slight increase in brake thermal efficiency (BTE). As a high CN fuel, LTFT will have a lower lean limit of combustion than a low CN fuel. With a short ignition delay, incomplete combustion products, CO and THC, are reduced because over-lean charge is avoided. Reduced bulk cylinder temperature reduces NOx emissions. PM emissions are also reduced due to the low aromatic content of LTFT fuel and the premixed combustion.

However, cetane number alone does not provide this effect. A means of reducing unburned CO and THC from PCCI combustion, in addition to PM and NOx, is to utilize a fuel with high n-alkane content and high cetane number. The key to this effect is to use a fuel with a low critical equivalence ratio.[52] In other words, one needs a fuel that burns to completion under lean, dilute, low temperature conditions. LTFT fuel has very high n-alkane content, which has higher reactivity compared to fuels with high aromatic content. As a result, LTFT fuel will auto-ignite at a lower equivalence ratio, which means it has a low "critical equivalence ratio".

Renewable diesel can be produced from animal fats or vegetable oils (referred to as lipids). As a renewable product, renewable diesel can reduce greenhouse gas emissions. Lipids are transformed into fatty acids using a hydrolysis process, and then a thermo-catalytic process removes oxygen by decarboxylation reaction.[53] By hydro-treating fats and oils with heat and hydrogen over a catalyst, renewable diesel, propane, CO_2 and H_2O are produced. Renewable

diesel has many similarities in terms of carbon footprint, renewewable energy content, cost of production and feedstock limitations as biodiesel, which is made from transesterification of lipids.[54] There is virtually no industrial scale Fischer-Tropsch fuel production today in the United States, but renewable diesel production could ramp up rapidly if sufficient lipid feedstock was available. The properties of renewable diesel such as CN and alkane content are very similar to LTFT. This research compares RD with LTFT fuel to examine if it provides the same benefit on CO and THC reduction.

2.4 Post injection

Post injection also provides an effective way to reduce PM emissions from diesel engines. Post injection means adding a short injection following the main injection. When injection dwell and the amount of fuel by post injection is properly adjusted, PM, NOx, CO and THC could be reduced simultaneously.[55]

One theory of soot reduction by post-injection is that fuel from post-injection interacts with the main-injection mixture. Post injection could enhance the mixing of the main-injection mixture with fresh oxygen and reduce the local equivalence ratio, which could reduce the formation and enhance the oxidation of soot. Studies also shown that the heat release from post injection could increase local temperatures and enhance the oxidation of soot generated from main-injection. The remaining soot from the main injection could be carried to the squish area and oxidizes there.[56,57]

Another theory of soot reduction by post-injection is that fuel injected by post-injection does not produce soot or produces very little soot. Desantes et al.[58] argues that there is a disconnection between the main and post combustion, which is called “split flame”. The

reduction of soot formation is due to the spray tip where soot are formed are not replenished with fuel when injection is terminated and then restarted.[59] Bobba et al.[60] assert that with early main injection, soot reduction is because fuel from post-injection is burning soot-free; while with late main injection, fuel from the post injection interacts with soot produced from the main injection both in the piston bowl and squish region.

Injection dwell has a profound impact on soot reduction from post-injection. Soot emissions cannot reduce or would even increase if injection dwells between main and post injection is too short or too long. With close-coupled post-injection, which means the injection dwell is short, soot reduction is mainly due to the enhanced fuel-air mixing and soot oxidation caused by increased temperature. The post injection jet could enter the squish region and improve soot oxidation there. Close-coupled post-injection could also avoid the fuel efficiency penalty.[61] Some study also shown that long dwell post-injection could result in higher soot reduction, which is caused by the "split flame" mechanism and also interaction of the post injection with soot from the squish volume.[62]

The effect of engine speed on soot reduction varies for different engines. For light duty engines, increased engine speed could enhance the soot reduction under post-injection conditions.[63] This is because high engine speed could increase the flow velocity and swirl in the cylinder. However, for heavy-duty engine, increased engine speed results in less soot reduction.[64] O'Connor et al.[64] also showed that increased engine load could reduce the percentage of soot reduction by post-injection. Under increased EGR level, post injection could more effectively reduce soot emissions.[65]

2.5 Soot formation and nanostructure

2.5.1 Soot formation and oxidation

Soot formation is a complex process which includes fuel pyrolysis or oxidative pyrolysis, soot nucleation, surface growth, coagulation/coalescence, agglomeration and soot oxidation,[66,67] as shown in Figure 2.3. Some of those processes occur simultaneously.

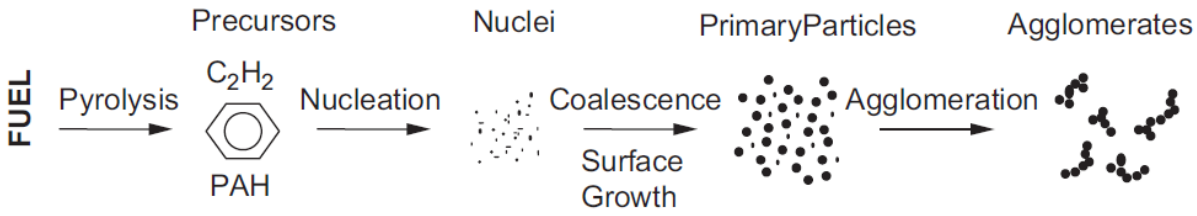

Figure 2.3 Soot formation process[68]

Fuel pyrolysis expands the definition of pyrolysis to include the fuel decomposition process without significant oxidation although even oxygen may present. Pyrolysis happens in regions where fuel/air ratio is high due to the fuel not being premixed well with air or due to a deficit of air. The products of fuel pyrolysis are important precursors and building blocks for soot.

Nucleation involves the formation of an embryonic species which grows faster than it decomposes or otherwise reacts.[69] Those nuclei provide sites for surface growth, which can greatly influence the total soot mass produced. Soot particle growth is a process in which gas species attach onto the soot surface. The nucleation of soot particle precursors requires higher temperatures, up to 1300-1600K,[18] while the growth of soot can proceed at lower temperatures. Keeping the mixture temperature below the soot nucleation temperature provides an effective way to reduce total soot emissions.

Collisions between soot primary particles can cause coagulation and aggregation.[70] Soot coagulation is also called coalescence, which occurs simultaneously with soot particle growth. Coagulation can result in larger and more varying shaped particles which are not round. Aggregation occurs when soot particles are out of the cylinder and stop growing. Large groups of particles are formed during this process.

Oxidation can occur throughout the soot formation process. Soot oxidation/gasification can be achieved with O_2, CO_2, H_2O (vapor) and NO_2, among which NO_2 is the most reactive at low temperatures (300-700^oC). Catalysts can also be used to modify the gasification mechanism and lower the activation energy.[71] Soot oxidation can be enhanced with increased temperature. However, higher temperature can also enhance soot formation. Increased temperature can reduce total soot mass only when fuel is well mixed with air.

2.5.2 Soot nanostructure

Soot emitted from diesel engines are usually observed as chain-like aggregates which are approximately 0.1-1μm in size, and composed of several tens to hundreds of primary spherical particles.[72] Soot primary particles can be described as having a shell/core structure. The core is amorphous carbon while the outer shell is composed of small graphene layers, most of which are parallel to the primary particle surface. According to Hurt et al.[73] this soot nanostructure is a thermodynamic equilibrium state for polyaromatic clusters under high temperature. The core/shell boundary is where orientation elastic strain overcomes the free energy difference between bulk isotropic and ordered phases. The small graphene layers can also be considered as short stacks with turbostratic structures called crystallites, which has an inter-layer spacing of

0.35-0.36 nm. Surface functional groups such as C=O, C-O-C and C-OH are also present on the surfaces of the primary soot particles.

2.6 Soot nanostructure and oxidative reactivity

Soot oxidation is an important issue for the regeneration of Diesel Particulate Filters (DPFs). Highly reactive soot which can oxidize at lower temperatures or higher rates is preferred. The reactivity of soot is highly dependent on its nanostructure.

2.6.1 The dependence of soot oxidative reactivity on its nanostructure

The surface functional groups, size and curvature of the graphene layers all affect the reactivity of soot particles.[74] The carbon atoms on the edge of graphene layers are much more reactive than those in the basal plane. Primary soot particles composed of smaller graphene layers have a higher edge/basal carbon atom ratio, which can result in higher reactivity.[74] The curvature of the graphene layers results from 5-membered rings. Within this structure, orbital overlap can cause bond strain, so the C-C bond is weakened, which also results in increased oxidative reactivity. In addition, soot with high oxygen content, which contains more oxygenated surface functional groups, also have a much higher reactivity.[75]

2.6.2 The dependence of soot nanostructure on synthesis condition

The nanostructure of soot is highly dependent on the synthesis conditions such as temperature, fuel type, air/fuel ratio, engine load and speed. According to Vander Wal et al.[76] once carbonization has taken place, soot nanostructure will not change unless exposed to extremely high temperature (>1800^{o}C). Low temperature (1250^{o}C) yields amorphous soot particles. While at high temperature (1650^{o}C), soot particles appear to have more organized nanostructure. Higher engine loads would result in more ordered soot nanostructure and a

slightly lower fractal dimension, which means the soot aggregations are more compact.[77] The aggregation particle size would also increase slightly with the increased engine load.

Fuel also has a strong influence on the soot nanostructure. Fuel which contains 5-membered rings yields more grephene layer curvatures than fuel that only contains 6-membered rings. Fuel that can produce more C_2 segments such as ethanol also results in more curvature, because C_2 fragments can build up C_5 rings. Oxygenated fuels such as biodiesel yield more disordered soot nanostructure and is more easily oxidized.[78] Fuel with high paraffinic content produces much less soot than fuel with high aromatic content.

2.6.3 Soot nanostructure change during oxidation

The nanostructure of soot changes during oxidation. Firstly, hydrocarbons trapped in soot particles can go through carbonization process by the extraction of hydrogen atoms, which results in growth of graphene layers.[79] Secondly, high temperature can provide the activation energy required for layers rearrangement and form energetically favorable structure.[80] In addition, active sites created during the oxidation process can also facilitate the growth of carbon grephene layers.[81] Vander Wal et al.[82] proved that the structure change during oxidation depends on the initial nanostructure of the soot particle. Internal burning of soot particles is facilitated by the developing and opening of pore areas. Soot produced from different fuels or operating conditions can go through different structural changes during the oxidation process, which also affects the oxidation rate constant. Song et al.[19] found that soot produced from B100 is far more reactive than soot from FT fuel, which goes through a shrinking core type of oxidation. Soot produced from B100 undergoes a unique oxidation process, which leads to a capsule-type oxidation and eventual formation of grapheme ribbon structures. They suggested that the incorporation of greater surface oxygen functionality in the B100 soot provides the means for more rapid

oxidation and drastic structural transformation during oxidation process. Al-Qurashi et al.[20] found that soot produced from 20% EGR condition show internal burning during the later stage of oxidation, while soot produced from 0% EGR condition only shows external oxidation. Because carbon removal from the particle interior is much faster than that from the exterior, soot produced from 20% EGR condition has higher reactivity compared to soot produced under 0% EGR condition. When internal burning or structure rearrangement occur, the reactivity of soot decreases due to the reduced density of active sites.[83]

Chapter 3.

Experimental

3.1 Experimental Instruments

3.1.1 Testing Engines

1) Single-cylinder engine

The first PCCI testing was conducted using a single cylinder engine based on a GM/Isuzu 1.7L, 4-cylinder, common-rail, direct injection diesel engine. As has been described by Zhu et al.[84] compression ratio was reduced from 19:1 to 15:1 in order to achieve PCCI combustion. The original piston was changed to one with a larger combustion bowl. The cylinder has 4 valves and a centrally placed fuel injector. An EGR cooler and EGR valve cools and meters the exhaust into the engine intake air.

A water-cooled Kistler 6041A pressure sensor was installed to measure in-cylinder pressure. Pressure data were recorded by CAS software with a resolution of 0.2^{o} crank angle, and 200 consecutive cycles for each testing point. Pressure traces were smoothed by a low-pass filter and a cubic spline algorithm. Apparent heat release rate (AHRR) was calculated according to a zero-dimensional single zone model. Bulk cylinder temperature was calculated with a combination of AHRR and ideal gas law.[85]

Table 3.1 Isuzu single cylinder engine specifications

Displacement	425cm^3
Bore	79.0 mm
Stroke	86.0 mm
connecting rod length	160.0 mm
wrist pin offset	0.6 mm
compression ratio	15:1
Valves	4/cylinder
Camshafts	2
fuel pressure	100-1400bar

2) Multi-cylinder engine

The engine used for PCCI and post-injection studies is a 2010 General Motors (GM) 1.9L ZDTH turbodiesel engine with a compression ratio of 17.5:1. The engine specifications are shown in Table 3.2. This engine has a common rail injection system with solenoid-type Bosch injectors. An AVL fuel conditioning cabinet that maintains a constant fuel supply temperature and pressure is applied to supply fuel to the engine. The fuel consumption is monitored by a MicroMotion mass flow meter. The engine's flywheel is coupled through a flexible driveshaft to a steady state DC dynamometer, which drives a constant engine speed while measuring torque via a load cell.

A Drivven/National Instruments ECU/DAQ cart was applied for engine control and data acquisition, which can implement a complex injection schedule consisting of up to 5 separate injections per cycle. Pressure traces were recorded with a resolution of 0.1 degree crank angle. Apparent heat release rate (AHRR) and bulk cylinder temperature were calculated from the cylinder pressure trace.

Table 3.2 GM multi-cylinder engine specifications

Displacement	1.909 L	**Number of Valves**	16 (2 in., 2 ex. per cyl.)
Stroke	90.4 mm	**Swirl Control**	1 intake port throttled
Bore	82.0 mm	**Max Power**	110 kW @ 4000 RPM
Connecting Rod	145 mm	**Max Torque**	315 N-m @ 2000 RPM
Compression ratio	17.5:1	**Injector Angle**	148 degrees
Cylinder Layout	Inline 4	**Nozzle Layout**	7 holes, .15mm diameter

3.1.2 Testing facilities

Gaseous emissions including CO_2, CO, THC, CH_4, NOx and O_2 concentrations were measured by a Horiba MEXA-7500DEGR emission bench. EGR rate was also calculated by the Horiba bench using measurements of exhaust and intake CO_2 concentrations, shown in Eq (3.1)

$$\text{EGR rate} = ([(CO_2\text{int}) - (CO_2\text{atm})]/[(CO_2\text{exh}) - (CO_2\text{atm})]) * 100\% \quad (3.1)$$

Filter smoke numbers (FSN) were measured by an AVL 415 smoke meter. Sampling volume was 1000 ml for each condition. An AVL 450s combustion noise meter was used to monitor engine combustion noise, in order to keep the noise of single cylinder engine below 90dB.

Particulate emissions were sampled using a Sierra Instruments BG-3 microdilution tunnel with a dilution ratio of 10:1. Total flow rate was 90 slpm, with sample flow rate of 9 slpm. Pallflex membrane Teflon filters with a diameter of 47 mm were used to collect PM. Four filters were collected for each condition with a sampling duration of 90 seconds. Filters were weighed 3 times after being conditioned in a constant humidity chamber for at least 24 hours. After loading, filters are also weighed 3 times after being re-conditioned for 1 hour in the same constant humidity chamber. The loaded filter conditioning time was reduced to 1 hour to minimize

soluble organic fraction (SOF) evaporation. Static charge was removed from filters using a pair of NRD 2U500 Micro Balance Ionizers, made of Polonium 210 with 500 μCi activity.

Particulate size distribution was measured by a TSI Scanning Mobility Particle Sizer (SMPS) consisting of a 3080 electrostatic classifier, a 3081 differential mobility analyzer, and a 3776 ultrafine condensation particle counter.

3.1.3 Fuel

Three different fuels are tested in PCCI studies: a conventional ultra low sulfur diesel fuel (ULSD), a synthetic fuel produced by a low temperature Fischer-Tropsch (LTFT) process from natural gas, and a renewable diesel (RD) fuel produced from camelina oil. Only one fuel, ULSD is used for the post-injection study. Key fuel properties are shown in Table 3.3.

ULSD serves as the baseline diesel in the PCCI studies. ULSD has much lower cetane number and higher aromatic content compared to the other two fuels; LTFT and RD have no or very little amount of aromatics. LTFT has very high n-alkane content, up to 72%, which was shown to produce very low PM and NOx emissions in previous studies.[86] Although the n-alkanes of RD is much lower compared to LTFT, it has similar amount of saturates. This means renewable diesel has higher fractions of slightly branched iso-alkanes. The renewable diesel used in this study has similar cetane number, density and H/C ratio as LTFT fuel. However, the viscosity of RD is much higher and the n-alkane content is much lower than LTFT. Although LTFT and RD have very similar T90, LTFT fuel has much lower T50 than RD. The low distillation temperature of LTFT fuel makes it easier to evaporate than RD.

Table 3.3 Fuel specifications

	ULSD	LTFT[87]	Renewable[88]
Cetane Number	45.1	81	89.2
C (wt%)	87.32	84.3	84.86
H (wt%)	13.34	15.2	15.09
Molar H/C	1.820	2.183	2.119
(A/F)s, dry	14.47	14.98	14.89
Density (kg/m^3)	831.8	760	784.4
Lower heating value (MJ/kg)	42.6	43.8	43.9
Aromatics(wt%)	31.5	0	0.7
Polycyclic aromatics (wt%)	8.3	0	0.1
Saturates (wt%)	-	99	94
n-Alkanes (wt%)*	32.3	72	32.2[24]
T50 (^{o}C)	256	236	300
T90 (^{o}C)	312	308	315
Kinematic viscosity @40^{o}C (mm^2/s)	2.40	1.87	3.61
Sulfur (ppm wt)	10	2	4.0

* Measurements from the present work unless noted otherwise

3.1.4 Test Conditions

1) PCCI combustion in single-cylinder engine

The three fuels, ULSD, LTFT and RD, were tested using conventional and PCCI combustion modes. The engine was operated at a steady state operating point of 1500 rpm and 3.5 bar indicated mean effective pressure (IMEP), which is a low load operating point common

in the duty cycle of passenger car diesel engines. Engine speed and load were kept constant for all fuels during both conventional and PCCI combustion modes to enable straight-forward comparisons. Both conventional and PCCI combustion modes used a single injection per cycle. Fuel injection pressure was 300 bar for conventional and 700 bar for PCCI combustion modes, respectively. Higher injection pressure is used in the PCCI operating condition because it advances end of injection (EOI) and increases mixing before start of combustion (SOC). In addition, higher injection pressure also gives more momentum to the fuel droplets, which helps fuel air mixing before ignition occurs. For conventional combustion, EGR rate was set to 25% and injection timing was adjusted to set CA50 (the crank angle of 50% burn) at 10 degrees after top dead center (aTDC). For PCCI combustion, EGR rate was set to 40% and injection timing was swept from the knock limit to the misfire limit in increments of 2 degrees for each of the three fuels. Increased levels of EGR under PCCI combustion can effectively prolong the ignition delay, improve fuel air mixing and reduce combustion temperature. The conventional and PCCI operating conditions used here are based on the operating conditions developed by Jacobs et al.[89] Both conventional and PCCI combustion apply a single injection strategy. Here the injection timing means the start of injector coil energizing. The knock limit was defined as when combustion noise from the engine reached 90 dB, while the misfire limit was defined as the point where the coefficient of variation (COV) of the IMEP reaches 5%.

Table 3.4 Operating conditions for single-cylinder engine PCCI study

		Conventional	PCCI
Speed (rpm)		1500	
IMEP (bar)		3.5	
Injection Pressure (bar)		300	700
EGR rate (%)		25	40
Injection Timing (^{o}ATDC)	ULSD	-10	-18, -16, -14, -12, -10, -8
	LTFT	-8	-10, -8, -6, -4, -2, 0
	RD	-8	-12, -10, -8, -6, -4, -2, 0

2) PCCI combustion in multi-cylinder engine

To better understand PCCI combustion in multi-cylinder engines, the same three fuels, ULSD, LTFT and RD, were tested under both conventional and PCCI combustion modes. The multi-cylinder engine was still operating at a steady state, low load condition at a same speed 1500 and 2.6 bar brake mean effective pressure (BMEP). Conventional combustion mode applies a spilt injection 1.6 ms before the main injection with a duration of 0.26ms, while PCCI combustion mode applies a single injection. For injection pressure, PCCI combustion still applies a higher injection pressure compared to conventional combustion mode. Fuel injection pressure was 394 bar for conventional combustion mode, which is a default setting for this engine, and 600 bar for PCCI combustion modes, respectively. Similarly for the single-cylinder engine study, EGR rate was set to 25% and injection timing was adjusted to set CA50 (the crank angle of 50% burn) at 10 degrees after top dead center (aTDC) for conventional combustion mode; EGR rate was set to 40% and injection timing was swept from the knock limit to the misfire limit in

increments of 2°CAD for PCCI combustion modes. Here the injection timing means the start of energizing the injector coil.

Table 3.5 Operating conditions for multi-cylinder engine PCCI study

		Conventional	PCCI
Speed (rpm)		1500	
BMEP		2.6 bar	
Boost (bar)		1.06	
Swril		93%	
Injection pressure (bar)		394	600
EGR rate (%)		25	40
Pilot Injection (°bTDC)		19.9	N/A
Main Injection timing (°bTDC)	ULSD	5.5	10.5, 8.5, 6.5, 4.5, 2.5
	LTFT	5.5	8.5, 6.5, 4.5, 2.5, 0.5, -1.5, -3.5
	RD	5.5	8.5, 6.5, 4.5, 2.5, 0.5, -1.5, -3.5

3) Post-injection

The impact of post-injection on engine emissions was also tested on the GM 1.9L multi-cylinder turbodiesel engine.[18] A baseline case was developed to compare with post-injection conditions. All baseline and post-injection conditions were operated at a constant speed and load which is 1800 rpm and 4.8 bar BMEP. This is a low to medium load representing a common engine operating point. All operating conditions include of a main injection at 3° bTDC, and a pilot injection which starts 1.6 ms before the main injection.

All post-injection conditions were developed by comparing with the baseline condition. All parameters except injection scheduling were held constant. Post-injection conditions were achieved by splitting a portion of the fuel injected during the main injection to the post injection.

For post-injections, the main injection was reduced by a certain percentage, and the post injection was scheduled a certain crank angle degrees after the end of the main injection. Since injection duration does not have a linear relationship with the amount of fuel injected, the injection duration of the post injection is adjusted by keeping torque constant. Since post-injection could lead to change in fuel consumption, the total fuel injected during the main and post injection under post-injection conditions could be different from the main injection for the baseline condition.

A test matrix was developed to understand the impact of the amount of fuel by post-injection and the dwell between main and post injection, which is shown in Table 3.6. This matrix follows the study of Martin et al.[18], which is shown in Appendix B. The reduction of fuel injected by main injection was reduced by 3%, 4.5%, 6%, 7.5%, 9%, and 10.5%. The injection dwell was 4, 10, and 16 crank angle degrees respectively. Bulk soot samples were collected from 4.5% and 7.5% fuel from post injection. Different characterization methods are applied to measure soot properties and relativities, as illustrated in Table 3.6. To further understand the mechanism of PM reduction by post-injection, conditions with reduced loads by taking out the post injection event are also designed, which is referred to as main injection only with reduced load conditions.

Table 3.6 Operating conditions for post injection study

Injection Dwell	Reduction of Main Injection Duration (%)					
	3	**4.5**	**6**	**7.5**	**9**	**10.5**
4ºCAD		TGA,XPS		TGA,XPS,Raman,TEM		
10ºCAD		TGA,XPS		TGA,XPS,Raman		
16ºCAD		TGA,XPS		TGA,XPS,Raman,TEM		
Main Only		TGA,XPS		TGA,XPS,Raman		
Baseline	TGA,XPS,Raman,TEM					

3.2 Soot characterization methods

In order to analyze the reactivity and other properties such as nanostructure and functional groups of soot generated from different engine operating conditions, various materials characterization techniques are applied, which will be discussed in the following sections.

A vacuum pump is used to draw exhaust gas through a Pallflex Emfab 90 mm membrane filter. Soot is then collected from the filter after a period of time using a spatula.

3.2.1 Thermogravimetric analysis (TGA)

A TA instruments STD Q600 Thermogravimetric analyzer with recording software is applied to characterize the oxidative reactivity and volatile organic fraction (VOF) of soot. Soot with higher reactivity oxidizes at a higher speed, which benefits the DPF regeneration process. Table 3.7 shows the procedure for thermogravimetric gravity analysis. Nitrogen is first introduced into the instrument and temperature is increased to the desired oxidation temperature (525 ℃/500 ℃) to drive off the VOF from soot. After 15mins of stabilization, air is introduced

for oxidation. Soot samples collected from the PCCI study are all oxidized at 525 ℃, while soot collected from the post-injection study are oxidized at 500 ℃.

Table 3.7 Thermogravimetric analysis procedure

Step	Procedure
0	Start with nitrogen
1	Ramp 10 ℃ to 30℃
2	Isothermal for 5mins (to stabilize sample)
3	Ramp 10℃ to 525℃/500℃
4	Isothermal for 15mins (to remove volatile matter)
7	Select zero air
8	Isothermal for 240mins

The apparent rate constant is used to represent the reactivity of PM. The apparent rate constant for soot oxidation is calculated according to the oxidation weight trace by the following equation[90]:

$$\frac{dm_c}{m_c} = -k_c \times p_{o_2} \times dt \qquad \text{(Equation 3-1)}$$

Where k_c is the apparent rate constant (1/Pa/min) for soot oxidation at the oxidation temperature, m_c is residual soot mass at time t, and P_{O2} is the partial pressure of oxygen (Pa) for the oxidation environment.

P_{O2} stays constant during the oxidation process, if kc is also assumed to be constant through the oxidation process, equation 3-1 could be derived to the following equation[91]:

$$\frac{m_c}{m_{c,0}} = e^{-k_c p_{o_2}(t-t_0)} \qquad \text{(Equation 3-2)}$$

Where $m_{c,0}$ is the initial mass of soot, t_0 means the starting time of oxidation. The left side of this equation is the percentage of mass left during the oxidation process, so this equation provides a more straight forward way to derive the rate constant k_c for soot samples. The overall rate constant k_c is calculated using curve fitting via Igor Pro. 6.1 software. The instantaneous rate constant at a certain stage of oxidation could also be calculated from equation 3-1.

3.2.2 Surface area analysis

BET surface area is used to represent the surface area and pore volume for soot samples. The surface area of soot samples was measured by a Nova 4200e BET surface area analyzer. Up to 200 data points could be collected. Ultimate vacuum achievable is 10mill torr. The minimum relative pressure (P/Po) resolution using nitrogen gas is 2×10^{-5}. Nitrogen absorption was performed at a temperature of 77K for 3 hours for each sample. The surface area was calculated by BET equation for a pressure range $P/P_0 = 0.0488 – 0.3$.

3.2.3 Raman spectroscopy

Raman spectroscopy is used to analyze the relative degree of order of soot samples. Soot with less degree of order has higher reactivity. A Renishaw inVia Raman Microscopy system equipped with a 532 nm solid-state laser and a 1800 lines/mm grating was used for spectrum collection through an Olympus SLMPlan 20× objective aperture for characterization of the nanostructural characteristics of the bulk soot samples. To avoid degradation of samples, the incident laser power on samples was reduced to 10% of the maximum power. All spectra were obtained in extended scan mode in the range of 2000 - 800 nm-1 with 10 exposures per second. Raman spectra were recorded at five different positions for each sample. In all, 15 - 20 accumulations were recorded for each position with cosmic ray removal to reduce noise in the spectra. IGOR Pro 6.10 (Wavemetrics Inc.) was applied to do curving fitting for the spectra,

using a 3L1G fitting method, following the recommendations by Sadezky et al.[92] A Lorentzian peak at 1590 cm^{-1} is G band, which represents graphite structure. A Lorentzian peak at 1350 cm^{-1} is D1 band, which represents disordered graphitic lattice, for example, graphene layer edges. A Lorentzian peak at 1200 cm^{-1} is D3 band, which represents amorphous carbon such as organic molecules. A Gaussian peak at 1500 cm^{-1} is D4 band, which represents carbon–carbon stretched bonds. The area ratio of the D1 and G band (AD1/AG) or the ratio peak intensity of the D1 and G band (ID1/IG) are usually used to describe the degree of order of soot structure. In addition, the full width at half maximum (FWHM) of the D1 and G peak can also indicate soot nanostructure.

3.2.4 X-ray diffraction (XRD)

XRD measures the crystalline size and interlayer spacing of soot particles. A Rigaku rotating anode X-ray powder diffactometer was used to generate XRD pattern for soot samples, which is equipped with a 12kW high intensity rotary anode generator, graphite diffracted beam nomochrometer, 2 wide-angle horizontal goniometers, and a scintillation counter detector. The incident beam was a Cu-Kα radiation with a wavelength of $\lambda = 0.154nm$. XRD is used for indication and quantification of compounds, lattice constant, crystal grain size and distortions[93]. Powder soot samples were pressed in to the cavity of a low-background quartz support then tested. XRD data was collected from $2\theta = 5^{o}$ to 110^{o} with steps of 0.02 degrees.

There are primarily three peaks in the XRD spectra of soot samples, a (002) peak around 25^{o}, (10) peak around 43^{o}, and a (110) peak around 77^{o}. Interlayer spacing (d002), stacking height (Lc), crystalline basal plane diameter (La) and average number of layers (N) could be calculated using the following equations.

The interlayer spacing d_{002} was calculated using Braggs equation:

$$d_{002} = \frac{\lambda_{incident}}{2\sin\theta_{002}} \quad \text{(Equation 3-3)}$$

where $\lambda_{incident}$ is the incident wavelength of Cu-Kα, which is 0.154nm, and θ_{002} is the peak position of the (002) peak.

Scherrer's equation is used to calculate the crystalline size. The crystal basal plane diameter L_a, and the stack height L_c can be derived from the following equations:

$$L_c = \frac{0.89\times\lambda_{incident}}{\beta_{002}\cos\theta_{002}} \quad \text{(Equation 3-4)}$$

$$L_a = \frac{1.84\times\lambda_{incident}}{\beta_{10}\cos\theta_{10}} \quad \text{(Equation 3-5)}$$

where θ_{002} is the peak position of the (002) peak, θ_{10} is the peak position of the (100) peak., β_{002} is the full width at half maximum of (002) peak, and β_{10} is the full width at half maximum of (100) peak.

The number of layers per crystalline could also be calculated by the following equation using crystalline height and interlayer spacing:

$$N = \frac{L_C}{d_{002}} \quad \text{(Equation 3-6)}$$

JADE software was used to analyze the XRD patterns and fit the background. Igor Pro. 6.1 was used to curve fitting the XRD patterns. Peak position and full width half maximum were obtained from the two softwares.

3.2.5 X-ray photoelectron spectroscopy (XPS)

Surface functional groups and elemental composition were analyzed by Kratos Axis Ultra X-ray Photoelectron Spectroscopy system with a monochromatic Al X-ray source. The Specimen Analysis Chamber (SAC) can reach a vacuum of 1 x 10^{-9} torr. The analysis area is 2*1mm with an energy resolution of 0.5 eV. Samples were pressed onto indium foils and then mounted on the sample bar by double-sided conductive tapes. Here indium foil is used to eliminate carbon and oxygen contamination from the sample bar and double-sided tapes. For survey scans, samples were scanned from binding energy 0 - 600 eV using pass energy of 160 eV. For C 1s core scan, 5 – 10 scans were averaged from binding energy 275 – 300 eV using pass energy of 20 eV. Similarly, for O 1s core scan, 10 – 15 scans were averaged from binding energy 520 – 540 eV using pass energy of 20 eV. CasaXPS software was used to analyze the elemental composition and also the bonding state of carbon and oxygen elements. Curve fittings of C 1s and O1s spectra were also analyzed by this software.

The peak positions for C 1s spectra fitting follows the work developed by Smith et al[94]. Table 3.8 shows the peak positions used for C 1s curve fitting. The peak position for C 1s curve were first adjusted to 284.4 eV and then fitted by the following assignments.

Table 3.8 Peak positions for interpretation of C 1s spectra

Peak	Assignment	BE (eV)
C-C	Cyclopentane ring atoms within cluster	283.2
C-C	Primary C-C/C-H bond, sp2 bonded carbons	284.4
C-C	C in cycloheptane or larger rings within clusters, sp3 bonded carbons	285.1
C-O	Ether and hydroxyl bonded C, C associated with ether bond in lactone/esters	286.2
C=O	Carbonyl groups and carbons attached to two ether/hydroxyl groups	287.1
COO	Carboxyl, lactone and ester groups	288.6
Pi	HOMO-LUMO transition for primary C-C peak	291.5

The FWHM of C-O, C=O and COO peaks are 1.5 times the FWHM of C-C bond peaks, the FWHM of Pi bond peak is 2 times the FWHM of C-C peaks.

The O 1s spectra are fitted as C-O bond at 533.2 eV and C=O bond at 531.4 eV. The FWHM of the two peaks are considered to be the same. All peaks used for C 1s and O 1s fitting are composed of 30% Gaussian peak and 70% Lorentizian peak.

3.2.6 Transmission electron microscopy (TEM)

Soot morphology and nanostructure were characterized by a JEOL 3011 Transmission Electron Microscope (TEM), with a 200kV field emissions source. Digital images were acquired by AMT Imaging 5.4 slow scan camera system. For initial soot particles, TEM samples were obtained directly from the exhaust by inserting a probe mounted with lacy carbon Cu grid. Soot particles were drawn to the cold lacy carbon Cu grid by thermophoretic force. For partially oxidized soot particles, soot was dispersed in an ethanol solution under ultrasonic bath for 1 hour. Then the solution was dropped onto lacy carbon Cu grid. Low resolution images showing soot

aggregation morphology were taken with magnification of 40,000x, and high resolution images showing soot nanostructure were taken with magnification of 400,000x.

3.2.7 Electron energy loss spectroscopy (EELS)

EELS is also applied to examine difference between initial soot structure and soot structure change during oxidation process. It could be applied to measure the relative abundance of δ and π bonding for the initial soot and soot during oxidation. EELS spectra were taken with a Gatan #965 Quantum ER energy filter equipped on the JEOL 3100R5 transmissions electron microscopy. The TEM has a cold field emissions gun with double Cs correctors. EELS spectra were taken using scanning TEM (STEM) mode. The EELS spectra were obtained with a 2.0 cm camera length with 30um aperture size and at an energy dispersion of 0.1 eV. In EELS spectra, zero loss peak and C 1s excitations are recorded by dual EELS mode. C 1s excitation spectra were calibrated by setting zero loss peak at 0 eV.

Chapter 4.

Impact of fuel on PCCI combustion in single-cylinder engine[95]

Partially-Premixed Compression Ignition (PCCI) combustion creates a partially premixed charge inside the cylinder before ignition occurs. As a result, NOx and particulate matter (PM) emissions can be reduced simultaneously, relative to conventional diesel combustion.

Three different fuels: Ultra Low Sulfur Diesel (ULSD), diesel fuel produced via alow temperature Fischer-Tropsch process (LTFT) and a Renewable Diesel (RD) are tested in this research. Engine combustion performance, PM, NOx, CO, total hydrocarbon (THC) emissions, particle size distribution, soot morphology and nanostructure are examined for conventional combustion and various PCCI conditions.

In this chapter, PCCI combustion is tested in a single-cylinder Isuzu engine with the three fuels mentioned above to study the impact of fuel on PCCI combustion and emissions reduction.

4.1 Apparent rate of heat release

Figure 4.1 shows the apparent rate of heat release (ROHR) for the three fuels. ULSD fuel has longer ignition delays compared to the other two fuels due to its low cetane number and high aromatic content, while LTFT fuel and RD have similar ignition delays for both conventional and PCCI combustion modes. Here ignition delay is defined as the time interval between start of injection and start of combustion, and start of combustion means the crank angle where the apparent ROHR becomes positive. For conventional combustion, the ignition delay for ULSD is about 13 degrees, and ignition delays are 11 degrees for LTFT and RD. During PCCI combustion modes, the ignition delays are around 10 degrees for ULSD and 8 degrees for LTFT and RD. Although the ignition delays for PCCI combustion are reduced by increased injection pressure, the high combustion rate shows PCCI combustion still has more premixing compared to conventional combustion.

During conventional combustion, ULSD has a higher maximum ROHR due to its lower cetane number and longer ignition delay, which tends to increase the fraction of premixed burn. LTFT and RD have higher cetane numbers and shorter ignition delays during conventional combustion. The reduced fraction of premixed burn reduces the maximum ROHR compared to ULSD. For PCCI combustion, high paraffin content fuels, LTFT and RD have higher maximum ROHR compared to high aromatic content fuel ULSD. This is because increased injection pressure and higher EGR rate already made the charge well premixed before ignition occurs. So the composition of the fuel dominates the speed of combustion. Because alkane rich fuels have greater auto-ignition tendency than aromatic fuels, LTFT diesel and RD have faster reaction speed and higher maximum ROHR during PCCI combustion modes.

All the three fuels show two stage ignition during PCCI combustion because of the lean, premixed conditions. For ULSD, there is negative temperature coefficient (NTC) behavior between the low temperature heat release and high temperature heat release. However, under the conditions studied in these experiments, the two heat release peaks are not distinguishable for LTFT and RD. The reason for this is the high cetane number of LTFT and RD fuels makes the auto-ignition process faster than for ULSD. All the three fuels show single stage combustion under the conventional combustion. The high cylinder temperature and pressure prior to auto-ignition during conventional combustion modes accelerates the combustion process. As a consequence, there is no separate peak for low temperature heat release for conventional combustion modes.

With retarded injection timing, ROHR decreases because the piston is moving away from TDC when combustion occurs. Cylinder expansion acts to decrease cylinder temperature, which increases ignition delay and reduces the rate of combustion. So peak ROHR decreases and combustion duration increases as injection timing is retarded.

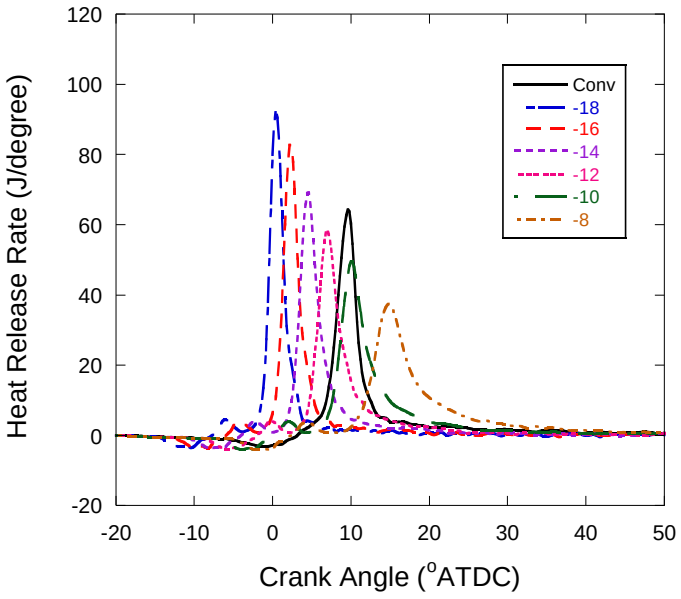
Heat Release Rate (J/degree)
Crank Angle (°ATDC)
Conv
-18
-16
-14
-12
-10
-8

(a)

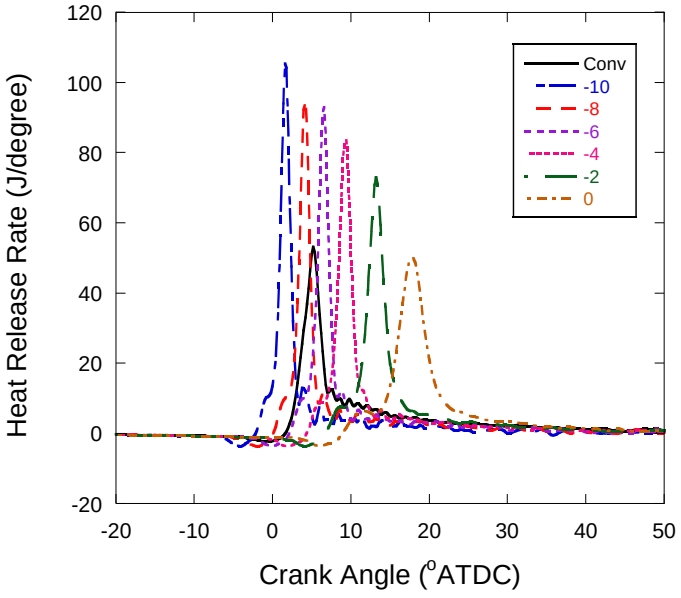
Heat Release Rate (J/degree)
Crank Angle (°ATDC)
Conv
-10
-8
-6
-4
-2
0

(b)

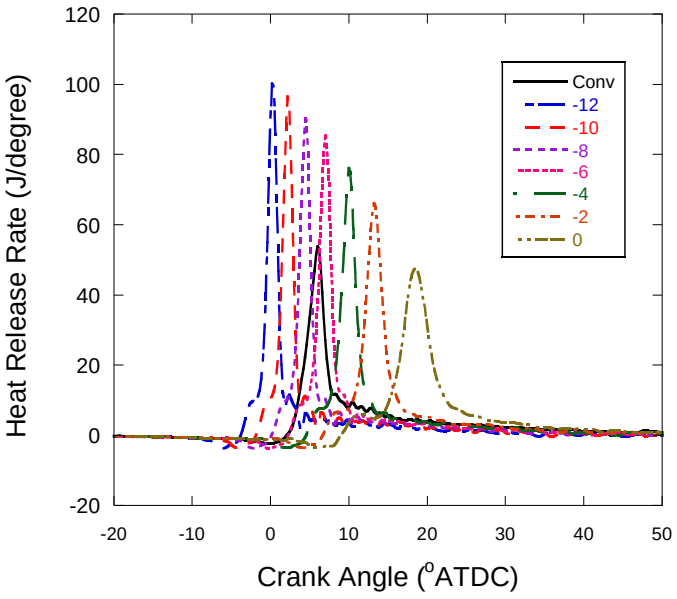

(c)

Figure 4.1 Heat release rate for conventional and PCCI combustion modes for (a) ULSD, (b) LTFT, and (c) RD fuel

4.2 NOx emissions

Figure 4.2 shows the NOx emissions for the three fuels. There are three important NOx formation processes[96]: 1) Thermal NOx, which is formed via the Zeldovich mechanism and occurs at temperatures above 1800K. The increase of temperature and reaction time can increase the formation of thermal NOx.[97] 2) Prompt NOx, which involves hydrocarbon fragments as intermediates in the formation of NOx. 3) Fuel NOx, which is generated from nitrogen-containing fuels. Thermal NOx is considered to be the dominant origin for NOx emissions from IC engines. As a consequence, the formation of NOx depends highly on temperature.[98]PCCI combustion can greatly reduce NOx emissions due to the reduced combustion temperature and reduced oxygen concentration. The higher heat capacity of CO_2 in the EGR gas can act as a

thermal sink. Increased rates of EGR can effectively increase the heat capacity of exhaust gas, and reduce oxygen content and combustion temperature, which can suppress NOx formation.

With retarded injection timing, the piston is moving away from TDC when combustion occurs, and cylinder temperature is reduced during the expansion stroke. Cylinder volume expansion can reduce cylinder temperature and combustion speed. More importantly, with the delay of combustion phasing, the time allowed for NOx formation under high temperature is also reduced. As a result, NOx emissions are further decreased with late injection timing under PCCI combustion.

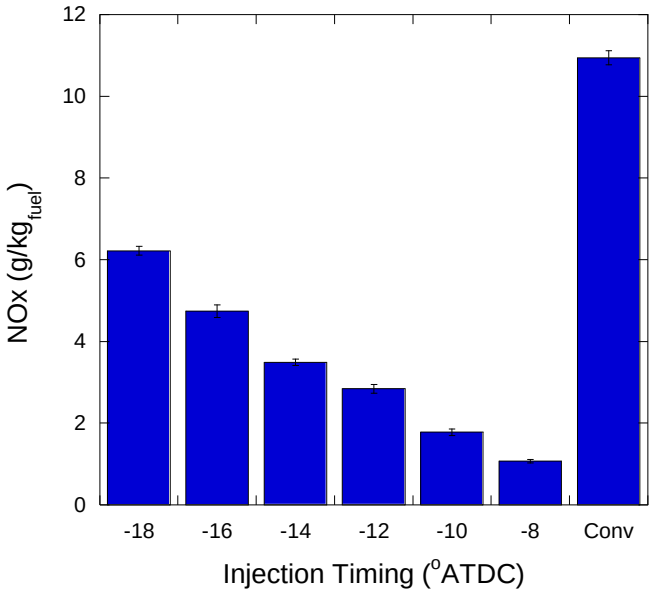

(a)

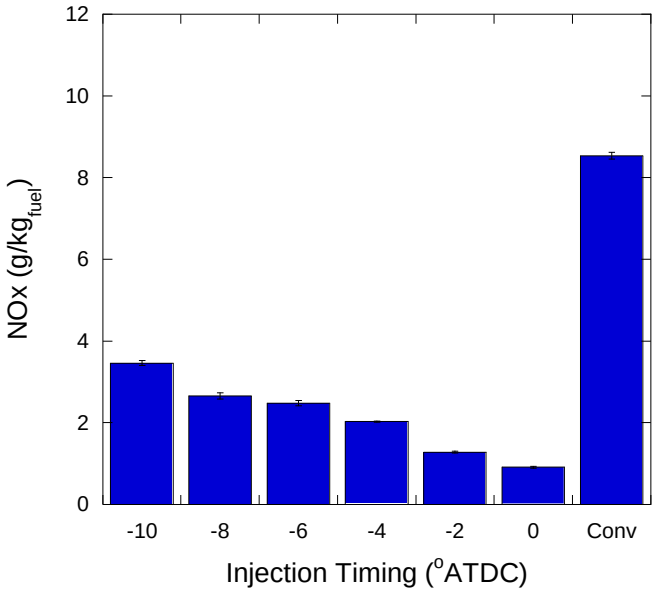

(b)

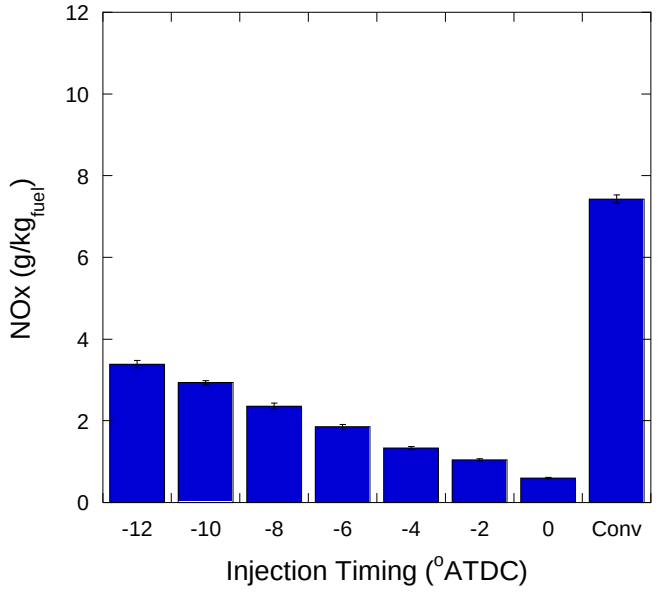

(c)

Figure 4.2 NOx emissions for conventional and PCCI combustion modes with (a) ULSD, (b) LTFT, and (c) RD fuel

ULSD yields higher NOx emissions than LTFT fuel and RD. Fuel with higher aromatic content generally has higher NOx emissions,[99] due to the higher adiabatic flame temperature for aromatic fuels. Although the maximum heat release rate of ULSD fuel is the lowest among the three fuels with similar CA50, according to Szybist et al.[100], timing for maximum cylinder temperature has the most significant correlation to NOx emissions as compared to maximum cylinder temperature, maximum heat release rate, and timing of maximum heat release. Figure 4.3 shows NOx emissions versus the timing of maximum cylinder temperature for the three fuels. ULSD reaches maximum cylinder temperature earlier compared to the other two fuels. This could be caused by the relatively earlier low temperature heat release. Cylinder temperature increases to a maximum quickly and then reduces slowly. As a result, longer time is provided for NOx formation if cylinder temperature reaches a maximum earlier. ULSD has a low cetane number, so it has a longer ignition delay, which can provide longer time for the charge to premix with air before combustion occurs. Higher combustion temperature and higher local oxygen concentration can both promote NOx formation.

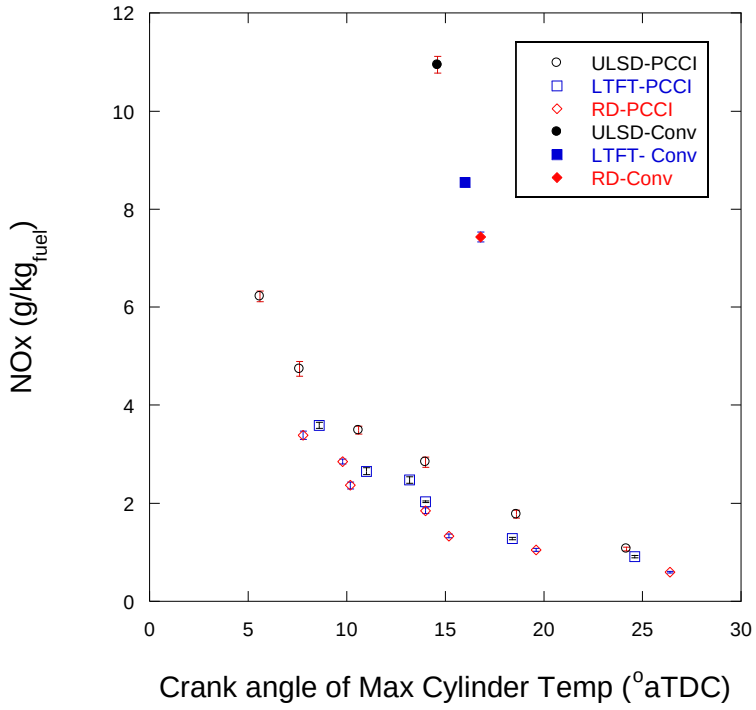

Figure 4.3 NOx emissions versus timing ofmaximum cylinder temperature with ULSD, LTFT, and RD under PCCI and conventional combustion modes

Northrop et al.[101] showed that NOx emissions are primarily a factor of combustion phasing under PCCI combustion, regardless the type of fuel, injection timing or pressure. They found similar NOx emissions among fuels for a given CA50, whether combustion phasing was adjusted by injection timing or pressure. Figure 4.4 shows the NOx emissions versus CA 50 for the three fuels in our study. NOx emissions are also strongly correlated with CA50 in this test. ULSD has slightly higher NOx emissions compared to the other two fuels under early PCCI combustion, due to the higher adiabatic flame temperature caused by the high aromatic content. Conventional combustion still has significantly higher NOx emissions with similar CA50 compared to PCCI combustion.

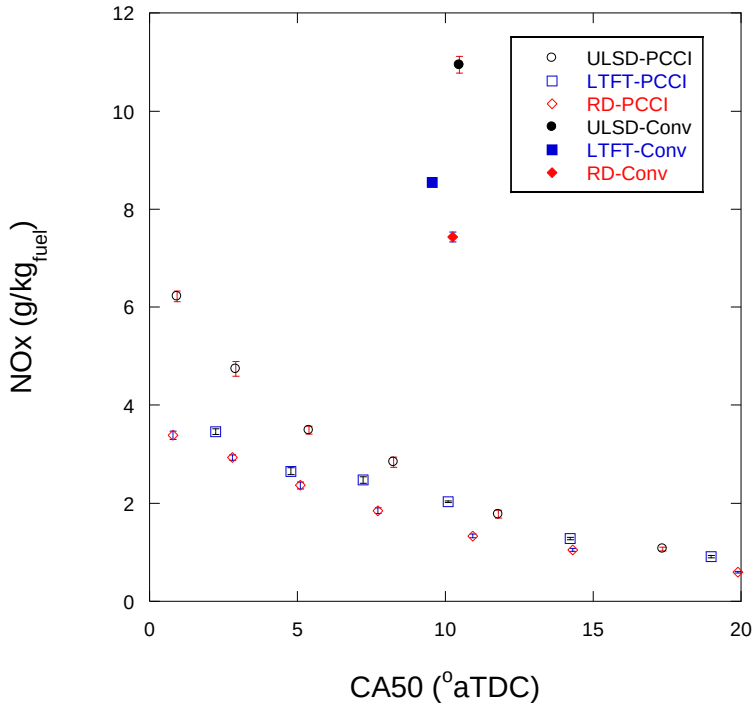

Figure 4.4 NOx emissions versus CA50 with ULSD, LTFT, and RD under PCCI and conventional combustion modes

4.3 CO and THC emissions

Figures 4.5 and4.6 show the CO and THC emissions. Hydrocarbon emissions from PCCI combustion are generated from several sources,[102] 1) over lean mixture from the clearance volume, crevice and squish volume; 2) over rich mixtures near the injector; 3) piston-top and ring crevice films; 4) liquid fuel dribble from the injector or late cycle vaporization from the injector sac. Increased CO emissions from PCCI combustion are mainly caused by the low combustion temperature, which lowers the concentration of OH radicals and results in reduced CO to CO_2 conversion rate.[103]CO mass typically originates from the crevice and boundary layer when the peak cylinder temperature is between 1000K and 1400K.[104]The incomplete combustion of over-lean mixtures is considered to be the major source of CO and THC emissions, especially

from the region near the injector where the fuel last to be injected has very low momentum.[105] As a consequence, PCCI combustion generally has higher CO and THC emissions as compared to convention combustion due to the increased ignition delay which can promote over-lean mixing and reduced combustion temperature. Han et al.[106] demonstrated that methods that extend PCCI ignition delay, such as increased EGR, increased gasoline portion in a diesel-gasoline fuel blend, or reduced intake pressure, tend to increase THC emissions. In contrast, CO emissions from PCCI combustion tend to be dominated by global equivalence ratio.

In the case of ULSD, early PCCI combustion produces lower CO and THC emissions than conventional combustion; late PCCI combustion produces higher CO and THC than conventional combustion. This is because the low cetane number ULSD results in longer ignition delay even during conventional combustion. As a result, THC and CO emissions are high for ULSD under conventional combustion due to the lean mixture formed prior to ignition. LTFT and RD have very short ignition delay during conventional combustion. For LTFT fuel, all PCCI combustion conditions produce both higher THC and CO emissions compared to conventional combustion. The PCCI combustion of RD produces higher CO emissions compared to conventional combustion. THC emissions from early PCCI combustion are slightly lower compared to conventional combustion, but late PCCI combustion leads to THC emissions that are higher compared to conventional combustion.

CO and THC emissions further increase with retarded injection timing under PCCI combustion, because combustion temperature reduces with late injection timing. With retarded injection timing, the prolonged ignition delay can also cause over mixing of fuel and air as well as fuel impingement, which can result in higher CO and THC emissions. In addition, the lack of time for combustion with delayed injection timing can also cause more incomplete combustion.

Both LTFT and RD have reduced THC and CO emissions compared to ULSD. The high cetane number fuels (LTFT and RD) have shorter ignition delay compared to low cetane number fuel ULSD. The reduced ignition delay can reduce the portion of over lean charge and fuel impingement on the cylinder wall, which can effectively reduce THC and CO emissions. Less premixed charge can also increase local combustion temperature and improve the concentration of radical pool, thus reduce incomplete combustion products CO and THC. In addition, aromatic hydrocarbons have higher ignition temperatures than alkanes. The lower reactivity and auto-ignition tendency of aromatics contributes to the increased THC and CO emissions.[107]Renewable diesel has higher CO and THC emissions compared to LTFT. This is because the renewable diesel used in this study has lower n-alkane content and high viscosity compared to LTFT fuel. As a consequence, renewable diesel produces higher THC and CO emissions compared to LTFT fuel. In addition, the higher viscosity and distillation temperature of renewable diesel can also result in larger fuel droplets and slow down the dispersion process of the fuel, consequently resulting in higher THC emissions compared to LTFT. However, while the RD fuel has a lower n-alkane content than the LTFT fuel, the renewable diesel has a substantial high content of total saturates (94wt%), shown in Table 2. While the renewable diesel contains 61.8 wt % iso-alkanes, these are only mildly branched iso-alkanes owing to the fatty acid profile of the original camelina from which the renewable diesel was produced. These lightly branched iso-alkanes will behave during ignition like moderate chain length n-alkanes, and effectively give the renewable diesel a similar capability to suppress CO and THC emissions as the LTFT fuel. Thus, the observations here with regard to the impact of alkane content on CO and THC emissions during low temperature combustion are consistent with the observations of Lilik and Boehman.[30]

A high saturate content can serve similarly to a high n-alkane content to suppress CO and THC emissions, for mildly branched iso-alkanes.

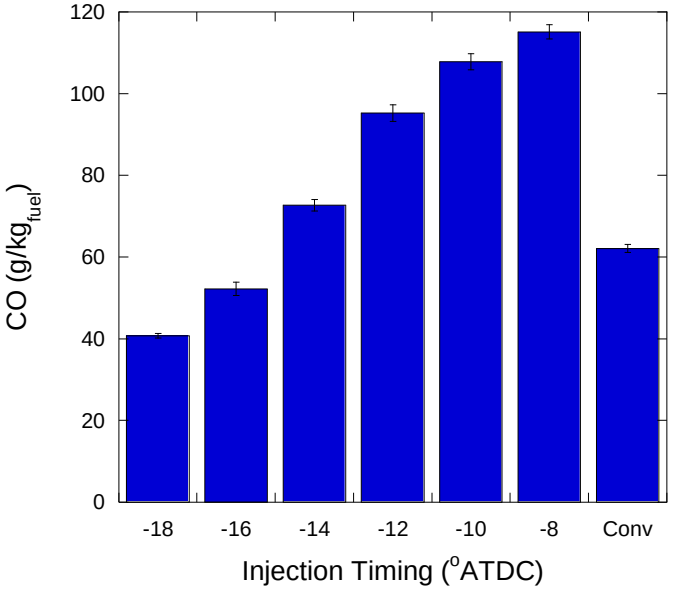

(a)

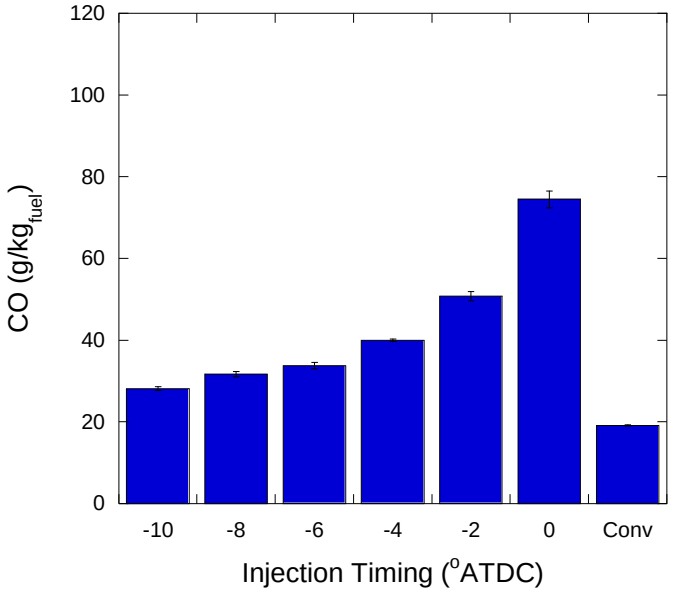

(b)

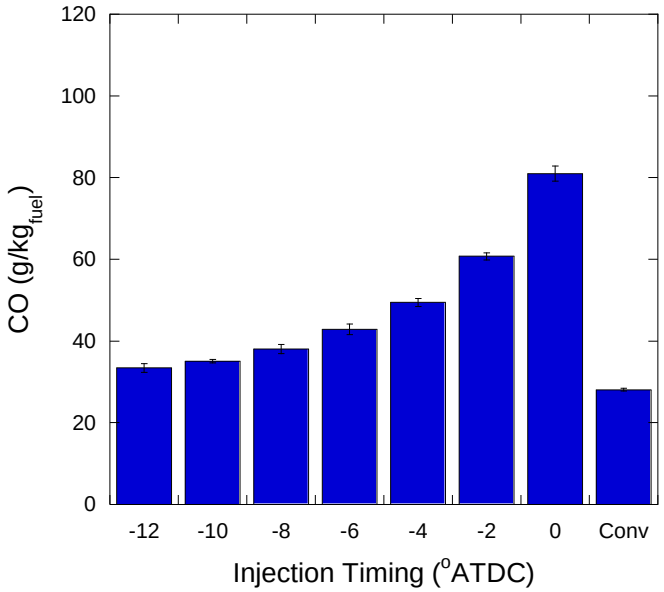

(c)

Figure 4.5 CO emissions for conventional and PCCI combustion modes with (a) ULSD, (b) LTFT, and (c) RD fuel

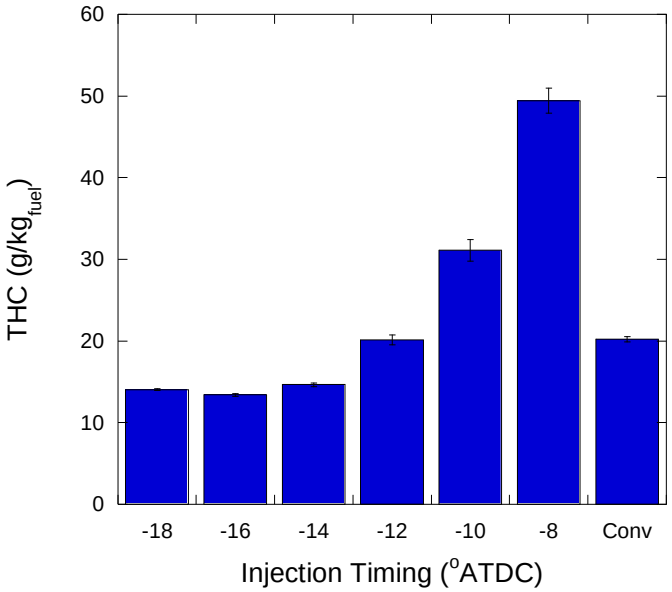

(a)

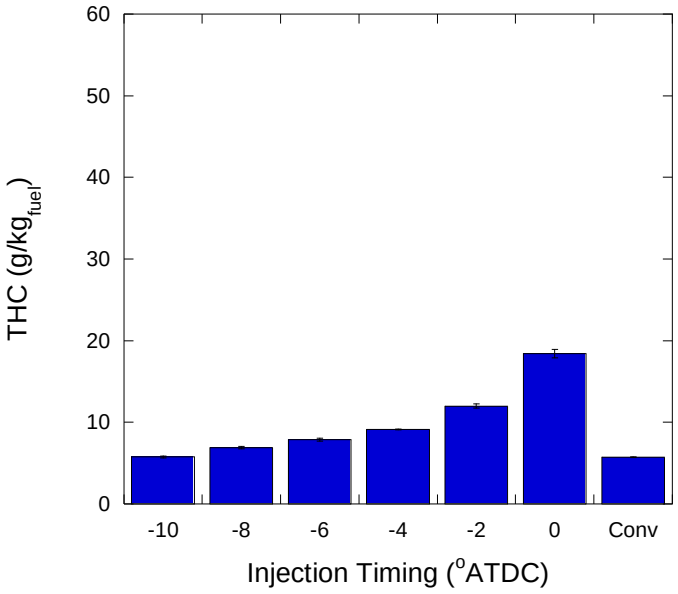

(b)

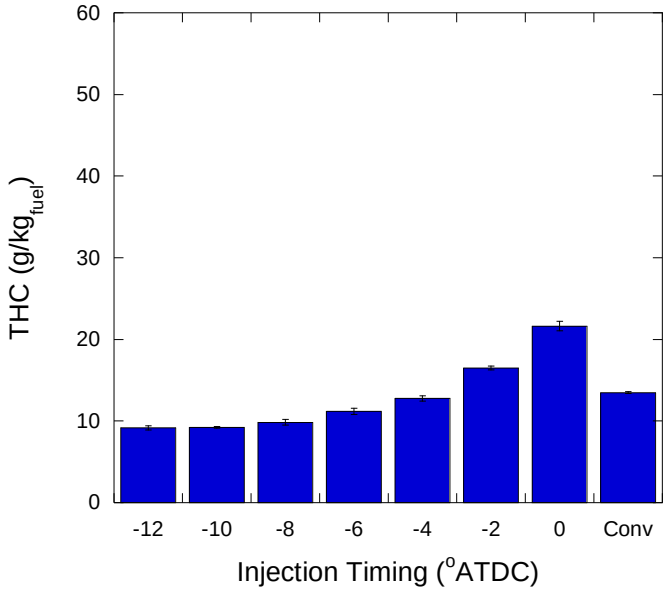

(c)

Figure 4.6 THC emissions for conventional and PCCI combustion modes with (a) ULSD, (b) LTFT, and (c) RD fuel

Figure 4.7 shows the correlation of ignition dwell with THC emission. Musculus suggested that THC emissions have a strong correlation with ignition dwell, which is the time interval between the end of injection and start of combustion.[105] Negative ignition dwell can avoid over lean combustion and reduce THC and CO emissions. In this study, all the cases have positive ignition dwell and relatively high THC emissions. With the increase of ignition dwell, THC increases for LTFT fuel and RD. However, ULSD has similar ignition dwell with various injection timings, and THC emissions increase with retarded injection timing, which may be caused by lower combustion temperature.

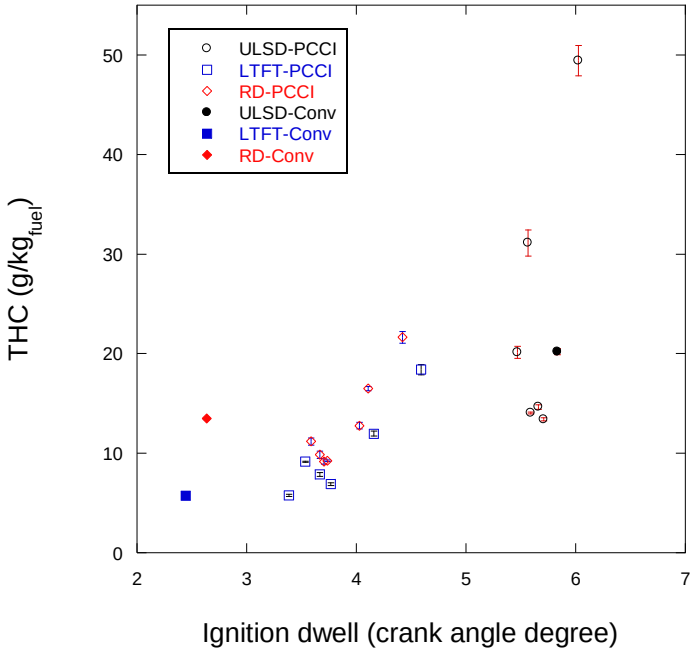

Figure 4.7 THC emissions versus timing ignition dwellwith ULSD, LTFT, and RD under PCCI and conventional combustion modes

4.4 Filter smoke number

Figure 4.8 shows exhaust filter smoke number measurements for the three fuels under both conventional and PCCI combustion modes. Under PCCI combustion, higher injection pressure and better premixing can reduce local equivalence ratio. Increased EGR ratio and modified combustion phasing can reduce combustion temperature. As a consequence, soot emissions are greatly reduced due to the reduced local equivalence ratio and combustion temperature, which avoids the in-cylinder conditions that promote soot formation.

ULSD has reduced filter smoke number compared to LTFT and RD, especially at conventional combustion. Very low FSN is observed for advanced combustion conditions, and ULSD still has slightly lower FSN than LTFT and RD. Low cetane number fuels are proved to have reduced soot emissions during PCCI combustion.[99] This is because lower cetane number fuels have prolonged ignition delay, which can enhance the fuel/air mixing. The low cetane number and reduced local equivalence ratio suppresses soot formation for ULSD. Aromatic content has the secondary effect on soot emissions. High aromatic fuel has the tendency to increase soot emissions.[108] Although ULSD has higher aromatic content, it does not necessarily result in higher soot emissions due to the prolonged ignition delay.

Filter smoke numbers are kept very low during PCCI combustion conditions, around 0.01-0.02. As injection timing is retarded during PCCI combustion, FSN first increases slightly and then decreases slightly. Soot production from an IC engine is a competition between soot formation and soot oxidation.[109] The combustion phasing is not optimized with very early injection timing, which reduces the peak cylinder temperature and suppresses the soot formation. With late injection timing, ignition delay is also prolonged due to reduced temperature. Combustion occurs during the expansion stroke which reduces the combustion temperature and

avoids soot formation. As a result, soot emissions are reduced with both early and late injection timing.

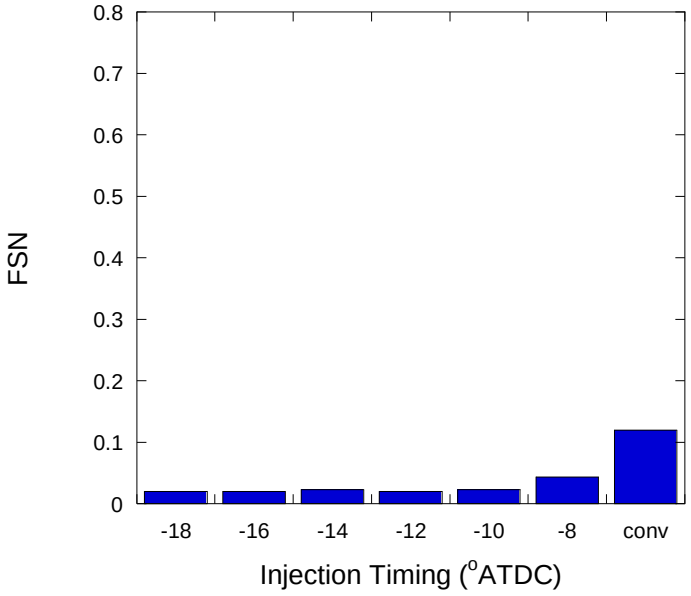

(a)

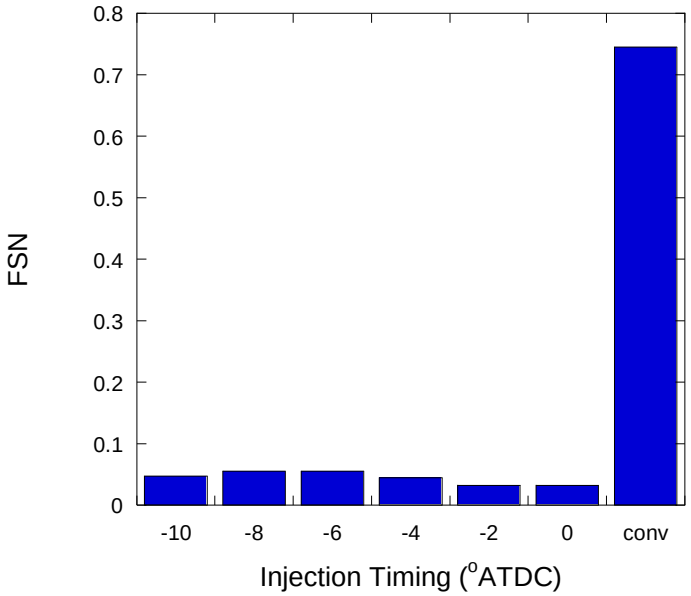

(b)

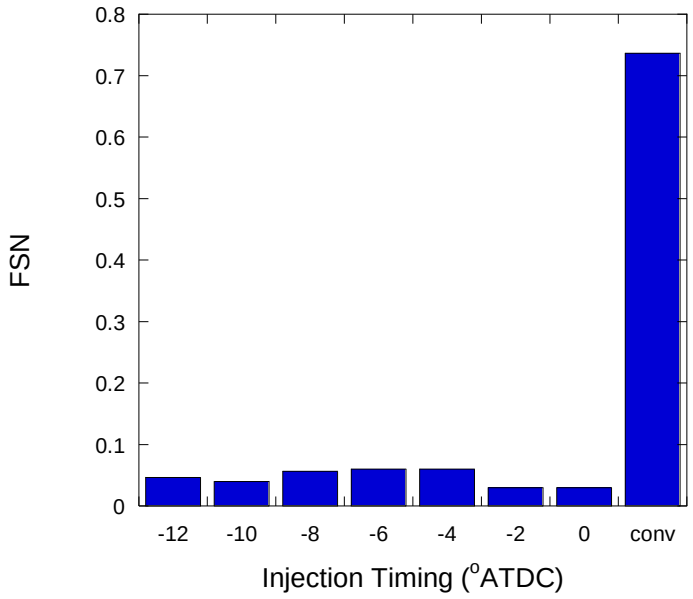

(c)

Figure 4.8 Filter smoke number for conventional and PCCI combustion modes of (a) ULSD, (b) LTFT, and (c) RD fuel

4.5 PM emissions

The nature of PM from PCCI combustion is quite different from PM of conventional combustion. The SOF of PM from PCCI combustion is much higher.[110]As shown in figure 4.9, conventional combustion produces much higher soot emissions according to the smoke numbers. However, ULSD has much higher PM emissions for PCCI combustion than conventional combustion due to the high SOF content under PCCI combustion. For LTFT fuel, which has relatively low SOF within PM emissions, PCCI combustion produces lower PM emissions than conventional combustion mode. For the case of renewable diesel, early PCCI combustion has similar PM emissions as conventional combustion, and PM emissions increase during late injection PCCI combustion.

Compared to LTFT, ULSD produces higher total PM emissions but lower soot emissions. This means there is a higher SOF of the PM produced by ULSD. This is also suggested by the higher THC emissions from ULSD fuel. An increase in cetane number[111] and reduction in aromatic content[112] can both reduce the SOF within PM emissions. As a low viscosity, high cetane number and n-alkane content fuel, LTFT fuel yields lower SOF content compared to ULSD under PCCI combustion.

LTFT and RD have similar soot emissions according to FSN result, which is a little higher than ULSD. However, RD has much higher filter PM emissions compared to LTFT fuel. This indicates the SOF is much higher for the PM emitted with RD. Low volatility fuels with higher boiling point, high viscosity and higher density can lead to worse charge mixing and incomplete combustion.[113] The higher density and viscosity of this particular renewable diesel fuel can affect the premixing of fuel and air. Larger initial fuel droplets can increase the unburned hydrocarbon contributes to the PM. Fuels with high distillation temperature can result in increased SOF within the PM emissions.[114] Although LTFT and renewable diesel have similar T90, the composition and carbon number of this renewable diesel is much more uniform than LTFT. This particular renewable diesel has much higher T10 and T50 than LTFT. The higher distillation temperature can slow the vaporization process and increase SOF of the PM emissions for renewable diesel.

Total PM emissions increase significantly as injection timing is retarded, especially for ULSD. However, soot emissions first increase then decrease with the delay of injection timing during PCCI combustion. The increase of total PM emissions is due to the increased SOF content, which is caused by the lack of time and temperature for complete combustion and increased unburned hydrocarbon emissions.

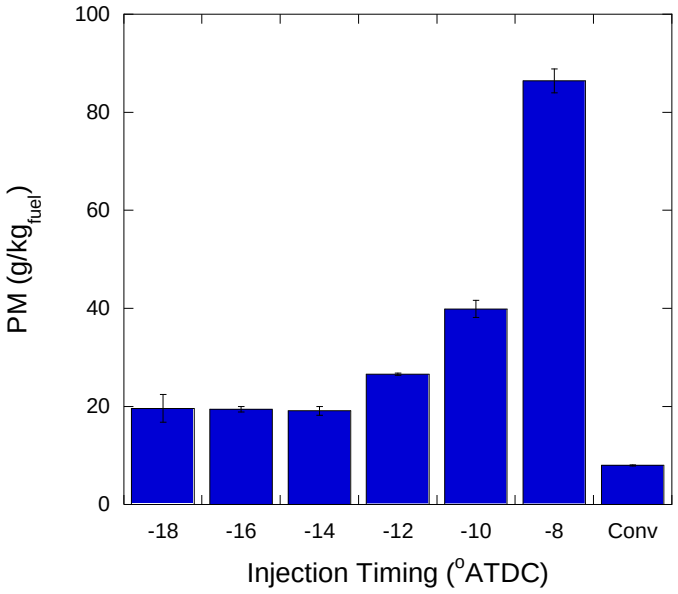
100
80
60
40
20
0
PM (g/kg$_{fuel}$)
-18
-16
-14
-12
-10
-8
Conv
Injection Timing (^{o}ATDC)

(a)

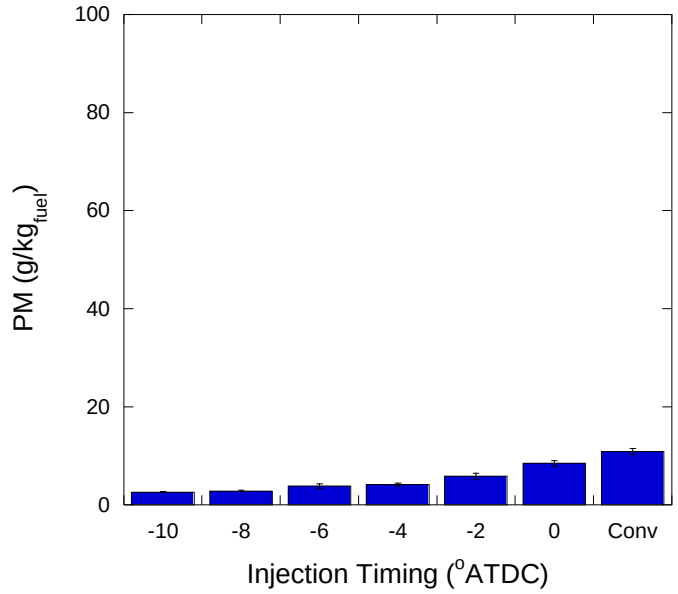
100
80
60
40
20
0
PM (g/kg$_{fuel}$)
-10
-8
-6
-4
-2
0
Conv
Injection Timing (^{o}ATDC)

(b)

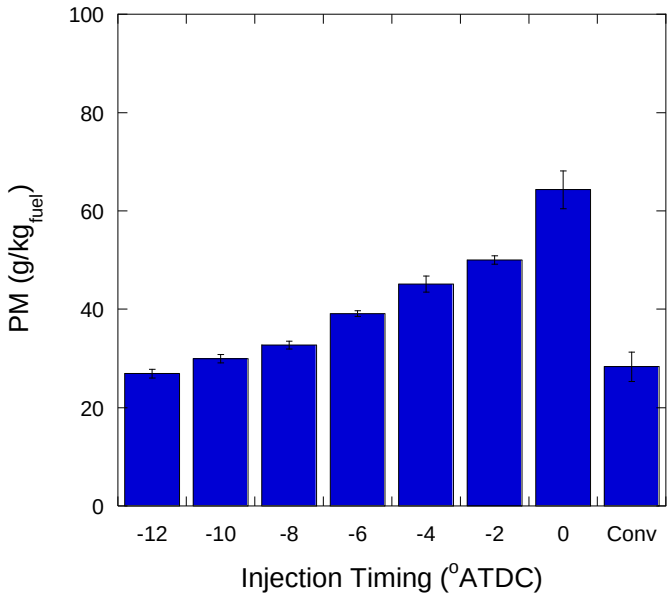

(c)

Figure 4.9 PM emissions for conventional and PCCI combustion modes with (a) ULSD, (b) LTFT, and (c) RD fuel

4.6 Particle size distribution

Figure 4.10 shows particle size distributions of PM emissions for the three test fuels. PCCI combustion generally shifts particles to smaller aggregation size compared to conventional combustion.[115,116] All the three fuels tested produce smaller particle aggregates under PCCI combustion conditions. For the case of ULSD, conventional combustion has the lowest particle number. While for LTFT fuel, conventional combustion has the highest particle number. Renewable diesel has similar particle numbers under PCCI and conventional combustion. Compared with the FSN and PM results, it can be concluded that during PCCI combustion, ULSD and this renewable diesel fuel produces much more SOF than the LTFT fuel does.

Under PCCI combustion conditions, ULSD has the highest total number of particles compared to the other two fuels. RD fuel yielded similar particle number emissions as the LTFT fuel, however the renewable diesel fuel yielded much larger mean particle size. This is due to the high viscosity and distillation temperature of the renewable diesel fuel tested here, which causes high SOF content in the PM and increases the size of particle aggregates. ULSD and RD have similar PM mass. However RD has much lower particle number. This may indicate a different mechanism of SOF production for RD compared to ULSD. The hydrocarbon composition may also be different between ULSD and RD. It is also possible that RD produced heavier THC, which condenses more on PM and the PM filters.

Total particle number increases and the size distribution moves to larger particle sizes as injection timing is retarded. Total PM and the SOF content increase with retarded injection timing, due to the lack of time for complete combustion. Compared to the FSN results, with similar soot emissions, high SOF content can increase PM aggregate size.

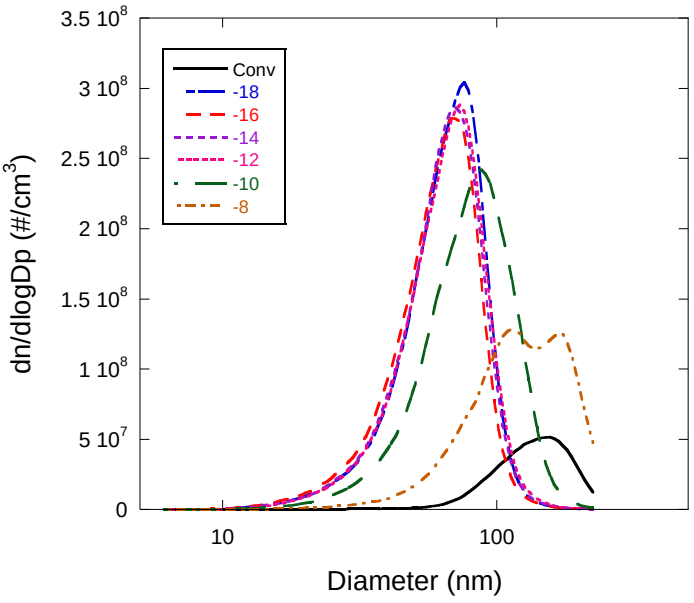
3.5 10^8
3 10^8
2.5 10^8
2 10^8
1.5 10^8
1 10^8
5 10^7
0
10
100
Diameter (nm)
dn/dlogDp (#/cm^3)
Conv
-18
-16
-14
-12
-10
-8

(a)

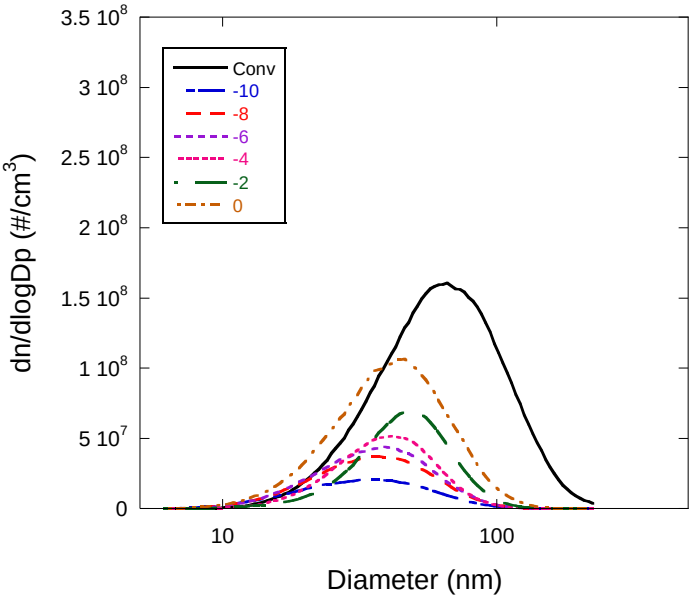
3.5 10^8
3 10^8
2.5 10^8
2 10^8
1.5 10^8
1 10^8
5 10^7
0
10
100
Diameter (nm)
dn/dlogDp (#/cm^3)
Conv
-10
-8
-6
-4
-2
0

(b)

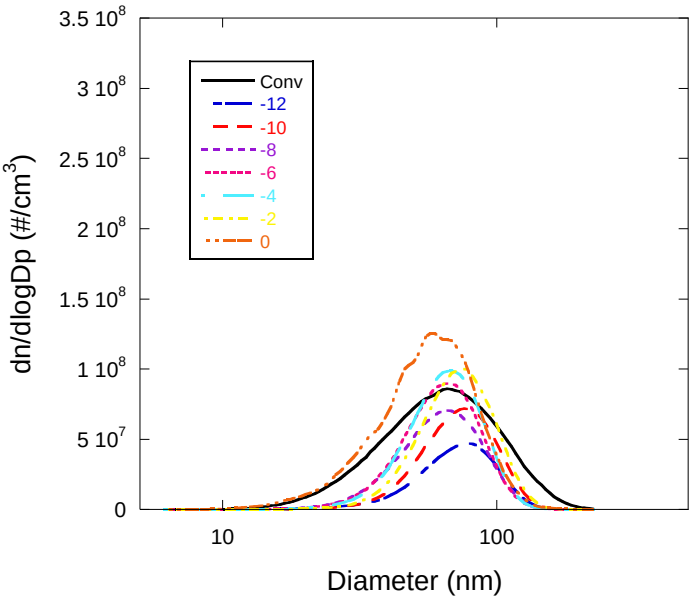

(c)

Figure 4.10 Particle size distribution for conventional and PCCI combustion modes with (a) ULSD, (b) LTFT, and (c) RD fuel

4.7 Brake specific fuel consumption (BSFC)

Figure 4.11 shows the BSFC for the three fuels at PCCI and conventional combustion conditions. PCCI combustion has slightly higher BSFC compared to conventional combustion, which results from the incomplete combustion and the non-optimized spontaneous ignition of the premixed charge. [117] BSFC is increased with early injection PCCI combustion because combustion occurs before the piston reaches TDC, and the enhanced heat transfer to the cylinder walls. BSFC also increases with late injection timing, because of reduced effective expansion ratio and fuel energy loss due to incomplete combustion. LTFT fuel and RD have slightly higher lower heating values(LHV) than ULSD, which results in slightly lower BSFC.

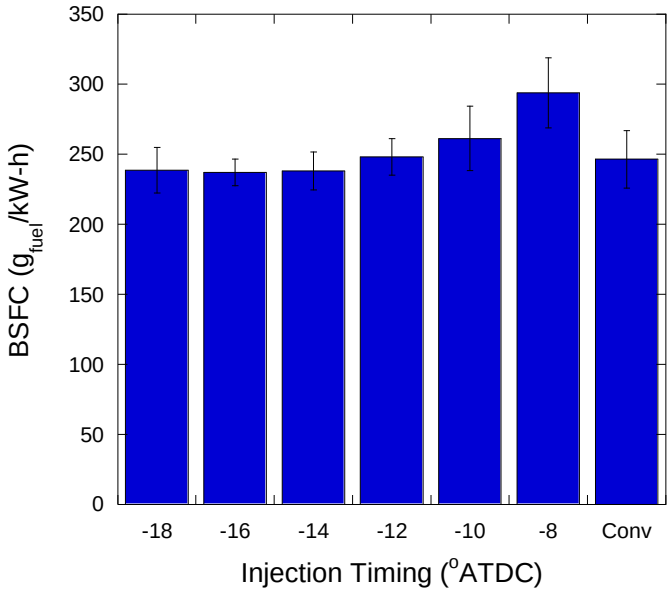
350
300
250
200
150
100
50
0
BSFC (g_{fuel}/kW-h)
-18
-16
-14
-12
-10
-8
Conv
Injection Timing (^{o}ATDC)

(a)

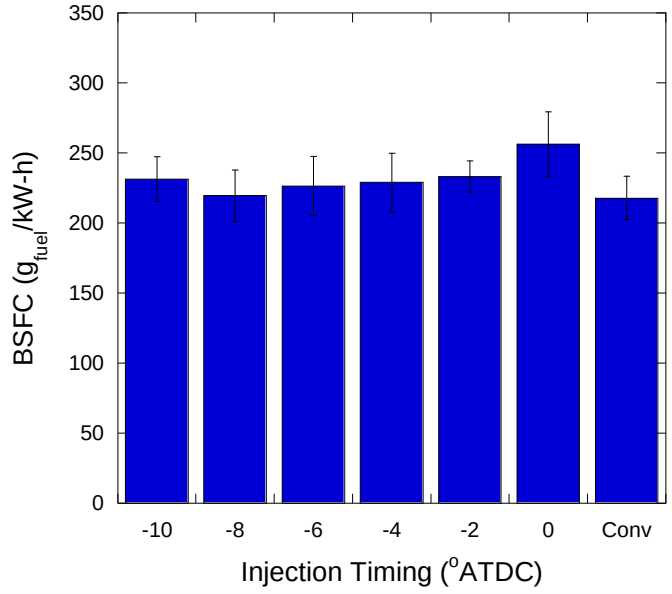
350
300
250
200
150
100
50
0
BSFC (g_{fuel}/kW-h)
-10
-8
-6
-4
-2
0
Conv
Injection Timing (^{o}ATDC)

(b)

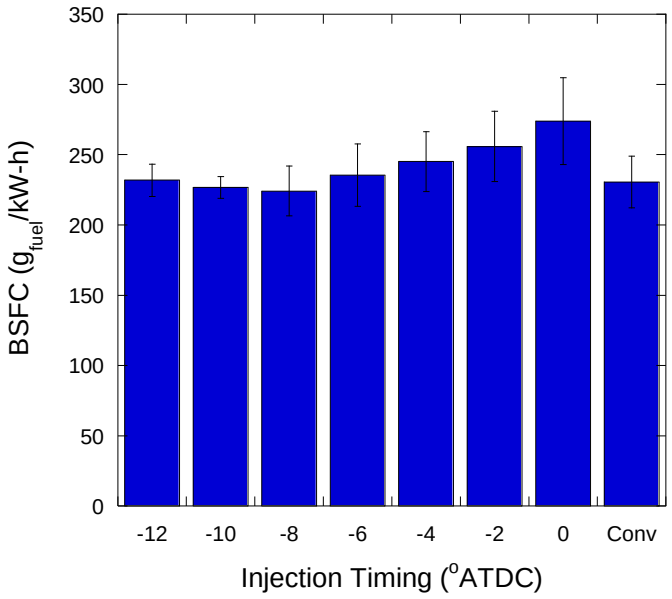

(c)

Figure 4.11 BSFC for conventional and PCCI combustion modes with (a) ULSD, (b) LTFT, and (c) renewable diesel

Brake thermal efficiency (BTE) is not affected significantly by the fuel type. LTFT and RD has slightly higher BTE compared to ULSD. PCCI combustion with optimized injection timing has similar or slightly higher BTE compared to conventional combustion. However, PCCI combustion with retarded injection timing has reduced BTE because combustion occurs during the expansion stroke which reduces the thermal efficiency.

4.8 THC-NOx trade-off

Although PCCI combustion provides an efficient way to reduce NOx and soot emissions simultaneously, THC and CO emissions increase due to reduced combustion temperatures and

increased mixing and dilution. Figure 4.12 shows the THC versus NOx emissions trade off of the three fuels. High cetane number and high alkane content fuel LTFT and RD produce less THC and CO emissions compared to higher aromatic ULSD fuel under PCCI combustion. However, NOx emissions depend more on the EGR ratio or in-cylinder O_2 concentration than the difference of fuel properties.[108]In addition, the high cetane number of LTFT and RD reduce ignition delay and further reduces the amount of over-mixing and overly lean combustion. For this reason, the high cetane number, low aromatic fuels, LTFT and RD, can significantly shift the NOx-THC trade-off curve.

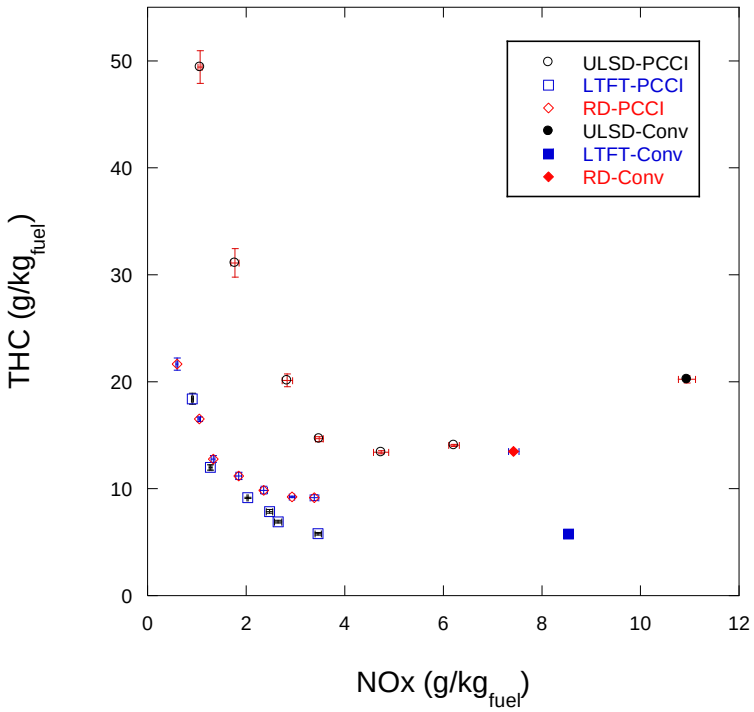

Figure 4.12 NOx emissions versus total hydrocarbon emissions for ULSD, LTFT and RD under PCCI and conventional combustion modes

4.9 Comparison of PCCI combustion and conventional combustion

In order to compare the emissions from PCCI and conventional combustion, Figure 4.13 shows a comparison of PCCI combustion and conventional combustion for CA50 around 10^{o}aTDC.Table 4.1 shows the conditions for each of the three fuels chosen. For conventional combustion, the injection timings are: ULSD -10^{o}aTDC, LTFT -8^{o}aTDC, and RD -8^{o}aTDC. For PCCI combustion, the injection timings are: ULSD -12^{o}aTDC, LTFT -6^{o}aTDC, and RD -6^{o}aTDC.

Table 4.1 Conditions for conventional and PCCI combustion modes when CA50 is 10^{o}aTDC

		Conventional	PCCI
Injection Pressure (bar)		300	700
EGR rate		25%	40%
Injection Timing (^{o}ATDC)	ULSD	-10	-12
	LTFT	-8	-6
	RD	-8	-6

With the same CA50 under PCCI and conventional combustion, NOx emissions are greatly reduced by PCCI combustion, due to the reduced combustion temperature. Reduced combustion temperature in PCCI combustion also largely avoids the soot formation. As a result, FSN is greatly reduced for all fuels by PCCI combustion (81-93%). For ULSD and RD, PCCI combustion has increased PM emissions compared to conventional combustion. This is caused by the increased SOF of the PM from PCCI combustion. LTFT fuel has reduced PM emissions during PCCI combustion due to reduced soot and low SOF, compared with the other two fuels.

All three fuels increase CO emissions slightly with PCCI combustion. This is caused by the over lean mixture and reduced combustion temperature. THC emissions are similar with

PCCI and conventional combustion. LTFT slightly increases THC emissions and RD reduces THC emissions slightly under PCCI combustion.

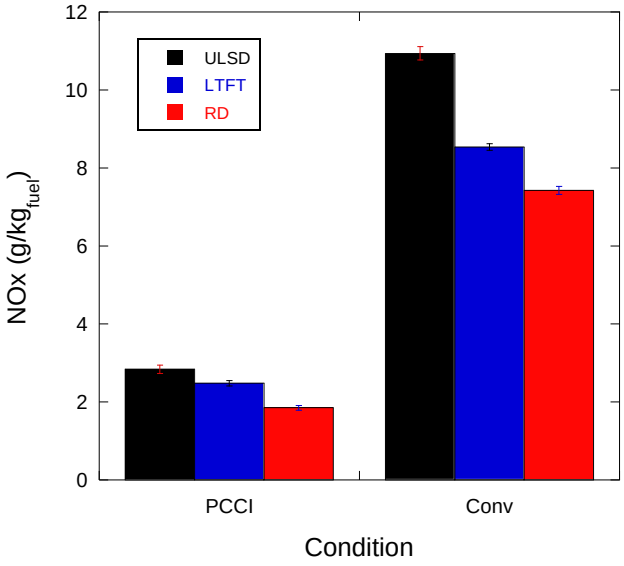

(a)

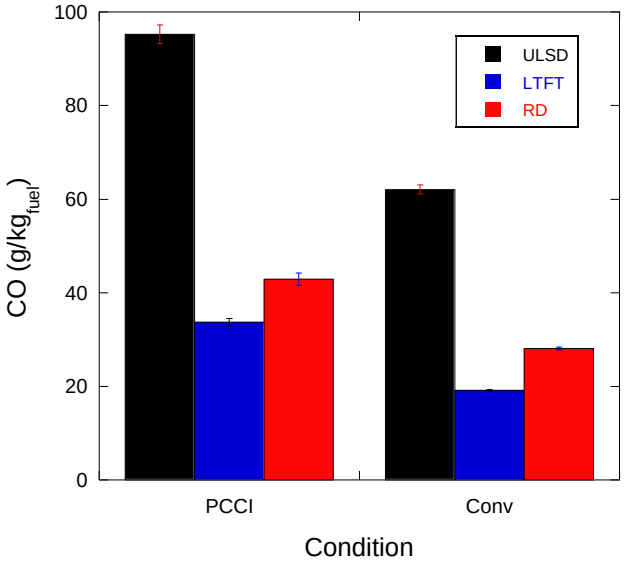

(b)

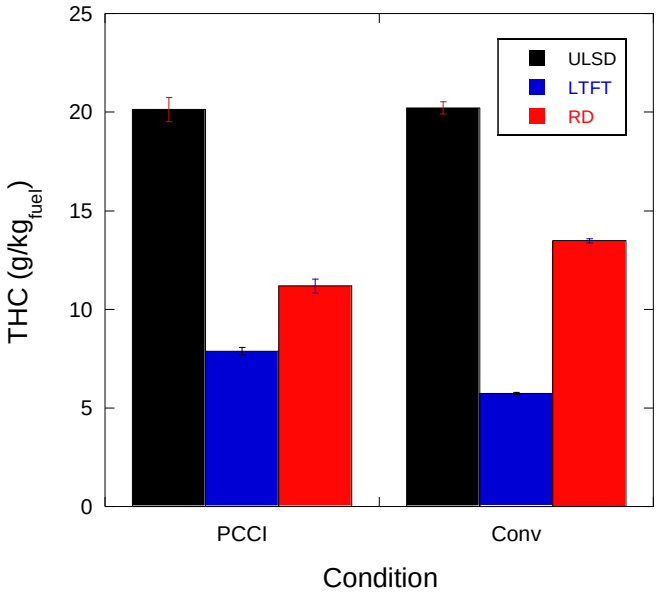
25
20
15
10
5
0
THC (g/kg$_{fuel}$)
ULSD
LTFT
RD
PCCI
Conv
Condition

(c)

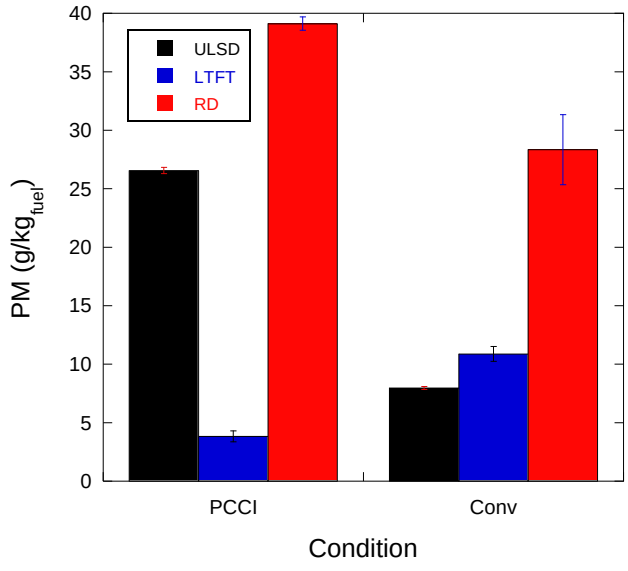
40
35
30
25
20
15
10
5
0
PM (g/kg$_{fuel}$)
ULSD
LTFT
RD
PCCI
Conv
Condition

(d)

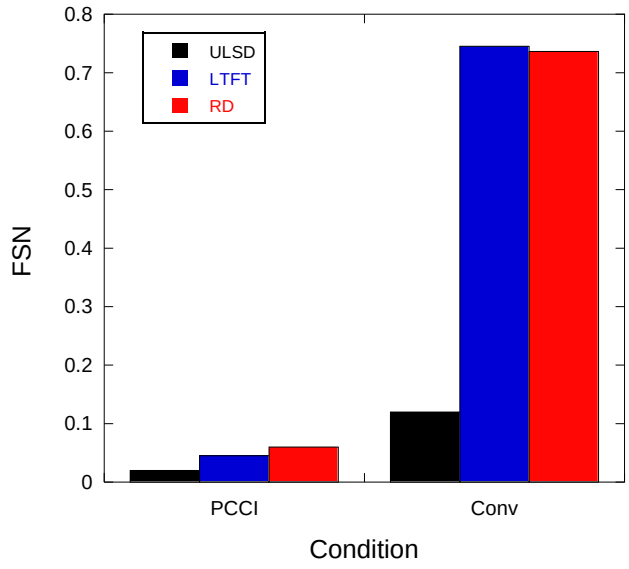

(e)

Figure 4.13 (a) NOx, (b) CO, (c)THC, (d) PM emissions, and (e) FSN for conventional and PCCI combustion modes when CA50 is 10°aTDC

4.10 Conclusion

Among the three fuels, LTFT fuel has the best performance due to its high n-alkane content and low viscosity. LTFT fuel has significantly lower PM emissions due to its low SOF, and has reduced CO, THC and NOx emissions compared to ULSD. Renewable diesel also reduces CO, THC and NOx emissions compared to ULSD. However, due to the lower n-alkane content and higher viscosity and distillation curve of renewable diesel compared to LTFT, it produces slightly higher CO and THC emissions and has significantly higher SOF within PM compared to LTFT fuel. High cetane number and low aromatic content fuels can effectively reduce PM and NOx emissions simultaneously. Fuels with high n-alkane content (e.g., LTFT) can effectively reduce incomplete combustion emissions CO and THC, as can fuels with a high

total saturates content, where the iso-alkanes are only mildly branched (e.g., renewable diesel). Both fuels appear to benefit from having a low critical equivalence ratio, achieved through different species (n-alkanes versus mildly branched iso-alkanes). In addition, low viscosity and low distillation temperature are shown in this work to be important factors for the reduction of emissions.

PCCI combustion is achieved with increased EGR and injection pressure in this study. It provides an effective way to reduce NOx and soot emissions, however, with increased CO and THC emissions. In this study, PCCI combustion results in higher CO emissions, similar THC emissions, lower NOx emissions, higher PM emissions and lower soot emissions.

With retarded injection timing in PCCI combustion, combustion phasing is retarded and combustion temperature is reduced. As a result, NOx emissions decrease, CO and THC emissions increase due to over lean combustion. Soot emissions first increase then decrease and PM emissions increase with as injection timing is retarded due to increased SOF content.

Chapter 5.

PCCI combustion in a multi-cylinder engine and soot nanostructure and reactivity

The emissions for ULSD, LTFT and RD fuels from PCCI combustion are discussed in Chapter 4. However, due to the low soot yield from the single cylinder engine, the properties of soot and their reactivity are not analyzed for the Isuzu engine. In this chapter, bulk soot samples are collected from both conventional and PCCI combustion conditions for the three fuels. The nanostructure and reactivity of soot from PCCI combustion conditions are analyzed by XPS, Raman spectroscopy and TEM.

5.1 Heat release rate

Figure 5.1 shows the apparent rate of heat release (ROHR) for the three fuels under conventional and PCCI conditions. Similar to PCCI combustion study in the single cylinder engine, ULSD has longer ignition delays because of its low cetane number relative to the LTFT and RD fuels. In addition, LTFT fuel and RD still have similar ignition delays for PCCI combustion.

LTFT and RD have higher cetane numbers and shorter ignition delays. The reduced fraction of premixed burn reduces the maximum ROHR compared to ULSD under both conventional and PCCI combustion modes.

For ULSD, ROHR decreases with retarded injection timing under PCCI combustion. This is because during late injection timings, cylinder expansion can reduce cylinder temperature, which increases the ignition delay and reduces the rate of combustion. As a consequence, with the retarded injection timing, peak ROHR decreases and combustion duration increases. However, with the retarded injection timing, LTFT and RD have increased peak heat release rate and less diffusion combustion, which is closer to the definition of PCCI combustion. This is because retarded injection timing can increase the ignition delay and create a better premixed charge for high ignition quality fuels, which promotes PCCI combustion.

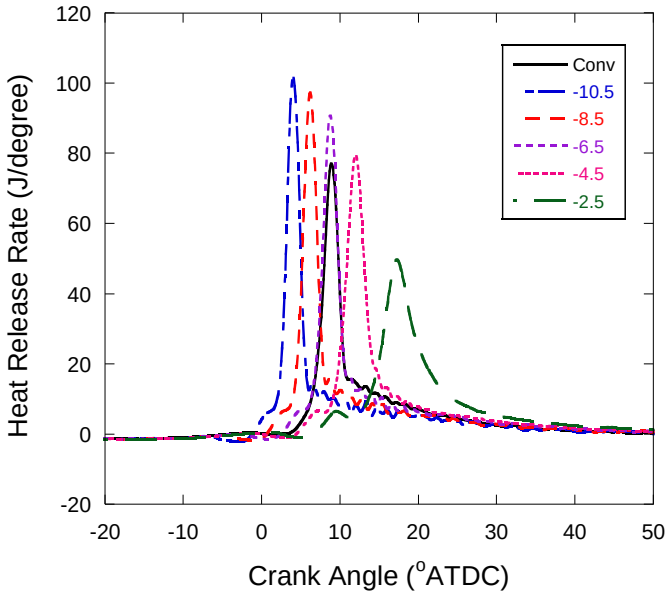

(a)

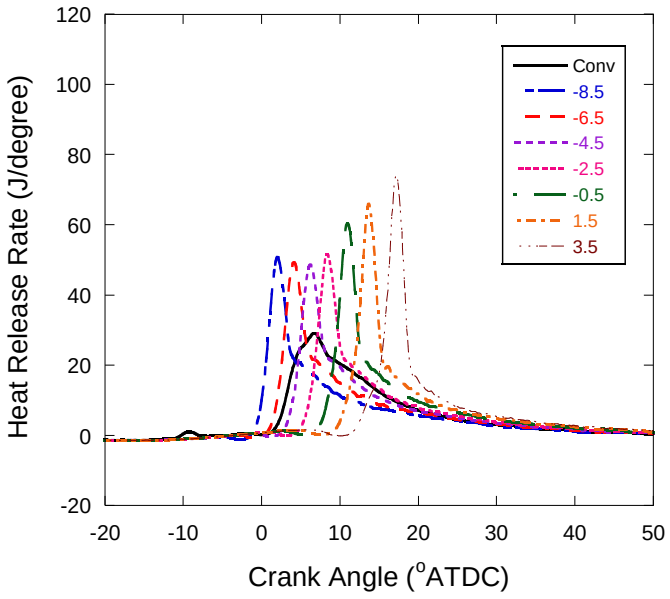

(b)

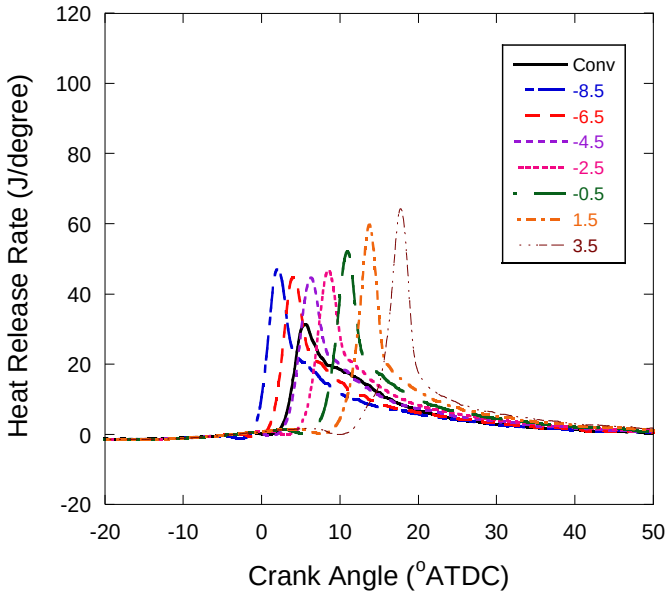

(c)

Figure 5.1 Heat release rate for conventional and PCCI combustion modes for (a) ULSD, (b) LTFT and (c) RD fuel

5.2 NOx emissions

Figure 5.2 shows the NOx emissions for the three fuels. NOx emissions from the multi-cylinder engine follow a very similar trend for NOx emissions as that from the single-cylinder engine. As has been discussed in Section 4.2, thermal NOx is the dominant pathway for NOx formation in diesel engines. Temperature has a great impact on NOx emissions. NOx emissions are greatly reduced by PCCI combustion mode due to the reduced combustion temperature and oxygen concentration. By increasing the EGR level, the heat capacity of the gas inside the cylinder has increased. As a result, NOx formation could be suppressed by the reduced temperature and oxygen concentration. Late injection PCCI combustion conditions (ULSD: 4.5^{o}CAD, LTFT and RD: -1.5^{o}CAD) reduces NOx emissions by 76-78% compared to conventional combustion conditions.

Similarly, NOx emissions reduce with retarding of injection timing. With delayed injection timing, cylinder temperature is further reduced because combustion occurs during the expansion stroke. Combustion speed is also reduced due to the cylinder volume expansion. In addition, the timing allowed for NOx formation under high temperature also reduces with retarded combustion phasing.

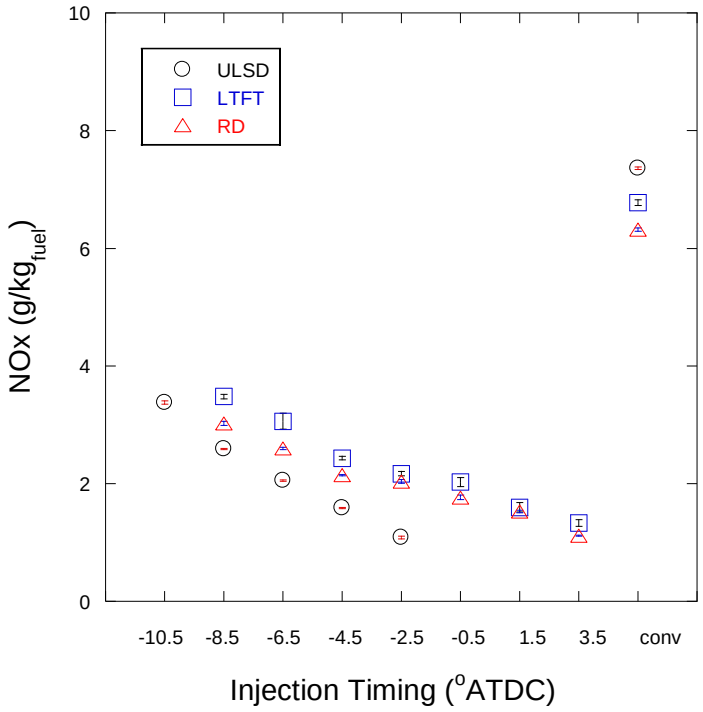

Figure 5.2 NOx emissions for conventional and PCCI combustion modes with ULSD, LTFT and RD fuel

5.3 CO and UHC emissions

Figure 5.3 shows the CO emissions, and Figure 5.4 shows the THC emissions. As has been discussed in Section 4.3, PCCI combustion produces higher CO and THC emissions due to the lean mixture and reduced combustion temperature, which could result in incomplete combustion. Late injection PCCI combustion conditions (ULSD: 4.5^{o}CAD, LTFT and RD: -1.5^{o}CAD) increases CO emissions by 40-77% and increases THC emissions by 11-24% compared to conventional combustion conditions. For all three fuels, CO and THC emissions increase with the retard of injection timing. This is because combustion temperature is further reduced, and the over lean mixing.

High cetane number fuels LTFT and RD reduces CO emissions by 60% and THC emissions by 62% compared to ULSD under late injection PCCI combustion, as discussed in Section 4.3. The shorter ignition delays for LTFT and RD can prevent over lean mixing and increase local combustion temperature. Both LTFT and RD have reduced THC and CO emissions compared to ULSD. The high alkane contents of LTFT and RD also contribute to the reduction of CO and THC emissions because alkane content has higher reactivity thus have lower ignition temperature. RD has similar CO and THC emissions compared to LTFT since both are high cetane number, high alkane content fuels.

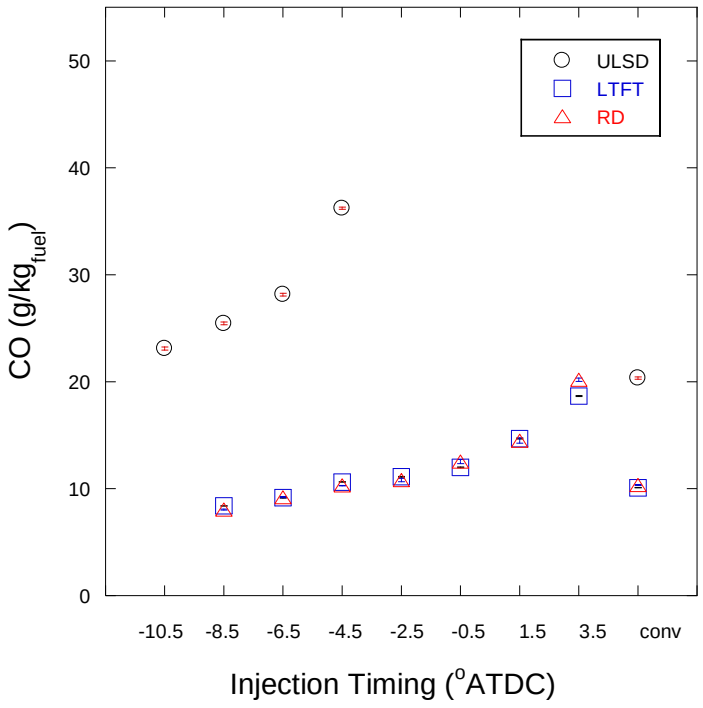

Figure 5.3 CO emissions for conventional and PCCI combustion modes with ULSD, LTFT and RD fuel

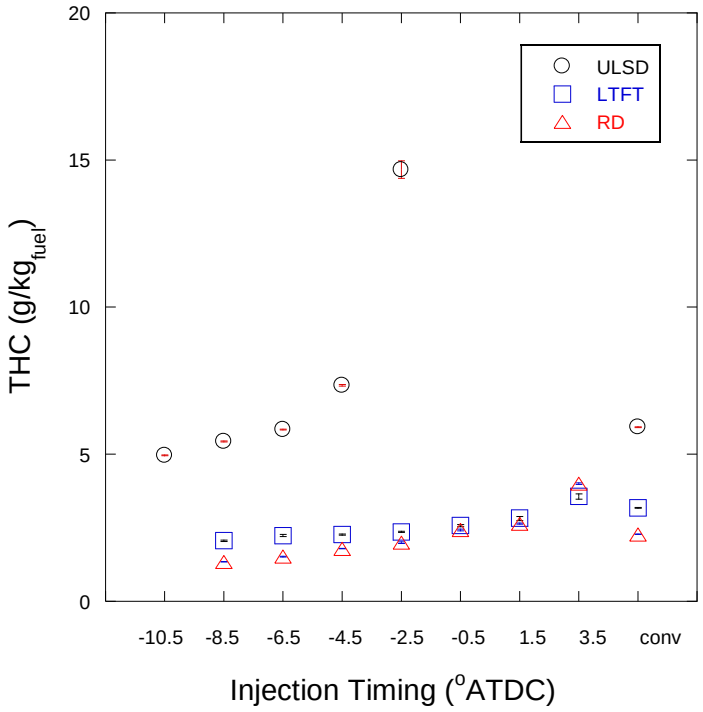

Figure 5.4 THC emissions for conventional and PCCI combustion modes with ULSD, LTFT and RD fuel

Figure 5.5 shows the THC versus NOx emissions trade off of the three fuels. Similar to single-cylinder PCCI study, high cetane number and high alkane content fuels LTFT and RD produce similar NOx emissions, however less THC and CO emissions than ULSD. As a consequence, high ignition quality fuels LTFT and RD can effectively improve the NOx-THC curve.

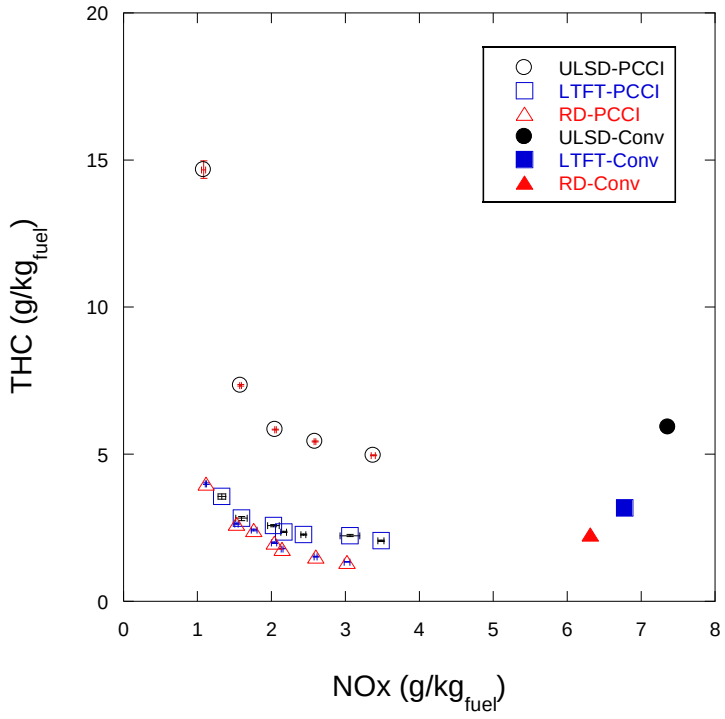

Figure 5.5 NOx emissions versus total hydrocarbon emissions for ULSD, LTFT and RD under PCCI and conventional combustion modes

5.4 Filter smoke number

Figure 5.6 shows exhaust filter smoke number (FSN) measurements for the three fuels under both conventional and PCCI combustion. Similar to the single-cylinder engine PCCI study, ULSD fuel has lower FSN compared to LTFT and RD, under both conventional and PCCI combustion. Low cetane number fuels yield reduced soot emissions during PCCI combustion.[118] As discussed in Section 4.4, low CN fuels have longer ignition delay leading to better fuel/air mixing, which could reduce soot emission. The ignition dwell could be negative for high CN fuels, which generates some diffusion burning and results in higher FSNs. For all three fuels,

FSN first increases then decreases with the retarding of injection timing during PCCI combustion, as explained previously.

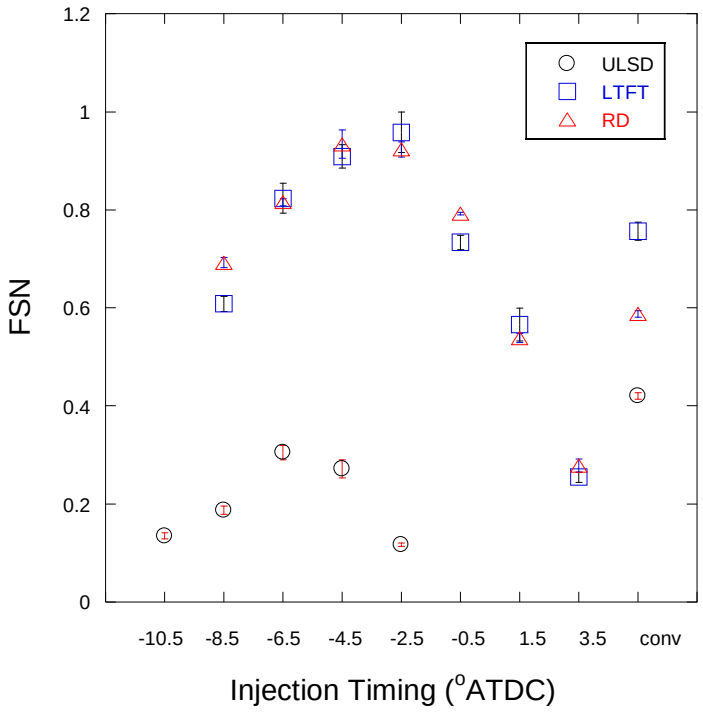

Figure 5.6 Filter smoke number for conventional and PCCI combustion modes of ULSD, LTFT and RD fuel

5.5 PM emissions

Similar to the single-cylinder engine study, ULSD produces similar or higher total PM emissions but lower soot emissions compared to LTFT and RD, as shown in Figure 5.7. This suggests PM produced from ULSD has higher SOF content compared to PM produced from LTFT and RD. The high CN, low aromatic content, and low viscosity fuel are producing PM with reduced SOF.

With the retarding of injection timing, PM emissions for LTFT and RD followed the same trend as FSN. However, PM emissions for ULSD increase greatly with retarding of the injection timing, despite its very low FSN under late PCCI combustion mode. This indicates that ULSD soot has very high SOF content under late injection PCCI condition. Soot from LTFT and RD has similar FSN and PM emissions except for two latest injection timing PCCI conditions. This is because the renewable diesel used in this study has high density and viscosity, as discussed in Section 4.5.

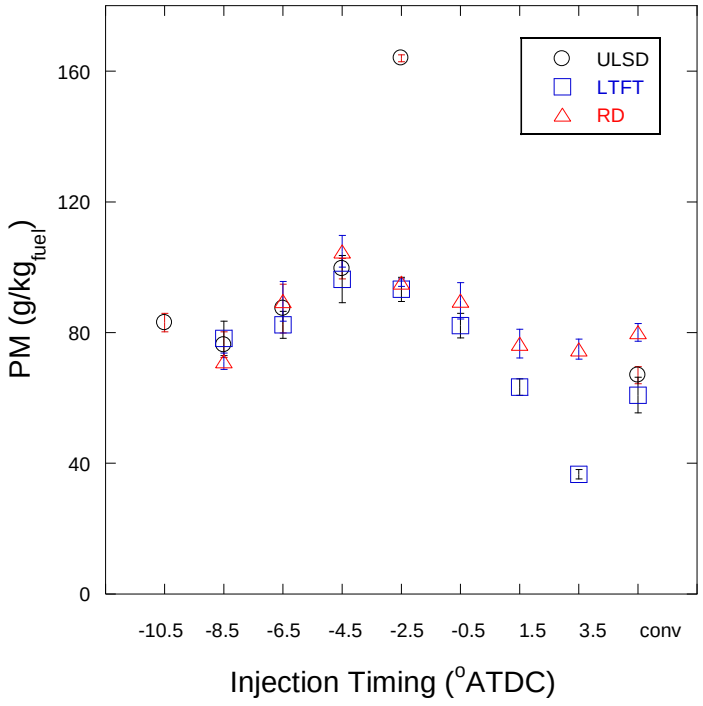

Figure 5.7 PM emissions for conventional and PCCI combustion modes with ULSD, LTFT and RD fuel

5.6 Particle size distribution

Figure 5.8 shows particle size distributions of PM emissions for the three test fuels. Total particle number follows a similar trend as total PM mass. For ULSD fuel, total particle number is

increased by PCCI combustion mode, especially with the latest injection timing condition due to the increased SOF content. For LTFT and RD, conventional and PCCI combustion modes have comparable particle number and size distributions. However, for the latest injection timing PCCI condition, both particle size and number are reduced, which indicates that the nature of the particles produced under this condition may be different from other conditions.

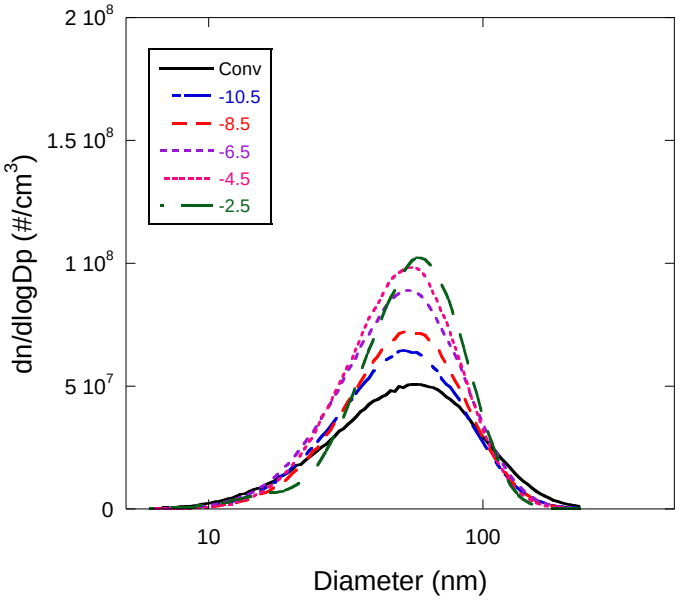

(a)

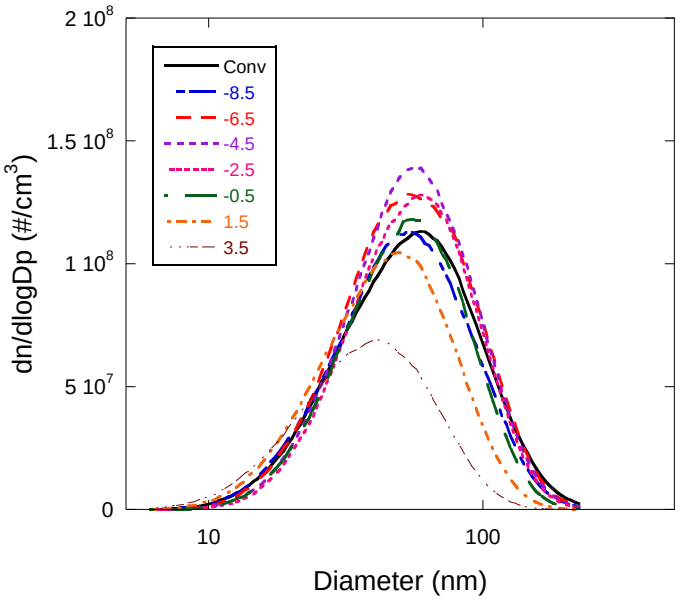

(b)

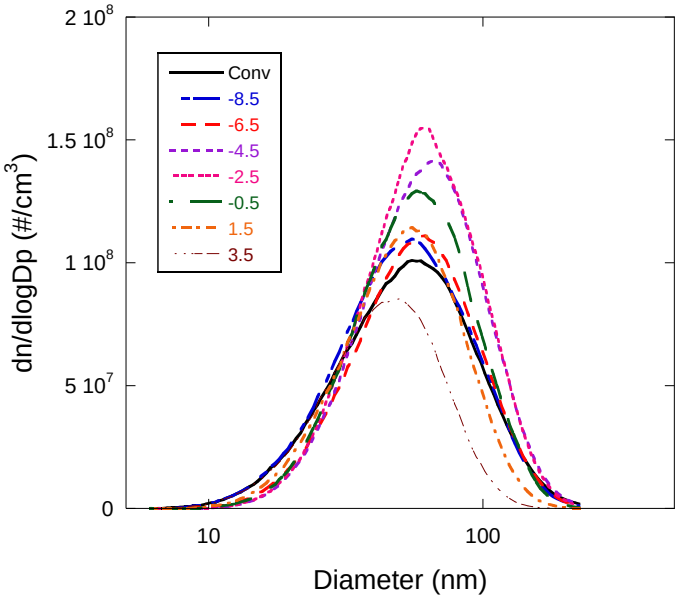

(c)

Figure 5.8 Particle size distribution for conventional and PCCI combustion modes with (a) ULSD, (b) LTFT and (c) RD fuel

5.7 BSFC and BTE

Figure 5.9 shows the BSFC for the three fuels at PCCI and conventional combustion conditions. Similar to that single-cylinder engine PCCI study, PCCI combustion results in slightly higher BSFC compared to conventional combustion. As explained in Section 4.8, BSFC increases with early or late injection timing due to the non-optimized combustion phasing. LTFT and RD have lower BSFC due to their higher LHV.

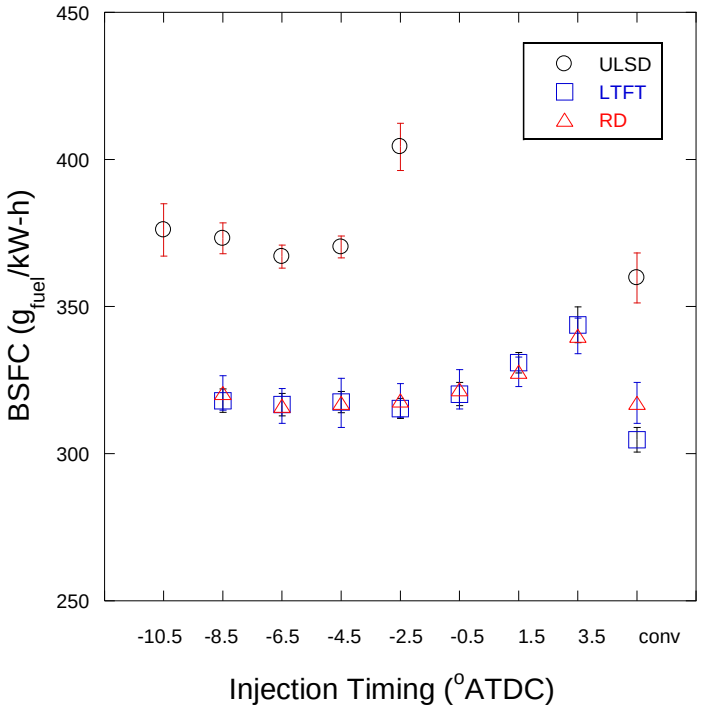

Figure 5.9 BSFC for conventional and PCCI combustion modes with ULSD, LTFT and RD fuel

LTFT and RD have similar BTE under all conditions, which is higher compared to ULSD, as shown in Figure 5.8. PCCI combustion with retarded injection timing has slightly reduced BTE because combustion occurs during the expansion stroke which reduces the thermal efficiency.

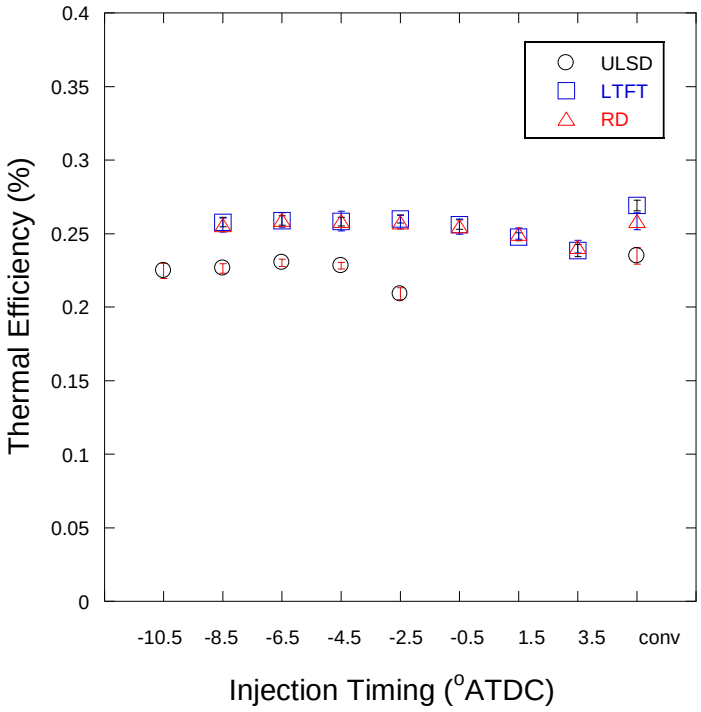

Figure 5.10 BTE for conventional and PCCI combustion modes with ULSD, LTFT and RD fuel

5.8 Soot reactivity analysis

Bulk soot samples are collected from 9 different conditions for this PCCI study, one from a conventional combustion condition and two from late injection PCCI combustion conditions for each fuel. VOF content and oxidative reactivity of the soot samples are measured by TGA, which is described in Section 3.2.1. VOF is measured under inert nitrogen environment up to 525°C, after that soot is oxidized at 525°C. The VOF content and time of 50% mass burn are shown in Table 5.1.

PM from PCCI combustion has higher VOF content compared to PM generated from conventional combustion, which is in agreement with several other PCCI studies.[110,119] This is because the reduced combustion temperature leads to an increased level of unburned

hydrocarbons condensed onto the surface of the soot aggregates. In addition, PM produced from LTFT and RD fuels have less VOF compared to PM produced from ULSD under conventional combustion condition. The reason for this is discussed in Section 4.5. As fuels with high cetane number and high alkane content, PM from LTFT and RD fuels yield lower VOF content than PM from ULSD. The low viscosity of LTFT fuel results in a further reduced VOF content compared to RD.

Table 5.1 Volatile organic fraction and time for 50% mass burn

Type of Fuel	Condition	VOF (%)	t50% (min)
ULSD	conventional	15.3	27.9
	PCCI - 4.5	17.5	23.8
	PCCI - 2.5	21.4	10.3
LTFT	conventional	9.9	73.2
	PCCI 1.5	14.2	43.6
	PCCI 3.5	22.1	36.7
RD	conventional	12.5	74.8
	PCCI 1.5	16.0	43.8
	PCCI 3.5	17.2	34.7

Figure 5.11 shows the oxidation curves of PM collected from conventional and PCCI combustion modes for ULSD, LTFT and RD fuels at 525^{o}C. Table 5.2 shows the overall apparent rate constant and the instantaneous rate constant at 25%, 50% and 75% mass burn. Late injection PCCI combustion produces soot with significantly higher reactivity compared to conventional combustion. The reaction rate constants of soot produced from late injection PCCI combustion are 1.2-2.2 times higher than soot from the conventional combustion conditions. As fuels with high cetane number and high paraffinic content, LTFT and RD produce soot with

lower reactivity compared to ULSD. The reaction rate constants of soot from LTFT and RD fuels are 47-66% lower than soot produced from ULSD. This result agrees with the findings of Song et al.[120] and Yehliu et al.[87] who found that LTFT fuel produces soot with lower reactivity compared to ULSD, and oxygenated fuel biodiesel produces soot with highest reactivity.

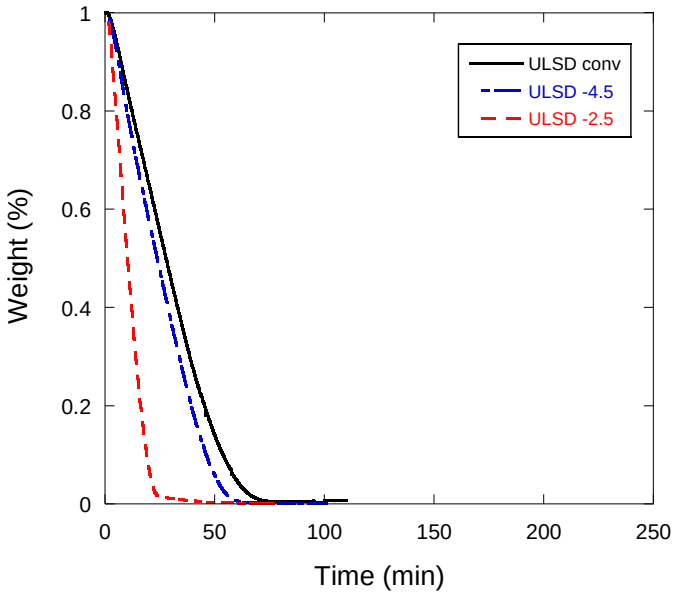

(a)

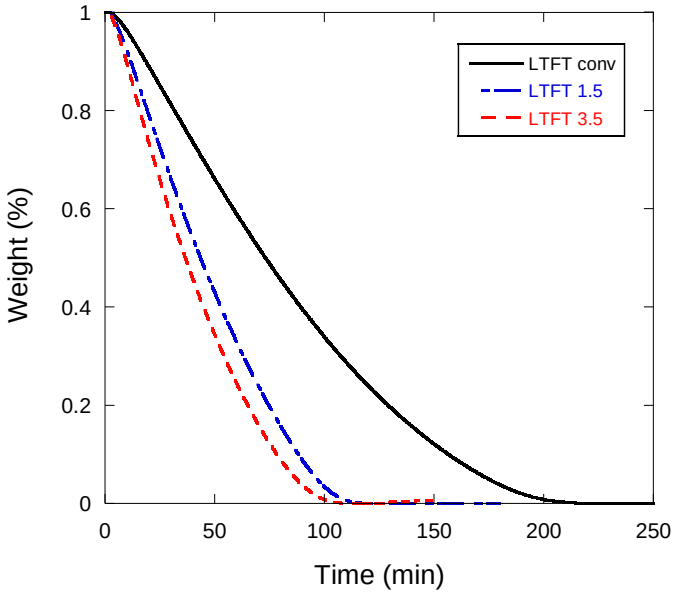

(b)

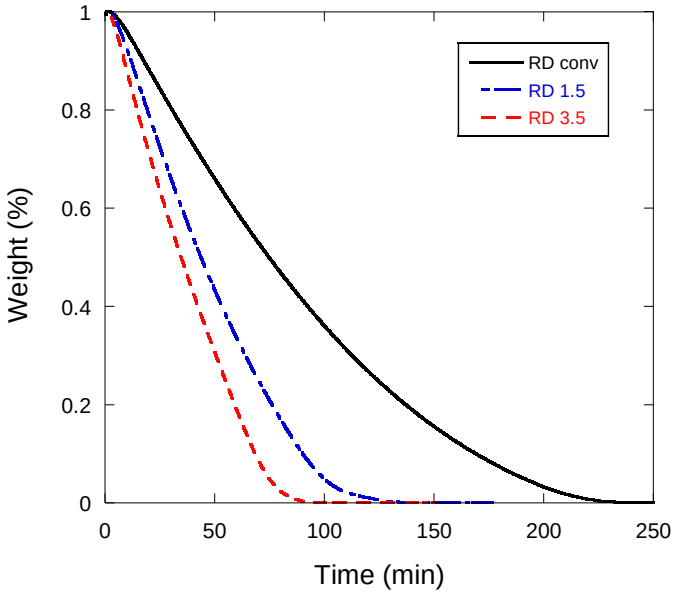

(c)

Figure 5.11 Thermogravimetric analyses for soot generated from conventional and late injection PCCI combustion modes with (a) ULSD, (b) LTFT and (c) RD fuel under isothermal oxidation at 525°C

Table 5.2 Overall apparent rate of constant and rate constant at different stages of oxidation at 525ºC

Type of Fuel	Condition	Overall Apparent Rate Constant (1/Pa/min)	Rate Constant at 25% mass burn (1/Pa/min)	Rate Constant at 50% mass burn (1/Pa/min)	Rate Constant at 75% mass burn (1/Pa/min)
ULSD	conventional	$1.45*10^{-6}$	$1.22*10^{-6}$	$1.80*10^{-6}$	$2.75*10^{-6}$
	PCCI - 4.5	$1.68*10^{-6}$	$1.43*10^{-6}$	$1.90*10^{-6}$	$3.46*10^{-6}$
	PCCI - 2.5	$2.87*10^{-6}$	$2.85*10^{-6}$	$3.41*10^{-6}$	$5.11*10^{-6}$
LTFT	conventional	$5.27*10^{-7}$	$4.70*10^{-7}$	$6.12*10^{-7}$	$6.26*10^{-7}$
	PCCI 1.5	$8.93*10^{-7}$	$8.22*10^{-7}$	$1.04*10^{-6}$	$1.67*10^{-6}$
	PCCI 3.5	$1.06*10^{-6}$	$9.77*10^{-7}$	$1.17*10^{-6}$	$1.72*10^{-6}$
RD	conventional	$5.14*10^{-7}$	$4.59*10^{-7}$	$5.65*10^{-7}$	$7.67*10^{-7}$
	PCCI 1.5	$8.97*10^{-7}$	$8.39*10^{-7}$	$1.02*10^{-6}$	$1.54*10^{-6}$
	PCCI 3.5	$1.13*10^{-6}$	$9.89*10^{-7}$	$1.02*10^{-6}$	$1.54*10^{-6}$

Although in this study, VOF correlates with the oxidative reactivity of PM, VOF content is not claimed as factor controlling PM reactivity, since VOF are driven off by thermal treatment under inert environment from the soot particles before oxidation. However, this thermal treatment process could open pore areas by removing VOF, which can increase the active areas open to oxidizer species.[121] The VOF content could relate to the amount of opened pore areas.

There are several factors which could explain why PM produced from PCCI combustion shows higher reactivity. To achieve PCCI combustion, higher EGR ratio and late injection timing are applied. Increased level of EGR could result in soot with higher reactivity. The reason could be explained as follow[122,123]: 1) Increased level of EGR could reduce the combustion temperature due to the thermal effect of CO_2, which could result in a less severe carbonization

process. As a consequence, less mature soot is produced. 2) Reduced temperature could reduce the concentration of reactive radical H, and decrease the production rate of PAH. This dilution effect of EGR can inhibit soot formation and result in soot with less developed nanostructure. 3) CO_2 could react with H radical and produce CO and OH radicals, or decompose into CO and O radicals. The OH and O radicals could react with soot precursors and suppress soot formation, which is considered as the chemical effect of EGR. With retarded injection timing under PCCI combustion, combustion temperature is lowered due to the delayed combustion phasing, and local equivalence ratio is reduced because of longer ignition delay. The two factors could result in PM with higher reactivity as explained previously. In addition, soot formation and oxidation history could be altered due to the change of combustion phasing. Soot produced from late injection timings experiences a shorter period under high temperatures, which could reduce the carbonization process, and result in soot with increased reactivity[124].

Fuel formulation also has a strong impact on the reactivity of soot. ULSD produces PM with higher reactivity in this study, which is in agreement with the work of Yehliu et al.[87] The reduced reactivity of PM from LTFT and RD fuels could be caused by the high CN of the two fuels. The shortened ignition delay could increase the local equivalence ratio and combustion temperature, which enhance soot formation and carbonization.

The reaction rate constant increases during the oxidation process. Firstly, the opened pore area during oxidation can increase the quantity of active sites. Secondly, graphene layers shrinks during oxidation process, which also increases the density of active sites. The two factors can all increase the oxidation reactivity of soot through the oxidation process.

Many factors could impact soot reactivity, such as surface area, surface functional groups, chemical composition and nanostructure, as discussed in Section 2.6. To investigate the impact of soot composition and structure on soot reactivity, various techniques are applied to measure the properties of soot generated from the three fuels under both PCCI and conventional conditions, which will be discussed in the following sections.

Soot produced from different fuels or engine operating conditions could go through different process of oxidation. To gain a better understanding of soot nanostructure change during oxidation, soot sample collected from the 9 conditions mentioned above were oxidized partially to 40% mass burn and 75% mass burn, and then examined by XPS, Raman spectroscopy, and TEM again.

5.9 Soot surface area analysis

Table 5.3 shows the initial BET surface area of PM collected from the 9 selected conditions. Surface area of soot shows no direct relationship with the rate of oxidation. It is considered that, instead of total surface area (TSA), active surface area (ASA) has a closer relationship with soot reactivity.[90] The total number of active site N_t could be described as: $N_t = \lambda * S_a$, where λ is the concentration of active sites on the surface, and S_a is the total surface area. Although TSA is found not to be directly related to soot reactivity, ASA is often found to increase with the increase of TSA.[125] In addition, total and active surface areas could change by different magnitude for different soot during the oxidation process, due to the removal of VOF, opened pore area and different oxidation processes. This change in TSA and ASA area during oxidation can also affect soot reactivity. In this work, initial soot BET surface area is generally increased by PCCI combustion mode. Soot produced from LTFT and RD has very similar rate of oxidation and surface areas under both late injection PCCI and conventional combustion mode.

Under late injection PCCI combustion conditions, ULSD produces soot with lower surface area compared to soot from LTFT and RD, however, with much higher reactivity. This may be caused by the relatively higher VOF content which blocks the pore areas. In addition, surface area increases with retarded injection timing under PCCI combustion for LTFT and RD fuels. However, ULSD shows the reverse effect, even though the particle aggregates are very small and the structure is amorphous under this particular condition. This indicates soot produced from ULSD late PCCI condition has dramatically different properties compared to the other soots.

Table 5.3 BET surface area for soot generated from ULSD, LTFT and RD under conventional and late PCCI conditions

Type of Fuel	Condition	Surface area (m^2/g)
ULSD	conventional	149
	PCCI - 4.5	160
	PCCI - 2.5	139
LTFT	conventional	149
	PCCI 1.5	189
	PCCI 3.5	213
RD	conventional	142
	PCCI 1.5	187
	PCCI 3.5	191

5.10 X-ray diffraction

Figure 5.12 shows the X-ray diffraction patterns for soot generated from ULSD, LTFT and RD under both conventional condition and late injection PCCI combustion conditions. Due to the amount of sample required, only the initial soot is examined by XRD. There are primarily three peaks in the XRD spectrums for soot, a (002) peak around 25^o, (10) peak around 43^o, and a

(110) peak around 77°. The peak locations and FWHM are similar for all samples except for the intensity of the spectrums.

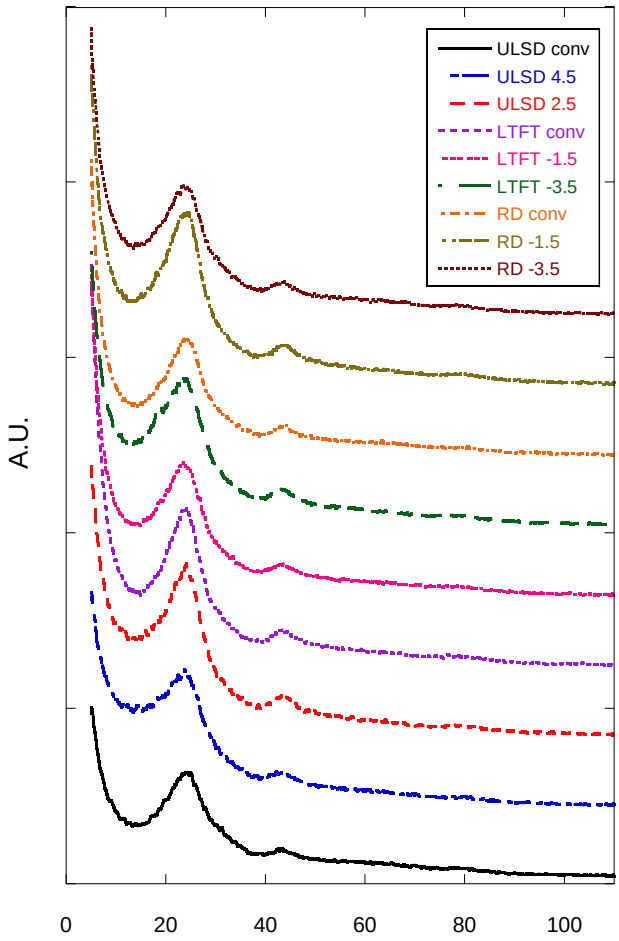

Figure 5.12 XRD patterns for soot collected from ULSD, LTFT and RD under both conventional and late injection PCCI conditions

Interlayer spacing (d_{002}), stacking height (L_c), crystalline basal plane diameter (L_a) and average number of layers (N) can be calculated using the equations described in Section 3.2.4. The results are shown in Table 5.4. The interlayer spacing d_{002} is around 0.375 nm, which is

much lower than the interlayer spacing of graphite 0.338.[126] This indicates a very low degree of graphitization.[127] Soot generated from PCCI conditions show a slightly smaller number of layers per crystallite. In addition, LTFT and RD at the latest PCCI conditions produce soot with smaller stacking height. No clear trend is shown for basal plane diameter of soot generated from the different fuels and conditions. This is because soot produced here is highly disordered and contains a significant amount of amorphous carbon. The uncertainty of the instrument is higher than the variation between samples. In addition, there are also limitations for using Scherrer's equation for amorphous materials.[128]

Table 5.4 Structure parameters from XRD spectra analysis

Type of Fuel	Condition	d002 (nm)	Lc (nm)	La (nm)	N
ULSD	conventional	0.372	1.882	3.154	5.06
	PCCI - 4.5	0.375	1.824	3.537	4.86
	PCCI - 2.5	0.375	1.815	3.470	4.84
LTFT	conventional	0.373	1.985	3.17	5.32
	PCCI 1.5	0.376	1.890	2.893	5.03
	PCCI 3.5	0.381	1.659	3.904	4.35
RD	conventional	0.370	1.758	3.245	4.74
	PCCI 1.5	0.376	1.821	3.634	4.84
	PCCI 3.5	0.373	1.673	3.256	4.49

5.11 X-ray photoelectron spectroscopy

To understand the oxidation process for the soot samples collected from the different fuels and combustion modes, collected soot samples are oxidized in a TA Instruments STD Q600 to 40% and 75% mass fraction burned. Those partially oxidized soot samples are re-examined by

XPS, Raman spectroscopy, and TEM to investigate their structural changes from different periods of oxidation.

Both survey scans and core scans of the C 1s peak and the O 1s peak are analyzed. From the survey scan, a semi-quantitative surface elemental composition could be analyzed from the specta. From the core scan for the C 1s and O 1s peaks, element bonding and functional groups can be interpreted.

Table 5.5 shows the elemental composition of as received soot collected from both conventional and late PCCI combustion modes for the three fuels. Only elemental carbon and oxygen are found in the XPS spectra, indicating that the concentration of elements from lubricating oil such as Ca, S and P are below the detection limit. Combustion mode has a major impact on soot composition, more so than fuel type. Soot produced from the conventional combustion mode has surface oxygen content around 8 – 10 atomic%. Late injection PCCI combustion mode produces soot with much higher oxygen content, around 22 atomic%. Soot produced from late injection PCCI combustion conditions contains much higher concentrations of oxygen compared to conventional combustion conditions, indicating higher concentrations of surface oxygen functional groups within late injection PCCI soot. Although surface oxygen content correlates well with oxidative reactivity, previous research has found that surface functional groups do not necessarily affect the reactivity of soot[129].

Table 5.5 Elemental composition for soot collected from conventional and PCCI conditions

Type of Fuel	Condition	C content (%)	O content (%)
ULSD	conventional	90.4	9.6
	PCCI - 4.5	81.8	18.2
	PCCI - 2.5	78.8	21.2
LTFT	conventional	92.7	7.3
	PCCI 1.5	82.5	17.5
	PCCI 3.5	76.2	23.8
RD	conventional	92.3	7.7
	PCCI 1.5	81.4	18.6
	PCCI 3.5	77.7	22.3

Figure 5.13 shows the peak deconvolution of the C 1s and O 1s spectra. C1s spectra are analyzed by the curve fitting method described in Section 3.2.5, following the work of Smith et al.[94] The main carbon peak is deconvoluted into sp2 and sp3 peaks[130], located at 284.4 eV and 285.1 eV. There is still a peak located around 283.2 eV representing cyclopentane ring atoms.[131] For oxygen functional groups, the peaks are assigned as follow:[132,133,134] C-O in alcohol groups around 286.1 eV; C=O in quinine or carbonyl groups around 287.1 eV; O=C-O in carboxylic acid or ester groups. In addition, there is a peak around 291-292 assigned to π and π^* carbons. The O 1s spectra are deconvoluted into two peaks[135], a C-O group at 533.2 eV and C=O group at 531.4 eV.

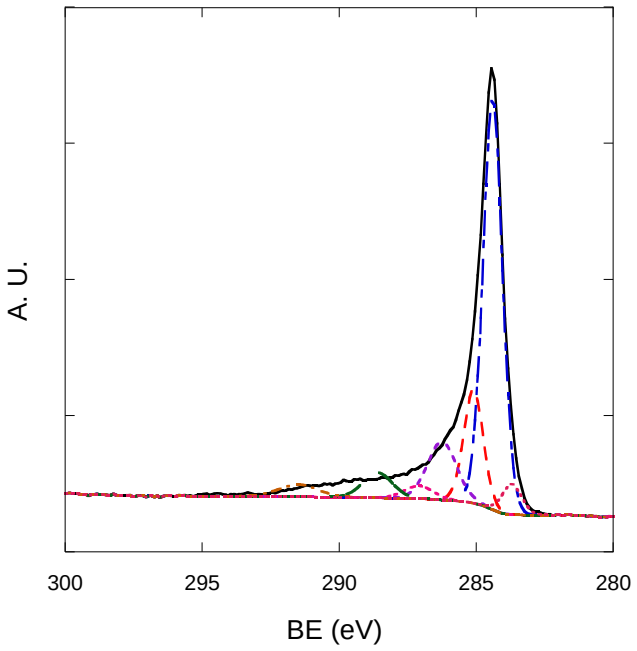

(a)

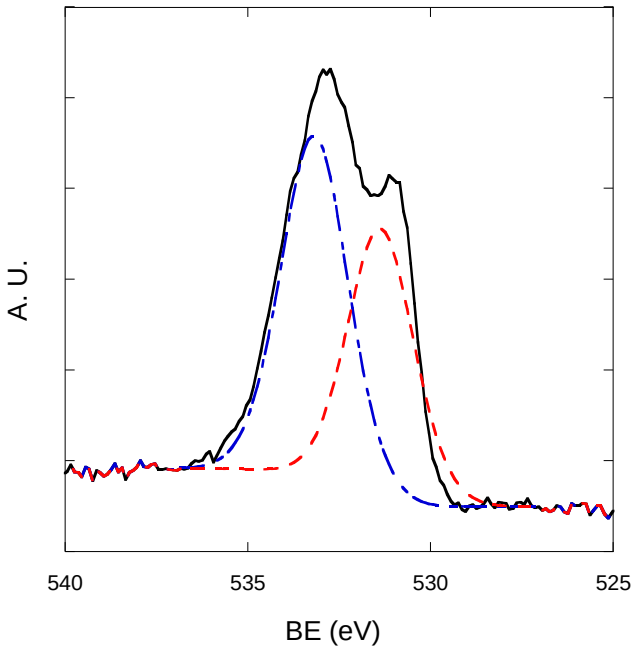

(b)

Figure 5.13 Peak deconvolution of (a) C 1s and (b) O 1s spectra

Table 5.6 shows the elemental state of the carbon atoms for different fuels and combustion conditions. Sp3 carbon and fullerene/cyclopentane ring carbon are considered to be amorphous and/or defective, which are more reactive. A significant increase of amorphous carbon is observed with late injection PCCI combustion mode, with an increase of oxygen containing functional groups. This can explain why the reactivity of soot from PCCI combustion is higher compared to soot produced from conventional combustion. Late injection timing and higher EGR ratio can effectively reduce the combustion temperature. Under lower combustion temperature and lower local equivalence ratio, soot has less mature nanostructure. In addition, the percentage of C=O groups increases slightly with PCCI combustion for LTFT and RD fuels.

Table 5.6 Element state analysis from C 1s and O 1s spectra of original soot

Fuel Type	Condition	C 1s (%)			O 1s (%)	
		sp2 Carbon	sp3 /ring Carbon	C-O/ C=O/COO	C-O	C=O
ULSD	conventional	56.1	19.8	21.2	98.6	1.4
	PCCI - 4.5	53.8	20.1	23.1	59.8	40.2
	PCCI - 2.5	45.5	29.4	24.6	61.1	38.9
LTFT	conventional	59.6	18.9	18.6	60.5	39.5
	PCCI 1.5	58.1	18.7	20.3	49.6	50.4
	PCCI 3.5	47.9	25.2	26.3	52.1	47.9
RD	conventional	57.5	19.9	19.6	56.0	44.0
	PCCI 1.5	46.9	22.8	28.6	52.7	47.3
	PCCI 3.5	41.5	25.5	30.7	51.8	48.2

Figure 5.14 shows the C 1s spectra of soot produced from the three fuels under conventional and late injection PCCI combustion. From the spectra, a significant increase in sp3 carbon and oxygen functional groups as well as a decrease in sp2 carbon intensity could be

observed under PCCI combustion for all three fuels. Figure 5.15 shows O1s spectra for soot produced from the three fuels. The spectra show that under conventional combustion mode, oxygen is mainly from C-O bonding. In addition, the intensities of oxygen peak for soot from LTFT and RD under conventional combustion are significantly lower than peaks for soot from PCCI combustion, indicating a lower surface oxygen concentration. Under PCCI combustion, an increased C=O peak could be found, especially in soot from LTFT and RD.

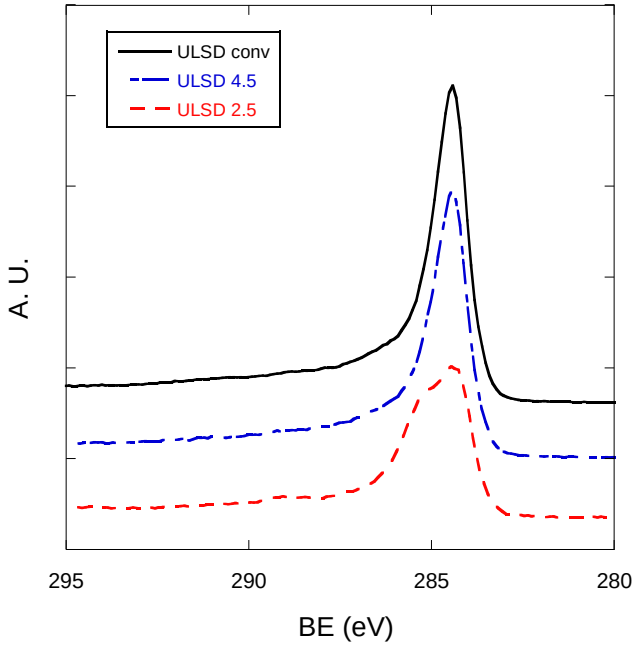

(a)

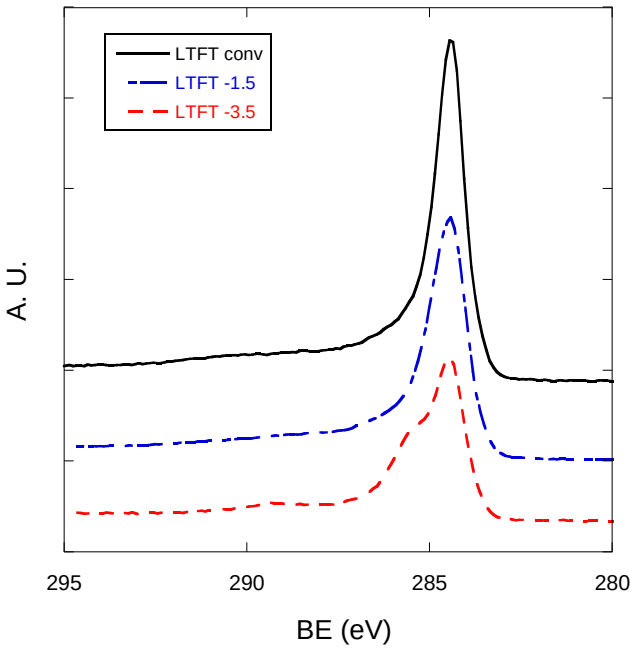

(b)

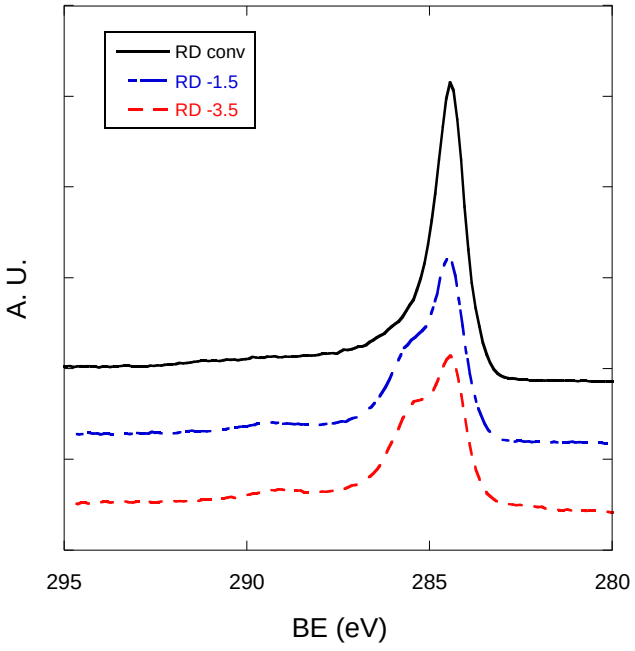

(c)

Figure 5.14 C 1s peaks for soot produced from (a) ULSD, (b) LTFT and (c) RD fuels under conventional and late injection PCCI combustion mode

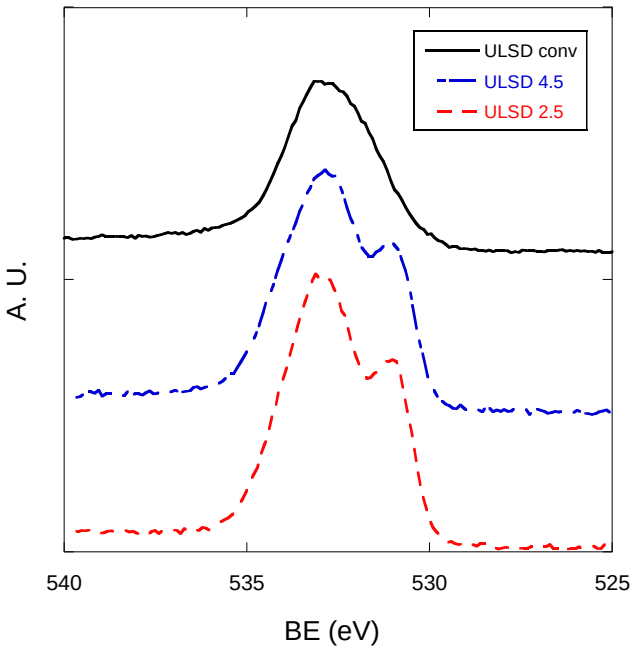
ULSD conv
ULSD 4.5
ULSD 2.5
A. U.
540
535
530
525
BE (eV)

(a)

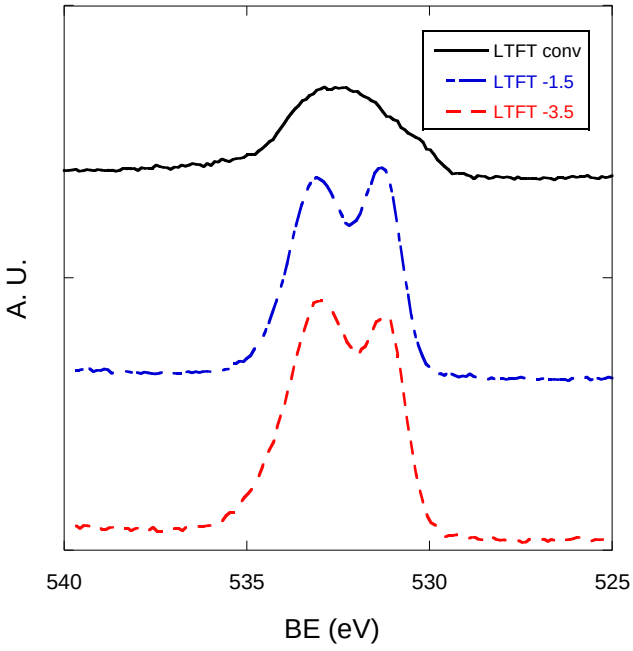
LTFT conv
LTFT -1.5
LTFT -3.5
A. U.
540
535
530
525
BE (eV)

(b)

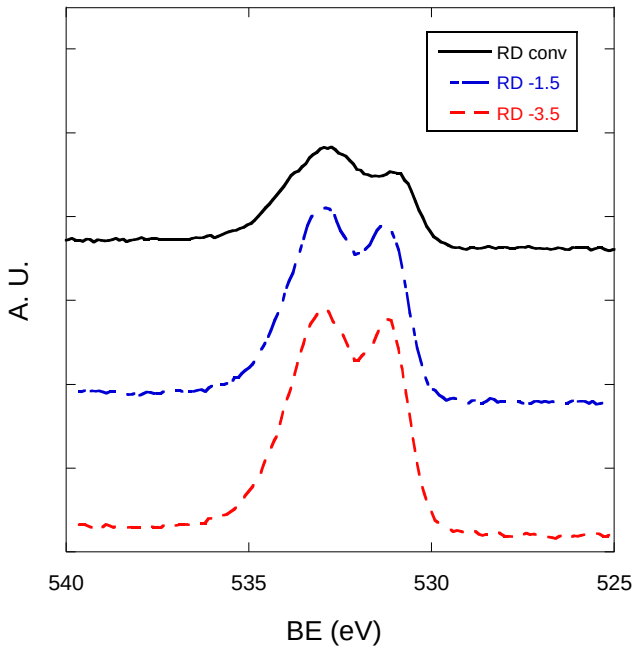

(c)

Figure 5.15 O 1s peaks for soot produced from (a) ULSD, (b) LTFT and (c) RD fuels under conventional and late injection PCCI combustion mode

Figure 5.16 shows the defect/graphitic carbon ratio versus the oxidative rate constant. Here the defect carbon means amorphous carbon with sp3 bonding and fullerene carbon. The graphitic carbon means graphite carbon with sp2 bonding. The figure shows that defect/graphitic carbon ratio correlates well with the rate constant of soot oxidation. Soot from conventional combustion has lower defect/graphitic ratio and lower oxidation rate constant compared to soot from PCCI combustion, as discussed previously. ULSD has lower CN than LTFT and RD fuels. As a result, longer time is provided for charge mixing and the local equivalence ratio is reduced. ULSD has higher defect carbon ratio and higher oxidation rate constant compared to LTFT and RD fuels. The bonding of amorphous carbon and fullerene carbon is weaker than the bonding of graphite carbon. So those “defect” carbon are more reactive and requires less activation energy

during oxidation. Fitting of the XPS C 1s peak can provide an effective way to predict and explain the oxidative reactivity of soot. Figure 5.17 shows the ratio of carbon atoms within oxygen functional groups versus the oxidation rate constant. Oxidation rate constant generally increase with surface oxygen functional groups. Some researches show that soot reactivity relates with surface oxygen content[87], while some show that surface oxygen content does not affect soot reactivity[136]. Carbon atoms bonded with oxygen functional groups should require less activation energy during the oxidation process. However, to prevent carbon nanostructure changes under high temperatures, initial soot is examined without pretreatment, so the oxygen functional groups could also result from VOF coated on the surface of the soot particles.

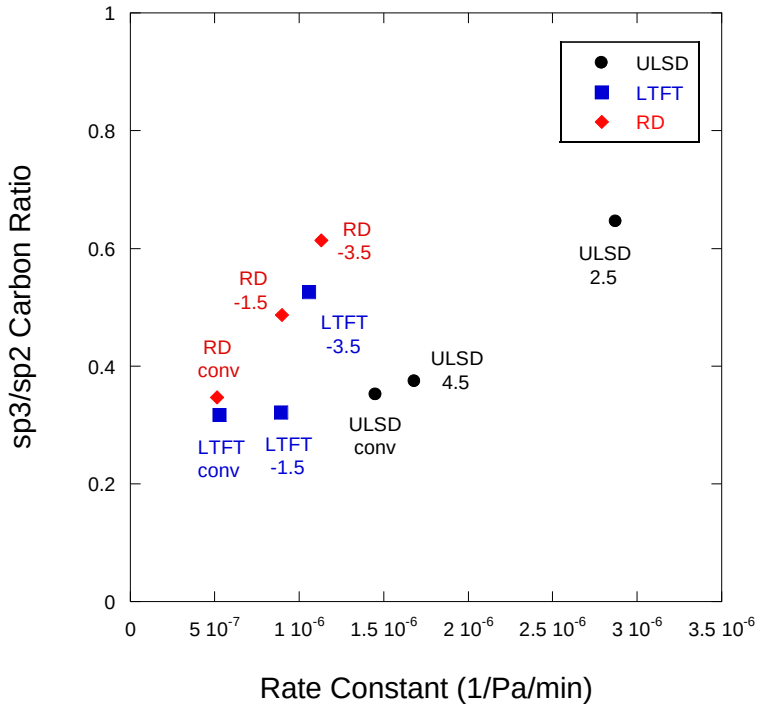

Figure 5.16 Defect/graphitic carbon ratio versus oxidative rate constant for ULSD, LTFT and RD fuels for both conventional and late injection PCCI combustion mode

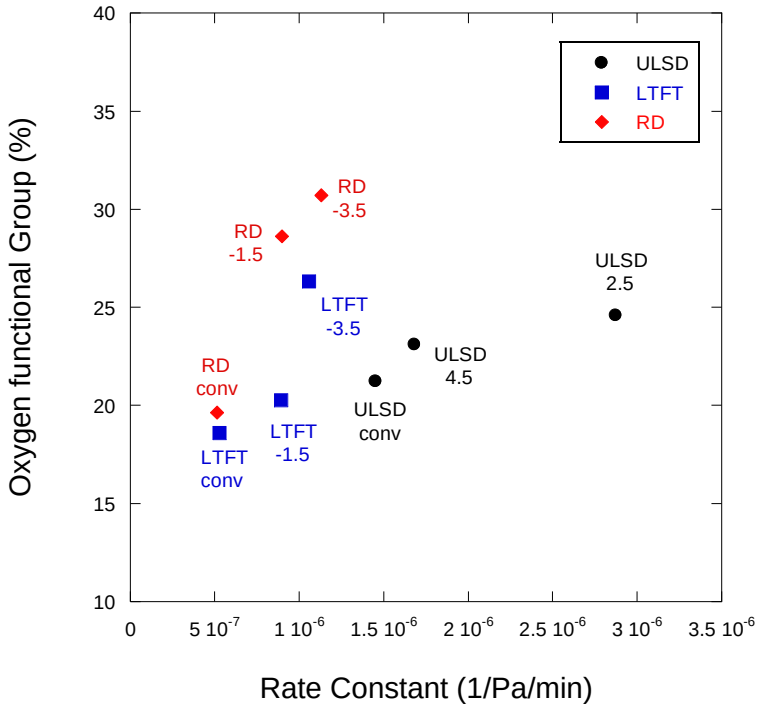

Figure 5.17 Oxygen functional content versus oxidative rate constant for ULSD, LTFT and RD fuels for both conventional and late injection PCCI combustion mode

Table 5.7 shows the surface carbon and oxygen concentrations of soot from different stages of oxidation. For all three fuels, surface oxygen concentration for conventional combustion mode stays unchanged at around 7-10 atomic% during the oxidation process. Under late injection PCCI combustion, oxygen content reduced from 17-23 atomic% to 9-12 atomic% during oxidation. Unlike the as received soot, surface oxygen concentration does not vary much with the type of fuel, combustion mode, or stage of oxidation. Soot samples from late injection PCCI combustion conditions have slightly higher oxygen concentration compared to soot from conventional combustion. Soot samples with 75% mass burn have slightly higher surface oxygen concentration compared to 40% mass burn soot samples. The high surface oxygen concentration

of as received PCCI soot may come from the high VOF content. In addition, carbon atoms within oxygen functional groups should oxidize first, which reduces the very high oxygen concentration of PCCI soot. Soot samples from PCCI combustion have less mature nanostructure which can provide more active sites to bond with oxygen atoms. This explains the slightly higher oxygen concentration of PCCI soot during oxidation.

Table 5.7 Surface carbon and oxygen concentrations at 40% and 75% burn

Fuel Type	Condition	40% burn		75% burn	
		C content (%)	O content (%)	C content (%)	O content (%)
ULSD	conventional	90.2	9.8	90.0	10.0
	PCCI - 4.5	90.1	9.9	88.4	11.6
	PCCI - 2.5	89.3	10.7	88.7	11.3
LTFT	conventional	92.2	7.9	90.9	9.1
	PCCI 1.5	89.7	10.3	87.5	12.5
	PCCI 3.5	89.1	10.9	88.3	11.7
RD	conventional	92.0	8.0	90.3	9.7
	PCCI 1.5	90.4	9.6	88.0	12.0
	PCCI 3.5	89.1	10.9	88.4	11.6

Tables 5.8 and 5.9 show the element state of C 1s and O 1s peaks at 40% and 75% mass burned. The properties of soot under the two stages of oxidation do not show much difference. Carbon elemental state and oxygen functional groups stay similar regardless of fuel type and combustion condition. Figure 5.18 shows the defect/graphitic carbon ratio of soot produced from the three fuels under different stages of oxidation. The defect/graphitic carbon ratio decreases

during oxidation. This indicates that amorphous carbon oxidizes before graphitic carbon. In addition, soot could go through structural changes during oxidation. Figure 5.19 shows the percentage of carbon atoms bonded with oxygen functional groups under the two stages of oxidation. There is no clear trend for the percentage of oxygen functional groups during oxidation. Soot from late injection PCCI combustion shows a higher percentage of oxygen functional groups from C 1s peak analysis, which is consistent with surface oxygen concentration analysis.

Table 5.8 Element state analysis of C 1s and O 1s spectra of soot at 40% burn

Fuel Type	Condition	C 1s (%)			O 1s (%)	
		sp2 Carbon	sp3/ring Carbon	C-O/ C=O/COO	C-O	C=O
ULSD	conventional	53.2	18.3	24.1	57.7	42.3
	PCCI - 4.5	53.1	18.0	24.7	59.4	40.6
	PCCI - 2.5	51.8	17.7	25.9	58.3	41.7
LTFT	conventional	54.6	17.1	23.4	58.6	41.4
	PCCI 1.5	56.2	17.5	23.4	55.4	44.6
	PCCI 3.5	54.3	14.6	25.8	57.5	42.5
RD	conventional	53.8	17.4	23.5	58.5	41.5
	PCCI 1.5	47.4	15.7	29.1	59.5	40.5
	PCCI 3.5	52.7	17.1	25.7	55.9	44.1

Table 5.9 Element state analysis of C 1s and O 1s spectra of soot at 75% burn

Fuel Type	Condition	C 1s (%)			O 1s (%)	
		sp2 Carbon	sp3/ring Carbon	C-O/ C=O/COO	C-O	C=O
ULSD	conventional	54.3	18.4	23.7	58.7	41.3
	PCCI - 4.5	53.7	16.8	25.3	56.6	43.4
	PCCI - 2.5	54.1	16.5	25.4	55.7	44.3
LTFT	conventional	55.8	17.6	23.5	56.4	43.6
	PCCI 1.5	46.5	12.7	30.3	55.0	45.0
	PCCI 3.5	52.6	12.7	27.9	58.2	41.8
RD	conventional	51.9	15.5	26.2	58.4	41.6
	PCCI 1.5	51.3	14.0	27.2	60.3	39.7
	PCCI 3.5	48.2	11.3	31.5	55.8	44.2

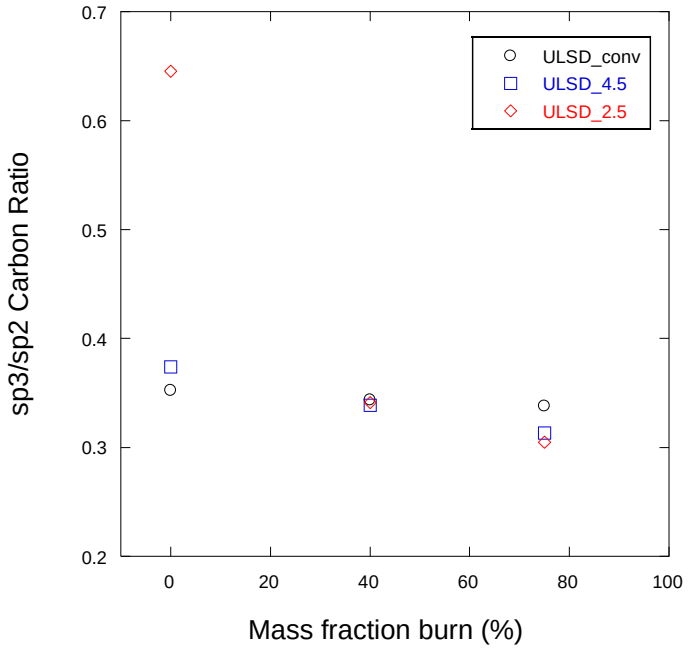

(a)

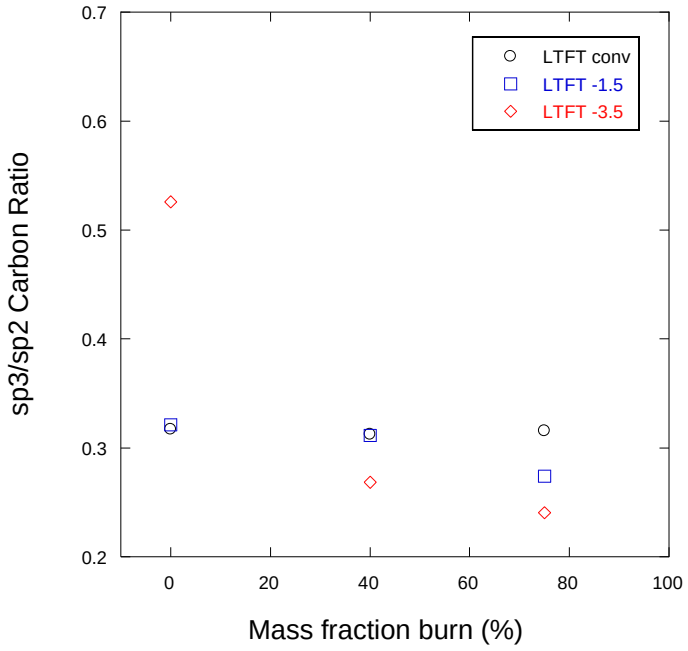

(b)

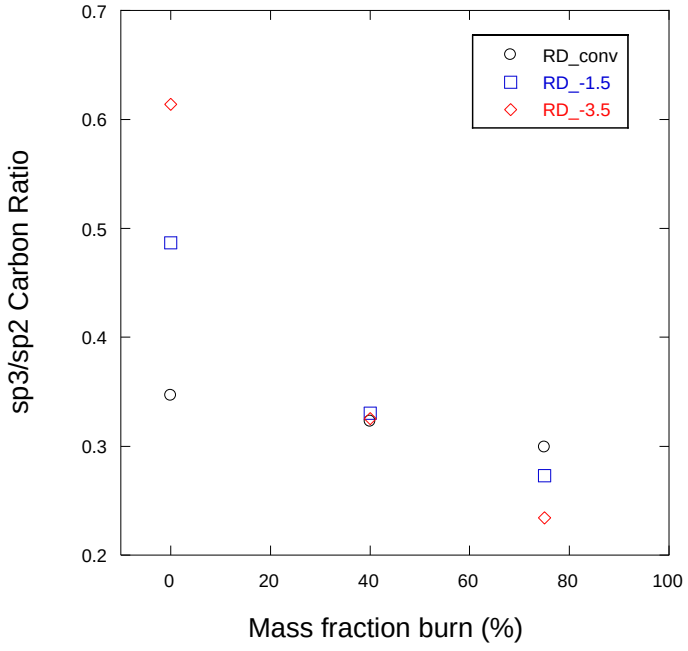

(c)

Figure 5.18 Defect/graphitic carbon ratios of soot from (a) ULSD, (b) LTFT and (3) RD fuels of as received soot, and soot at 40% and 75% mass burned

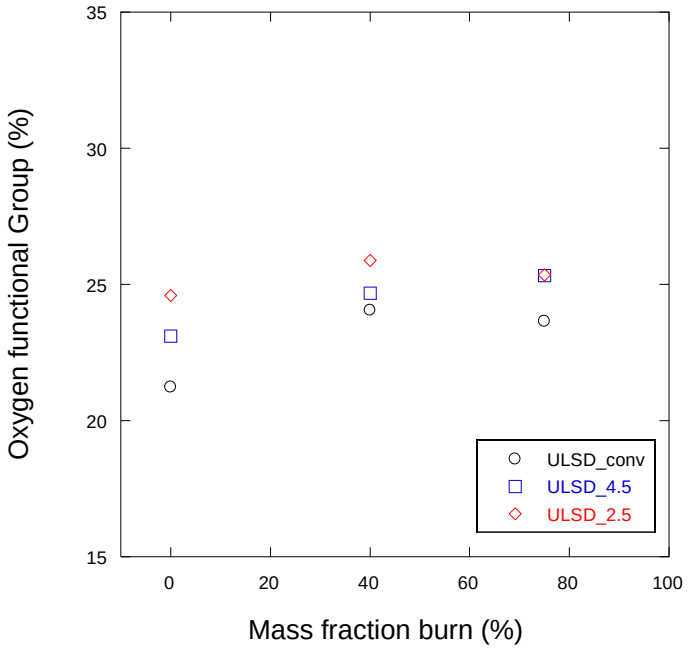
Oxygen functional Group (%)
35
30
25
20
15
0
20
40
60
80
100
Mass fraction burn (%)
ULSD_conv
ULSD_4.5
ULSD_2.5

(a)

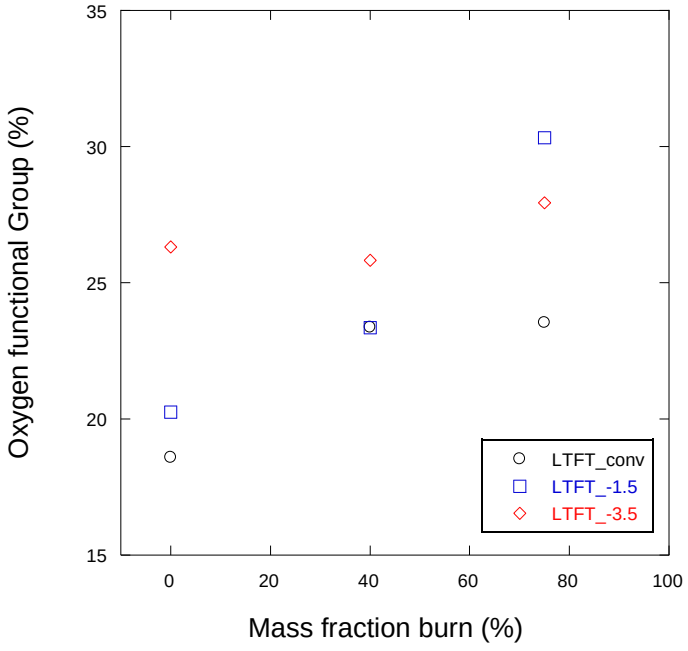
Oxygen functional Group (%)
35
30
25
20
15
0
20
40
60
80
100
Mass fraction burn (%)
LTFT_conv
LTFT_-1.5
LTFT_-3.5

(b)

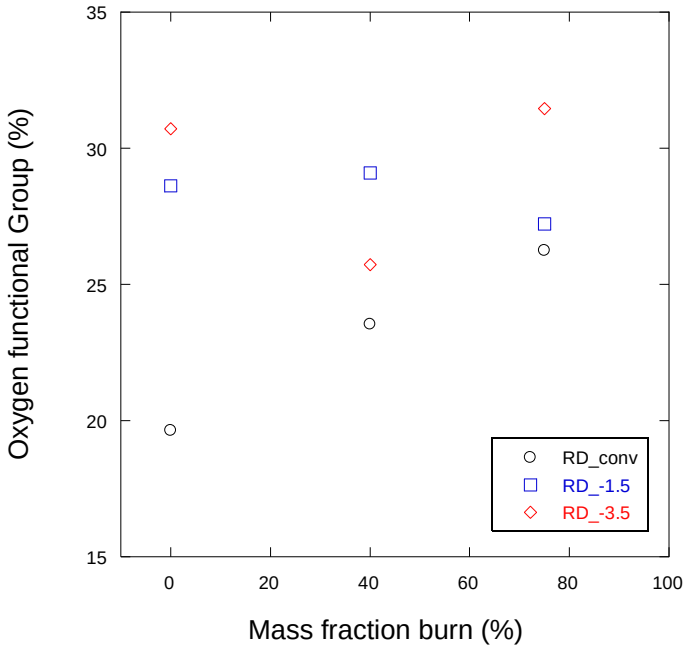

(c)

Figure 5.19 Ratio of carbon bonded with oxygen functional groups of soot from (a) ULSD, (b) LTFT and (c) RD of as received soot, and soot at 40% and 75% mass burned

5.12 Raman spectroscopy

The curve fitting of spectra follows the method developed by Seong et al.[137], which is a 3L1G method. The curve fitting method is also illustrated in Figure 5.20. The three Lorentizan bands are at 1200cm^{-1} (D4), 1350 cm^{-1} (D1), and 1590 cm^{-1} (G); the Gaussian band is at 1500cm^{-1} (D3). The degree of structural disorder could be interpreted by analyzing the spectra. Both G and D1 peaks represent the features of sp2 bonding. The G mode has E_{2g} symmetry, which involves the in-plane bond-stretching motion of sp2 carbon atoms. The D1 peak comes from the breathing mode of A_{1g} symmetry, which is only present in disordered carbons such as carbon atoms on graphene edges.[138] The D3 peak represents the stretching of sp3 bonding of amorphous carbon. The intensity ratio or area ratio of D1 and G band, and the FWHM of D1 and G band are

usually used as indicators of carbon material disorder.[139] The I_{D1}/I_G or A_{D1}/A_G ratios can be used to represent the density of edge sites.[140] The FWHM of D1 peak can provide information about the distribution of crystallite sizes, and relative abundance of structural disorder.[141] In addition, the G peak broadens as the graphite structure becomes disordered within the carbon layers.[142] The intensity or area of the D3 peak could be used to represent amorphous carbon.[143]

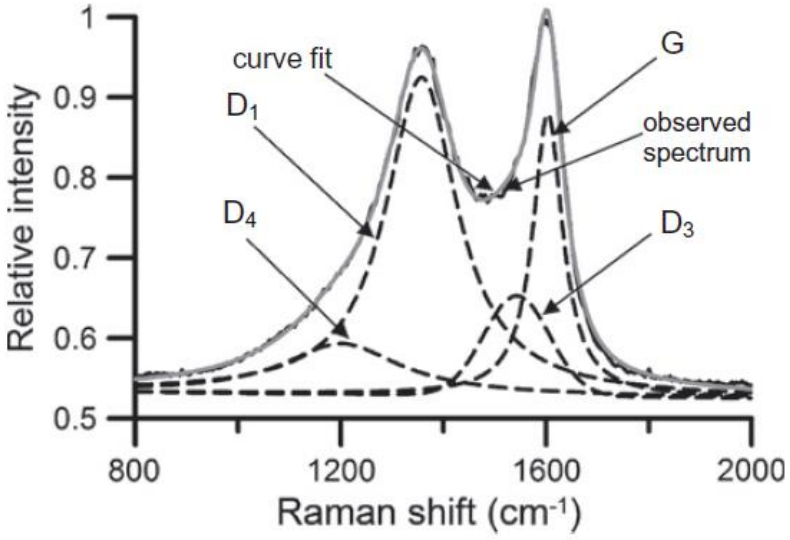

Figure 5.20 Raman spectroscopy peak fitting[144]

From Figure 5.21, linear relationships could be observed between the D1band FWHM and the oxidation rate constant of soot produced from the three fuels under both conventional and PCCI conditions. A broadened D1 band means a higher density of grephene edge sites. The relationship between G band FWHM and oxidation rate constant has similar trend. The increased G band FWHM also indicates higher degree of disorder for soot particles. PCCI combustion results in soot with larger D1 and G band FWHM for all three fuels, which also have higher oxidation rate constant. So it can be indicated that, the reduced combustion temperature and local equivalence ratio of PCCI combustion can not only increase the density of amorphous carbon,

but also can result in particles with smaller graphene layers, higher density of edge sites and more disordered nanostructure. In addition, ULSD produces soot with larger D1 and G band FWHM and higher rate constant compared to LTFT and RD soot. Low CN ULSD also produces soot with smaller graphene size and higher reactivity.

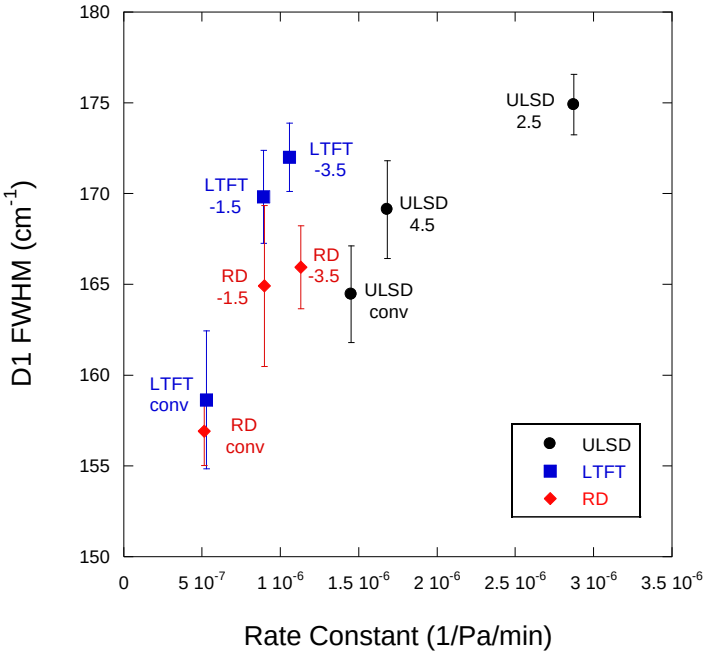

(a)

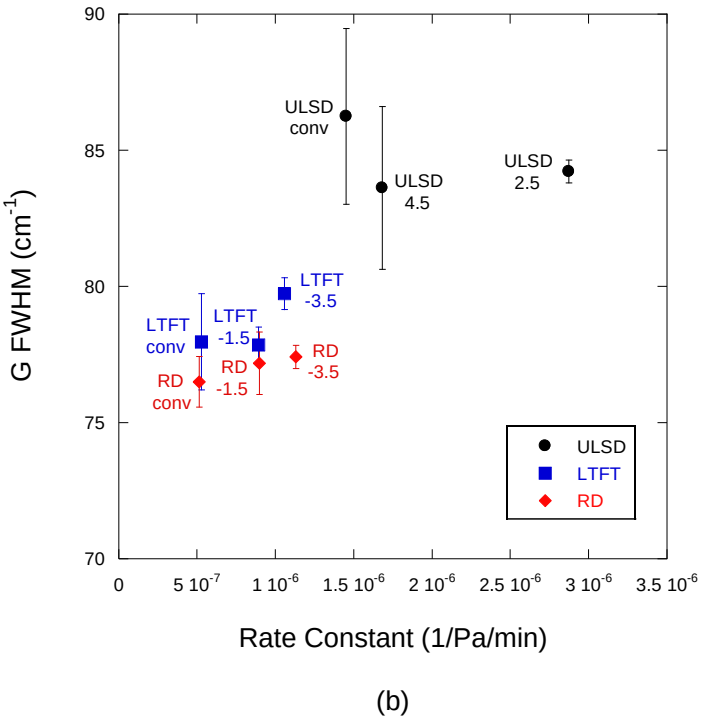

Figure 5.21 FWHM of (a) D1 and (b) G band versus rate constant

Figure 5.22 shows the I_{D1}/I_G of as received soot and soot at 40% and 75% mass burned. I_{D1}/I_G increases during the oxidation process for soot from all three fuels and both combustion modes. This is different from previous work, which reported an I_{D1}/I_G decrease during oxidation due to the thermal annealing effect.[145] However, I_{D1}/I_G increases during oxidation for this study. One possible reason is that the high density of amorphous carbon also goes through thermal annealing which formed small graphene layers and increased the graphene edge carbon density.

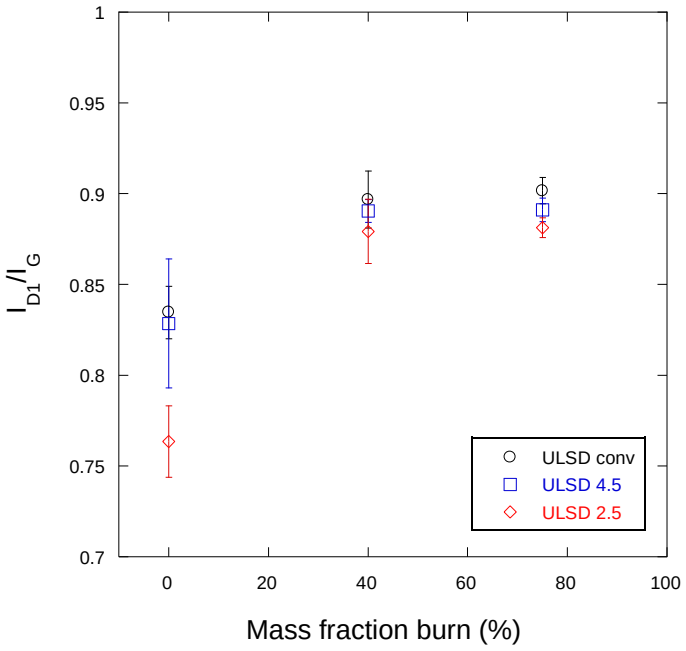
1
0.95
0.9
0.85
0.8
0.75
0.7
I_{D1}/I_G
0
20
40
60
80
100
Mass fraction burn (%)
ULSD conv
ULSD 4.5
ULSD 2.5

(a)

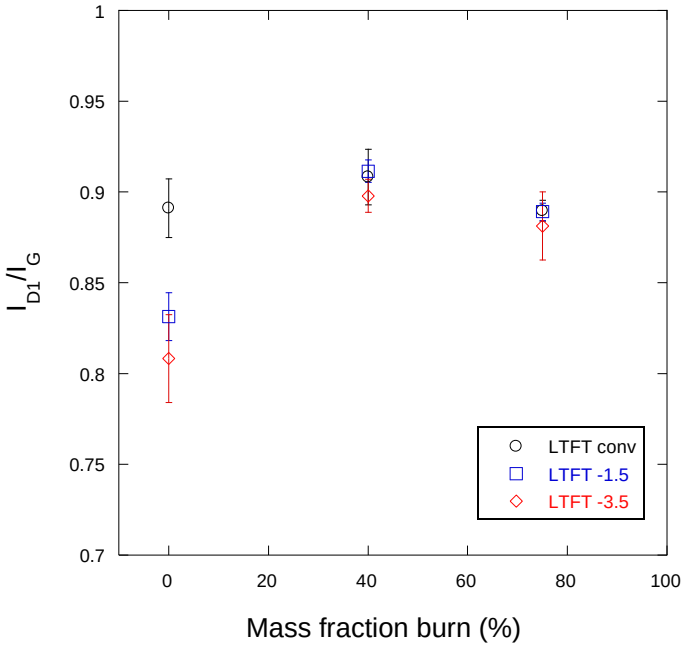
1
0.95
0.9
0.85
0.8
0.75
0.7
I_{D1}/I_G
0
20
40
60
80
100
Mass fraction burn (%)
LTFT conv
LTFT -1.5
LTFT -3.5

(b)

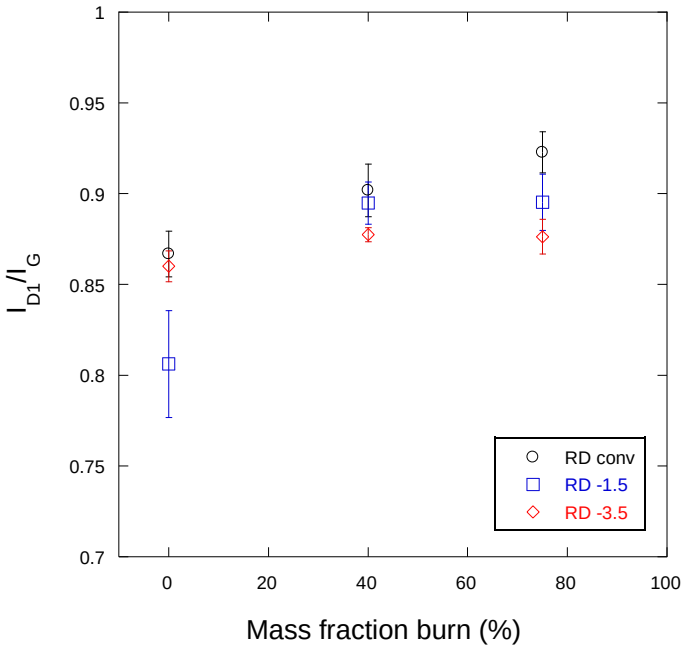

(c)

Figure 5.22 Intensity of D1 peak and G peak ratio of soot from (a) ULSD, (b) LTFT and (3) RD of as received soot, and soot at 40% and 75% mass burned

Figure 5.23 shows the D1 FWHM of soot under different stages of oxidation. D1 band FWHM of soot during oxidation stays similar with the as received soot. Figure 5.24 shows the G FWHM of soot at 40% and 75% mass burned. For ULSD, G band FWHM decreases slightly during oxidation. This could be caused by the thermal annealing effect mentioned previously. However, for LTFT and RD, G band FWHM follows a similar trend as I_{D1}/I_G, which increases during oxidation, indicating a reduced degree of order of the graphite structure in the soot particles.

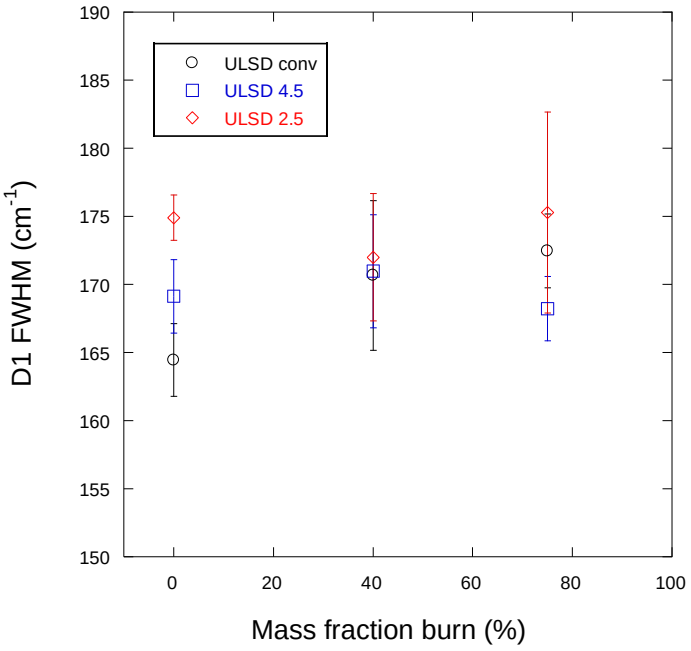
ULSD conv
ULSD 4.5
ULSD 2.5
D1 FWHM (cm-1)
Mass fraction burn (%)
190
185
180
175
170
165
160
155
150
0
20
40
60
80
100

(a)

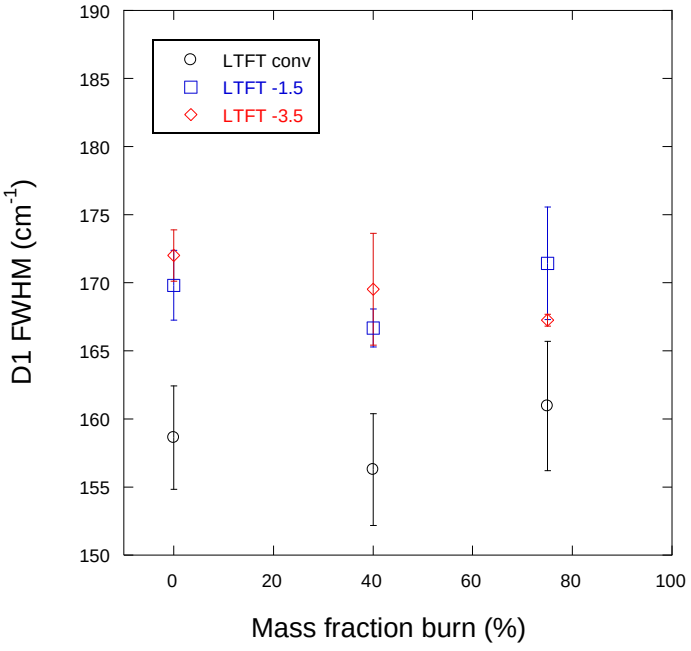
LTFT conv
LTFT -1.5
LTFT -3.5
D1 FWHM (cm-1)
Mass fraction burn (%)
190
185
180
175
170
165
160
155
150
0
20
40
60
80
100

(b)

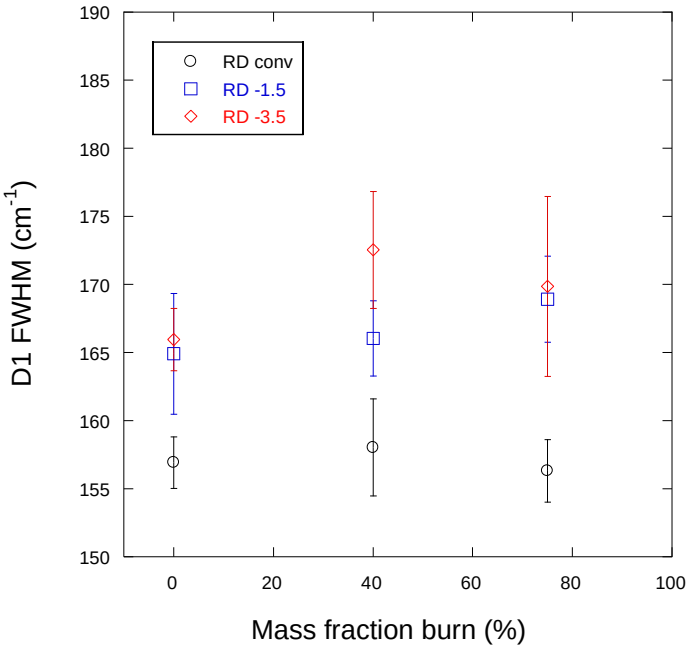

(c)

Figure 5.23 Ratio FWHM of D1 band of soot from (a) ULSD, (b) LTFT and (3) RD of as received soot, and soot at 40% and 75% mass burned

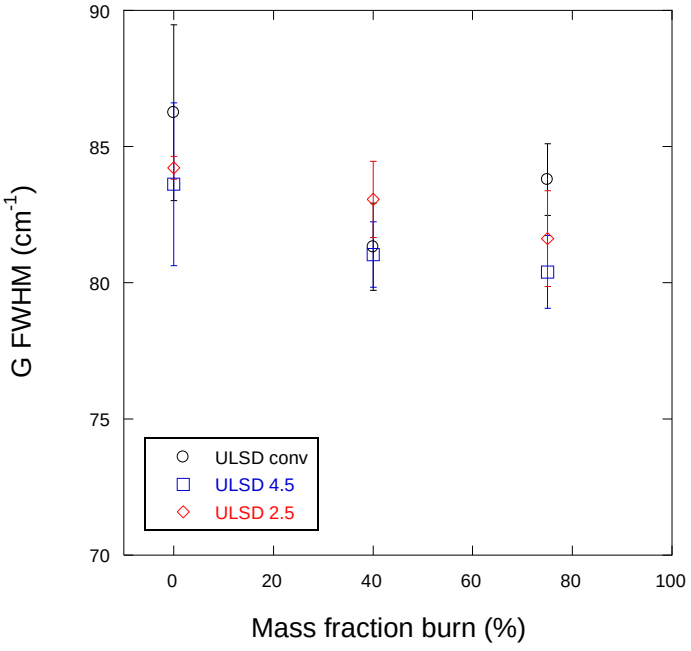

(a)

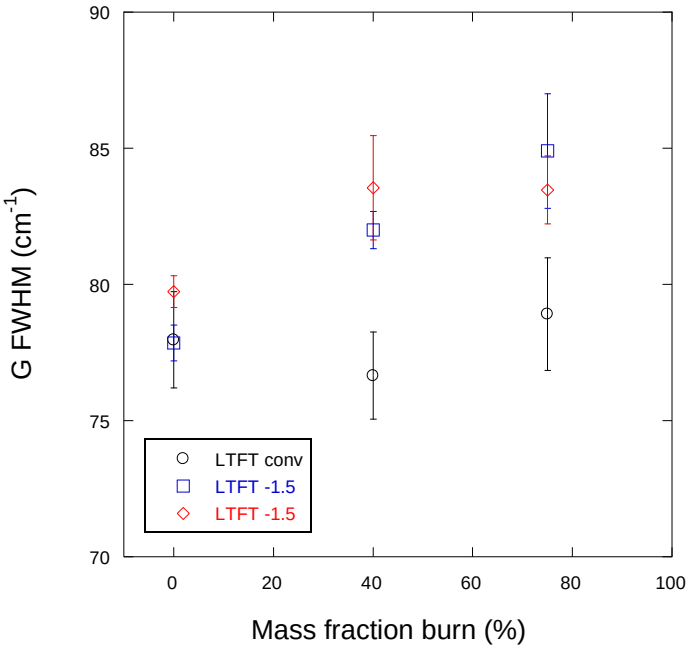

(b)

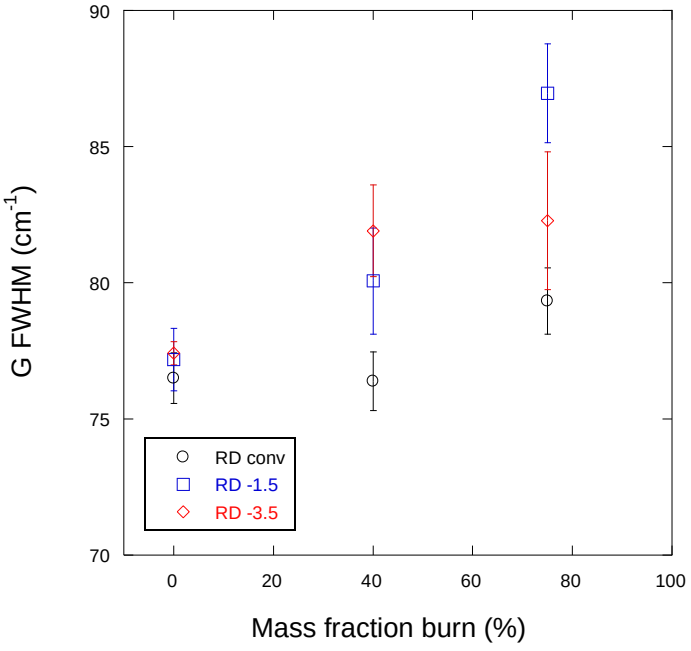

(c)

Figure 5.24 Ratio FWHM of G band of soot from (a) ULSD, (b) LTFT and (3) RD of as received soot, and soot at 40% and 75% mass burned

5.13 Transmission electron microscopy

Figures 5.25-5.27 show the TEM images for ULSD, LTFT and RD under both conventional and late injection PCCI combustion conditions. For each condition, the figures show both low resolution images at 40,000x and high resolution images at 400,000x. TEM images with magnification of 40,000x show that soot produced from PCCI combustion displays similar fractal-like structure as soot produced from conventional combustion. However, soot from late injection PCCI combustion has a much smaller primary particle size and aggregation size compared to soot from conventional combustion for all three fuels. The primary particle and particle aggregate sizes are around 25nm and 400 nm for conventional combustion soot, while 10nm and 150 nm for late injection PCCI combustion soot. This agrees with the LTC study of Seong et al.,[146] who found that soot from LTC has shown much smaller aggregate size and much more disordered nanostructure. Smaller primary particle size could result in higher specific surface area. Since oxygen adsorption at active carbon sites is important to the oxidation process, smaller particle size with higher surface/volume ratio could have enhanced oxidative reactivity.[147] Smaller primary particles could result from an enhanced soot oxidation under high temperatures or suppressed soot formation.[148] It could be anticipated here that reduced equivalence ratio and temperature can effectively suppress soot surface growth. Thus, smaller primary particles are produced. The formation of large aggregates is avoided because of smaller primary particle sizes and reduced density of primary particles. Soot produced from ULSD under PCCI combustion mode with injection timing of 2.5^{o}bTDC shows extremely small primary particles with very blurred boundaries between particles. For this reason, two PCCI conditions are examined for each fuel. However, LTFT and RD do not show this effect with very late injection timing due to their relatively high CNs.

As described in Section 2.5.2, soot usually has a core/shell nanostructure. The core is mainly composed of amorphous carbon, while the shell has small graphene layers which are parallel to the particle surface. High resolution TEM images show that soot produced from conventional combustion mode displays a relatively distinct core/shell structure. However, soot produced from late injection PCCI combustion conditions displays a more disordered nanostructure. There are multiple cores within each particle and the graphene layers do not show parallel orientation with some stacking order between adjacent crystallites due to the low combustion temperature.[73] Soot produced from ULSD for the late injection PCCI combustion condition even shows completely amorphous nanostructure. Soot structure rearrangement cannot take place under the relative low temperatures of PCCI combustion. The observations from HRTEM images are in accordance with bulk testing results from XPS and Raman spectroscopy: soot produced from PCCI combustion shows higher amorphous content, and shorter graphene layers with higher concentrations of defects. According to Vander Wal et al.,[149] soot with smaller graphene layers has a higher concentration of edge sites, which is more reactive compared to carbon atoms in the basal plane. In addition, curvature of the graphene layers can cause bond strain and result in weakened C-C bonds, which can also increase the reactivity of soot particles. As a consequence, the less ordered soot produced from PCCI combustion mode has higher reactivity.

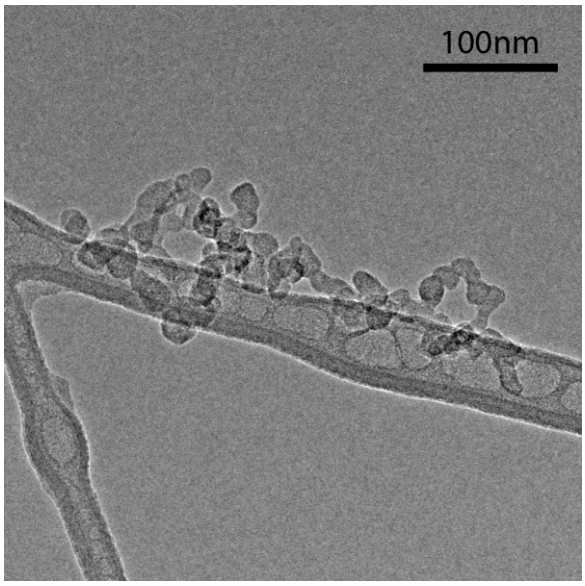

(a)

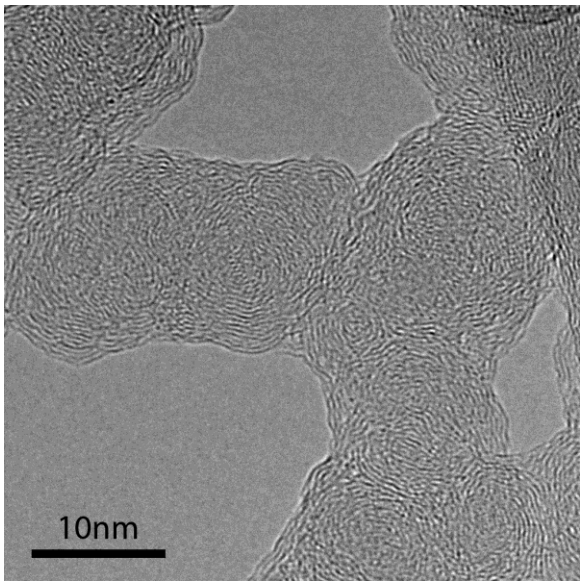

(b)

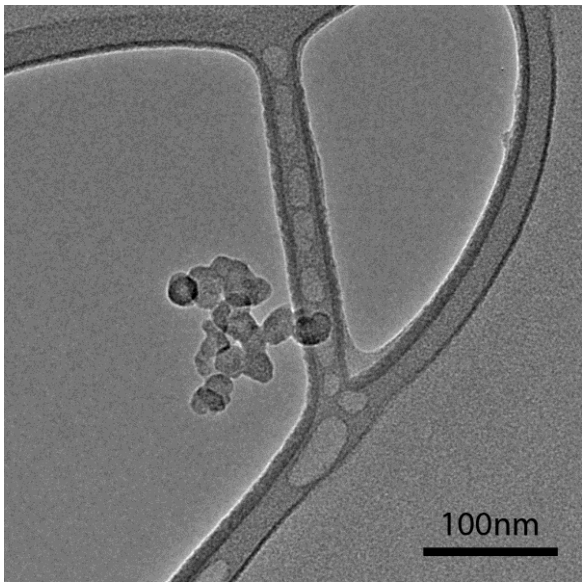

(c)

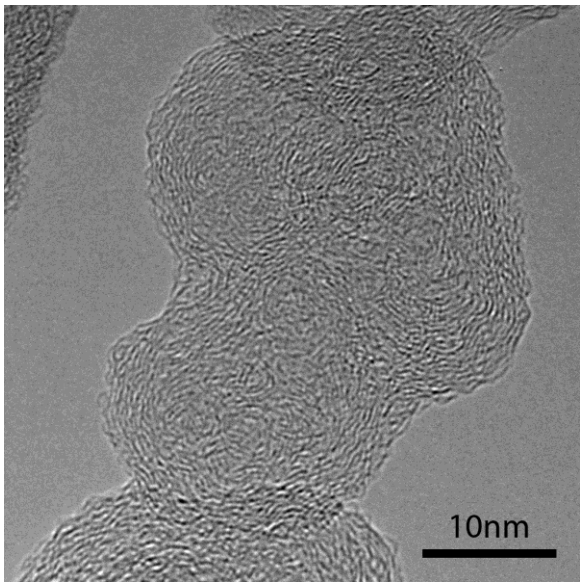

(d)

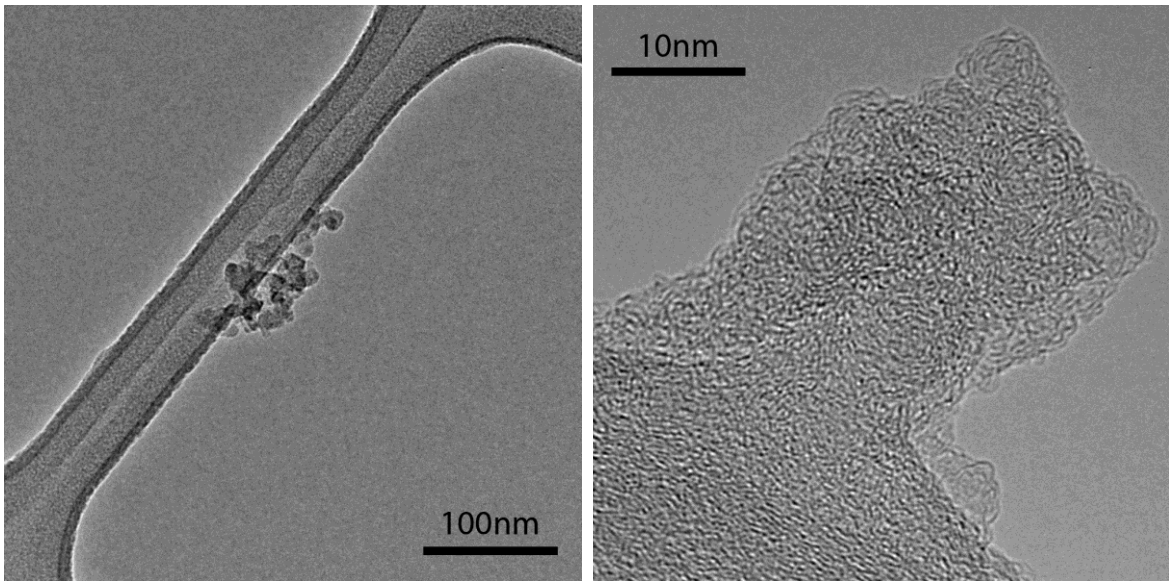

(e) **(f)**

Figure 5.25 TEM images for soot produced from ULSD under conventional combustion mode at (a) 40,000x (b) 400,000x, PCCI combustion mode at injection timing 4.5°bTDC at (c) 40,000x (d) 400,000x, and PCCI combustion mode at injection timing 2.5obTDC at (e) 40,000x and (f) 400,000x

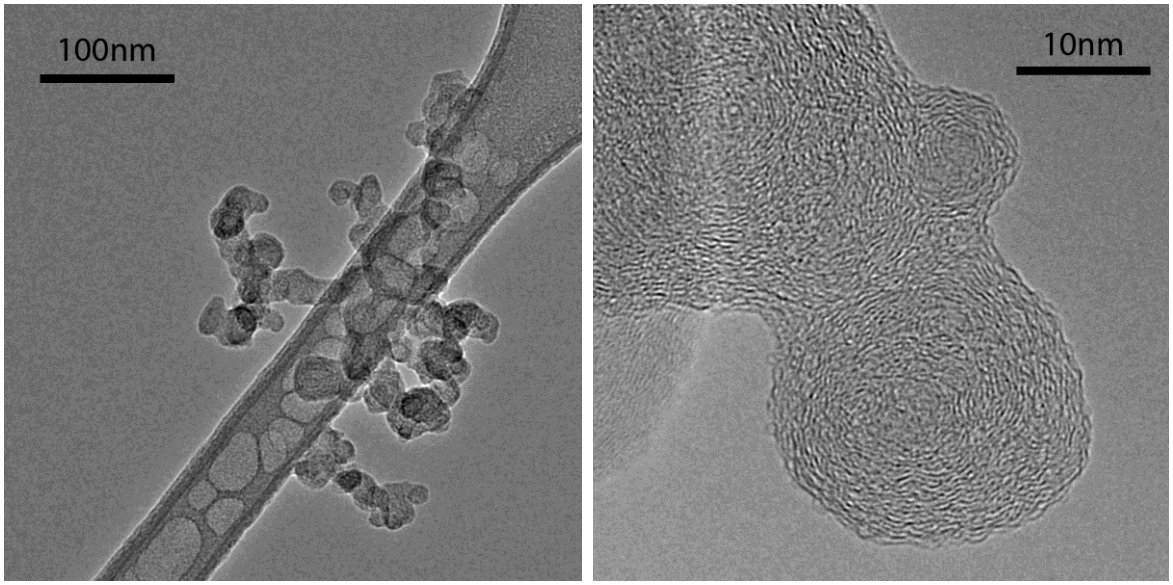

(a) **(b)**

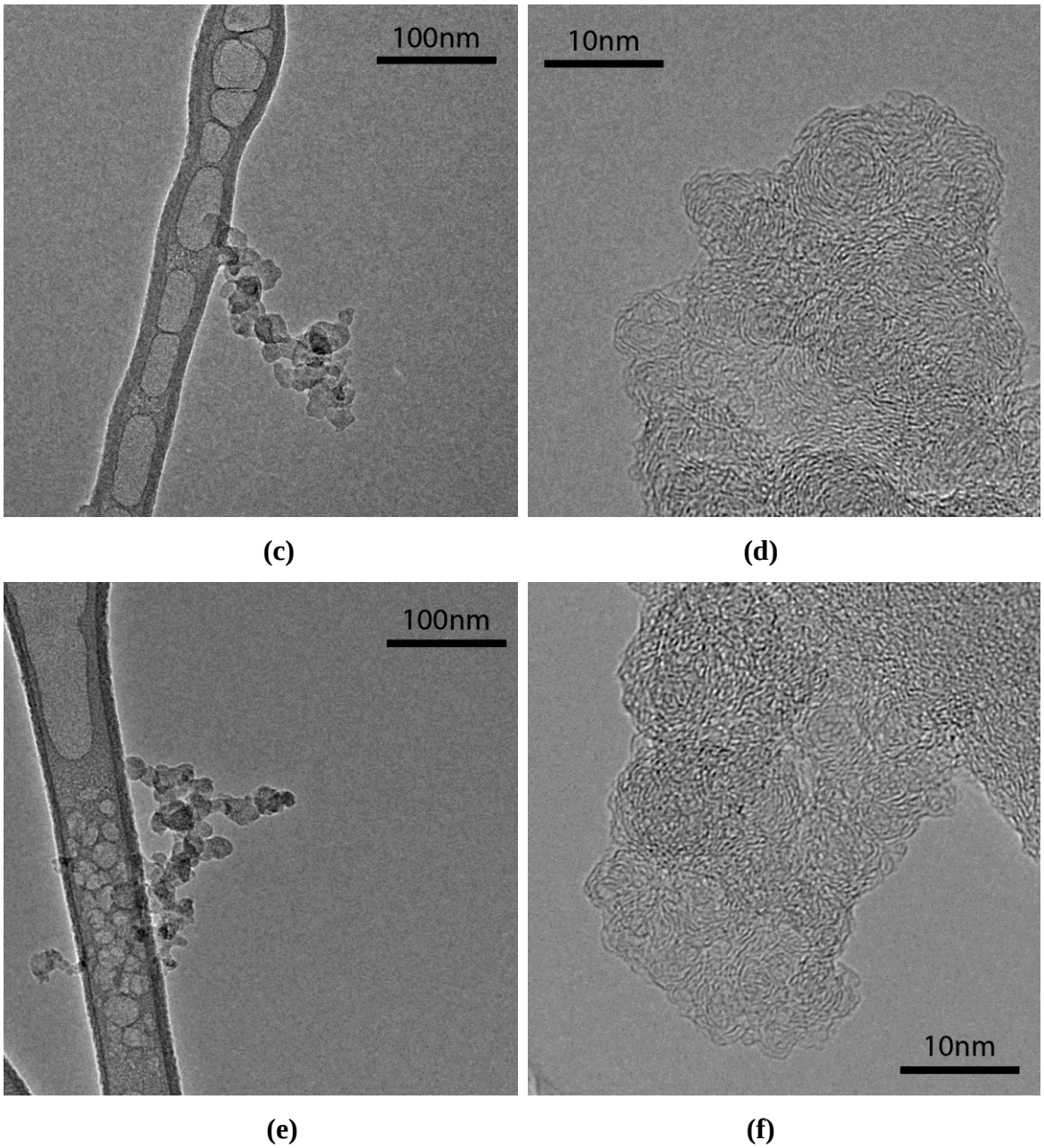

Figure 5.26 TEM images for soot produced from LTFT under conventional combustion mode at (a) 40,000x (b) 400,000x, PCCI combustion mode at injection timing -1.5°bTDC at (c) 40,000x (d) 400,000x, and PCCI combustion mode at injection timing -3.5°bTDC at (e) 40,000x and (f) 400,000x

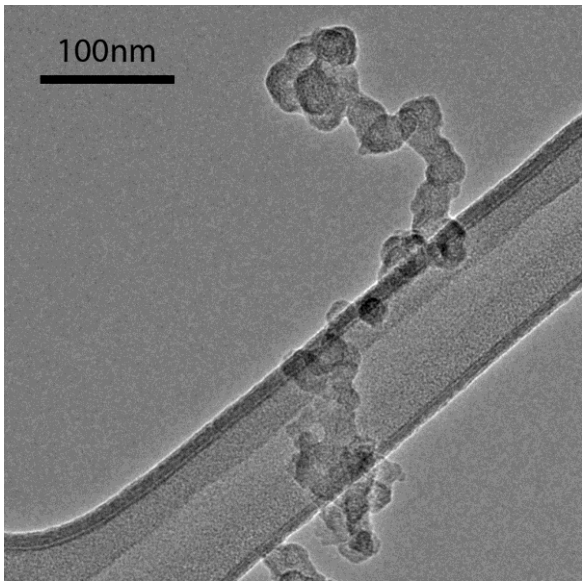

(a)

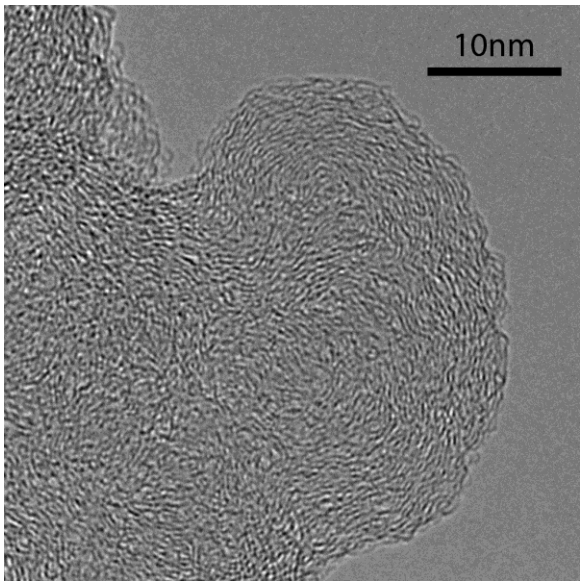

(b)

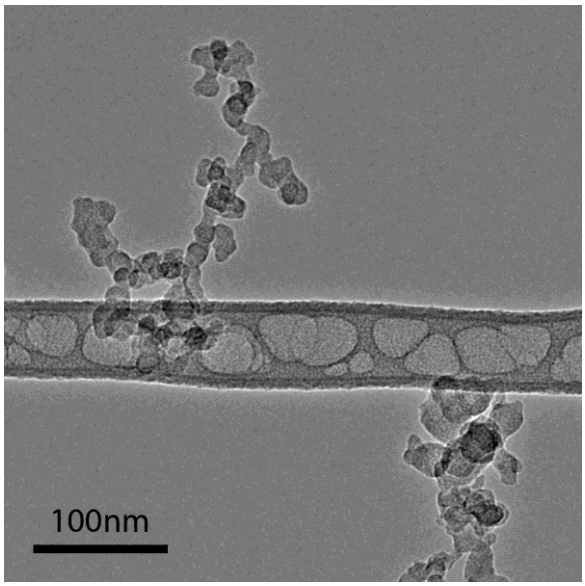

(c)

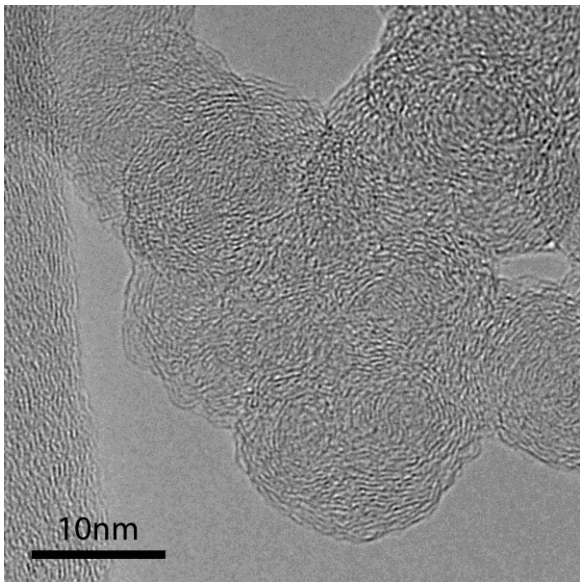

(d)

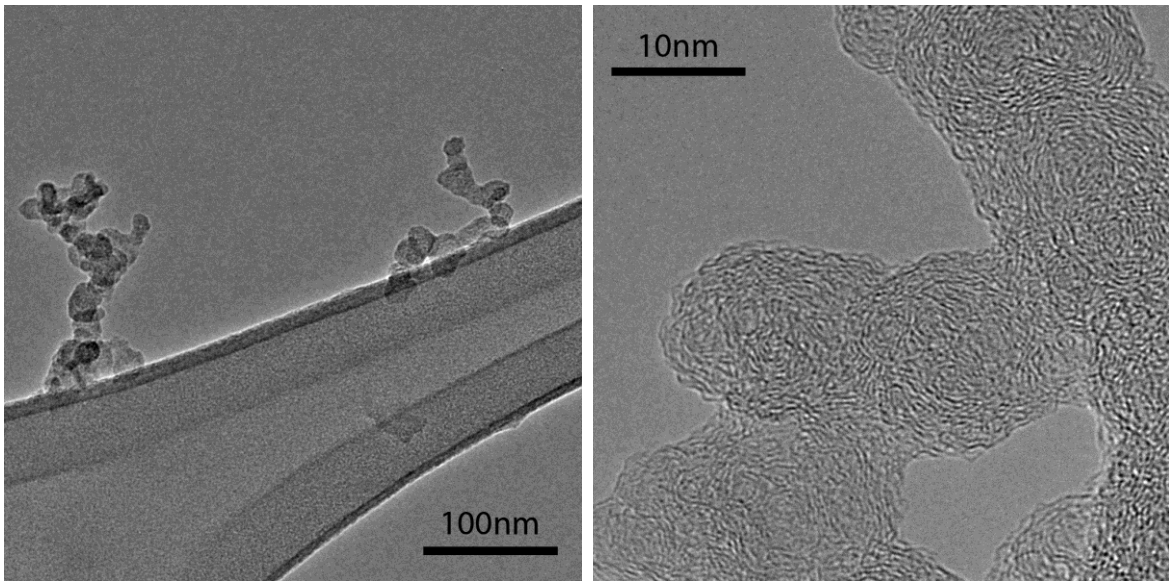

(e) **(f)**

Figure 5.27 TEM images for soot produced from RD under conventional combustion mode at (a) 40,000x (b) 400,000x, PCCI combustion mode at injection timing -1.5^{o}bTDC (c) 40,000x (d) 400,000x, and PCCI combustion mode at injection timing -3.5^{o}bTDC at (e) 40,000x (f) 400,000x

Figures 5.28 – 5.34 show the TEM images of partially oxidized soot at 40% and 75% mass burned, under oxidation temperature 525^{o}C. Soot aggregates show a coagulation effect and much larger aggregation are found during the oxidation process, especially for soot produced under PCCI conditions. In addition, partially oxidized soot aggregates are more compact and show higher fractal dimensions. Soot produced from LTFT and RD fuel under conventional combustion mode show internal oxidation. This is because the inner core of the soot particles is composed of amorphous carbon which is more reactive. For 40% mass burned soot, pore area development[150] with some extent of surface burning is still dominant. The pore areas cannot be observed from HRTEM images at this stage of oxidation. At 75% mass burned, soot became hollow inside after the micropores are fully opened so that the amorphous carbon from inner core is burned. Soot produced from ULSD and PCCI conditions show a shrinking-core type of oxidation. The primary particle size decreases during oxidation. No layer rearrangement is

observed here. Soot particles also become more disordered during oxidation, which agrees with the Raman spectroscopy result. From XPS and Raman Spectroscopy analysis, it could be anticipated that, amorphous carbon oxidizes with graphene layers shrinking. This is because certain crystallite directions are unfavorable for thermal annealing, such as cross-linkings. The joining of graphene layers is prevented when the orientation of the graphene layers is not parallel or in stacking order.[151] In addition, no curvature flattening effect was observed, which could allow better ordering and reduces reactivity.[152] For soot produced from PCCI conditions, both primary soot particles and soot aggregates merge together and show blurred boundaries instead of layer rearrangement. This confirms the overall amorphous nanostructure of PCCI soot.

Song et al.[19] and Al-Qurashi et al.[20] has observed that less ordered and more reactive soot produced from biodiesel or under EGR conditions shows an internal burning mechanism, which is possibly caused by the porosity development in less ordered soot particles. However, in this study, the least reactive soot displays internal burning mechanism, which is produced from LTFT and RD under conventional combustion condition. This could be caused by the overall amorphous structure of soot produced under PCCI combustion. So the outer shell of PCCI soot particles is also very reactive and the inner core does not oxidize first even if micropores exist.

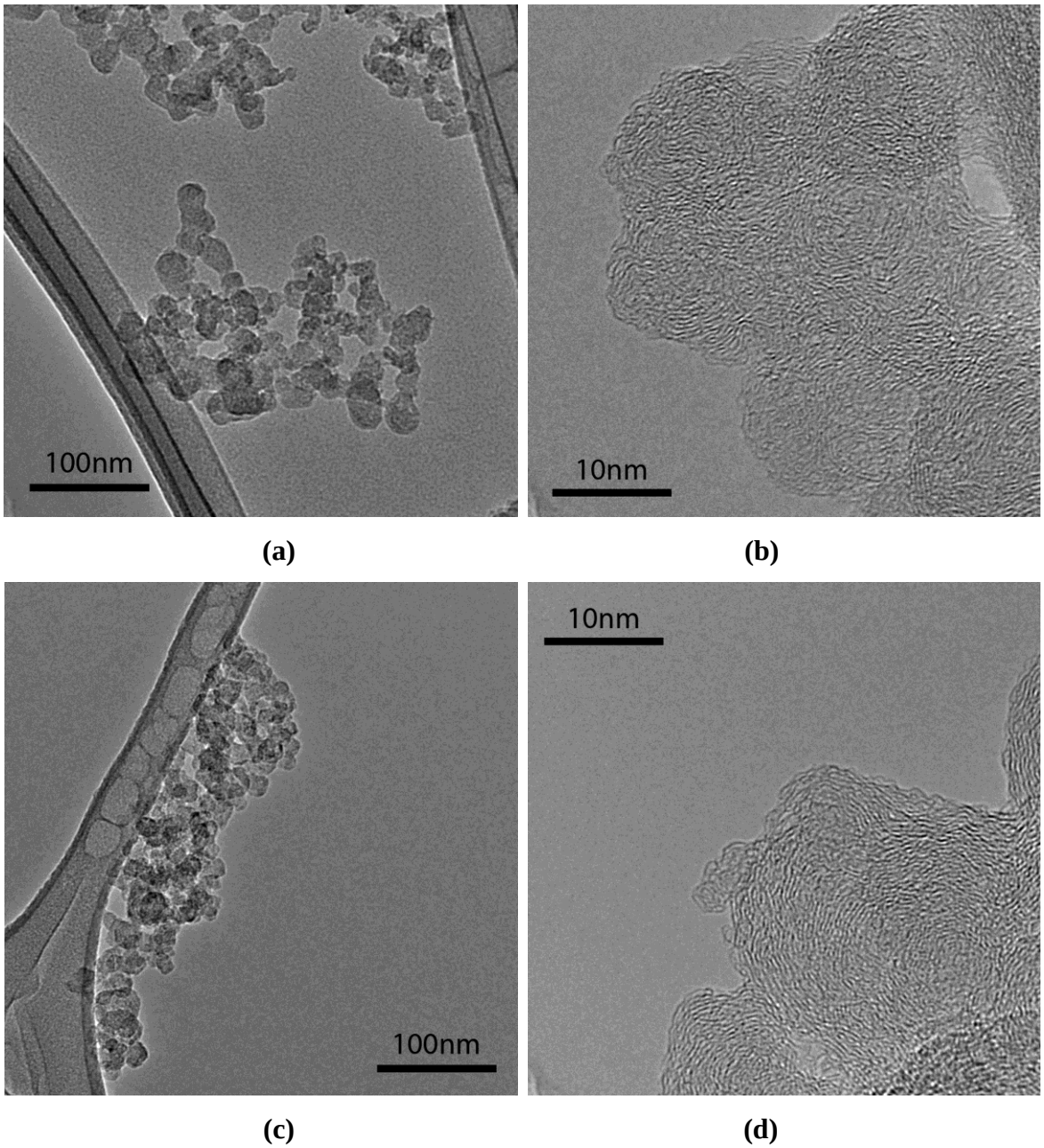

Figure 5.28 TEM images for soot produced from USLD conventional combustion mode after 40% mass burn at (a) 40,000x (b) 400,000x and 75% mass burn at (c) 40,000x (d) 400,000x

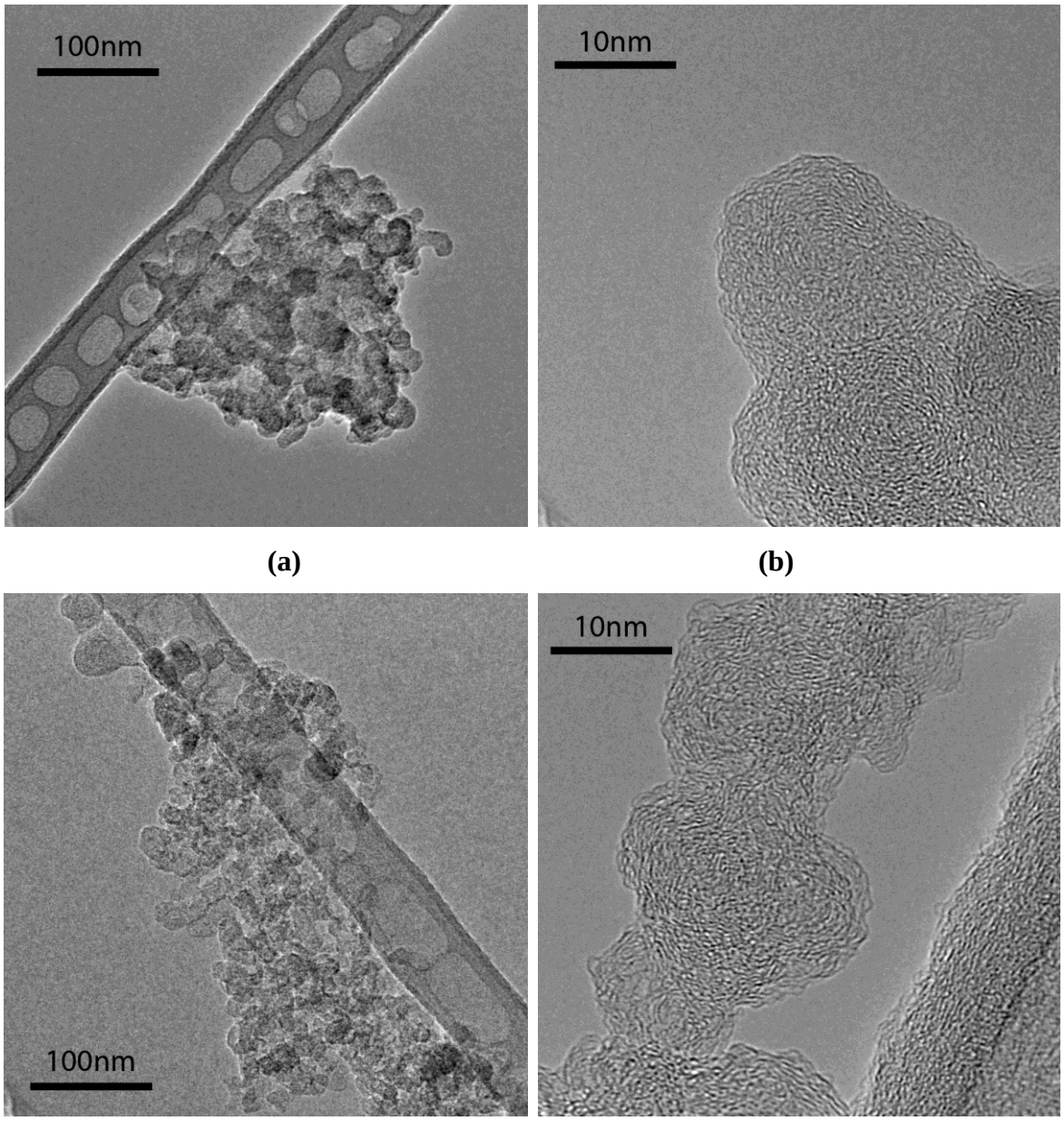

Figure 5.29 TEM images for soot produced from USLD PCCI combustion mode with injection timing 4.5° bTDC after 40% mass burn at (a) 40,000x (b) 400,000x, and 75% mass burn at (c) 40,000x (d) 400,000x

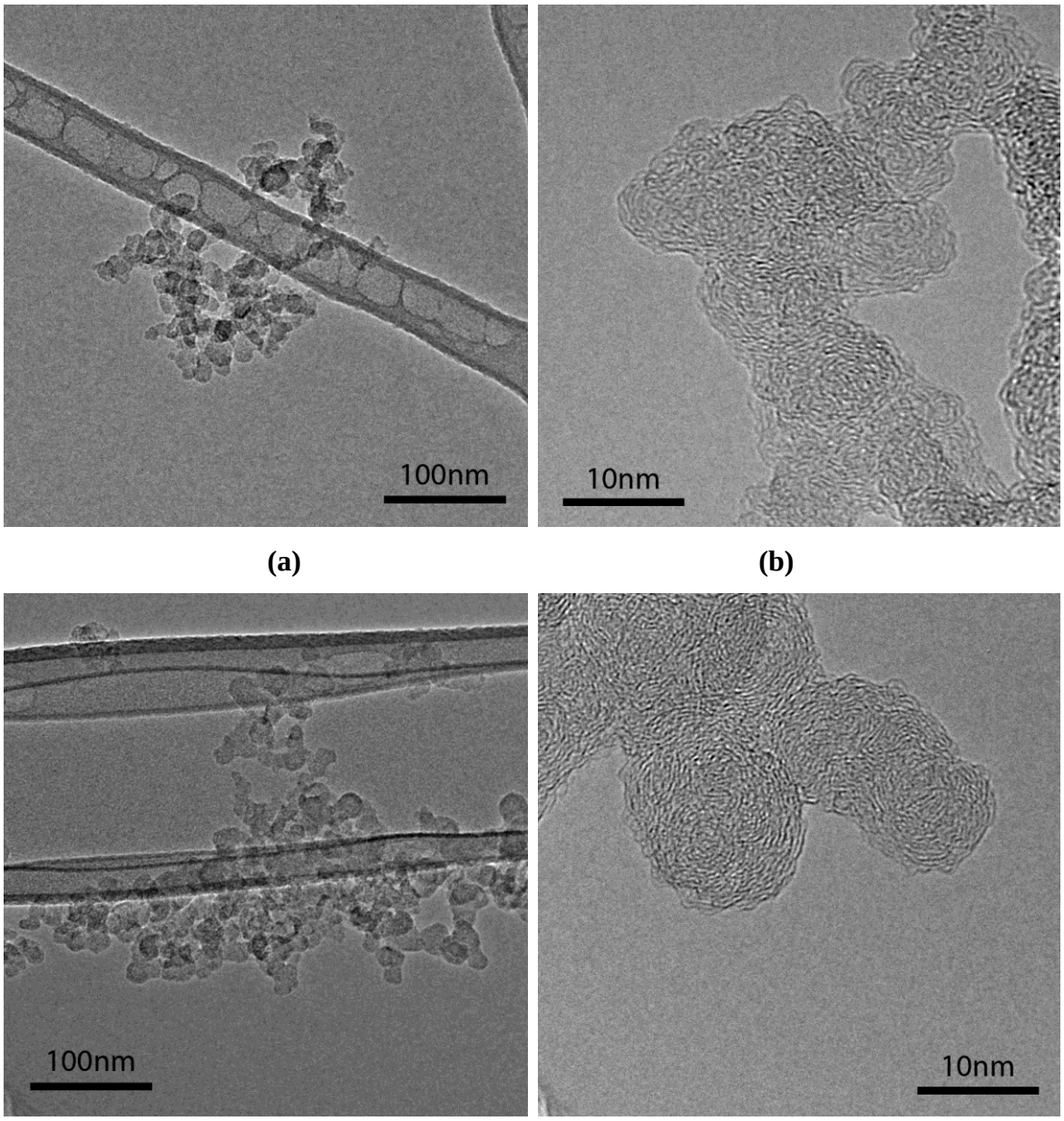

Figure 5.30 TEM images for soot produced from USLD PCCI combustion mode with injection timing 2.5° bTDC after 40% mass burn at (a) 40,000x (b) 400,000x, and 75% mass burn at (c) 40,000x (d) 400,000x

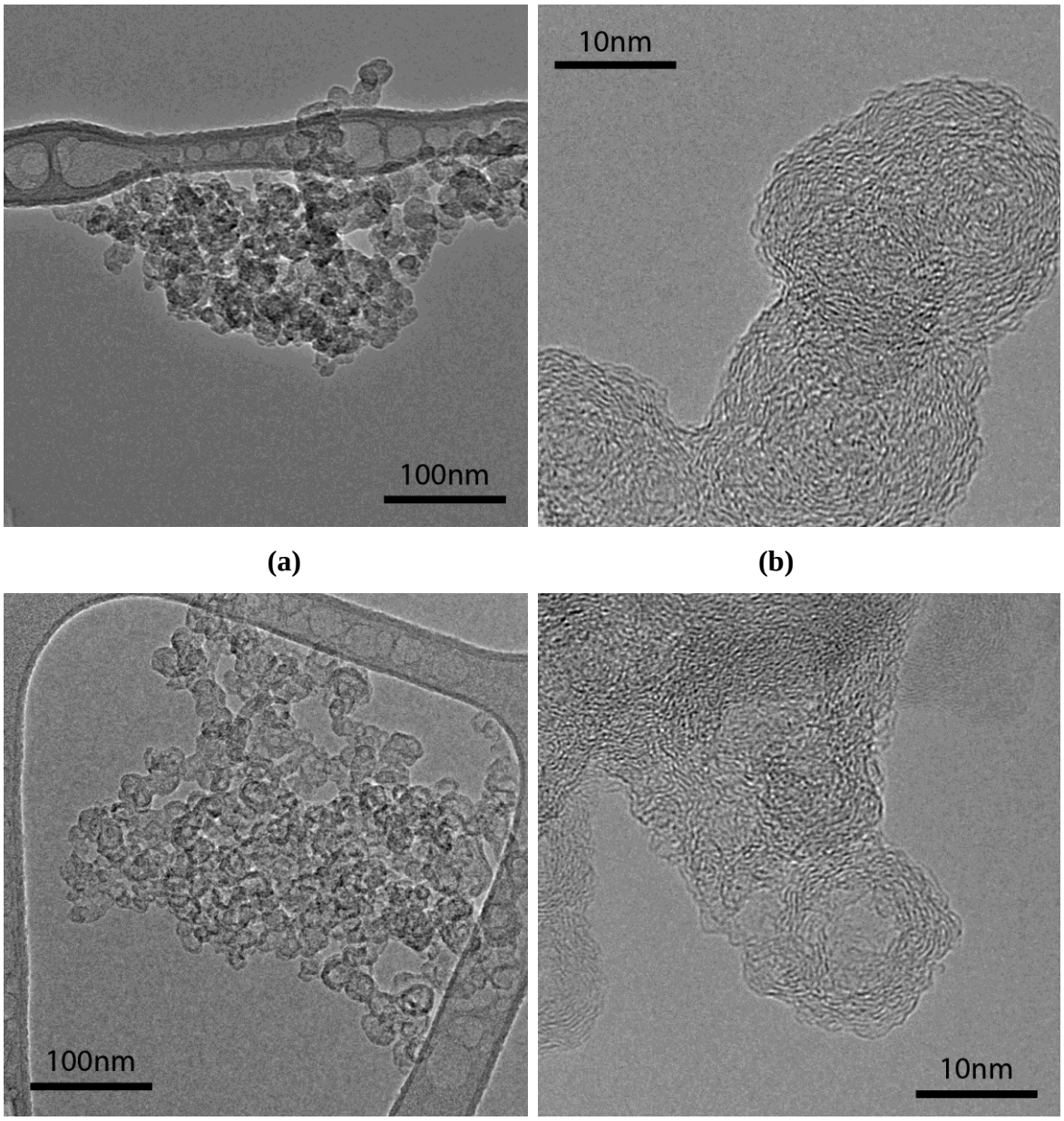

Figure 5.31 TEM images for soot produced from LTFT conventional combustion mode after 40% mass burn at (a) 40,000x (b) 400,000x, and 75% mass burn at (c) 40,000x (d) 400,000x

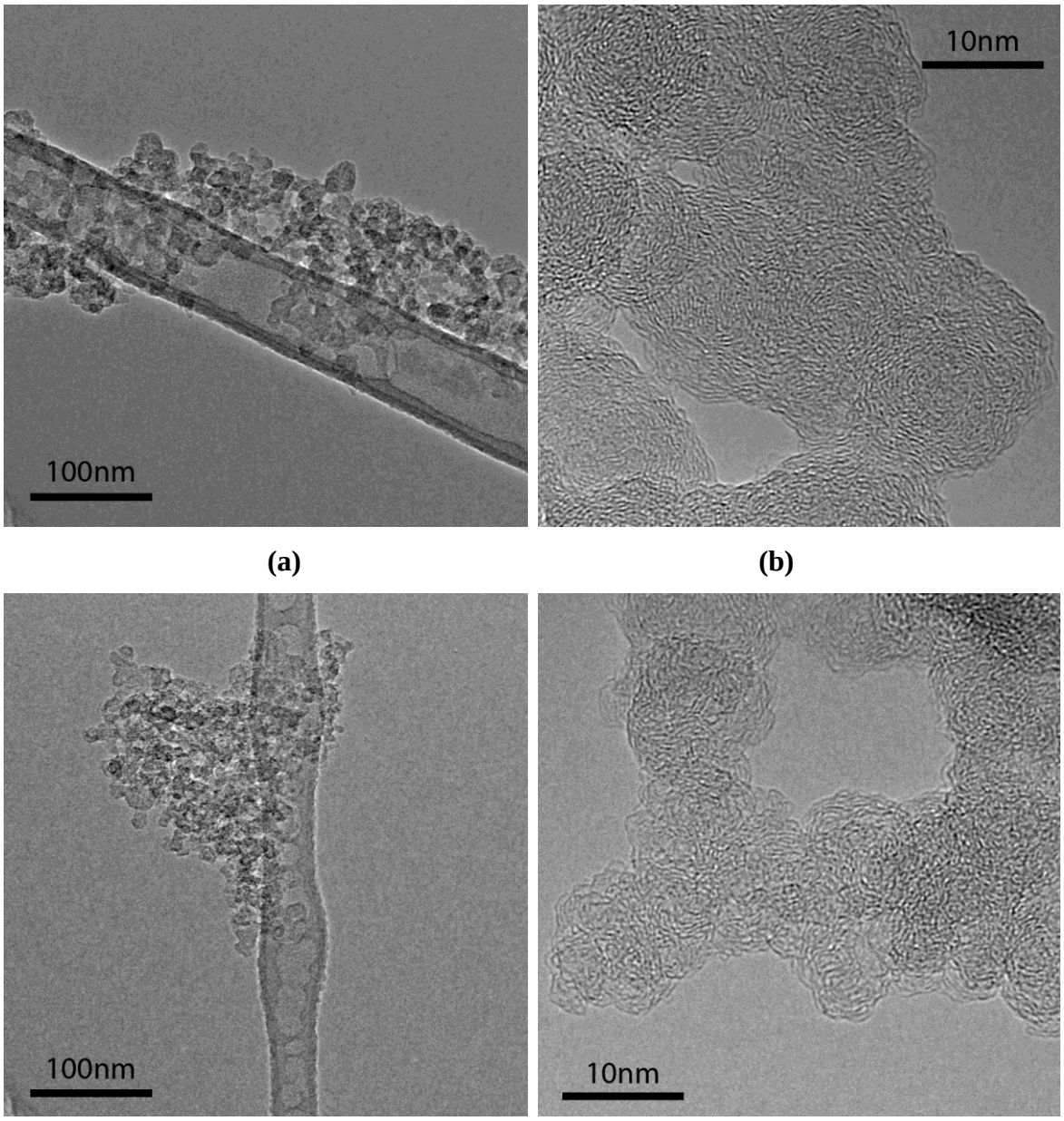

Figure 5.32 TEM images for soot produced from LTFT PCCI combustion mode with injection timing -3.5° bTDC after 40% mass burn at (a) 40,000x (b) 400,000x, and 75% mass burn at (c) 40,000x (d) 400,000x

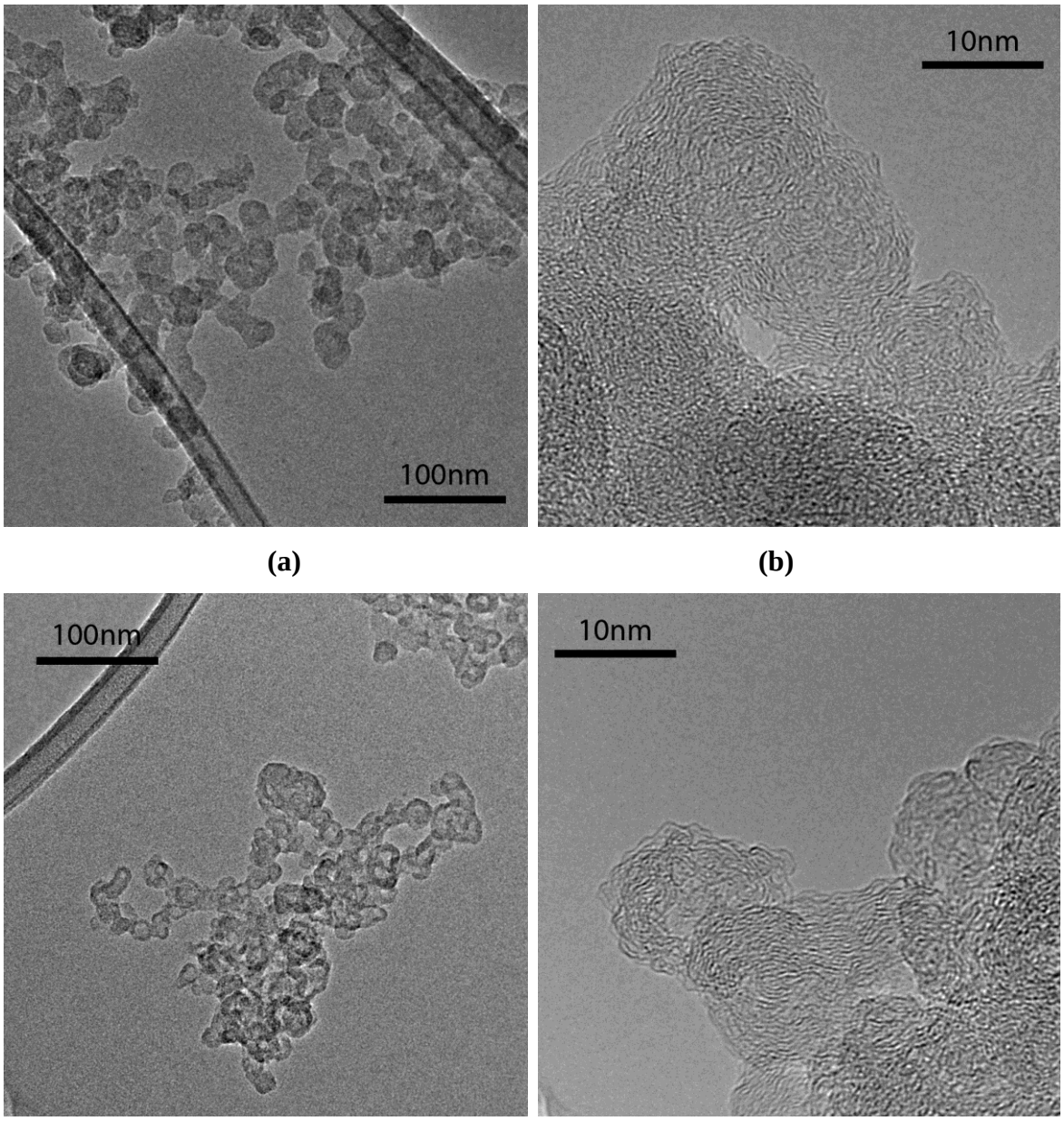

(a) **(b)**

(c) **(d)**

Figure 5.33 TEM images for soot produced from RD conventional combustion mode after 40% mass burn at (a) 40,000x (b) 400,000x, and 75% mass burn at (c) 40,000x (d) 400,000x

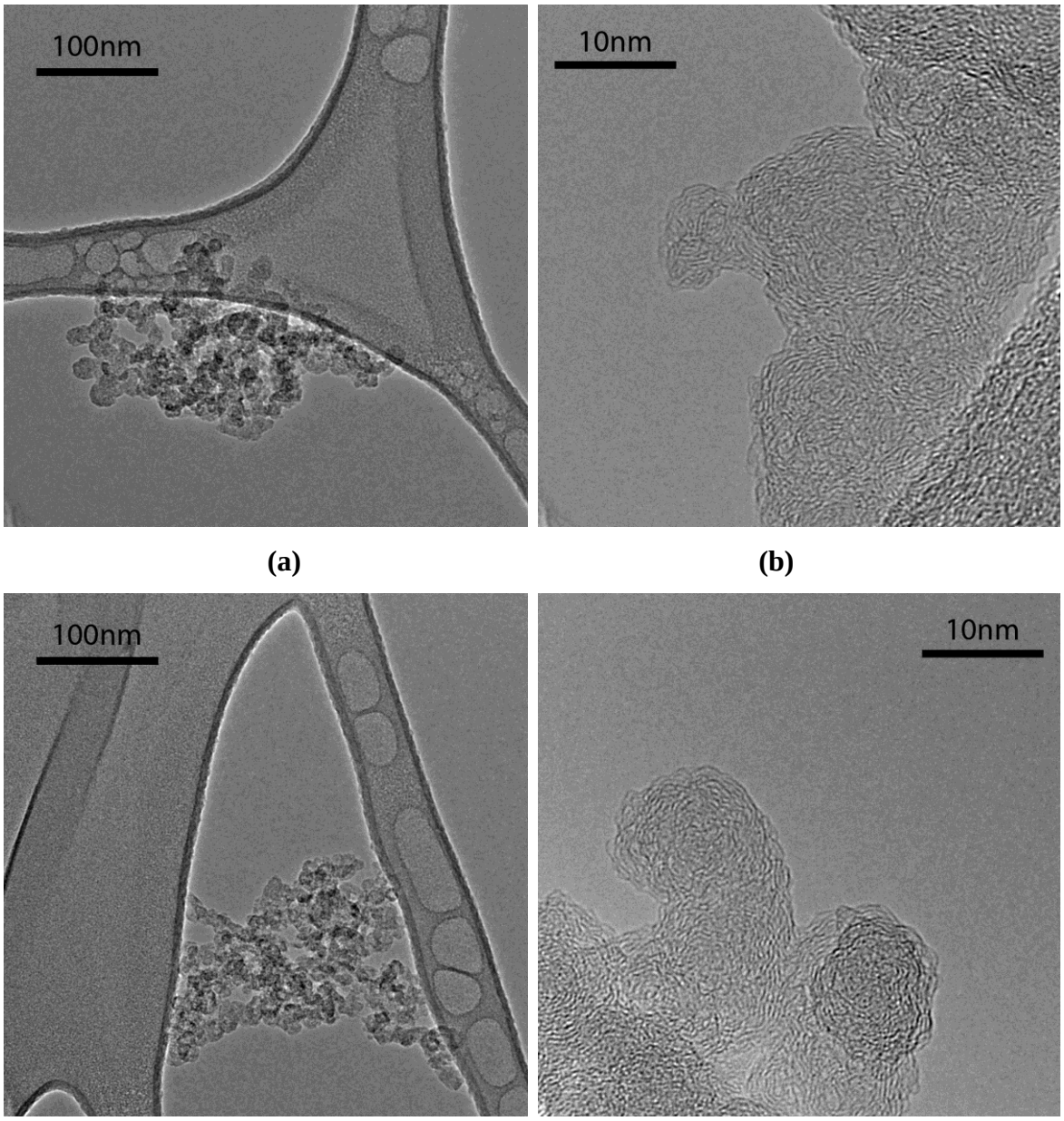

Figure 5.34 TEM images for soot produced from RD PCCI combustion mode with injection timing -3.5° bTDC after 40% mass burn at (a) 40,000x (b) 400,000x, and 75% mass burn at (c) 40,000x (d) 400,000x

5.14 Electron energy loss spectroscopy

From EELS spectra, near-edge structure of carbon K-ionization edge could be deduced.[153] The peak at energy loss 285 eV represents transitions of C 1s electrons to unoccupied π* state, which reflects sp2 hybridized graphite carbon. The peak at energy loss around 291 eV represents transitions of C 1s electrons to unoccupied σ* state, which reflects sp3 hybridized amorphous carbon. The peak area or intensity ratio of π* and σ* peaks could indicate the degree of order of the soot particles.[154]

Figure 5.35 shows the EELS spectra for initial and partially oxidized soot particles for ULSD, LTFT and RD under both conventional and PCCI combustion conditions. The intensity ratio of π* and σ* peaks does not show much variation between the soot samples. Similar to the XPS result, soot generated from PCCI conditions show slight smaller π*/σ* ratio compared to soot from conventional combustion for all three fuels. However, unlike XPS peak fitting, the sp3/sp2 carbon ratio does not decrease during the oxidation process. Instead, I_{π^*}/I_{σ^*} decreases during oxidation. One possible reason is that the very amorphous initial soot particles go through rearrangement or degradation under the high energy of the electrons beams. Because soot morphology is observed to have changed after EELS spectrum is taken.[155] Under conventional combustion mode, where LTFT and RD fuel show internal burning mechanism, I_{π^*}/I_{σ^*} first decrease at 40% mass burn, then increase slightly at 75% mass burn. This is consistent with the result of Song et al.[19] who also observed internal burning and rearrangement phenomena of biodiesel soot during oxidation. During the initial stage of oxidation (40% burn), soot became less ordered because of surface burning and pore development. Then the structures became more ordered because the amorphous core oxidizes first combined with the thermal annealing effect.

This is consistent with high resolution TEM images, where hollow particles could be observed at 75% mass burn.

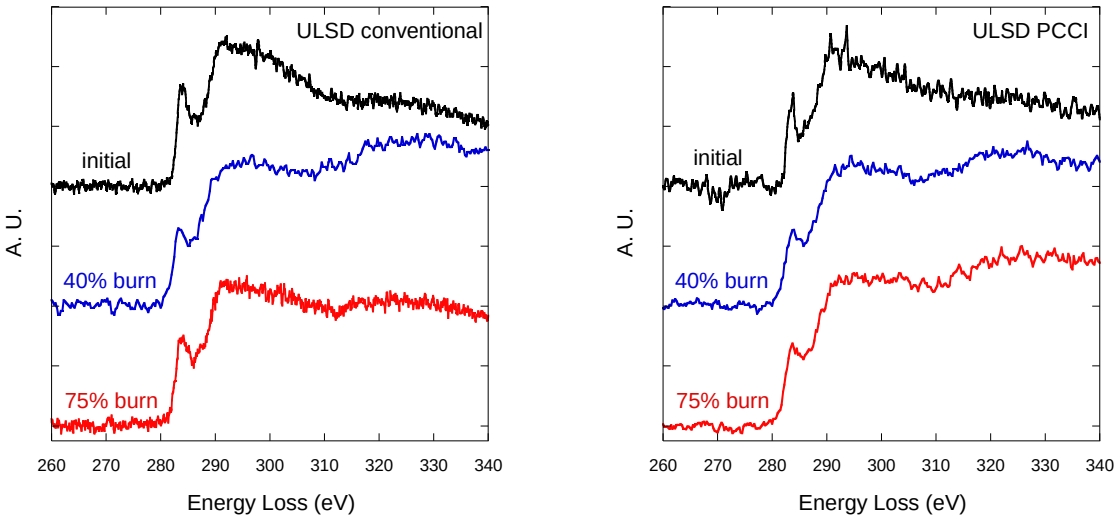

(a)

(b)

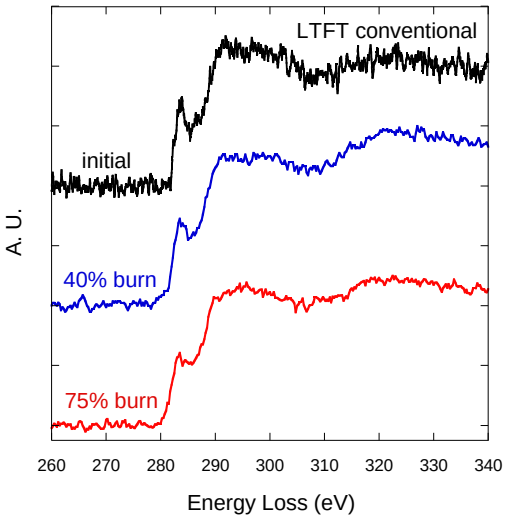

(c)

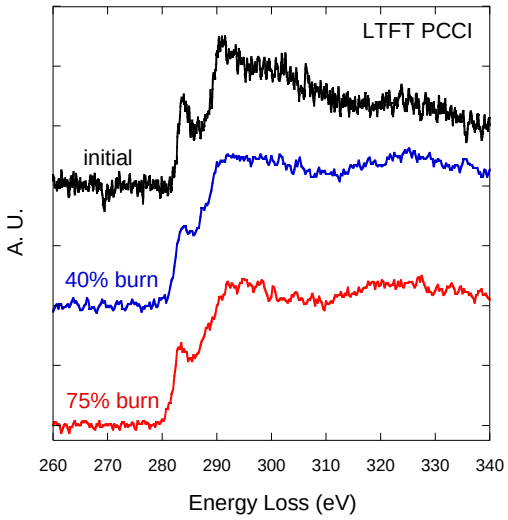

(d)

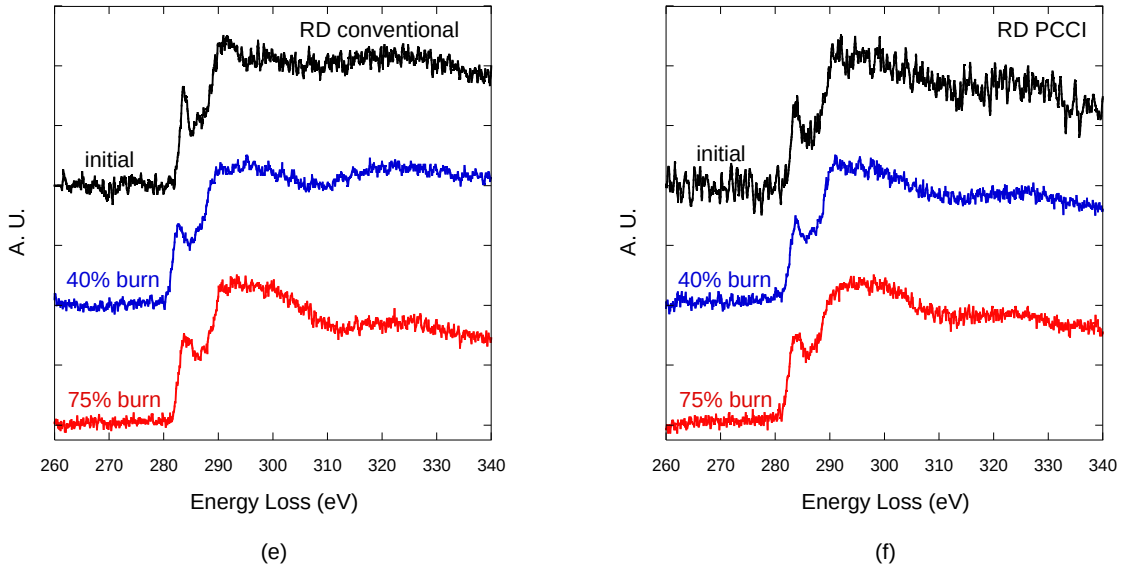

Figure 5.35 EELS spectra for initial and soot oxidized for 40% and 75% mass burn

5.15 Summary

Soot produced form late injection PCCI combustion conditions shows higher reactivity than soot from conventional combustion conditions. The reaction rate constants of soot produced from late injection PCCI combustion are 1.2-2.2 times higher than soot from the conventional combustion conditions. LTFT and RD fuels produce soot with lower reactivity compared to ULSD under both conventional and PCCI combustion modes. The reaction rate constants of soot from LTFT and RD fuels are 47-66% lower than soot produced from ULSD. Soot produced under PCCI combustion has higher BET surface areas, surface oxygen content and amorphous carbon contents. Amorphous carbon content and surface oxygen content correlate well with the oxidation rate constant. In addition, Raman spectroscopy shows that soot from PCCI combustion has smaller graphene layers. As a result, soots from PCCI combustion have higher reactivity than soots from conventional combustion. The primary particle and particle aggregate sizes are around 25nm and 400 nm for conventional combustion soot, while 10nm and 150 nm for late

injection PCCI combustion soot. TEM images also show that soots from PCCI combustion have less ordered nanostructure. PCCI combustion has lower cylinder temperature and local equivalence ratio resulted from higher EGR ratio and longer ignition delay. Those factors caused the soots formed under PCCI combustion conditions have less mature nanostructure and higher reactivity.

Soots from LTFT and RD fuels under conventional combustion show internal burning during the oxidation process. However, soots with higher reactivity which are produced from PCCI combustion and ULSD show shrinking core oxidation. This can be caused by the overall amorphous nanostructure of PCCI soots. No layer rearrangement is observed during the oxidation process for both conventional and PCCI soots. Amorphous carbon content and graphene layer size both decrease during oxidation.

Chapter 6.

Effect of post injection on soot nanostructure and reactivity

Post injection is proved to reduce PM emissions. However, the properties of soot produced under post injection conditions have not been investigated. The research in this chapter discusses the impact of post injection dwell and size on soot reactivity. In addition, the oxidation processes of post injection soots are also analyzed.

6.1 Heat release rate

Figure 6.1 shows the apparent rate of heat release (ROHR) of baseline condition and 7.5% post injection with different injection dwells. Fuel with post injection has similar maximum rate of heat release as the baseline condition, indicating a similar premixed burn during the main injection. There is a reduced diffusion burn for post injection conditions and for the main injection only condition. For post injection conditions, the heat release curve first follows the reduced load main injection only condition. After the post injection heat release peak, the heat release curves overlap with the baseline condition. Another important observation here is that post injection fuel at 4^{o}CAD after the main injection has much shorter ignition delay and also lower AHRR compared to fuel injected 10^{o}CAD and 16^{o}CAD after the main injection. This is

because with close-coupled post injection, fuel from post injection is introduced into the region where flame from the main injection still exists, so close-coupled post injection fuel goes through diffusion type combustion.[156] As a consequence, combustion occurs gradually, resulting in a relatively low heat release peak. This means close-coupled post injection undergoes a different process compared to long dwell post injection. The heat release peak of post injection with 16°CAD injection dwell is slightly higher than post injection with 10°CAD injection dwell. This is because for this study load is kept constant and thermal efficiency is reduced with very late post injection. As a consequence, more fuel is post injected with 16°CAD injection dwell.

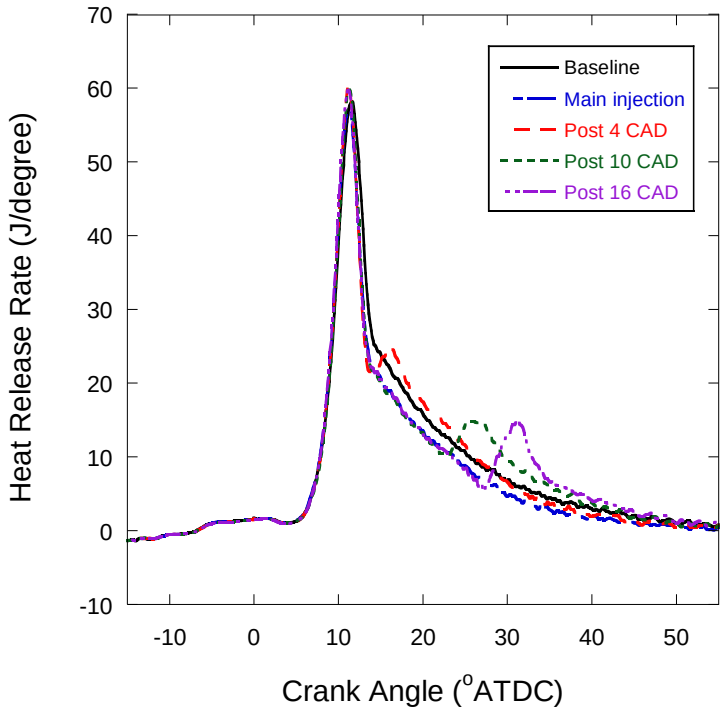

Figure 6.1 Heat release rate for baseline, main injection only and 7.5% post injection with injection dwell 4°CAD, 10°CAD and 16°CAD

6.2 Brake specific fuel consumption

Figure 6.2 shows the BSFC for baseline, post injection and main injection only conditions. BSFC does not vary much by post injection. Close-coupled post injection conditions reduce BSFC by 1% compared to baseline condition. With the increase of injection dwell, BSFC increases. For retarded post injections, the BSFC of post injection conditions are 1% higher than baseline condition. Main injection only conditions have higher BSFC due to the reduced load. This result is in accordance with the work from Zhuang et al.[157] Benajes et al.[61] found that combustion speed increases with close-coupled post injection since the spray can entrain air across its front edge. As a consequence, BSFC decreases with improved combustion phasing. However, with delayed post injection, this benefit is outweighed by cylinder expansion and prolonged combustion duration. BSFC increases slightly due to the worsened thermal efficiency.[158]

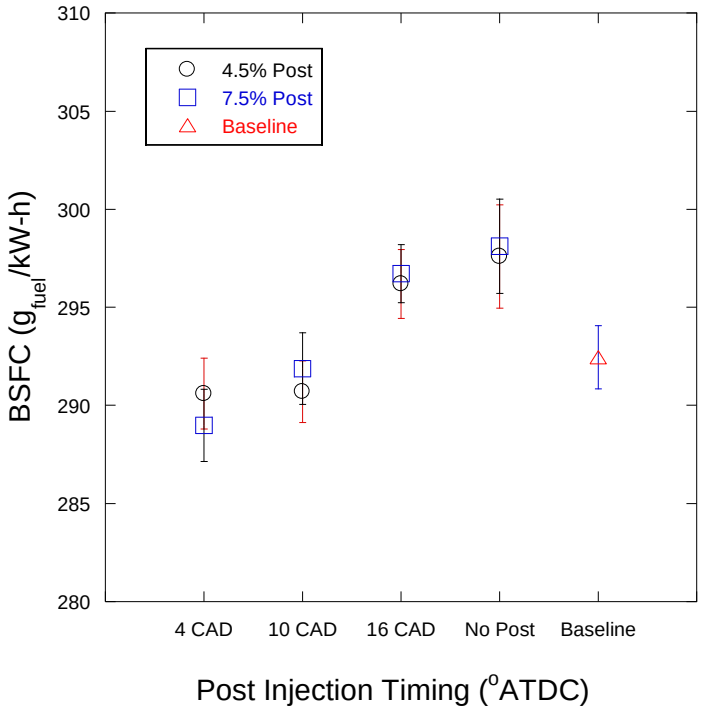

Figure 6.2 BSFC for baseline, main injection only and post injection conditions

6.3 NOx emissions

Figure 6.3 shows NOx emissions for baseline, main injection only, 4.5% and 7.5% post injection conditions with three different injection dwells. For close-coupled post injection conditions with injection dwell 4^{o}CAD, NOx emissions increase by 3-5% compared to the baseline condition. Long dwell post injection decreases NOx emissions by 7-8% compared to the baseline condition. NOx emissions not only decrease with the delay of post injection schedule, but also with the increased portion of post injection. Although NOx emissions are also low for main injection only with reduced load conditions, the total fuel injected per cycle is also reduced. As a consequence, NOx emissions per kg fuel are higher compared to post injection conditions with long injection dwell.

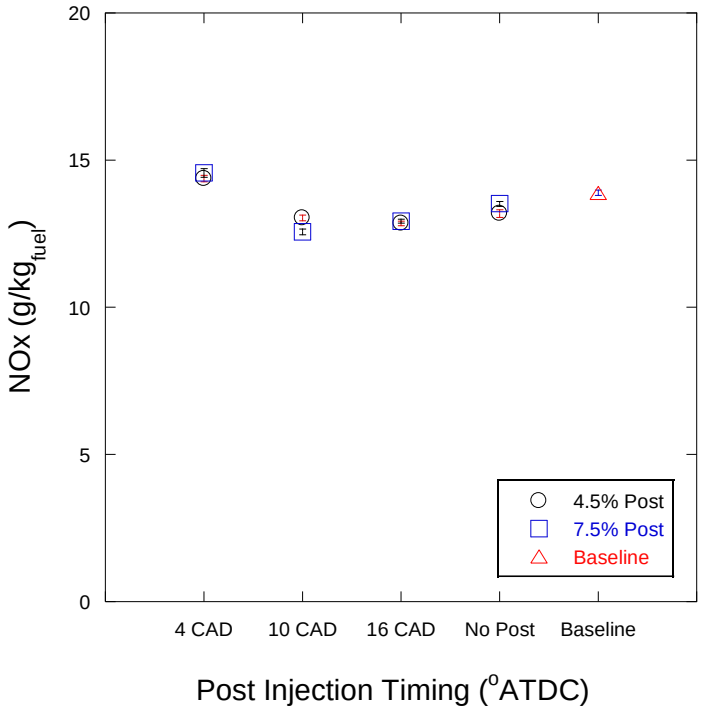

Figure 6.3 NOx emissions for baseline, main injection only and post injection conditions

As discussed in Section 4.2, NOx emissions have a strong correlation with combustion temperature. Fuel from post injection could interact with the main injection flame. The momentum of the post injection jet could enhance air entrainment into the flame.[159] With close-coupled post injection at 4^{o}CAD after the end of the main injection, improved fuel-air mixing could result in increased combustion speed, heat release rate and higher local combustion temperature, which promotes NOx formation. However, for long dwell post injection conditions, NOx emissions are reduced because less fuel is injected during the main injection compared to the baseline condition, which reduces peak cylinder temperature. Due to cylinder expansion, fuel from post injection does not raise cylinder temperature as much as close coupled post injection or the baseline condition, which results in reduced NOx formation.[160]

6.4 CO and THC emissions

Figures 6.4 and 6.5 show CO and THC emissions for baseline, main injection only, 4.5% and 7.5% fuel post injection conditions. CO emissions reduce by 7-8% under close-coupled post injection conditions and stay similar when the injection dwell is long. CO emissions increase significantly under main injection only conditions because of reduced engine load and cylinder temperature. THC emissions follow a similar trend as CO emissions. Close-coupled post injection conditions reduce THC emissions by 14-28% compared to the baseline condition. With retardation of the post injection, THC emissions increase. If post injection timing is very late, THC emissions become similar or slightly higher than the baseline condition. Main injection only with reduced load conditions have the highest THC emissions because less fuel is injected so that combustion temperature is reduced.

As discussed in Section 4.3, CO emissions are mainly caused by reduced cylinder temperature which lowered the concentration of OH radicals and resulted in reduced CO to CO_2 conversion rate. THC emissions mainly come from over lean regions such as crevices and the squish volume. Chartier et al. [161] found that without post injection, no significant chemiluminescence signal or OH fluorescence are detected near the injector area. This indicates the lack of second-stage ignition in this upstream region. However, with post injection, the mixture close to the injector shows a significant chemiluminescence signal and strong OH fluorescence, indicating more complete combustion near this region. This could explain the reduction of THC and CO emissions from post-injection conditions. In addition, the increased temperature caused by post-injection can also benefit the complete oxidation of CO and THC. However, with a large post injection, which is not considered in our testing, this effect vanishes because fuel from post injection has higher momentum and does not stay near the injector region.

Some mixture can also spread into the squish area and contribute to THC emissions. In addition, when post injection timing is delayed, the temperature increase diminishes due to cylinder expansion[162]. Also, shorter reaction time is provided for THC and CO oxidation, resulting in incomplete combustion of fuel from the post injection. As a consequence, THC and CO emissions increase with prolonged ignition dwell.

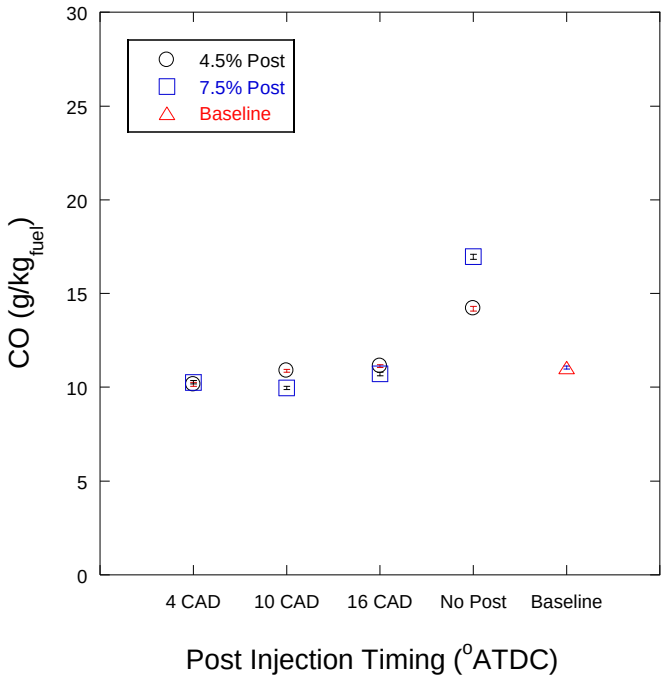

Figure 6.4 CO emissions for baseline, main injection only and post injection conditions

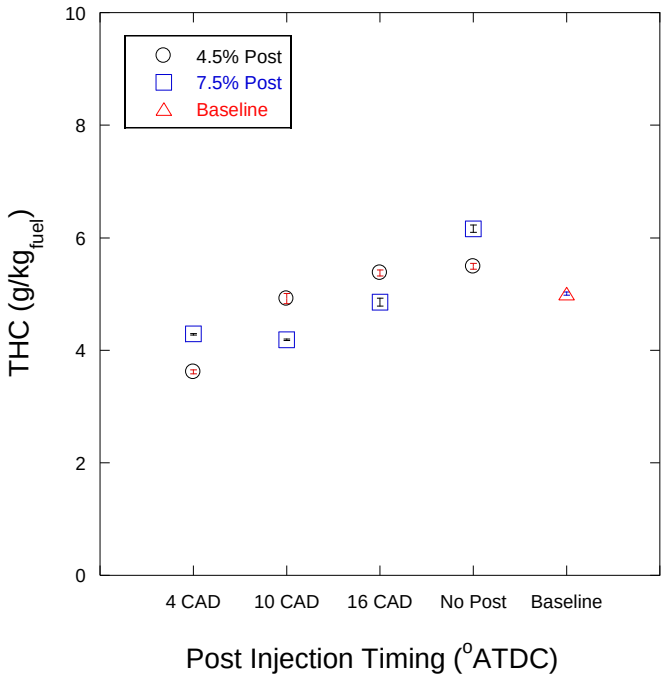

Figure 6.5 THC emissions for baseline, main injection only and post injection conditions

6.5 FSN and PM emissions

Figure 6.6 shows the FSN for baseline, 4.5% and 7.5% post injection and main injection only conditions. To better understand the mechanism of post injection on soot emissions reduction, filter smoke number is measured from 3% to 10.5% main injection duration reduction in increments of 1.5%, as shown in Table 6.1. Close-coupled post injection conditions have relative higher FSN compared to long dwell post injection conditions. Both close-coupled and long dwell post injection conditions can effectively reduce soot emissions compared to the baseline condition. With the increased portion of post injection, FSN first decreases then increases. With 7.5% post injection, soot reduction is optimized. Long dwell post injection (injection dwell of 10^{o}CAD and 16^{o}CAD) has very similar FSN to that for main injection only with reduced load condition except for the 10.5% post injection case. Figure 6.7 shows the PM

emissions for baseline and 7.5% post injection conditions. Main injection only condition has higher PM emissions per kg fuel. This is because less fuel is injected per cycle. PM emissions follow a very similar trend with FSN for baseline and post injection conditions. So it could be anticipated that soot produced from different conditions have similar VOF content.

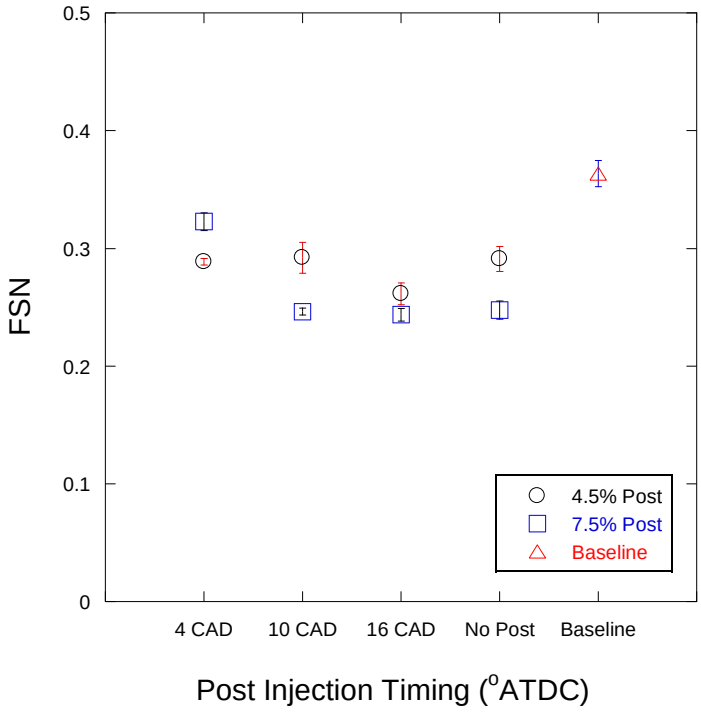

Figure 6.6 FSN for baseline, main injection only and post injection conditions

Table 6.1 FSN for baseline, main injection and post injection conditions

Injection Dwell	Reduction of Main Injection Duration (%)					
	3	**4.5**	**6**	**7.5**	**9**	**10.5**
4°CAD	0.315	0.289	0.280	0.323	0.355	0.434
10°CAD	0.329	0.292	0.267	0.246	0.276	0.348
16°CAD	0.329	0.261	0.243	0.244	0.267	0.313
Main Only	0.336	0.291	0.256	0.248	0.249	0.235
Baseline	0.364					

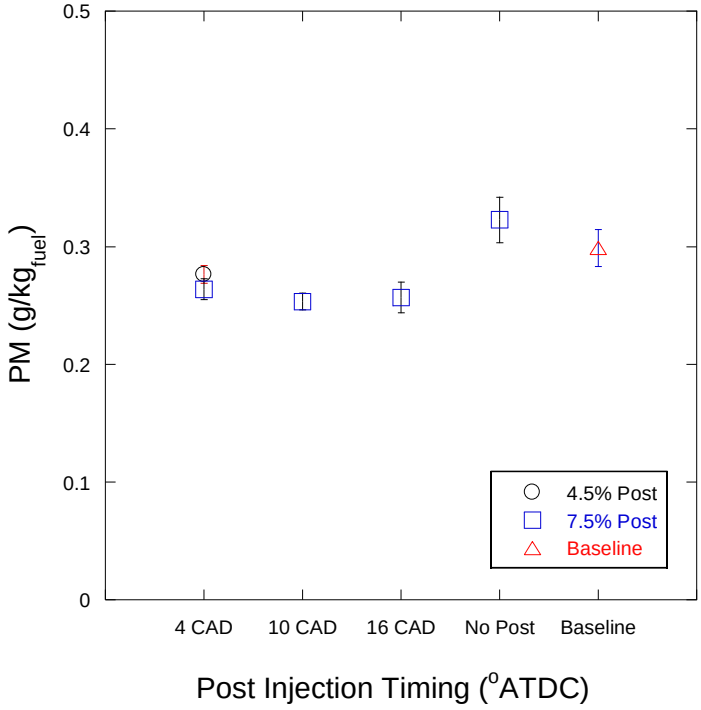

Figure 6.7 PM emissions for baseline, main injection only and post injection conditions

Several mechanisms are believed to contribute to the soot reduction by post injection: 1) Enhanced mixing due to post injection. The momentum of the post injection jet can improve the air entrainment of the main injection flame and enhance the oxidation of soot from the main injection.[163,164] Konno et al.[165] conducted a "combustion chamber for disturbance" (CCD) experiment and found that soot reduction increases with higher CCD jet momentum. This proved that the enhanced fuel/air mixing and turbulence created by the post injection can improve soot oxidation; 2) Additional heat release caused by burning of the post injection fuel could delay the temperature drop, and allow better soot oxidation. Hotta et al.[56] suggested that soot from the main injection is taken to the squish area by the post injection and oxidized there. Bobba et al.[60]

measured increased soot temperature in the squish region with post injection, which supports Hotta's theory; and 3) Reduced soot formation caused by reducing "jet replenishment". This is because under spilt injection conditions, the head of fuel spray, which is the region for soot formation, is not replenished by newly injected fuel.[166] Thus, soot formation could have a non-linear relationship with injection duration. In addition, when fuel replenishment is halted, more air could enter the reaction zone, which enhances the soot oxidation process.[167] Moreover, fuel from post injection produces less soot due to the lower temperature during the expansion stroke, thus resulting in reduced total soot emissions.

Generally, long dwell post injection conditions have higher soot reduction compared to close-coupled post injection conditions. When injection dwell is 4^{o}CAD, the post injection jet enters the main injection flame and goes through diffusion combustion. Although increased temperature could enhance soot oxidation, there is less mixing under those conditions. For long dwell post injection conditions, there are relatively longer ignition delays for post injection jets, which could reduce soot formation from the post injection fuel.[168] The momentum of the post injection jet also enhances the fuel air mixing of the main injection flame. Soot reduction is optimized at 6 - 7.5% post injection fuel. When less fuel is injected by post injection, there is less enhancement of mixing and temperature increase later during the cycle to suppress soot formation and improve soot oxidation. Therefore, more soot is produced from the relatively long main injections with a small post injection. For large post injections, fuel from post injection produces more soot which cannot be oxidized under the low temperature during the expansion stroke, resulting in relatively higher soot emissions.

6.6 SMPS and surface area

Figure 6.8 shows the particle size distribution under baseline, main injection only and different injection dwells for 4.5% and 7.5% post injection conditions. Post injection only reduces the magnitude of particulate number, but has no effect on the mode of the total particle concentration size distribution, which is in agreement with the study of Bertoia et al.[169] This suggests that post injection does not have much impact on the agglomeration process during soot formation. Post injection conditions also have lower total particle number compared to main injection only condition, which agrees with the filter PM mass result. The optimized PM reduction conditions, 7.5% fuel post injection have lower particle number compared to 4.5% fuel post injection conditions. Injection dwell does not have much influence on the particle number. With same amount of post injection fuel, particle size distribution does not change.

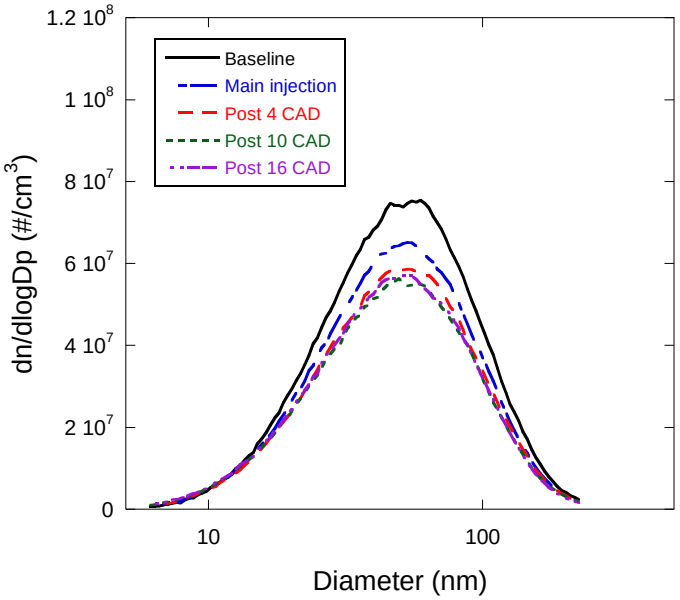

(a)

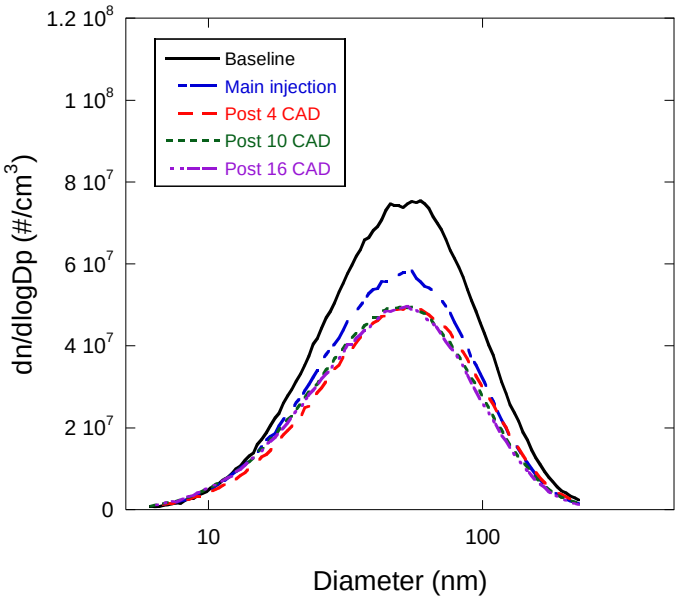

(b)

Figure 6.8 Particle size distributions for baseline, main injection only and (a) 4.5 and (b) 7.5% post injection with injection dwell 4°CAD, 10°CAD and 16°CAD

Table 6.2 shows the BET surface area of soot samples collected from the baseline condition and two 7.5% post injection conditions, one close-coupled post injection condition with injection dwell of 4°CAD, and one long dwell post injection condition with injection dwell of 16°CAD. The BET surface areas of the soot samples from the three conditions are very similar. This means that soot from different post injection conditions have similar surface area and pore volume compared to the baseline condition, regardless of ignition dwell. Because soot particle aggregate size and surface area are similar, it could be anticipated that particles produced from post injection conditions have similar primary particle size compared to the baseline condition, which is also proved by TEM images. Although PM produced from baseline and post injection conditions have very similar BET surface area, as discussed in Section 5.9, they do not

necessarily result in similar oxidation reactivity. Instead of total surface area, active surface area and soot nanostructure have greater impact on soot reactivity.

Table 6.2 BET surface area of PM from baseline and post injection conditions

Condition		Surface area (m^2/g)
Baseline		164
7.5% post injection	4^oCAD	162
	16^oCAD	163

6.7 Soot reactivity analysis

Bulk soot samples are collected from the baseline condition, 4.5% and 7.5% post injection conditions and reduced load main injection only conditions with reduced load. Soot samples collected from the post injection study are analyzed under TGA, to obtain their VOF and apparent rate constant for oxidation at 500^oC.

Figure 6.9 shows the VOF of soot from the baseline, main injection only and post injection conditions. VOF does not vary much with post injection, and has a similar trend as THC emissions. Close-coupled post injection yields lower VOF compared to the baseline condition, while long dwell post injection yields higher VOF compared to the baseline condition. This is because with close-coupled post injection, increased cylinder temperature promotes the complete oxidation of fuel, which reduces the excess hydrocarbon condensed on soot particle aggregates. However, with retarded post injection, cylinder expansion reduces combustion temperature and results in increased amount of unburned hydrocarbons condensed on soot particle aggregates. Main injection only conditions also have increased hydrocarbon emissions

because less fuel is injected per cycle, which reduces the combustion temperature and results in a higher amount of hydrocarbon condensed on the particles.

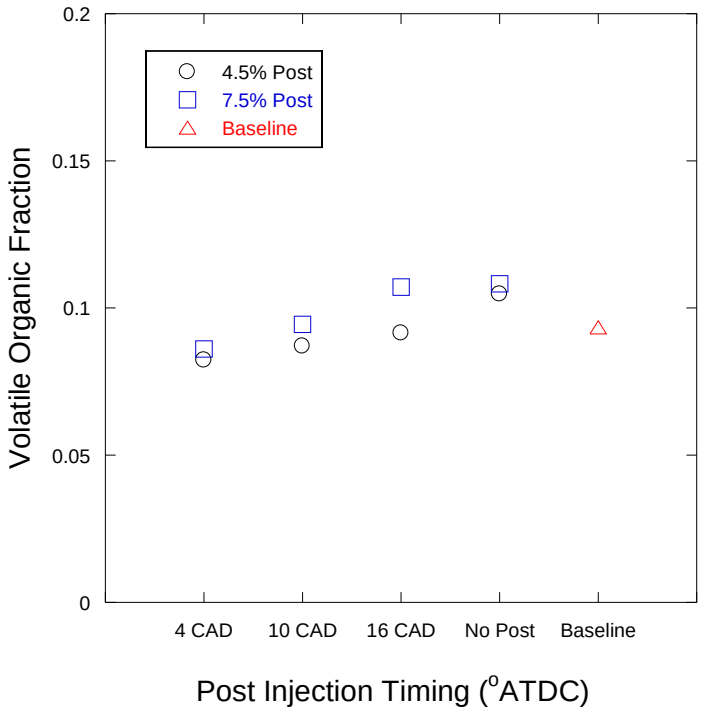

Figure 6.9 VOF of PM for baseline, main injection only and post injection conditions

Table 6.3 shows the overall apparent rate constant of soot collected from baseline, main injection only and post injection conditions and the instantaneous rate constant at 25%, 50% and 75% mass burned. Figure 6.10 compares the oxidation curve of soot from close-coupled (4°CAD) and long dwell (16°CAD) post injection conditions with the baseline condition. From the oxidation rate constant and oxidation curves, it could be observed that with increased injection dwell, the reactivity of soot increases. The reaction rate constants of soot from close-coupled post injection conditions increase by 10-13% compared to baseline condition, while the reaction

rate constants of soot from long dwell post injection decrease by 37-39% compared to baseline condition. Soot from main injection only conditions and 10°CAD post injection conditions have similar reactivity as the baseline condition.

Table 6.3 Overall apparent rate of constant and rate constant at different stages of oxidation at 500°C

Condition		Overall Apparent Rate Constant (1/Pa/min)	Rate Constant at 25% mass burn (1/Pa/min)	Rate Constant at 50% mass burn (1/Pa/min)	Rate Constant at 75% mass burn (1/Pa/min)
Baseline		$7.93*10^{-7}$	$6.61*10^{-7}$	$8.97*10^{-7}$	$1.37*10^{-6}$
4.5%	4°CAD	$6.92*10^{-7}$	$5.70*10^{-7}$	$8.11*10^{-7}$	$1.37*10^{-6}$
	10°CAD	$9.99*10^{-7}$	$8.52*10^{-7}$	$1.10*10^{-6}$	$1.76*10^{-6}$
	16°CAD	$1.09*10^{-6}$	$9.59*10^{-7}$	$1.22*10^{-6}$	$1.89*10^{-6}$
	Main Injection	$8.33*10^{-7}$	$7.27*10^{-7}$	$9.33*10^{-7}$	$1.43*10^{-6}$
7.5%	4°CAD	$7.17*10^{-7}$	$6.01*10^{-7}$	$7.84*10^{-7}$	$1.28*10^{-6}$
	10°CAD	$7.76*10^{-7}$	$6.36*10^{-7}$	$9.05*10^{-7}$	$1.36*10^{-6}$
	16°CAD	$1.10*10^{-6}$	$9.43*10^{-7}$	$1.25*10^{-6}$	$1.88*10^{-6}$
	Main Injection	$6.79*10^{-7}$	$5.62*10^{-7}$	$7.14*10^{-7}$	$1.28*10^{-6}$

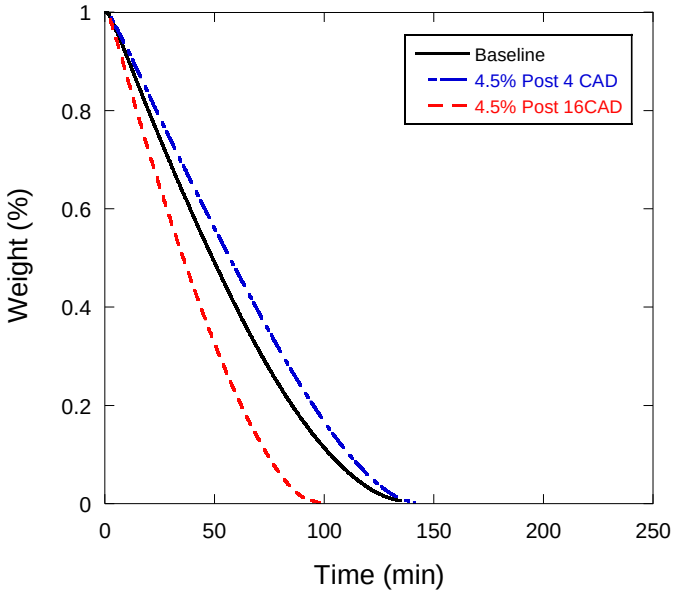

(a)

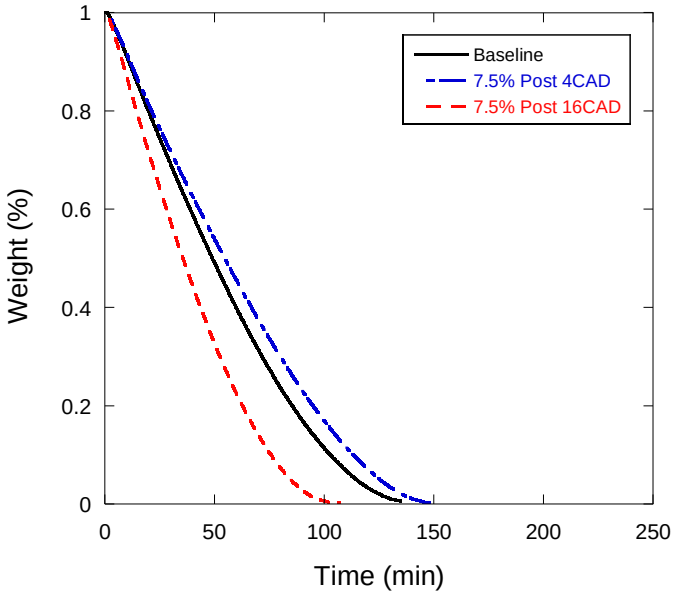

(b)

Figure 6.10 Normalized mass from isothermal oxidation of PM from baseline and (a) 4.5 and (b) 7.5% post injection with injection dwell 4°CAD and 16°CAD at 500°C

Desantes et al.[170] and Arregle et al.[171] came up with the "split flame" theory and believe that the combustion of the main injection fuel and the post injection fuel are independent. In their view, the reduction of PM emissions by post injection is because fuel from the post injection does not contribute to total soot production. In other words, fuel from post injection does not introduce additional soot emissions regardless of injection dwell. This "split flame" theory is supported by the experimental result that post injection conditions produce very similar PM emissions as that with the main injection only condition, regardless of the injection dwell. However, O'Connor et al.[172] reported that post injection fuel must have an interaction with the main injection flame. The enhance mixing and increased temperature of post injection can suppress soot formation or improve the soot oxidation process.

In our study, long dwell post injection conditions (injection dwell 10^{o}CAD and 16^{o}CAD) also have very similar FSN with main injection only conditions. However, the difference in PM reactivity suggests that fuel from post injection does influence the main injection flame. In addition, a significant portion of soot should be produced from the post injection flame according to the difference in PM reactivity. With close-coupled post injection, fuel from post injection enters into the main injection flame region. So the post injection jet has a short ignition delay and goes through diffusion type combustion where local equivalence ratio is high. In addition, close-coupled post injection also results in higher combustion rate and local temperature. As discussed in Section 5.8, soot reactivity decreases with the increase of equivalence ratio and temperature. High temperature could enhance the soot structural rearrangement process, which results in soot with lower reactivity. With long dwell post injection, in-cylinder soot distribution becomes dispersed and breaks into separate pockets.[173] The post injection jet breaks the soot pockets from

the main injection into smaller pockets and increases the flame surface area. The enhanced mixing could suppress soot formation and improve soot oxidation as well as produce soot with higher reactivity from the main injection flame. For delayed post injection timing, the combustion of the post injection jet occurs under relatively low temperature and equivalence ratio. As a consequence, soot produced under long dwell post injection conditions has less mature nanostructure and higher reactivity.

6.8 XRD analysis

Figure 6.11 shows the X-ray diffraction patterns for soot generated from the baseline, main injection only and post injection conditions. There are primarily three peaks in the XRD spectra for soot, a (002) peak around 25^{o}, (10) peak around 43^{o}, and a (110) peak around 77^{o}. The peak locations and FWHM does not show much variation between different operating conditions.

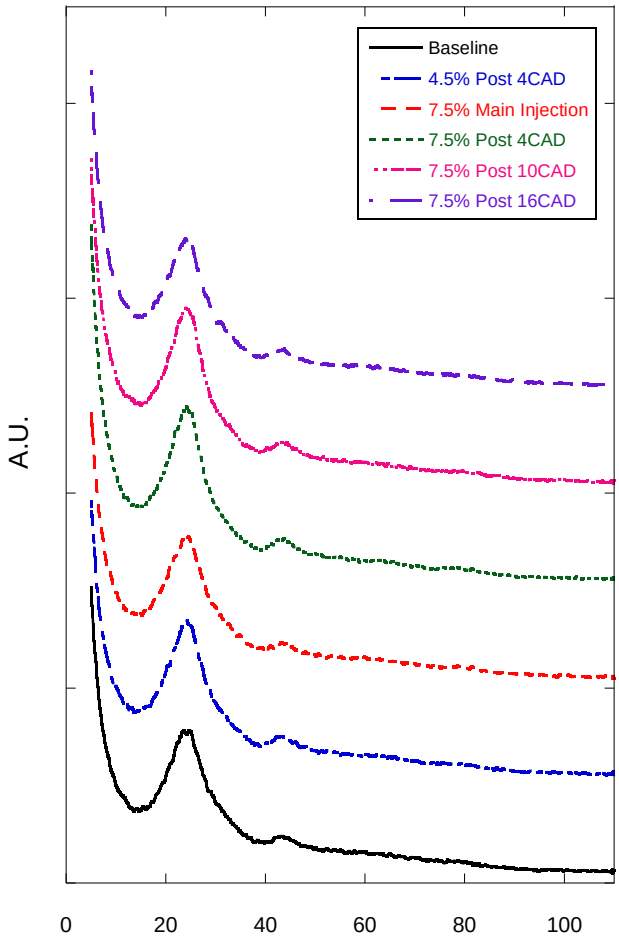

Figure 6.11 XRD patterns for soot collected from baseline, main injection only and post injection conditions

Table 6.4 shows the interlayer spacing (d_{002}), stacking height (Lc), crystalline basal plane diameter (La) and average number of layers (N), which are calculated from peak positions and FWHMs. The interlayer spacing here is around 0.366 nm, higher than the interlayer spacing of graphite which is 0.338 nm, indicating a certain degree of disorder. Stacking height Lc and basal plane diameter La show some correlation with reactivity. With the increase of injection dwell, Lc

and La decrease, and soot reactivity increases. This is because with shorter graphene layers, the higher portion of edge carbon atoms increases the reactivity of the soot particles.[74]

Table 6.4 Interlayer spacing, stacking height, crystalline basal plane diameter and average number of layers from XRD pattern analysis

Condition		d002 (nm)	Lc (nm)	La (nm)	N
Baseline		0.364	1.71	3.59	4.70
4.5%	4°CAD	0.365	1.71	3.19	4.69
7.5%	4°CAD	0.367	1.83	3.59	4.97
	10°CAD	0.367	1.76	3.15	4.68
	16°CAD	0.367	1.68	2.98	4.57
	Main Injection	0.366	1.63	3.69	4.44

6.9 X-ray photoelectron spectroscopy

Soot samples produced from different operating conditions are examined by XPS, Raman spectrometry, and TEM to investigate the impact of nanostructure on their reactivity. In addition, partially oxidized soot at 40% and 75% mass burned are also examined by these techniques to understand their structural change during oxidation.

Table 6.5 shows the elemental composition of soot generated from the baseline, main injection only and different post injection conditions. From the XPS survey scan, a semi-quantitative surface elemental composition can be obtained. Only carbon and oxygen elements are found in the XPS spectra, indicating other elements from the fuel or lubricating oil below the detection limit. With the increase of injection dwell and post injection amount, surface oxygen content increases. Main injection only with reduced load conditions have similar surface oxygen

content as the baseline condition. Soot from close-coupled post injection conditions has lower surface oxygen content while soot from long dwell post injection conditions have higher surface oxygen content compared to the baseline condition. Surface oxygen content increases with the decrease of soot formation temperature. In this study, surface oxygen content correlates well with oxidation rate constant, although it is believed that surface oxygen content does not necessary affect soot reactivity.[37] The separation of oxygen functional groups during oxidation can open micropores or active cites, which increases the reactivity of soot particles. However, the surface oxygen content may only be an artifact of exposure of the soot to flames during the combustion and expansion processes.

Table 6.5 Elemental compositions for soot from baseline main injection only and post injection conditions

Condition		C content (%)	O content (%)
Baseline		93.3	6.7
4.5%	4^{o}CAD	93.3	6.7
	10^{o}CAD	92.6	7.4
	16^{o}CAD	92.0	8.0
	Main Injection	93.1	6.9
7.5%	4^{o}CAD	91.8	8.2
	10^{o}CAD	90.0	10.0
	16^{o}CAD	88.5	11.5
	Main Injection	92.4	7.6

Table 6.6 Element state analysis for C 1s and O 1s spectra of original soot

Condition		C 1s (%)			O 1s (%)	
		Sp2 Carbon	Sp3/ring Carbon	C-O/ C=O/COO	C-O	C=O
Baseline		56.5	20.0	20.2	51.4	48.6
4.5%	4°CAD	56.6	20.4	19.8	50.0	50.0
	10°CAD	54.8	20.6	21.5	53.5	46.5
	16°CAD	54.4	20.8	21.4	49.8	47.6
	Main Injection	56.8	19.5	20.6	51.5	48.5
7.5%	4°CAD	55.9	20.5	20.4	53.1	47.0
	10°CAD	54.0	20.8	21.9	55.2	44.8
	16°CAD	48.1	21.6	23.8	58.2	41.8
	Main Injection	56.3	20.4	20.7	55.7	44.3

Core scans of the C 1s and O 1s peaks are deconvoluted using the method described in Sections 3.2.5 and 5.11. The relative abundance of graphitic carbon with sp2 bonding, amorphous carbon with sp3 bonding, and carbon bonded with oxygen functional groups could be analyzed from the C 1s peak. The relative concentrations of C-O and C=O can be analyzed from the O 1s peak. The elemental composition derived from the C 1s and O 1s peaks are shown in Table 6.5. Amorphous carbon with sp3 bonding is considered to be more reactive compared to graphitic carbon with sp2 bonding, due to their higher density of dangling bonds.[174] Figure 6.12 shows the defect/graphitic carbon ratio versus oxidation rate constant. Defect carbon is defined as amorphous and fullerene carbon.[175] With the increase of defect/graphitic carbon ratio, soot reactivity increases. The percentage of carbon atoms bonded with oxygen functional groups has

very similar trend to that of surface oxygen content from the survey scan. Figure 6.13 shows the relationship between carbon atoms bonded with oxygen functional groups versus oxidation rate constant. It can be observed that both defect/graphitic carbon ratio and the concentration of oxygen functional groups have good correlation with oxidation rate constant. This further proved that soots produced under low temperature [176] and low equivalence ratio have less mature nanostructure and more surface oxygen functional groups, thus resulting in higher reactivity. The type of oxygen functional groups does not have a clear trend with operating conditions.

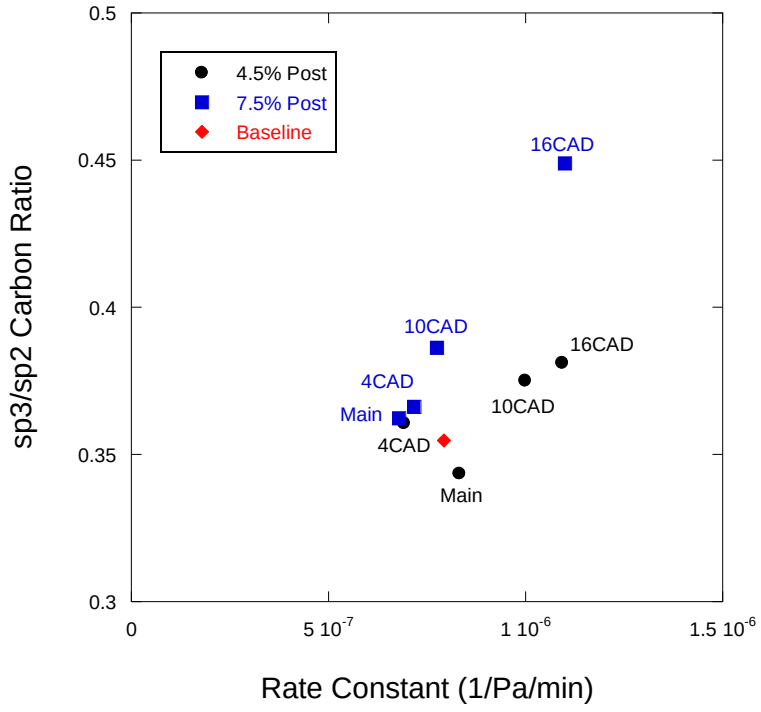

Figure 6.12 Defect/graphitic carbon ratios versus oxidation rate constant

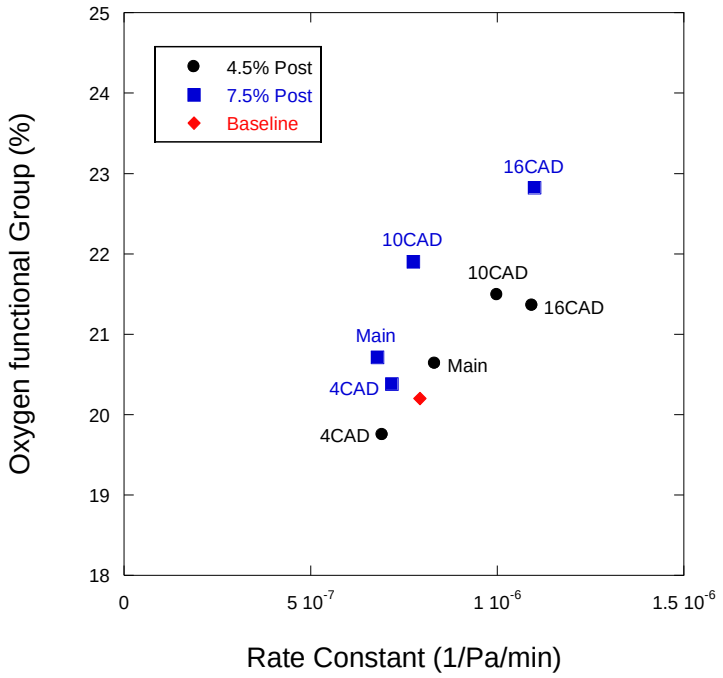

Figure 6.13 Percentage of carbon atoms bonded with oxygen functional groups versus oxidation rate constant

Figures 6.14 and 6.15 show the core scan of the C 1s and O 1s peaks. From the C 1s core scan, it is clear that soots produced from long dwell post injection conditions have relatively higher sp3 peak compared to the baseline and main injection only conditions, while soots produced from close-coupled post injection conditions have slightly higher sp2 peak intensity. The intensities of the O 1s peak are also increased by long dwell post injection conditions and deceased slightly by close-coupled post injection conditions compared to baseline condition.

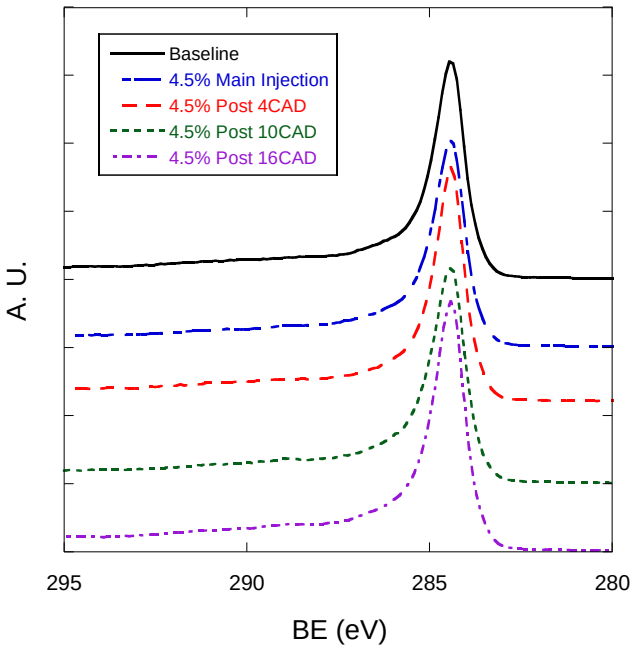

(a)

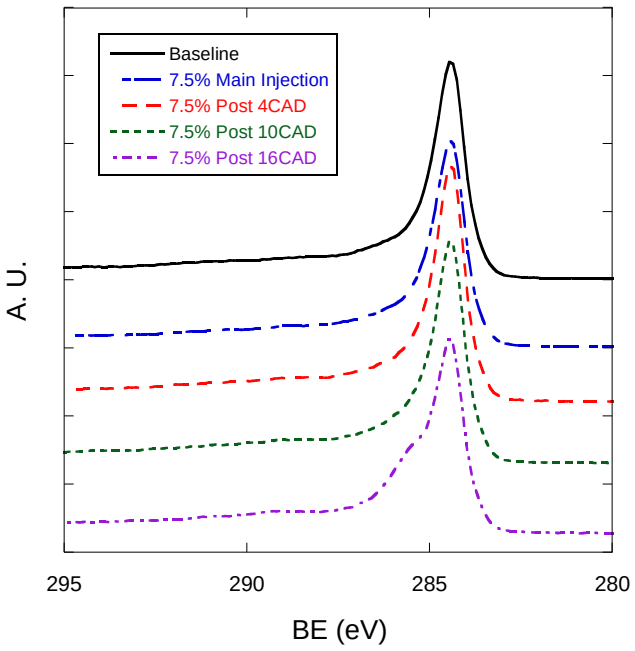

(b)

Figure 6.14 C 1s core scan peaks for baseline, main injection only and (a) 4.5 and (b) 7.5% post injection with injection dwell 4°CAD, 10°CAD and 16°CAD

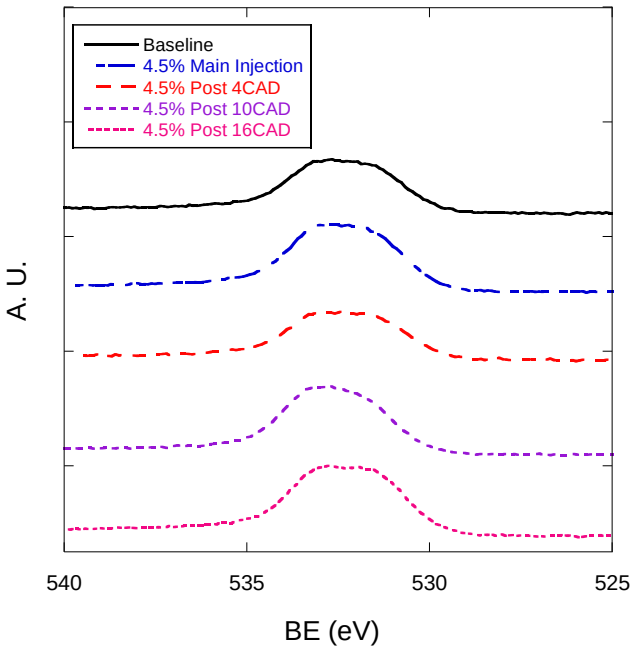

(a)

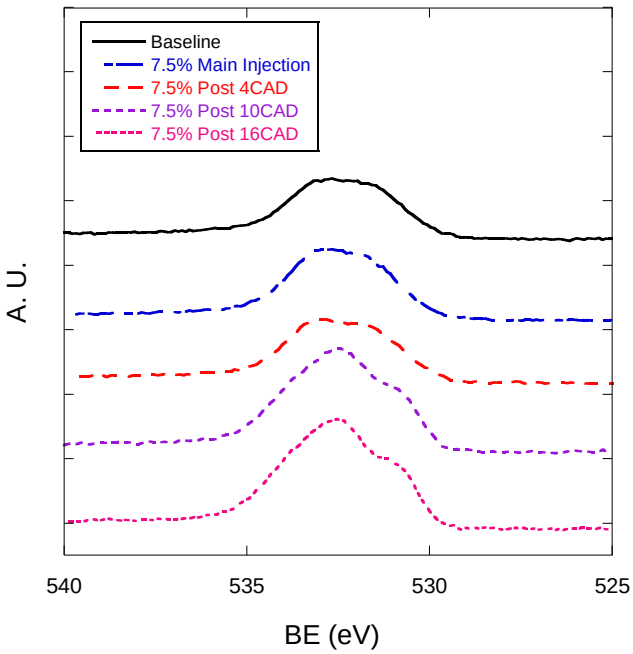

(b)

Figure 6.15 O 1s core scan peaks for baseline, main injection only and (a) 4.5 and (b) 7.5% post injection with injection dwell 4°CAD, 10°CAD and 16°CAD

Table 6.7 Element composition of soot at 40% and 75% mass burned

Condition		40% burn		75% burn	
		C content (%)	O content (%)	C content (%)	O content (%)
Baseline		92.0	8.0	91.6	8.4
4.5%	4°CAD	92.6	7.4	91.6	8.4
	10°CAD	92.6	7.4	92.1	8.0
	16°CAD	92.8	7.2	92.2	7.8
	Main Injection	92.6	7.4	92.1	7.9
7.5%	4°CAD	92.3	7.7	91.8	8.2
	10°CAD	92.0	8.0	91.3	8.7
	16°CAD	91.9	8.1	91.4	8.6
	Main Injection	92.6	7.5	91.9	8.1

Table 6.7 shows the surface elemental composition of soot samples at 40% and 75% mass burned. Surface oxygen concentrations generally increase slightly during oxidation, except for the 7.5% long dwell post injection conditions. Oxygen concentration is between 7.1% - 8.1% for 40% mass burned soot, and 7.8% - 8.8% for 75% mass burned soot. Tables 6.8 and 6.9 show the elemental state of carbon and oxygen atoms during oxidation. Figure 6.16 shows the defect/graphitic carbon ratio during oxidation. Defect/graphitic carbon ratio first increases then decreases during oxidation. Amorphous carbon with sp3 bonding oxidizes during the first stage of oxidation which reduces the defect/graphitic carbon ratio, then the short graphene layers decompose during the later stage of oxidation, so that defect/graphitic carbon ratio increases. Figure 6.17 shows the concentration of carbon atoms bonded with oxygen functional groups during oxidation, which follows a similar trend with surface oxygen concentration and increases slightly during oxidation. This means that the active sites, to which oxygen atoms can be bonded

increase during oxidation. This increase in active cites during oxidation also explains the increase in oxidation rate constant through the oxidation process.

Table 6.8 Elemental state analysis for C 1s and O 1s spectra of 40% mass burn soot

Condition		C 1s (%)			O 1s (%)	
		Sp2 Carbon	**Sp3/ring Carbon**	**C-O/ C=O/COO**	**C-O**	**C=O**
Baseline		55.4	18.3	22.3	56.9	43.1
4.5%	4°CAD	55.9	18.3	21.7	53.5	46.5
	10°CAD	56.5	19.5	21.0	54.2	45.9
	16°CAD	57.5	19.0	20.6	52.3	47.7
	Main Injection	58.7	16.4	21.6	54.0	46.1
7.5%	4°CAD	55.5	17.8	22.5	57.9	42.1
	10°CAD	56.3	18.0	22.2	53.6	46.4
	16°CAD	55.8	18.2	22.1	58.6	41.4
	Main Injection	56.7	17.0	22.3	57.2	42.8

Table 6.9 Elemental state analysis for C 1s and O 1s spectra of 75% mass burned soot

Condition		C 1s (%)			O 1s (%)	
		Sp2 Carbon	**Sp3/ring Carbon**	**C-O/ C=O/COO**	**C-O**	**C=O**
Baseline		52.5	18.9	23.5	57.0	43.0
4.5%	4°CAD	53.8	19.1	23.0	53.0	47.0
	10°CAD	57.3	16.4	23.0	52.8	47.2
	16°CAD	55.1	18.5	22.5	50.9	49.1
	Main Injection	57.5	18.8	21.2	52.0	48.0
7.5%	4°CAD	58.4	19.2	20.5	55.9	44.1
	10°CAD	54.1	17.9	23.7	53.4	46.6
	16°CAD	54.8	17.3	23.6	55.4	44.6
	Main Injection	55.4	18.7	22.4	54.4	45.6

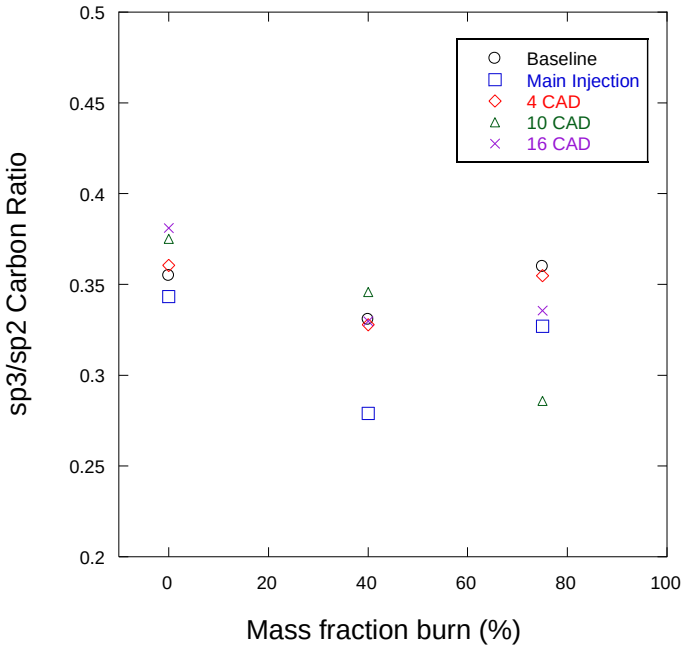

(a)

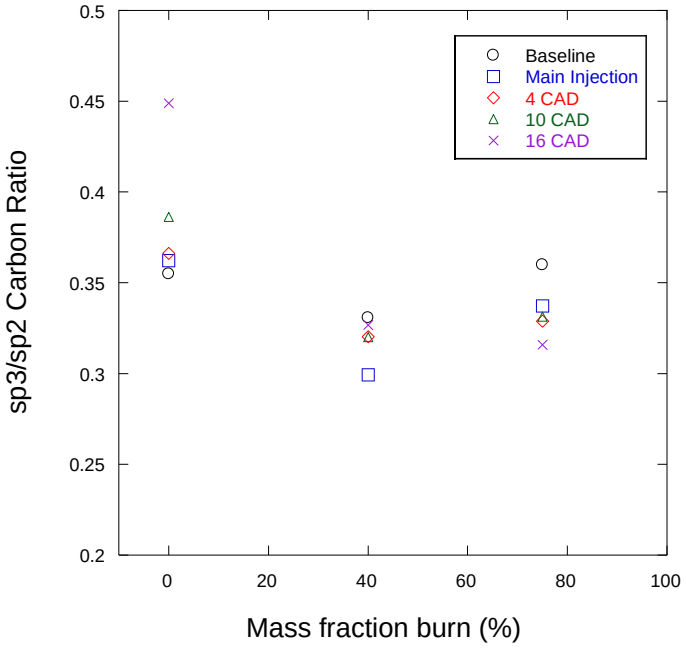

(b)

Figure 6.16 Defect/graphitic carbon ratios for baseline, main injection only and (a) 4.5 and (b) 7.5% post injection conditions of initial, 40% and 75% mass burned soot

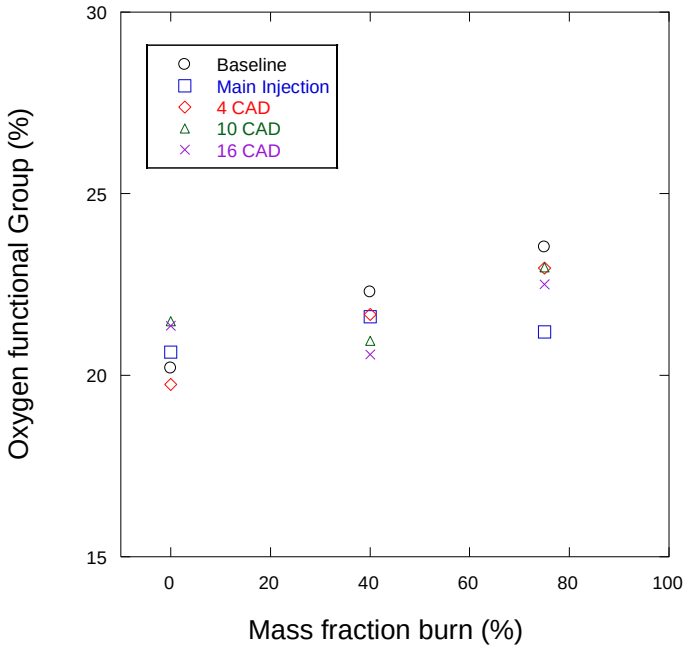

(a)

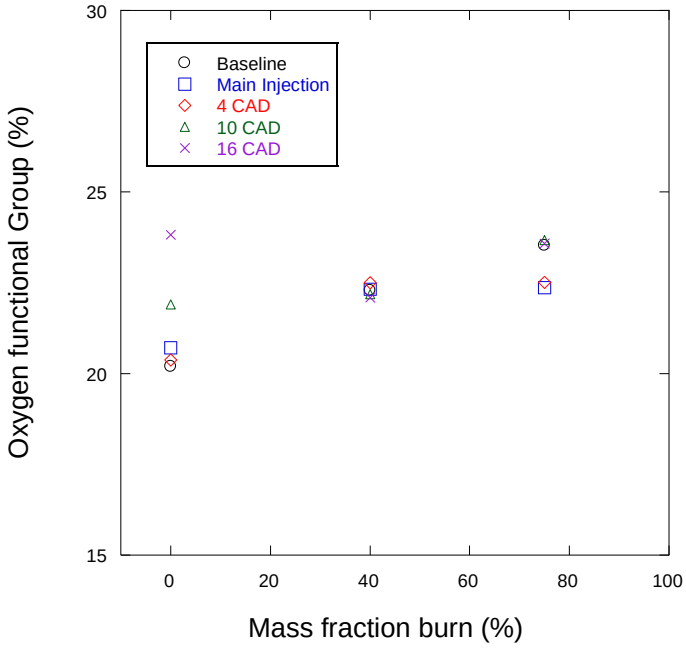

(b)

Figure 6.17 Percentage of carbon atoms bonded with oxygen functional groups for baseline, main injection only and (a) 4.5 and (b) 7.5% post injection conditions of initial, 40% and 75% mass burned soot

6.10 Raman spectroscopy

Raman spectroscopy is applied to the soot samples and analyzed using the method described in Sections 3.2.3 and 5.12. A 3L1G fitting method is used for peak deconvolution, to interpret the degree of structural order of the soot aggregates. The G peak represents the in-plane bond-stretching motion of graphite carbon atoms, while The D1 peak represents the breathing mode of carbon atoms on graphene edges. The intensity ratio of the D1 and G band (I_{D1}/I_G) or the area ratio of the D1 and G band (A_{D1}/I_G) can be used to indicate the density of edge sites, thus providing information on the size of graphene layers. In addition, the FWHM of D1 and G band are also used to indicate the distribution of crystallite sizes, and relative abundance of structural disorder.

Figure 6.18 shows the relationship between the FWHM of D1 band and oxidation rate constant of soot samples from baseline and 7.5% post injection conditions. With increased oxidation rate constant, the D1 band FWHM increases, indicating a higher density of edge sites. Soot produced from long dwell post injection conditions shows higher D1 band FWHM. This means soot samples produced from long dwell post injection conditions not only have higher amorphous carbon content but also have shorter graphene layers. Both factors contribute to their increased reactivity.

The changes of I_{D1}/I_G and D1 FWHM during different stages of oxidation for baseline and 7.5% post injection soot are shown in Figure 6.19. Both I_{D1}/I_G and D1 FWHM increase during the first stage of oxidation. This means the size of graphene layers shrinks during the early stage of oxidation. So soot samples first go through shrinking core type of oxidation. During the late stage of oxidation (75% mass burned) I_{D1}/I_G and D1 band FWHM stay similar with early stage of oxidation (40% mass burned), indicating the density of edge site carbon

atoms does not change much during the late stage of oxidation. The difference between I_{D1}/I_G for the soot samples is within the error range. However, soot from long dwell post injection conditions show higher D1 FWHM during oxidation, indicating a higher edge carbon atom ratio through the oxidation process. Because edge carbon atoms are more reactive, soot reactivity increases with the increase of edge carbon atom ratio.

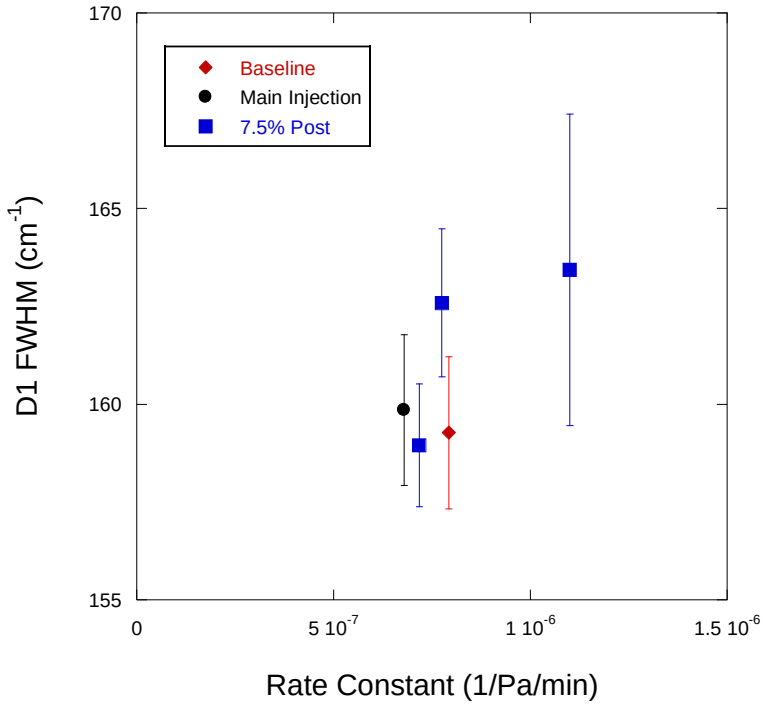

Figure 6.18 D1 band FWHM versus soot oxidation rate constant for soot from baseline, main injection only and 7.5% post injection conditions

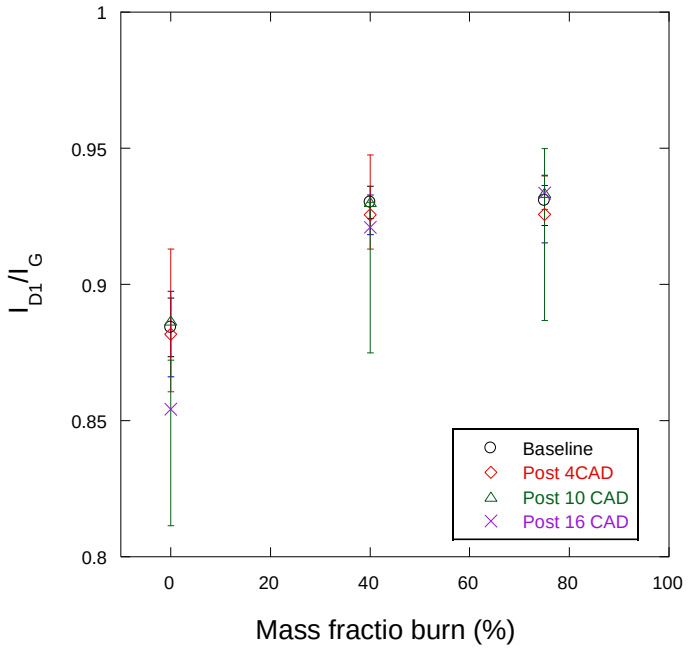

(a)

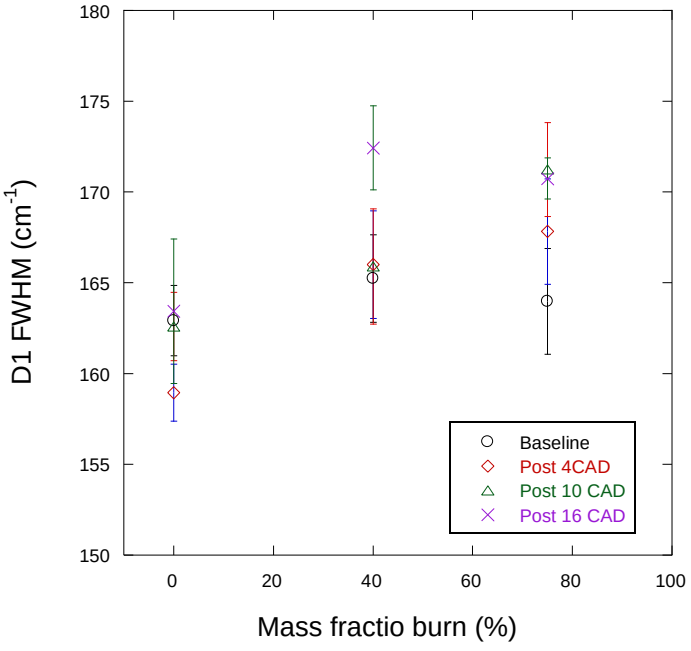

(b)

Figure 6.19 (a) ID1/IG and (b) D1 band FWHM for initial soot, 40% and 75% mass burned soot from baseline and 7.5% post injection conditions

6.11 Transmission electron microscopy

Figure 6.20 shows the TEM images of soot particles from the baseline, and 7.5% post injection conditions. For each condition, a low resolution TEM image with magnification 40,000x shows the morphology of particle aggregates, and a high resolution image at 400,000x shows the nanostructure of the primary soot particles. Soot particles from different conditions show similar primary particle sizes around 30nm and also similar aggregation particle sizes around 300-400nm. This is in agreement with particle size distribution and BET surface area results. Particle aggregates show similar fractal structure between the baseline and post injection conditions. Primary soot particles are usually composed of a core/shell structure. The core is mainly amorphous carbon, while the shell contains small graphene layers parallel to the particle surface. From high resolution TEM images, it can be observed that soot particles from close-coupled post injection conditions have a smaller amorphous core, and more ordered graphene layers compared to the baseline and long dwell post injection conditions. As discussed previously, with decreased amorphous carbon and increased degree of order of graphene layers, the density of active sites decreases so that the reactivity of the soot decreases. Soot from long dwell post injection conditions show higher portion of amorphous carbon and less ordered graphene layers, which results in higher reactivity. Those observations are also in accordance with bulk soot measurement results such as via XPS and Raman spectrometry. The difference between nanostructure, rather than morphology, impacts the reactivity of soot particles from this post injection study.

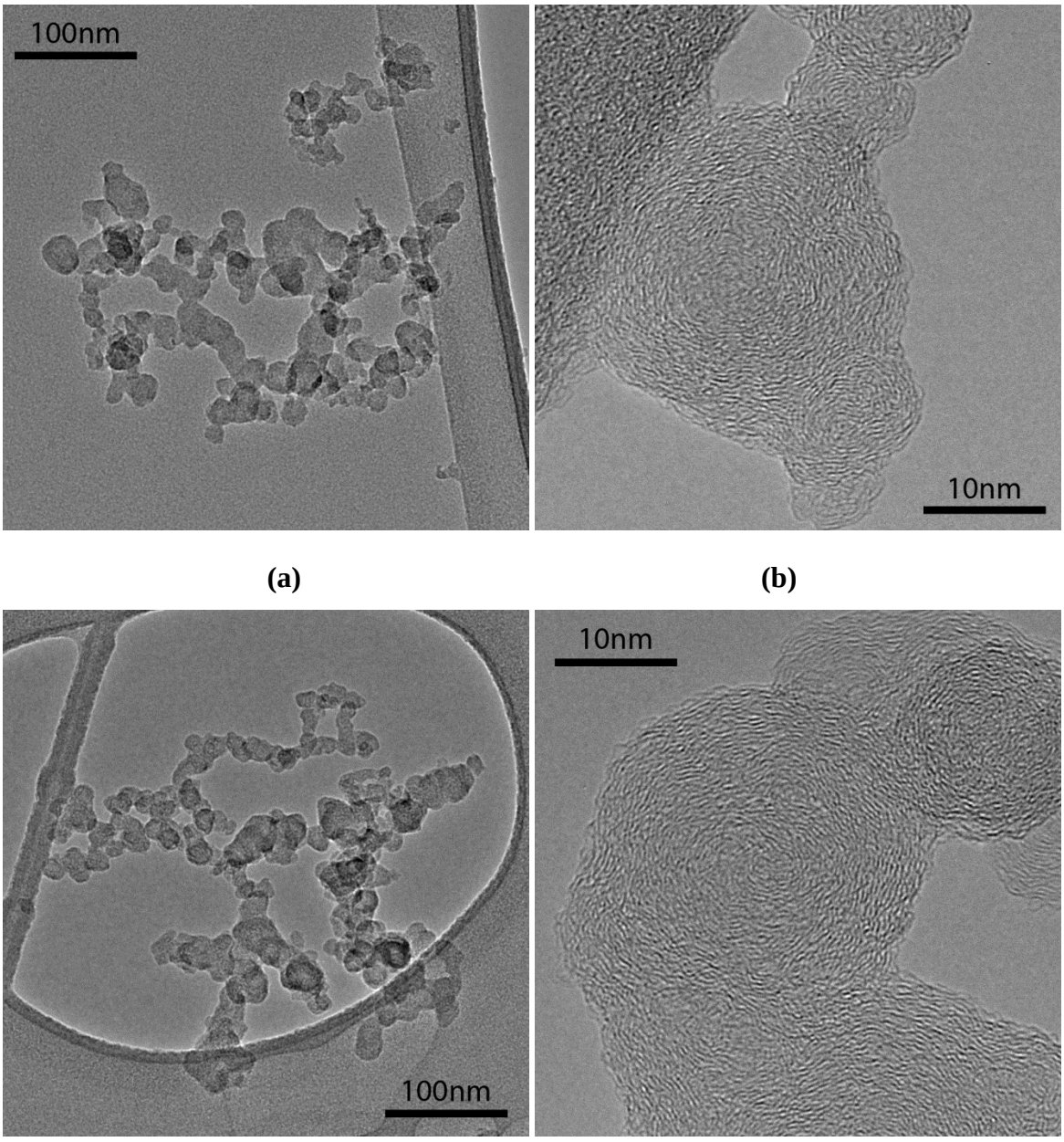

(a) **(b)**

(c) **(d)**

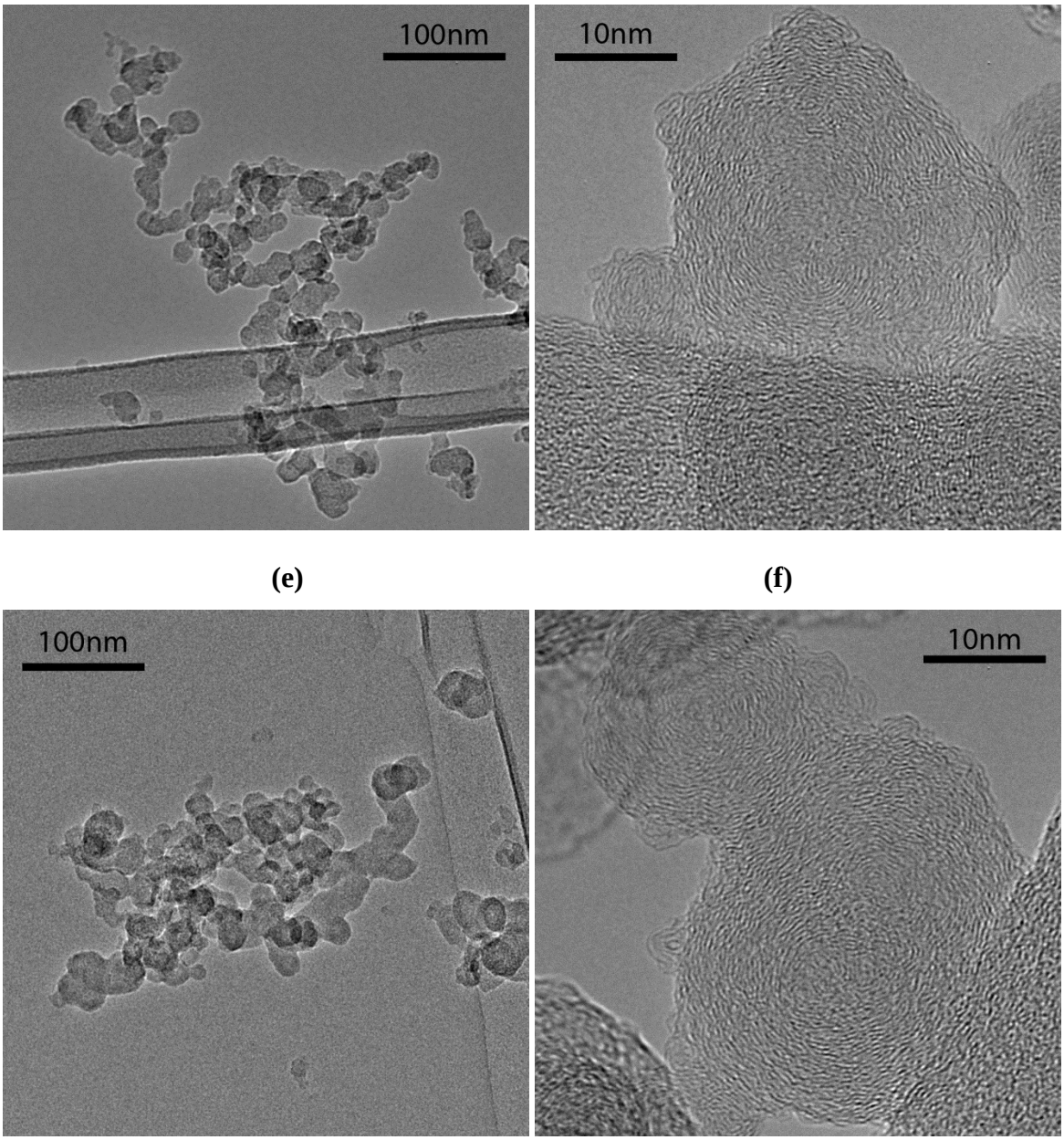

Figure 6.20 TEM images for soot produced from baseline condition at (a) 40,000x (b) 400,000x, and 7.5% post injection conditions with injection dwell 4°CAD at (c) 40,000x (d) 400,000x, 10°CAD at (e) 40,000x (f) 400,000x, and 16°CAD at (g) 40,000x (h) 400,000x

Figures 6.21-6.23 show the morphology and nanostructure of soot particles under different stages of oxidation from the baseline, close-coupled post injection (4^{o}CAD), and long dwell post injection (16^{o}CAD) conditions. Soot samples from the baseline condition and post injection conditions both show shrinking core type of oxidation. The size of primary particles decreases during oxidation. Primary particle size is around 20nm for 40% mass burned and around 10-15nm for 75% mass burned. Soot particle aggregates show a coagulation effect during oxidation. Soot particle aggregate size increase during oxidation, the number of primary particles within each aggregation particle also increase greatly. In addition, particle aggregates become more compact during oxidation, the fractal dimensions for particle aggregates increase greatly for partially oxidized soot. There is no indication of graphene layer rearrangement during the oxidation process. The similar structural change during oxidation indicates that soot produced from the baseline condition and different post injection conditions behave the same way. The difference in reactivity is mainly caused by the difference of local equivalence ratio and formation temperature during soot formation. The shrinking core oxidation without layer rearrangement indicates an overall disordered nanostructure of soot from these conditions.

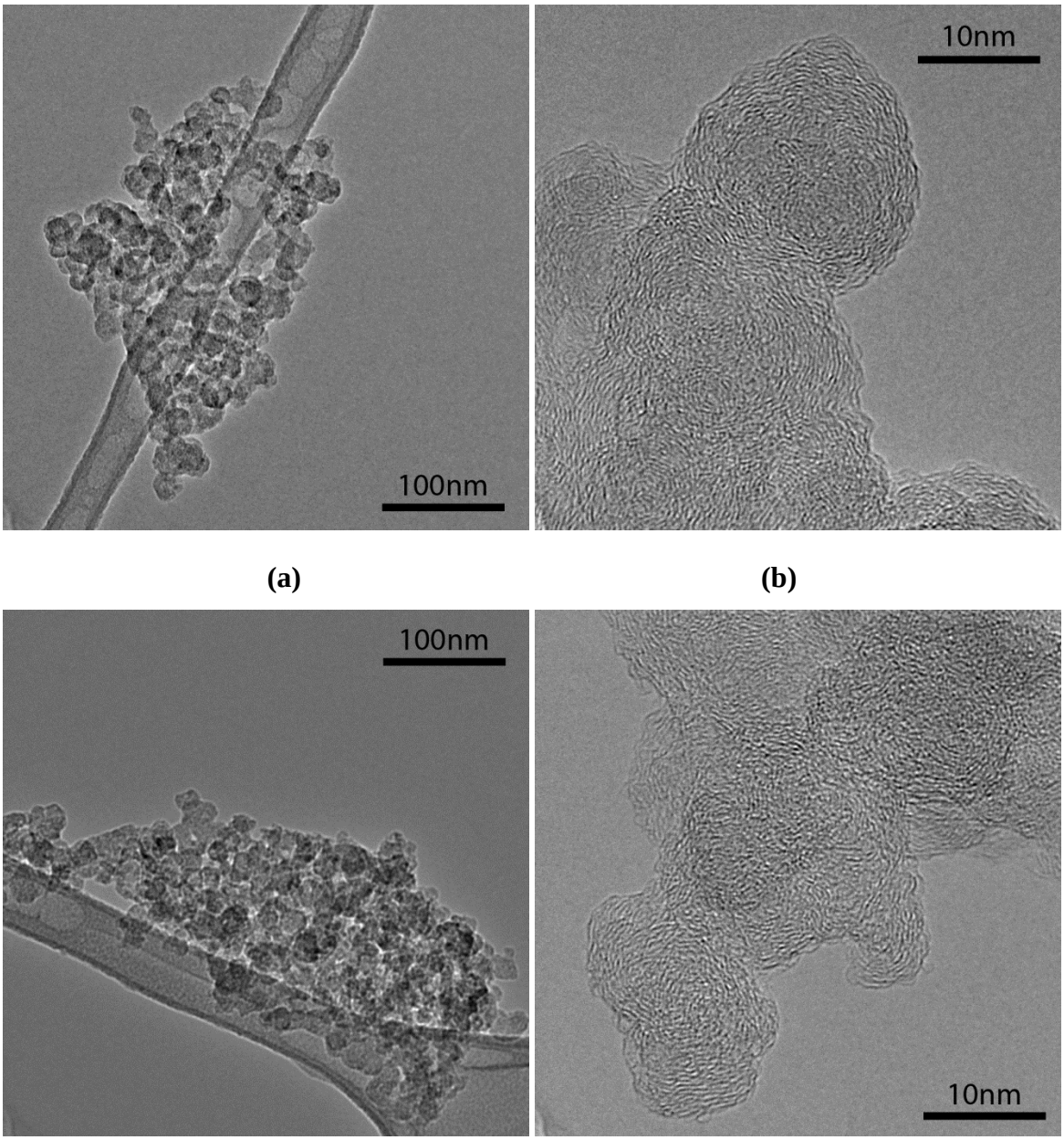

(a) **(b)**

(c) **(d)**

Figure 6.21 TEM images for soot produced from baseline condition at 40% mass burned with magnification (a) 40,000x (b) 400,000x, and 75% mass burned with magnification (c) 40,000x (d) 400,000x

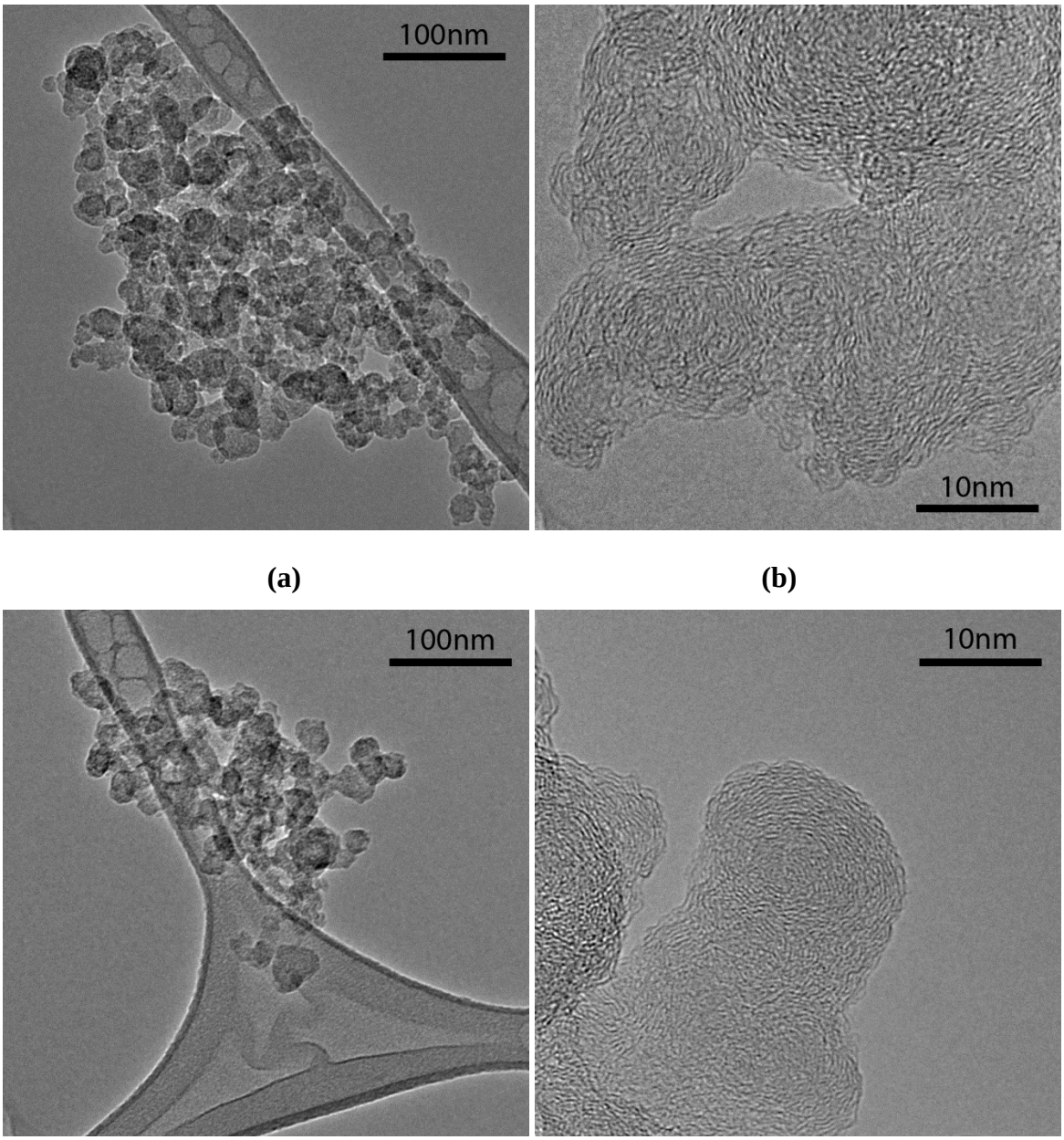

Figure 6.22 TEM images for soot produced from 7.5% post injection condition with injection dwell 4°CAD at 40% mass burned with magnification (a) 40,000x (b) 400,000x, and 75% mass burned with magnification (c) 40,000x (d) 400,000x

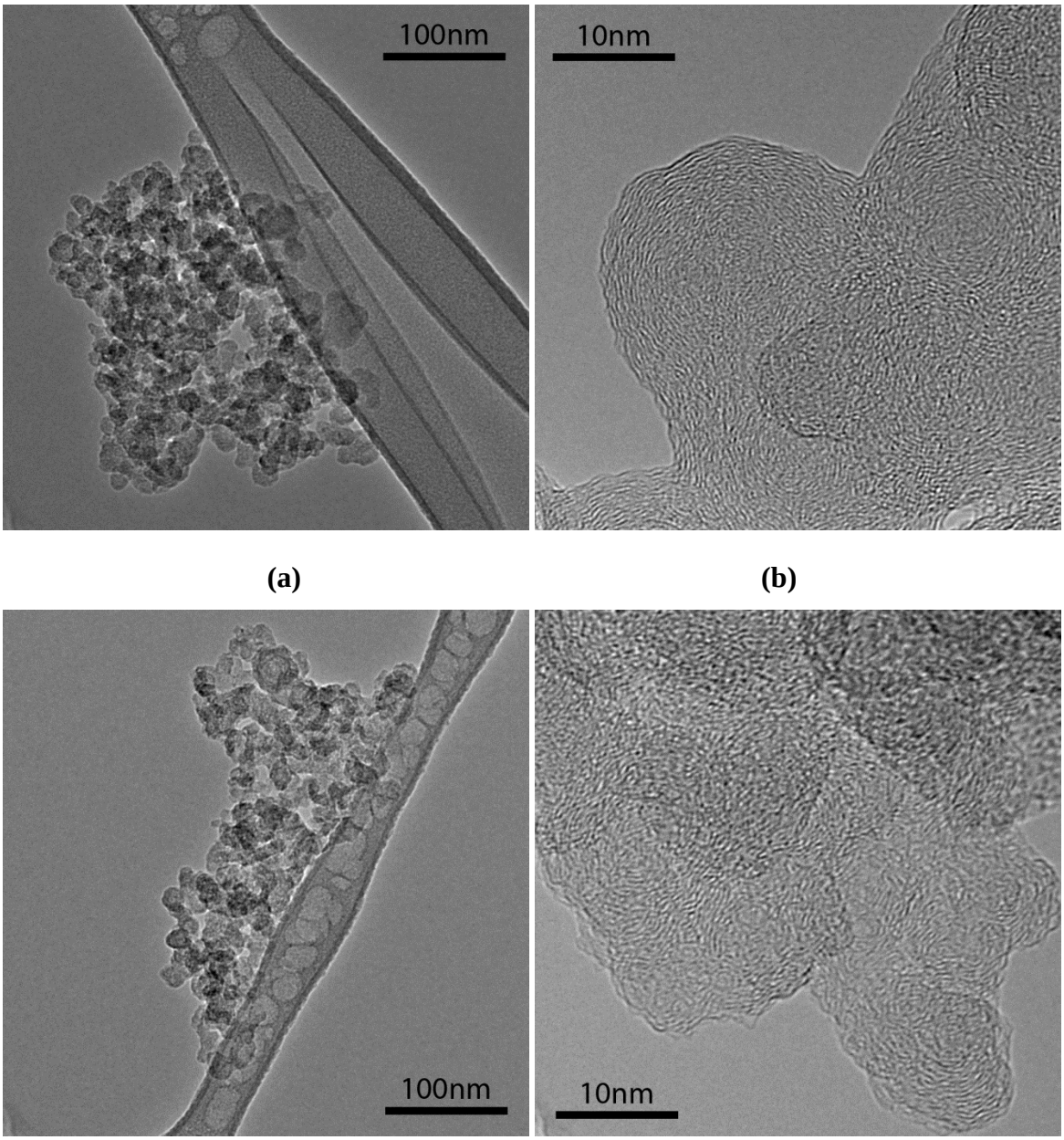

Figure 6.23 TEM images for soot produced from 7.5% post injection condition with injection dwell 16°CAD at 40% mass burned with magnification (a) 40,000x (b) 400,000x, and 75% mass burned with magnification (c) 40,000x (d) 400,000x

6.12 Summary

Soot emissions are decreased by 11-21% under close-coupled post injection conditions and 28-33% under long dwell post injection conditions. Long dwell post injection is more effective for PM reduction compared to close-coupled post injection. Soot reduction is optimized when post injection size is 6-7.5% of total fuel injected. NOx emissions are increased by 3-5% under close-coupled post injection conditions, while decreased by 7-8% under long dwell post injection conditions. CO emissions are decreased by 7-8% and THC emissions are decreased 14-28% by close-coupled post injection conditions. CO and THC emissions keep similar or slightly increase under long dwell post injection conditions. BSFC decreases by 1% under close-coupled combustion and increases by 1% under long dwell post injection.

The reactivity of soot decreases when injection dwell is short and increases with the prolonging of injection dwell. The reaction rate constants of soot from close-coupled post injection conditions increase by 10-13%, while the reaction rate constants of soot from long dwell post injection decrease by 37-39% compared to baseline condition. The primary soot particle and particle aggregate sizes, particle size distributions and BET surface areas do not vary with different post injection conditions. Soot reactivity correlates well with amorphous carbon content and graphene layer size. With the increase of injection dwell, amorphous carbon content increases and graphene layer size decreases. Soot particles show shrinking core oxidation without layer rearrangement.

For close-coupled post injection conditions, fuel injected during post injection increases the combustion rate and cylinder temperature, which increases NOx formation, and enhances PM oxidation. High temperature also enhances graphene layer rearrangement, which decreases soot reactivity. For long dwell post injection conditions, cylinder expansion decreases the combustion

speed of post injection fuel. However, the post injection jet still enhances the mixing of main injection flame and promotes soot oxidation. As a consequence, soot produced from long dwell post injection has higher reactivity compared to baseline condition.

Chapter 7.

Conclusions and future work

7.1 Conclusions

7.1.1 PCCI

PCCI combustion is achieved with increased EGR level and injection pressure in this study. Late injection PCCI combustion can reduce NOx emissions by 76-78% and reduce soot emissions by 25-35%. High CN, high alkane content fuels LTFT and RD lowers CO emissions by 60% and THC emissions by 62% compared to ULSD under late injection PCCI combustion. LTFT and RD also have relatively smaller increase of CO and THC emissions under late injection PCCI combustion conditions. LTFT and RD only increase CO emissions by 40-45% and THC emissions by 11-16% under late injection PCCI combustion, while ULSD increases CO emissions by 78% and THC emissions by 24% under late injection PCCI combustion. NOx and PM emissions are similar for the three fuels under both conventional and PCCI combustion conditions. So high ignition quality fuels LTFT and RD can reduce NOx and PM emissions without a significant penalty on CO and THC emissions under PCCI combustion. However, LTFT and RD fuels have higher FSN compared to ULSD under both conventional and PCCI combustion, indicating a higher portion of carbonaceous soot and lower VOF within the PM. RD

provides similar benefit compared to LTFT under PCCI combustion mode. So RD can be used as a substitute for LTFT fuel.

Under reduced combustion temperature and equivalence ratio, PCCI combustion produces soot with higher surface oxygen concentration, higher portion of amorphous carbon and shorter graphene layers. As a consequence, the reaction rate constants of soot produced from late injection PCCI combustion are 1.2-2.2 times higher than soot from the conventional combustion conditions. The reaction rate constants of soot from LTFT and RD fuels are 47-66% lower than soot produced from ULSD due to their high CNs.

The primary particle and particle aggregate sizes are around 25nm and 400 nm for conventional combustion soot, while 10nm and 150 nm for late injection PCCI combustion soot. Soot produced from LTFT and RD fuel under conventional combustion mode show internal burning during oxidation. However, soots with higher reactivity produced from PCCI combustion and ULSD fuel show shrinking core oxidation, due to their overall amorphous nanostructure. Layer rearrangement does not occur during oxidation process for soot from both conventional and PCCI combustion. The size of graphene layers and the percentage of amorphous carbon decreases during oxidation.

7.1.2 Post injection

Close-coupled post injection reduces soot emissions by 11-21%, THC emissions by 14-28%, and CO emissions by 7-8%. However, NOx emissions increase by 3-5% due to the increased cylinder temperature. Long-dwell post injection reduces soot emissions by 28-33%, and NOx emissions by 7-8%. Long dwell post injection conditions produce similar or slightly

increased CO and THC emissions. BSFC decreases by 1% under close-coupled post injection conditions, while increases by 1% under long-dwell post injection conditions. Long dwell post injection is more effective in soot reduction. Soot reduction is optimized with 6-7.5% fuel during post injection.

Compared to baseline condition, the reaction rate constants of soot from close-coupled post injection conditions increase by 10-13%, while the reaction rate constants of soot from long dwell post injection conditions decrease by 37-39%. With the increase of injection dwell, soot reactivity increases. Surface oxygen concentration and amorphous carbon content increase with the increase of injection dwell and post injection portion.

Compared to soot from baseline condition, soot produced from post injection conditions has similar primary particle sizes around 30 nm, similar aggregation particle sizes around 400 nm and similar BET surface areas around 163m^2/g. Soot from all condition goes through shrinking core oxidation. No layer rearrangement is observed for soot from baseline or post injection conditions. During the oxidation process, amorphous carbon content and first decrease then increase, graphene layer size decreases, and surface oxygen content increases.

7.2 Future work

7.2.1 Investigation of soot oxidation behavior and mechanism

1) Biodiesel soot reactivity and oxidation process from PCCI combustion condition

Biodiesel is found to produce higher NOx emissions, lower PM, CO and THC emissions under both conventional[96] and PCCI[118] combustion conditions compared to diesel fuels. In

addition, soot produced from biodiesel shows higher oxidative reactivity compared to soot produced from other diesel fuels.[177] However, there is no study regarding the properties and oxidation behavior of biodiesel soot generated under PCCI combustion conditions. The same methodology used in this study could be used to investigate the oxidation behavior of biodiesel soot from PCCI combustion to examine if soot from biodiesel still shows higher reactivity under PCCI combustion. In addition, the structure change during oxidation of soot produced from biodiesel soot can also be investigated.

2) Soot from gasoline direct injection (GDI) engine

With the development of GDI engines, the regeneration of gasoline particulate filter (GPF) has become a critical issue. Thus, the reactivity of soot from GDI engines is also an important topic.[178] Soot produced from GDI engine has dramatically different properties in terms of nanostructure, aggregation and primary particle sizes. Soot from GDI engine generally has smaller primary and aggregation particle size.[179,180] Kyeong et al.[181] also found that soot produced from GDI engines shows a bimodal distribution. The reactivity of soot from various operating condition of GDI engines can be investigated using the methods applied in this thesis to provide insight into GDI soot properties and GPF regeneration.

3) Soot oxidation mechanism

Song et al.[19] found that the graphene layers of biodiesel soot rearrange and form ribbon like structures during the later stage of oxidation. Al-Qurashi et al.[20] found that soot produced under EGR conditions shows internal burning and higher reactivity with some degree of layer rearrangement. However, the study in Chapter 5 shows that the less reactive soot produced under

conventional combustion conditions shows internal burning during the oxidation process. The detailed mechanism of different oxidation processes are not fully understood and can be further investigated. The relation between the chemical properties of biodiesel soot and their thermal annealing effect can also be examined. It can be hypothesized that there are higher oxygen content in biodiesel soot which induced the structural rearrangement.

4) Impact of pre-treatment temperature and time on soot reactivity

Soot oxidation reactivity testing using TGA was carried out after pre-treatment under high temperatures of 500^{o}C or 525^{o}C in this study to drive off VOF. An increase of graphite structure or crystallite growth was believed to occur under high temperatures. [182] As a consequence, soot reactivity generally decreases with the increase of heat treatment temperature and time. Yehliu found that heat treatment time does not impact soot reactivity.[183] However, this research observed increased reactivity with the increased timing of heat pre-treatment. The mechanism of reactivity change with heat treatment should be further investigated.

7.2.2 Improve technical approach

1) Using *in situ* TEM to investigate oxidation mechanism

In this research, soot samples are partially oxidized under TGA and then examined using TEM. In order to better understand the soot oxidation process, *in Situ* TEM or alleged environmental TEM can be applied to monitor the soot oxidation process directly. For *in situ* TEM, the gas environment and temperature of the specimen can be controlled while keeping the sample under observation.[184] The structure change and/or rearrangement during the oxidation process can be examined directly under the environmental TEM, which can provide better insight into the mechanism and kinetics of soot oxidation.

2) Nuclear magnetic resonance (NMR) and mass spectrometry (MS)

Although XPS provides an effective method measuring the relative abundance and state of elements in soot particles such as carbon and oxygen, it cannot measure hydrogen atoms. Thus, the impact of abundance and chemical state of hydrogen atoms on the reactivity of soot is not investigated. Mass spectrometry (MS) can be used to detect the percentage of hydrogen atoms in soot particles, while nuclear magnetic resonance (NMR) can be used to measure the chemical state of hydrogen atoms. Those two techniques can be applied in future work to examine the impact of fuel and combustion mode on soot hydrogen content and the impact of hydrogen content and chemical state on soot reactivity.

3) Improve Raman spectrometry fitting method

Several curve fitting methods have been used by researchers to analyze Raman spectroscopy, including 4L1G, 3L1G methods with different peak fitting positions.[185,186] In this study, a 3L1G method developed by Seong et al.[137] is applied. This method is proved to be effective to indicate soot reactivity. However, the disordered peak around 1620cm^{-1} becomes important for less ordered soot samples. In addition, the peak around 1500cm^{-1} which represents the amorphous carbon is in between of the D1 and G peaks. Thus, for highly amorphous soot samples, it is very challenging to deconvolute the three peaks. A better peak fitting method and peak positions should be developed to analyze less ordered soot particles.

4) Improve fringe analysis algorithm

Vander Wal and Yehliu et al. have developed a fringe analyzing method to measure the length and tortuosity of graphene layers to explain the reactivity difference between soot samples.[187] Soot particles with shorter fringes have more carbon atoms on the graphene layer

edges, which are more reactive; soot particles with higher degree of curvature have higher bond strain between C-C bonds, which also results in higher reactivity. However, this methodology has limitations measuring amorphous carbon or soot particles with very small graphene layers. Modifications can be made to this algorithm to improve the sensitivity of fringe length and tortuosity analysis for highly amorphous soot particles.

Appendices

Appendix A

TEM images for soot from single cylinder Isuzu engine

Figure A.1 shows the TEM images for the three fuels under conventional combustion, and both early and late injection PCCI combustion from single cylinder Isuzu engine. TEM images with magnification of 40,000 x show that soot produced from PCCI combustion displays similar fractal-like structure as soot produced from conventional combustion. However, soot from early PCCI combustion has a much smaller mean particle aggregate size compared to conventional combustion for all three fuels, while soot from the late PCCI combustion has larger primary particle sizes.

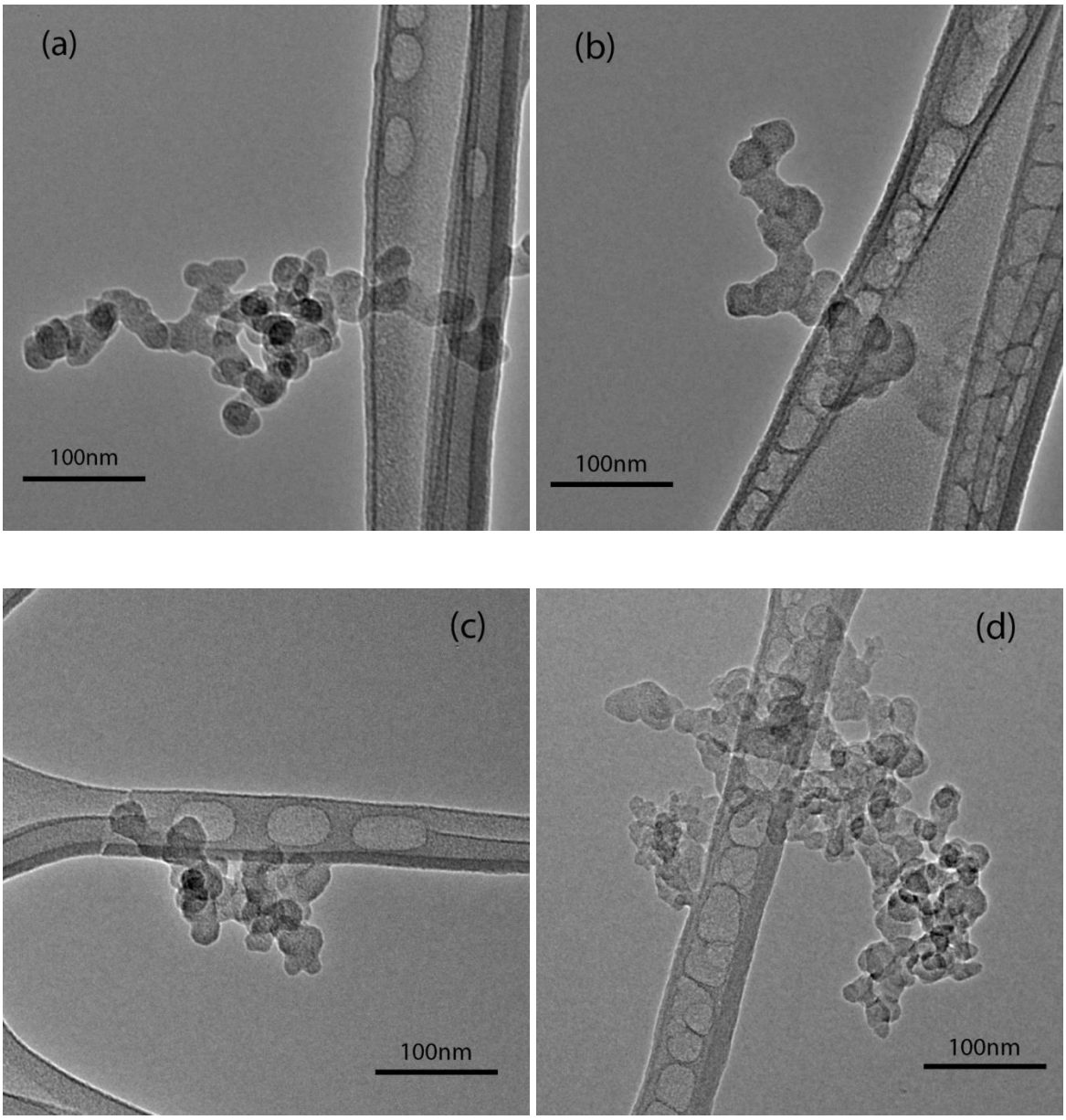
(a)
100nm
(b)
100nm
(c)
100nm
(d)
100nm

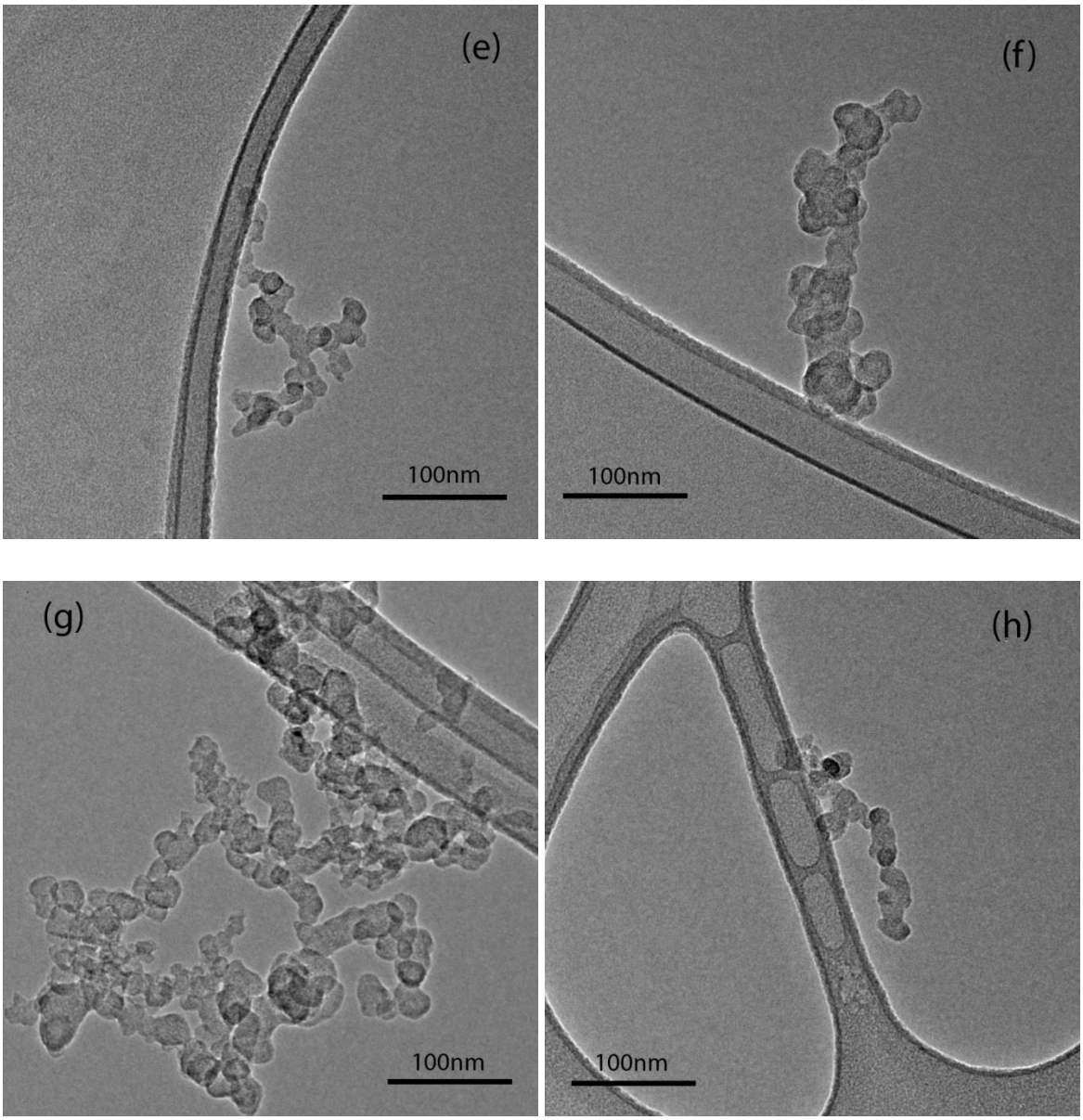
(e)
100nm
(f)
100nm
(g)
100nm
(h)
100nm

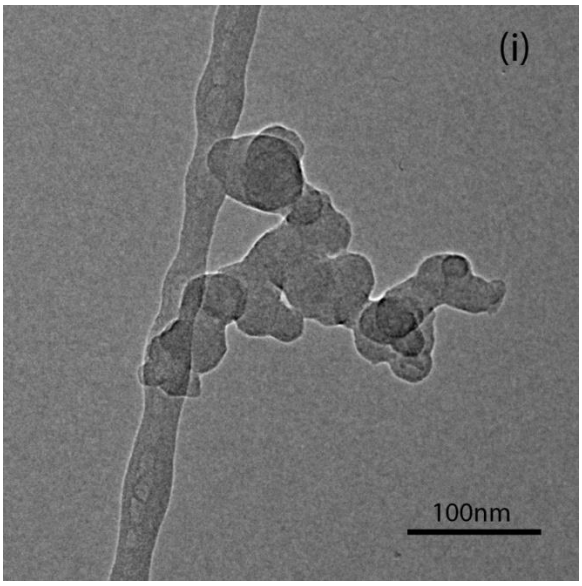

Figure A. 1 Soot morphology of (a) ULSD conventional combustion, (b) ULSD PCCI combustion with injection timing -18°ATDC, (c) ULSD PCCI combustion with injection timing -8°ATDC, (d) LTFT conventional combustion, (e) LTFT PCCI combustion with injection timing -10°ATDC, (f) LTFT PCCI combustion with injection timing 0°ATDC, (g) RD conventional combustion, (h) RD PCCI combustion with injection timing -12°ATDC, (i) RD PCCI combustion with injection timing 0°ATDC at magnification of 40,000x

Figure A.2 shows the high resolution TEM images of soot produced from the three fuels under conventional, early and late injection PCCI combustion from single cylinder Isuzu engine, with a magnification of 400,000x. From high resolution TEM images, it also can be concluded that soot produced from late PCCI combustion has much larger primary particle size compared to conventional and early PCCI combustion. Early injection PCCI combustion also produces smaller primary soot particles compared to conventional combustion. With retarded injection timing, cylinder temperature is higher when fuel is injected. Fuel pyrolysis is promoted with high temperature and more soot precursors are formed. Exhaust temperature is also higher with late fuel injection, which can promote soot growth. As a consequence, PM emissions increase and primary soot particle size increases with the retarding of injection timing.

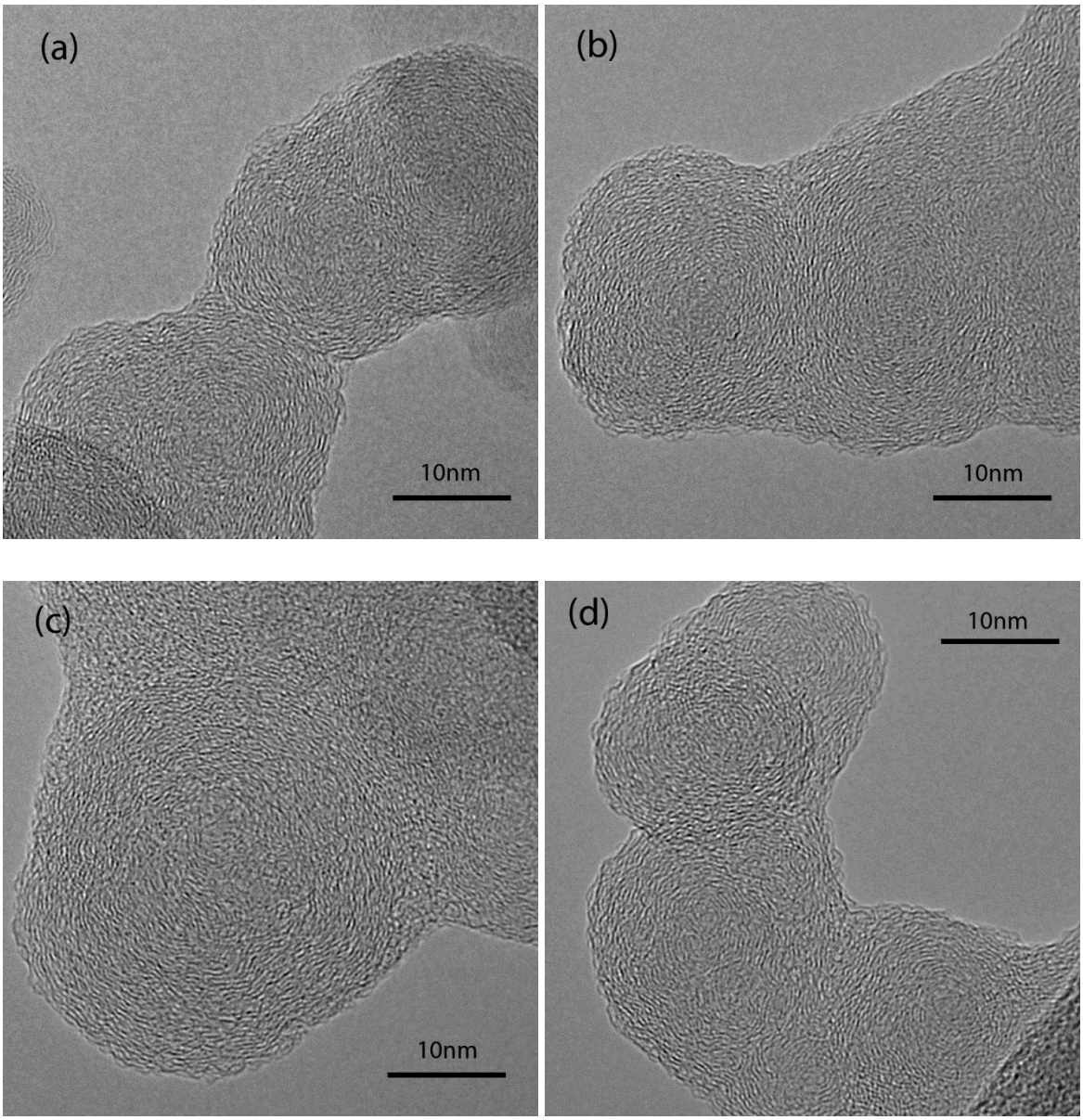
(a)
10nm
(b)
10nm
(c)
10nm
(d)
10nm

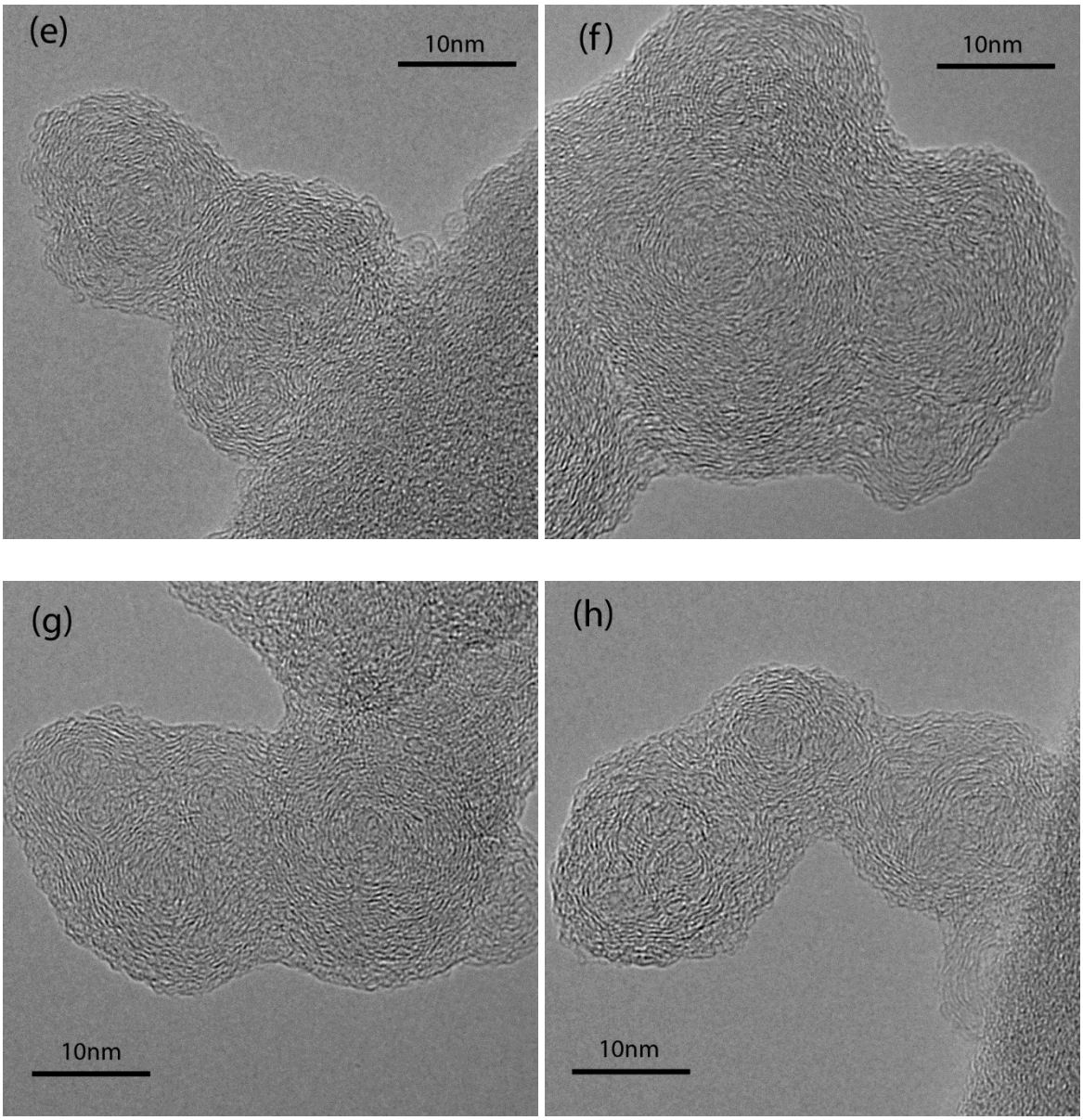
(e)
10nm
(f)
10nm
(g)
10nm
(h)
10nm

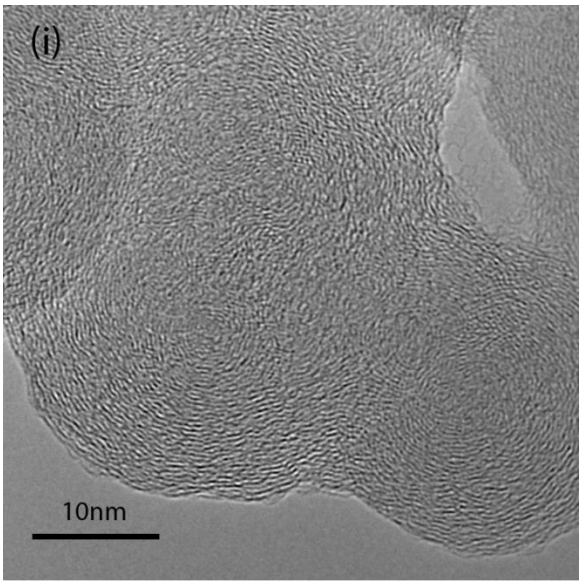

Figure A. 2 Soot nanostructure of (a) ULSD conventional combustion, (b) ULSD PCCI combustion with injection timing -18°ATDC, (c) ULSD PCCI combustion with injection timing -8°ATDC, (d) LTFT conventional combustion, (e) LTFT PCCI combustion with injection timing -10°ATDC, (f) LTFT PCCI combustion with injection timing 0°ATDC, (g) RD conventional combustion, (h) RD PCCI combustion with injection timing -12°ATDC, (i) RD PCCI combustion with injection timing 0°ATDC at magnification of 400,000x

Appendix B

Post injection schedule, BSFC and emissions

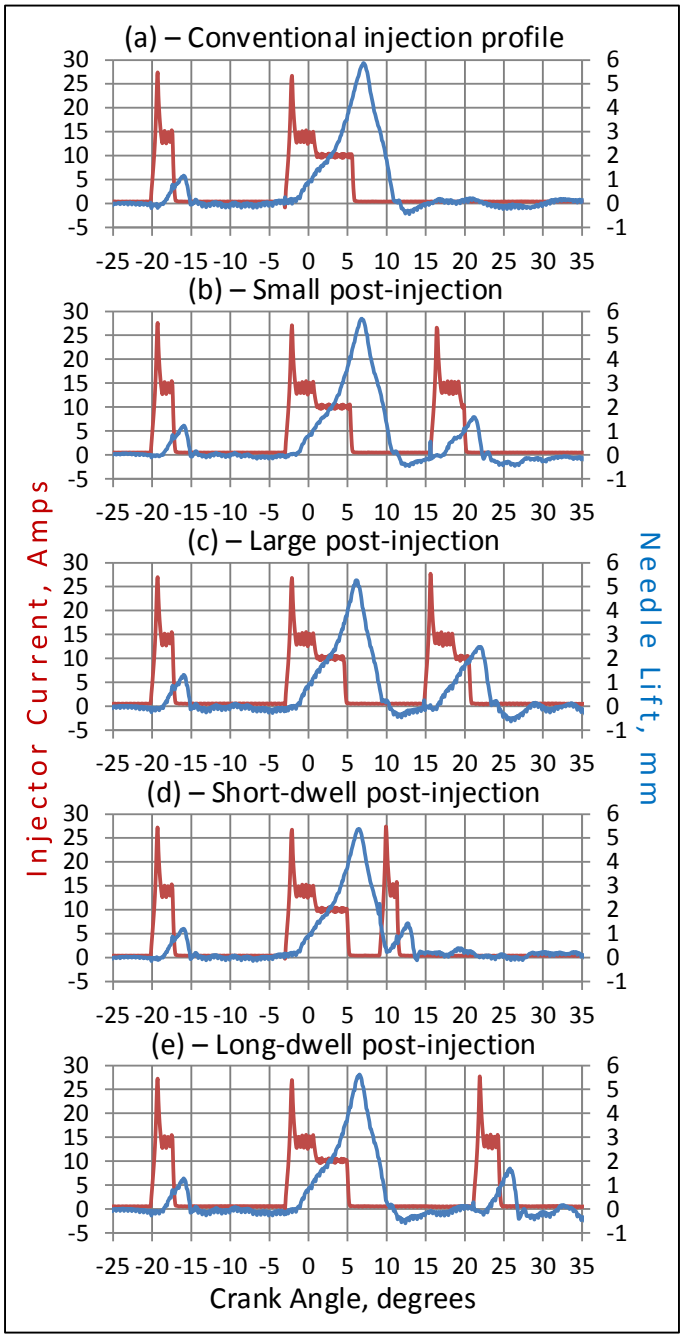

Figure B. 1 Example of injection schedules and injector current for (a) baseline condition, (b) 3% post injection with injection dwell 10°CAD, (c) 12% post injection with injection dwell 10°CAD (d) 7.5% post injection with injection dwell 4°CAD, and (e) 7.5% post injection with injection dwell 16°CAD[18]

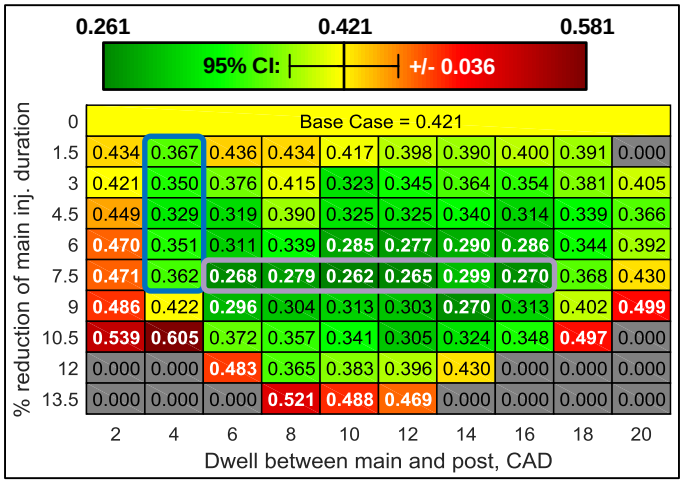

Figure B. 2 Filter smoke number, varying post-injection schedule. Close-coupled regime highlighted in blue, long-dwell regime highlighted in violet[18]

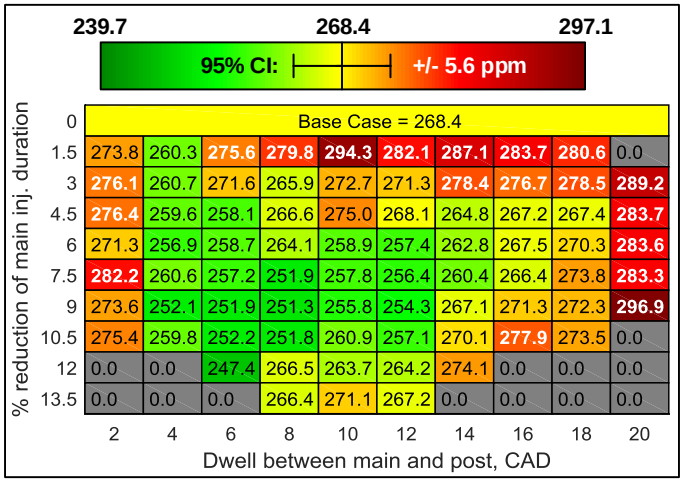

Figure B. 3 CO emissions, varying post-injection schedule[18]

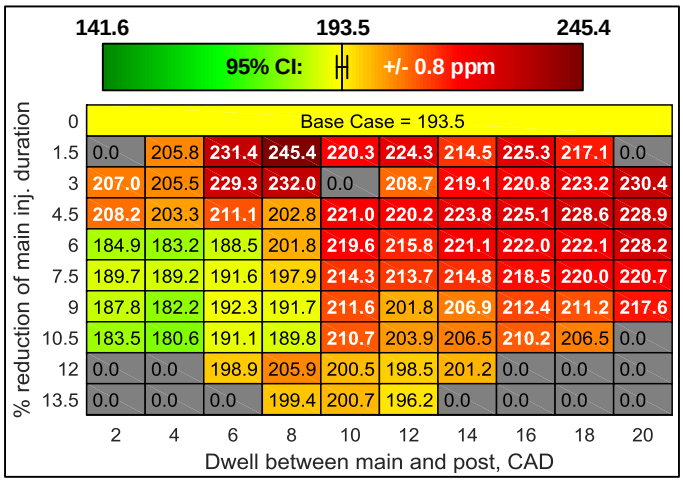

Figure B. 4 THC emissions, varying post-injection schedule[18]

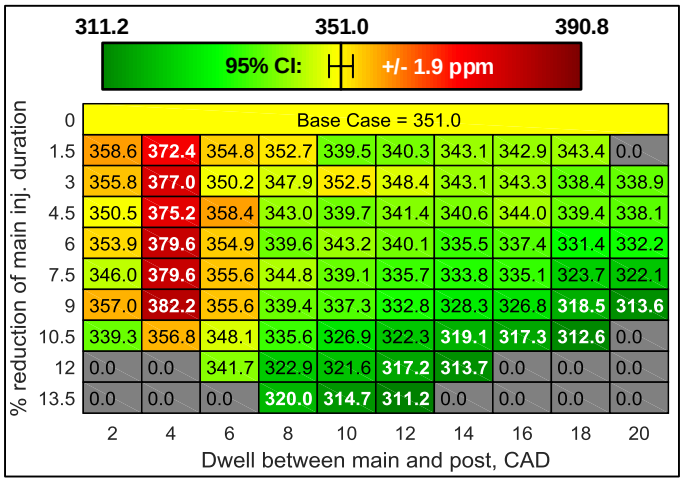

Figure B. 5 NOx emissions, varying post-injection schedule[18]

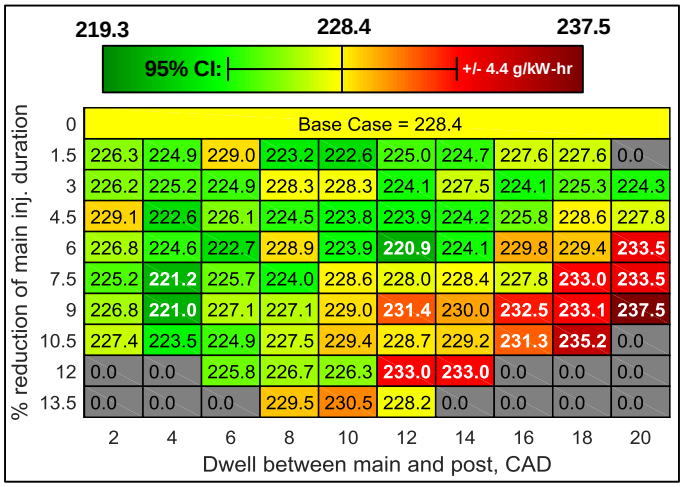

Figure B. 6 Brake specific fuel consumption, varying post-injection schedule[18]

References

(1) Schwarze, P. E.; Øvrevik, J.; Lag, M.; Refsnes, M.; Nafstad, P.; Hetland, R. B.; Dybing, E. Particulate matter properties and health effects: consistency of epidemiological and toxicological studies. *Hum. Exp. Toxicol.* **2006**, 25, 559- 579.

(2) Murtagh, M. J.; Sherwood, D. L.; Socha, L. S. Development of a diesel particulate filter composition and its effect on thermal durability and filteration performance. *SAE Tech. Pap*. **1994**, 940235.

(3) Dec, J. E. Advanced compression-ignition engines-understanding the in-cylinder processes. *P. Combust. Inst.* **2009**, 32, 2727-2742.

(4) Noehre, C.; Andersson, M.; Johansson, B.; Hultqvist, A. Characterization of partially premixed combustion. *SAE Tech. Pap*. **2006**, 2006-01-3412.

(5) Lu, X.; Han, D.; Huang, Z. Fuel design and management for the control of advanced compression-ignition combustion modes. *Prog. Energ. Combust.* **2001**, 37, 1-43.

(6) Kitano, K.; Nishiumi, R.; Tsukasaki, Y.; Tanaka, T.; Morinaga, M. Effects of fuel properties on premixed charge compression ignition combustion in a direct injection diesel engine. *SAE Tech. Pap*. **2003**, 2003-01-1815.

(7) Demirbas, A. Political, economic and environmental impacts of biofuels: A review. *Appl. Energ*. **2009**, 86, S108-S177.

(8) Neely, G. D.; Sasaki, S.; Huang, Y.; Leet, J. A.; Stewart, D. W. New diesel emission control strategy to meet US Tier 2 emissions regulations. *SAE Tech. Pap*. **2005**, 2005-01-1091.

(9) O'Connor, J.; Musculus, M. Optical investigation of the reduction of umburned hydrocarons using close-coupled post injection at LTC conditions in a heavy-duty diesel engine. *SAE Tech. Pap*. **2013**, 2013-01-0910.

(10) Horibe, N.; Komizo, T.; Sumimoto, T.; Wang, H.; Smoke reduction effects by post injection for various injection parameters and com ustion chamber shapes in a diesel engine. *SAE Tech. Pap*. **2014**, 2014-01-2643.

(11) Hountalas, D.; Lamaris, V.; Pariotis, E.; Ofner, H. Parametric study based on a phenomenological model to investigate the effect of post fuel injection on HDDI diesel engine performance and emissions-model validation using experimental data. *SAE Tech. Pap*. **2008**, 2008-01-0641.

(12) Zhang, F.; Xu, H.; Zhang J.; Tian, G.; Kalghatgi, G. Investigation into light duty dieseline fuelled partially-premixed compression ignition engine. *SAE Tech. Pap*. **2011**, 2011-01-1411.

(13) Lilik, G. K.; Boehman A. L. Advanced diesel combustion of a high cetane number fuel with low hydrocarbon and carbon monoxide emissions. *Energ. Fuel*. **2011**, 25, 1444-1456.

(14) Chryssakis, C. A.; Assanis, D. N.; Kook, S.; Bae, C. Effect of multiple injections on fuel-air mixing and soot formation in diesel combustion using direct flame visualization and CFD techniques. *Proceedings of ICES2005*, **2005**, ICES2005-1016.

(15) Dronniou, N.; Lejeune, M.; Balloul, I.; Higelin, P. Combination of high EGR rates and multiple injection strategies to reduce pollutant emissions. *SAE Tech.Pap*. **2005**, 2005-01-3726.

(16) Reitz, R. D.; Choi, C. Y. An experimental study on the effects of oxygenated fuel blends and multiple injection strategies on DI diesel engine emissions. *Fuel*. **1999**, 78, 1303-1317.

(17) Yehliu, K.; Lilik, G. K.; Vander Wal, R. L. Sun, C.; Boehman, A. L. Impacts of advanced diesel combustion operation on soot nanostructure and reactivity. *Int. J. Engine Res*. **2016**.

(18) Martin, J.; Sun, C.; Boehman, A.; O'Connor, J. Experimental study of post injection scheduling for soot reduction in a light-duty turbodiesel engine. *SAE Tech. Pap*. **2016**, 2016-01-0726.

(19) Song, J.; Alam, M.; Boehman, A. L.; Kim U. Examination of the oxidation behavior of biodiesel soot. *Combust. Flame*. **2006**, 146, 589-604.

(20) Al-Qurashi, K.; Boehman, A. L. Impact of exhaust gas recirculation (EGR) on the oxidative reactivity of diesel engine soot. *Combust. Flame*. **2008**, 155, 675-695.

(21) Shaughnessy, W. J.; Venigalla, M. M.; Trump, D. Health effects of ambient levels of respirable particulate matter (PM) on healty, young-adult population. *Atmos. Environ*. **2015**, 123, 102-111.

(22) MicroRNAs are associated with blood-pressure effects of exposure to particulate matter: Results from a mediated moderation analysis. *Environ. Res*. **2016**, 146, 274-281.

(23) Johnson, J. H.; Bagley, S. T.; Gratz, L. D. A review of diesel particulate control technology and emissions effects. *SAE Tech. Pap*. **1994**, 940233.

(24) Wirojsakunchai, E.; Schroeder, E.; Kolodziej, C.; Foster, D. E.; Schmidt, N.; Root, T.; Kawai, T.; Suga, T.; Nevius, T.; Kusaka T. Detailed diesel exhaust particulate characterization and real-time DPF filtration efficiency measurements during PM filling process. *SAE Tech. Pap*.**2007**, 2007-01-0320.

(25) Konstandopoulos, A. G.; Kostoglou, M.; Skaperdas, E.; Papaioannou, E.; Zarvalis, D.; Kladopoulou, E. Fundamental studies of diesel particulate filters: transient loading, regeneration and aging. *SAE Tech. Pap*. **2000**, 2000-01-1016.

(26) Khair, M. K. A review of diesel particulate filter technologys. SAE Tech. Pap. 2003, 2003-01-2303.

(27) Salvat, O.; Marez, P.; Belot, G. Passenger car serial application of a particulate filter system on a common rail direct injection diesel engine. *SAE Tech. Pap*. **2000**, 2000-01-0473.

(28) Allansson, R.; Blakeman, P. G.; Cooper, B. J.; Hess, H.; Silcock, P. J.; Walker, A. P. Optimising the low temperature performance and regeneration efficiency of the continuously regeneration diesel particulate filter (CR-DPF) system. *SAE Tech. Pap*. **2002**, 2002-01-0428.

(29) Johnson, T. V. Diesel emissions control in review. *SAE Tech. Pap*. **2008**, 2008-01-0069.

(30)Papagiannakis, R.G.; Hountalas, D.T. Combustion and exhaust emission characteristics of a dual fuel compression ignition engine operated with pilot diesel. *Energ. Convers. Manage*. **2004**, 45, 2971-2987.

(31) Yao, M.; Zheng, Z.; Liu, H. Progress and recent trends in homogeneous charge compression ignition (HCCI) engines.*Prog. Energ. Combust*. **2008**, 35, 389-437.

(32) Lewander, M.; Ekholm, K.; Johansson, B.; Tunestal, P.; Milovanovic, N.; Keeler, N.; Harcombe, T.; Bergstrand, P. Investigation of the combustion characteristics with focus on partially premixed combustion in a heavy duty engine. *SAE Tech. Pap.***2008**, 2008-01-1658.

(33) Nguyen, L. D. K.; Sung, N. W.; Lee, S. S.; Kim, H. S. Effects of split injections, oxygen enriched air and heavy EGR on soot emissions in a diesel engine. *Int. J. Automot. Techn.***2011**, 12, 339-350.

(34) Sakai, A.; H Takeyama, H.; Ogawa, H.; Miyamoto, N. Improvements in premixed charge compression ignition combustion and emissions with lower distillation temperature fuels. *Int. J. Engine Res.* **2005**, 6, 433-442.

(35) Kim, K.; Kim, D.; Jung, Y.; Bae, C. Spray and combustion characteristics of gasoline and diesel in a direct injection compression ignition engine. *Fuel.* **2013**, 109, 616–626.

(36) Kiplimo, R.; Tomita, E.; Kawahara, N.; Yokobe, S. Effects of spray impingement, injection parameters, and EGR on the combustion and emission characteristics of a PCCI diesel engine. *Appl. Therm. Eng.* **2012**, 37, 165-175.

(37) Kiplimo, R.; Tomita, E.; Kawahara, N.; Zhou S.; Yokobe, S. Effects of Injection pressure, timing and EGR on combustion and emissions characteristics of diesel PCCI engine. *SAE Tech. Pap.* **2011**, 2011-01-1769.

(38) Agarwal, D.; Sinha, S.; Agarwal, A. K. Experimental investigation of control of NOx emissions in biodiesel-fueled compression ignition engine. *Renew. Energ*. **2006**, 31, 2356-2369.

(39) Zhang, Y. Boehman, A. L. Impact of biodiesel on NOx emissions in a common rail direct injection diesel engine. *Energ. Fuel*. **2007**, 21, 2003-2012.

(40) Manente, V.; Johansson, B.; Tunestal, P. Characterization of partially premixed combustion with ethanol: EGR sweeps, low and maximum loads. *J. Eng. Gas Turb. Power.* **2010**, 132, 082802.

(41) Lewander, M.; Johansson, B.; Tunestal, P.; Keeler, N.; Tullis, S.; Milovanovic, N.; Bergstrand, P. Evaluation of the operating range of partially premixed combustion in a multi cylinder heavy duty engine with extensive EGR. *SAE Tech. Pap.* **2009**, 2009-01-1127.

(42) Cho, K.; Han, M.; Sluder, C. S.; Wagner, R. M.; Lilik, G. K. Experimental investigation of the effects of fuel characteristic on high efficiency clean combustion in a light-duty diesel engine. *SAE Tech. Pap.* **2009**. 2009-01-2669.

(43) Hildingsson, L.; Kalghatgi, G.; Tait, N.; Johansson, B.; Harrison, A. Fuel octane effects in the partially premixed combustion regime in compression ignition engines. *SAE Tech. Pap.* **2009**, 2009-01-2648.

(44) Ickes, A. M., Bohac, S. V., Assanis, D. N., Effect of Fuel Cetane Number on a Premixed Diesel Combustion Mode, *Int. J. Engine Res.* **2009**, 10(4), 251-263.

(45) Han, D., Ickes, A., Bohac, S. V., Zhen, H., Assanis, D. N. Premixed Low-Temperature Combustion of Blends of Diesel and Gasoline in a High Speed Compression Ignition Engine. *P. Combust. Inst.* **2011**, 33(2), 3039-3046.

(46) Weall, A.; Collings, N. Gasoline fuelled partially premixed charge compression ignition in a light duty multi cylinder engine: A study of low load and low speed operation. *SAE Tech. Pap.* **2009**, 2009-01-1791.

(47) Neill, W. S.; Chippior, W.L.; Gulder, O.L.; Cooley, J.; Richardson, E.K.; Mitchel,l K.; Fairbridge, C. Influence of fuel aromatic type on the particulate matter and NOx emissions of a heavy-duty diesel engine. *SAE Tech. Pap.* **2001**, 2001-01-1856.

(48) Ogawa, H.; Miyamoto, N.; Sakai, A.; Akao, K. Combustion in a two-stage injection PCCI engine with lower distillation-temperature fuels. *SAE Tech. Pap.* **2004,** 2004-01-1914.

(49) Ren, Y.; Huang, Z.; Miao, H.; Di, Y.; Jiang, D.; Zeng. K. Combustion and emissions of a DI diesel engine fuelled with diesel-oxygenate blends. *Fuel.* **2008**, 87, 2691-2697.

(50) Gill, S.S.; Tsolakis, A.; Herreros, J.M.; York, A.P.E. Diesel emissions improvements through the use of biodiesel or oxygenated blending components. *Fuel*. **2012**, 95, 578-586.

(51) Broustail, G.; Halter, F.; Seers, P.; Moreac, G.; Mounain-Rousselle, C. Comparison of regulated and non-regulated pollutants with iso-octane/butanol and iso-octane/ethanol blends in a port-fuel injection spart-ignition engine. *Fuel*. **2012**, 94, 251-261.

(52) Lilik, G. K.; Boehman, A. L. Effects of fuel ignition quality on equivalence ratio for autoignition. *Energ. Fuel.* **2013**, 27, 1586-1600.

(53) Ogunkoya, D.; Roberts, W. L.; Fang, T.; Thapaliya, N. Investigation of the effects of renewable diesel fuels on engine performance, combustion, and emissions. *Fuel.* **2015**, 140, 541-554.

(54) Knothe, G. Biodiesel and renewable diesel: A comparison. *Prog. Energ. Comb*. **2010**, 36, 364-373.

(55) O'Connor, J; Musculus, M. Effect of load on close-coupled post-injection efficacy for soot reduction in an optical heavy-duty diesel research engine. *J. Eng. Gas Turb. Power.* **2014**, 136, 101509.

(56) Hotta, Y.; Inayoshi, M.; Nakakita, K.; Fujiwara, K.; Sakata, I. Achieving lower exhaust emissions and better performance in an HSDI diesel engine with multiple injection. 2005, *SAE Tech. Pap*. **2005,** 2005-01-0928.

(57) Chen, S.K. Simultaneous reduction of NOx and particulate emissions by using multiple injections in a small diesel engine. 2000, *SAE Tech. Pap*. **2000**, 2000-01-3804.

(58) Desantes, J.M.; Arregle, J.; Lopez, J. J.; Garcia, A. A comprehensice study of diesel combustion and emissions with post-injection. 2007, *SAE Tech. Pap*. **2007**, 2007-01-0915.

(59) Han, Z.; Uludogan, A.; Hampson, G. J.; Reitz, R. D. Mechanism of soot and NOx emissions reduction using multiple-injection in a diesel engine. 1996, *SAE Tech. Pap*. **1996**, 960633.

(60) Bobba, M.; Musculus. M.; Neel W. Effect of post injections on in-cylinder and exhaust soot for low-temperature combustion in a heavy-duty diesel engine. *SAE Tech. Pap*. **2010**, 2010-01-0612.

(61) Benajes, J.; Molina, S.; and Garcia, J. Influence of pre- and post-injection on the performance and pollutant emissions in a HD diesel engine. *SAE Tech. Pap*. **2001**, 2001-01-0526.

(62) Payri, F.; Benajes, J.; Pastor, J.; and Molina, S. Influence of the post-injection paytern on performance, soot and NOx emissions in a HD diesel engine. *SAE Tech pap*. **2002**. 2002-01-0502.

(63) Badami, M.; Mallamo, F.; Millo, F.; Rossi, E. Experimental investigation on the effect of multiple injection strategies on emissions, noise and brake specific fuel consumption of an automotive direct injection common-rail diesel engine. *Int. J. Eng. Res*. **2003**, 4, 299-314.

(64) O'Connor, J.; Musculus, M. Post injections for soot reduction in diesel engines: a review of current understanding. *SAE Tech. Pap*. **2013**, 2013-01-0917.

(65) Pierpont, D.; Montgomery, D.; and Reitz, R. Reducing particulate and NOx emissions by using multiple injections and EGR in a DI diesel. *SAE Tech Pap*. **1995**, 950217.

(66) Dobbins, R.A.; Fletcher, R.A.; Chang, H. C. The evolution of soot precursor Particles in a diffusion flame. *Combust. Flame*. **1998**, 115, 285-189.

(67) Smith, O. I. Fundamentals of soot formation in flames with application to diesel engine particulate emissions. *Prog. Energ. Combust.* **1981**, 7, 275-291.

(68) Tree, D. R.; Svensson, K. I. Soot processes in compression ignition engines. *Prog. Energ. Combust.* **2007**, 272-309.

(69) Glassman, I. Soot formation in combustion processes. In: Proceedings of the 22nd international symposium on combustion. The Combustion Institute, **1988**.

(70) Jacobson, M. Z.; Kittelson, D. B.; Watts, W. F. Enhanced coagulation due to evaporation and its effect on nanoparticle evolution. *Environ. Sci. Technol*. **2005**, 39, 9486-9492.

(71) Stanmore, B. R.; Brilhac, J. F.; Gilot, P. The oxidation of soot: a review of experiments, mechanisms and models. *Carbon.* **2011**, 39, 2247-2268.

(72) Ishiguro, T.; Takatori, Y.; Akihima, K. Microstructure of diesel soot particles probed by electron microscopy: First observation of inner core and outer shell. *Combust. Flame*. **1997**, 108, 231-234.

(73) Hurt, R. H.; Crawford, G. P.; Shim, H. S. Equilibrium nanostructure of primary soot particles. *P. Combust. Inst.* **2000**, 28, 2539-2546.

(74) Vander Wal, R. L.; Tomasek, A. J. Soot oxidation: dependence upon initial nanostructure. *Combust Flame*. **2003**, 134, 1-9.

(75) Song, J.; Zello, V.; Boehman, A. L. Comparison of the impact of intake oxygen enrichment and fuel oxygenation on diesel combustion and emissions. *Energ. Fuel*. **2004**, 18, 1282-1290.

(76) Vander Wal, R. L.; Tomasek, A. J. Soot nanostructure: dependence upon synthesis conditions. *Combust. Flame*. **2004**, 136, 129-140.

(77) Soewono, A.; Rogak, S. Morphology and raman spectra of engine-emitted. *Aerosol Sci. Tech*. **2011**, 45, 1206-1216.

(78) Boehman, A. L; Song, J.; Alam. M. Impact of biodiesel blending on diesel soot and the regeneration of particulate filters. *Energ. Fuel*. **2005**,19, 1857-1864.

(79) Senneca, O.; Russo, P.; Salatino, P.; Masi, S. The relevance of thermal annealing to the evolution of coal char gasification reactivity. *Carbon*. **1997**, 35, 141-151.

80 Dahn, J. R.; Xing, W.; Gao. Y. The “falling cards model” for the structure of microporous carbon. *Carbon*. **1997**, 35, 823-830.

(81) Hurt, R. H.; Dudek, D. R.; Longwell, J. P.; Sarofim, A. F. The phemena of gasification-induced carbon densification and its influence on pore structure evolution. *Carbon*. **1988**, 26, 433-439.

(82) Vander Wal. R. L.; Yezerets, A.; Currier, N. W.; Kim, D. H.; Wang, C. M. HRTEM study of soot collected from diesel particulate filters. *Carbon*. **2007**, 45, 70-77.

(83) Zhang, X. Dukhan, A.; Kantorovich, I. I.; Bar-Ziv, E.; Kandas, A.; Sarofim, A. F. Structural changes of char particles during chemically controlled oxidation. *The 26th (international) symposium on combustion*. **1996**, 3111-3118.

(84) Zhu, H.; Bohac, S. V.; Huang, Z.; Assanis, D. N. Emissions as functions of fuel oxygen and load from a premixed low-temperature combustion mode. *Int. J. Engine Res.* **2014**, 15, 731-740.

(85) Zhang, Y. Low temperature oxidation behavior of soot generated from the combustion of a biodiesel surrogate in a diffusion flame. The Pennsylvania State University: University Park, PA, **2010**.

(86) Wang, W.; Thapaliya, N.; Campos, A.; Stikeleather, L. F.; Roberts, W. L. Hydrocarbon fuels from vegetable oils via hydrolysis and thermo-catalytic decarboxylation. *Fuel.* **2012**, 95, 622-629.

(87) Yehliu, K.; Vander Wal, R. L.; Armas, O.; Boehman, A. L. Impact of fuel formulation on the nanostructure and reactivity of diesel soot. *Combust. Flame.* **2012**, 159, 3597-3606.

(88) Advanced alternative and renewable diesel fuels: detailed characterization of physical and chemical properties. CRC Report No. AVFL-19-2. **2013**.

(89) Jacobs, T. J.; Bohac, S. V.; Assanis, D. N.; Szymkowicz, P. G. Lean and Rich Premixed Compression Ignition Combustion in a Light-Duty Diesel Engine. *SAE Tech. Pap*. **2005**, 2005-01-0166.

(90) Radovic, L. R.; Walker, P. L.; Jenkins, R. G. Importance of carbon active sites in the gasification of coal chars. *Fuel*. **1983**, 62, 849-856.

(91) Jenkins, R. G.; Nandi, S. P.; Walker, P. L. Reactivity of heat-reacted coals in air at 500 degrees C. *Fuel*. **1973**, 52, 288-293.

(92) Sadezky A, Muckenhuber H, Grothe H, Niessner R and Poschl U. Raman microspectroscopy of soot and related carbonaceous materials: spectral analysis and structural information. *Carbon*. **2005**, 43, 1731–1742.

(93) Tai, F. C. Wei, C.; Chang, S. H.; Chen, W. S. Raman and X-ray diffraction analysis on unburned carbon powder refined from fly ash. *J. Raman Sectrosc*. **2010**, 41, 933-937.

(94) M. Smith; L. Scudiero; J. Espinal, J. McEwen; M. Garcia-Perez. Improving the deconvolution and interpretation of XPS spectra from chars by ab initio calculations. *Carbon*. **2016**, 110, 155-171.

(95) Sun, C.; Kang, D.; Bohac, S. V.; Boehman, A. L. Impact of fuel and injection timing on partially premixed charge compression ignition combustion. *Energ. Fuel*. **2016**, 30, 4331-4345.

(96) Hoekman, S. K., Robbins, C. Review of the effects of biodiesel on NOx emissions. *Fuel Process. Technol.* **2012**, 96, 237-249.

(97)Mueller, C. J.; Boehman, A. L.; Martin, G. C. An experimental investigation of the origin of increased NOx emissions when fueling a heavy-duty compression-ignition engine with soy biodiesel. *SAE Tech. Pap.* **2009**, 2009-01-1792.

(98) Glaude, P. A.; Fournet, R.; Bounaceur, R.; Molière, M. Adiabatic flame temperature from biofuels and fossil fuels and derived effect on NOx emissions. *Fuel Process. Technol.* **2010**, 91, 229-235.

(99) Zannis, T. C.; Hountalas, D. T. DI diesel engine performance and emissions from the oxygen enrichment of fuels with various aromatic content. *Energ. Fuel*. **2004**, 18, 659-666.

(100) Szybist, J. P.; Kirby, S. R.; Boehman, A. L. NOx emissions of alternative diesel fuels: A comparative analysis of biodiesel and FT diesel. *Energ. Fuel.* **2005**, 19, 1484-1492.

(101) Northrop, W.F.; Bohac, S. V.; Assanis, D. N. Premixed low temperature combustion of biodiesel and blends in a high speed compression ignition engine. *SAE Tech. Pap.* **2009**, 2009-01-0133.

(102) Petersen, B.; Miles, P.; Ekoto, I. Optical investigation of UHC and CO sources from biodiesel blends in a light-duty diesel engine operating in a partially premixed combustion regime. *SAE Tech. Pap.* **2010**, 2010-01-0862.

(103) Dijkstra, R.; Di Blasio, G.; Boot, M.; Beatrice, C.; Bertoli, C. Assessment of the effect of low cetane number fuels on a light duty CI engine: Preliminary experimental characterization in PCCI operating condition. *SAE Tech. Pap.* **2011**, 2011-24-0053.

(104) Aceves, S. M.; Flowers, D. L.; Espinosa-Loza, F.; Martinez-Frias, J. Piston-liner crevice geometry effect on HCCI combustion by multi-zone analysis. *SAE Tech. Pap.* **2002**, 2002-02-2869.

(105) Musculus, M. P. B.; Lachaux, T.; Pickett, L. M.; Idicheria, C. A. End-of-injection over-mixing and unburned hydrocarbon emissions in low-temperature-combustion diesel engines. *SAE Tech. Pap*. **2007**, 2007-01-0907.

(106) Han, D., Ickes, A. M., Bohac, S. V., Huang, Z., Assanis, D. N. HC and CO emissions of premixed low-temperature combustion fueled by blends of diesel and gasoline, *Fuel.* **2012**, 99, 13-19.

(107) Pflaum, H.; Hofmann, P.; Geringer, B.; Weissel, W.; Potential of hydrogenated vegetable oil (HVO) in a modern diesel engine. *SAE Tech. Pap.* **2010**, 2010-32-0081.

(108) De Ojeda, W.; Bulicz, T.; Han, X.; Zheng, M.; Cornforth, F. Impact of fuel properties on diesel low temperature combustion. *SAE Tech. Pap.* **2011**, 2011-01-0329.

(109) Dec, J. A Conceptual Model of DI Diesel Combustion Based on Laser-Sheet Imaging. *SAE Tech. Pap.* **1997**, 970873.

(110) Parks, J. E.; Prikhodko, V.; Storey, J. M. E.; Barone, T. L.; Lewis Sr, S. A.; Kass, M. D.; Huff, S. P. Emissions from premixed charge compression ignition (PCCI) combustion and affect on emissions control devices. *Catal. Today.* **2010**, 151, 278-284.

(111) Wang, J.; Wu, F.; Xiao, J.; Shuai, S. Oxygenated blend design and its effects on reducing diesel particulate emissions. *Fuel.* **2009**, 88, 2037-2045.

(112) Uchida, M.; Akasaka, Y. A comparison of emissions from clean diesel fuels. *SAE Tech. Pap.* **1999**, 1999-01-1121.

(113) Zhu, L.; Zhang, W.; Liu, W.; Huang, Z. Experimental study on particulate and NOx emissions of a diesel engine fueled with ultra low sulfur diesel, RME-diesel blends and PME-diesel blends. *Sci. Total Environ.* **2010**, 48, 1050-1058.

(114) Suzuki, H.; Montajir, R. M.; Kawai, T.; Ishii, H.; Goto, Y. Exhaust emissions behavior of mixed fuels having different component cetane number and boiling point. *SAE Tech. Pap.* **2003**, 2003-01-1868.

(115) Barone, T. L.; Lall, A. A.; Storey, J. M. E.; Mulholland, G. W.; Prikhodko, V. Y.; Frankland, J. H.; Parks, J. E.; Zachariah, M. R.; Size-resolved density measurements of particle emissions from an advanced combustion diesel engine: effect of aggregate morphology. *Energ. Fuel.* **2011**, 25, 1978-1988.

(116) Storey, J. M. E.; Lewis, S. A.; Parks, J. E.; Szybist, J. P.; Barone, T. L.; Prikhodko, V. Y. Mobile source air toxics (MSATs) from high efficiency clean combustion: catalytic exhaust treatment effects. *SAE Tech. Pap.* **2008**, 2008-01-2431.

(117) Simescu, S.; Fiveland, S. B.; Dodge L. G. An experimental investigation of PCCI-DI combustion and emissions in a heavy-duty diesel engine. *SAE Tech. Pap.* **2003**, 2003-02-0345.

(118) Leermakers, C. A. J.; Luijten, C. C. M.; Somers, L. M. T.; Kalghatgi, G. T.; Albrecht, B. A. Experimental study of fuel composition impact on PCCI combustion in a heavy-duty diesel engine. *SAE Tech. Pap*. **2011**, 2011-01-1351.

(119) Zinola, S.; Lavy, J. Detailed particulate characterization from HCCI combustion for future DPF development. *SAE Tech. Pap*. **2009**, 2009-01-1185.

(120) Song, J.; Alam, M.; Boehman. A. L. Impact of alternative fuels on soot properties and DPF regeneration. *Combust. Sci. Technol*. **2007**, 179, 1991-2037.

(121) Collura, S.; Chaoui, N.; Azambre, B.; Finqueneisel, G.; Heintz, O; Krzton, A.; Koch, A.; Weber, J.V. Influence of the soluble organic fraction on the thermal behaviour, texture and surface chemistry of diesel exhaust soot. *Carbon*, **2005**, 43, 605-613.

(122) Al-Qurashi, K.; Lueking, A. D.; Boehman, A. L. The deconvolution of the thermal, dilution, and chemical effects of exhaust gas recirculation (EGR) on the reactivity of engine and flame soot. *Combust. Flame*. **2011**, 158, 1696-1704.

(123) Du, D. X.; Axelbaum, R. L.; Law, C. K. Influence of the soluble organic fraction on the thermal behavior, texture and surface chemistry of diesel exhaust soot. *23rd symp. (International) combustion*, **1990**, 23, 1501-1577.

(124) Davis, K. A.; Hurt, R. H.; Yang, H. Y. C.; Headley, T. J. Evolution of char chemistry, crystalUnity, and ultrafine structure during pulverized-coal combustion. *Combust. Flame*. **1995**, 100, 31-40.

(125) Neeft, J. P. A.; Nijhuis, T. X.; Smakman, E.; Makkee, M.; Moulijn, J. A. Kinetics of the oxidation of diesel soot. *Fuel*, **1997**, 76, 1129-1135.

(126) Belenkov, E. A. Formation of Graphite Structure in Carbon Crystallites. *Inorg. Mater*. **2001**, 37, 1094-1101.

(127) Atria, J. V.; Rusinko Jr, F.; Schobert, H. H. Structural ordering of Pennsylvania anthracites on heat treatment to 2000-2900 ^{o}C. *Energ. Fuel*. **2002**, 16, 1343-1347.

(128) Burton, A. W.; Ong, K.; Rea, T.; Chan, I. Y. On the estimation of average crystallite size of zeolites from the Scherrer equation: A critical evaluation of its application to zeolites with one-dimensional pore systems. *Micropor. Mesopor. Mat*. **2009**, 117, 75-90.

(129) Yehliu K.; Armas, O.; Vander Wal, R. L.; Boehman, A. L. Impact of engine operating modes and combustion phasing on the reactivity of diesel soot. *Combust. Flame*. **2013**, 160, 682-691.

(130) Vander Wal, R. L. Laser-induced incandescence: excitation and detection conditions, material transformations and calibration. *Appl. Phys. B*. **2009**, 96, 601-611.

(131) Puziya, A. M.; Poddubnaya, O. I.; Sochab, R. P.; Gurgulb, J.; Wisniewskic, M. XPS and NMR studies of phosphoric acid activated carbons. *Carbon*. **2008**, 46, 2113-2123.

(132) Seong, H. J.; Boehman, A. L. Studies of soot oxidative reactivity using a diffusion flame burner. *Combust. Flame*. **2012**, 159, 1864-1875.

(133) Seong, H. J.; Boehman, A. L. Imapct of intake oxygen enrichement and oxidative reactivity and properties of diesel soot. *Energy. Fuel*. **2011**, 25, 602-616.

(134) Plomp, A. J.; Su, D. S.; de Jong, K. P.; Bitter, J. H. On the nature of oxygen-containing surface groups on carbon nanofibers and their role for platinum depositionsAn XPS and titration study. *J. Phys. Chem. C* **2009**, 113, 9865–9869.

(135) Desimoni, E.; Casella, G. I.; Morone, A.; Salvi, A. M. XPS determination of oxygen-containing functional groups on carbon-fiber surfaces and the cleaning of these surfaces. *Surf. Interface Anal*. **1990**, 15, 627-634.

(136) Messerer, A.; Niessner, R.; Poschl, U. Comprehensive kinetic characterization of the oxidation and gasification of model and real diesel soot by nitrogen oxides and oxygen under engine exhaust conditions: Measurement, Langmuir–Hinshelwood, and Arrhenius parameters. *Carbon*, **2006**, 44, 307-324.

(137) Seong, H. J.; Boehman, A. L. Evaluation of Raman parameters using visible Raman Microscopy for soot oxidative reactivity. *Energ. Fuel*. **2013**, 27, 1613-1624.

(138) Ferrari, A. C.; Robertson, J. Interpretation of Raman spectra of disordered and amorphous carbon. *Phys. Rev. B*. **2001**, 61, 14095-14107.

(139) Sheng, C. Char structure characterized by Raman spectroscopy and its correlations with combustion reactivity. *Fuel*. **2007**, 86, 2316-2324.

(140) Knaer, M.; Carrara, M.; Rothe, D.; Niessner, R.; Ivleva, N. P. Changes in structure and reactivity of soot during oxidation and gasification by oxygen, studied by Micro-Raman spectroscopy and temperature programmed oxidation. *Aerosol Sci. Tech*. **2009**, 43, 1-8.

(141) Jawhara, T.; Roid, A.; Casado, J. Raman spectroscopic characterization of some commercially available carbon black materials. *Carbon*. **1995**, 1561- 1565.

(142) Ruiz, M. P.; Guzman de Villoria, R.; Millera, A.; Alzueta, M. U.; Bilbao, R. Influence of the temperature on the properties of the soot formed from C_2H_2 pyrolysis. *Chem. Eng. J*. **2007**, 127, 1-9.

(143) Belenkov, E. A. Formation of graphite structure in carbon crystallites. *Inorg. Mater*. **2001**, 37, 928-934.

(144) Lapuerta, M.; Oliva, F.; Agudelo, J. R.; Boehman, A. L. Effect of fuel on soot nanostructure and consequences on loading and regeneration of diesel particulate filters. *Combust. Flame*. **2012**. 159, 844-853.

(145) Ivleva, N. P.; Messerer, A.; Yang, X.; Niessner, R.; Poschl, U. Raman microspectroscopic analysis of changes in the chemical structure and reactivity of soot in a diesel exhaust aftertreatment model system. *Environ. Sci. Technol.* **2007**, 41, 3702-3707.

(146) Seong, H.; Lee, K. O.; Choi, S. Characterization of particulate morphology, nanostructures and size in low-temperature combustion with biofuels. *SAE Tech. Pap.* **2012**, 2012-01-0441.

(147) Pahalagedara, L.; Sharma, H.; Kuo, C.; Dharmarathna, S.; Joshi, A.; Suib, S. L.; Mhadeshwar, A. B. Structure and oxidation activity correlations for carbon blacks and diesel soot. *Energ. Fuel*. **2012**, 26, 6757-6764.

(148) Zhu, J.; Lee, K. O.; Yozgatligil, A.; Choi, M. Y. Effects of engine operating conditions on morphology, microstructure, and fractal geometry of light-duty diesel engine particulates. *P. Combust. Inst*. **2005**, 30, 2781-2789.

(149) Vander Wal, R. L.; Mueller, C. J. Initial investigation of effects of fuel oxygenation on nanostructure of soot from a direct-injection diesel engine. *Energ. Fuel*. **2006**, 20, 2364-2369.

(150) Walker, P. L. Complications introduced from gasification-induced densification of disordered carbons. *Carbon*. **1996**, 34, 1603.

(151) Vander Wal, R. L.; Choi, M. Y. Pulsed laser heating of soot: morphological changes. *Carbon*. **1999**, 37, 231-239.

(152) Knauer, M.; Schuster, M. E.; Su, D.; Schlogl, R.; Niessner, R.; Ivleva, N. P. Soot structure and reactivity analysis by Raman microspectroscopy, temperature-programmed oxidation, and high-resolution transmission electron microscopy. *J. Phys. Chem. A*. **2009**, 113, 13871-13880.

(153) Muller, J. O., Su, D. S.; Jentoft, R. E.; Wild, U.; Schlogl, R. Diesel engine exhaust emissions: oxidative behavior and microstructure of black smoke soot particulate. *Environ. Sci. Technol*. **2006**, 40, 1231-1236.

(154) Muller, J. O.; Su, D. S.; Wild, U.; Schlogl, R. Bulk and surface structural investigations of diesel engine soot and carbon black. *Phys. Chem. Chem. Phys*. **2007**, 9, 4018-4025.

(155) Seong, H.; Lee, K.; Choi, S. Effects of engine operating parameters on morphology of particulates from a gasoline direct injection (GDI) engine. *SAE Tech. Pap*. **2013**, 2013-01-2574.

(156) Park, C.; Hook, S.; Bae, C. Effects of multiple injections in a HSDI diesel engine equipped with common rail injection system. *SAE Tech. Pap*. **2004**, 2004-01-0127.

(157) Zhuang, J.; Qiao, X.; Bai, J.; Hu, Z. Effect of injection-strategy on combustion, performance and emissions characteristics in a DI-diesel engine fueled with diesel from direct coal liquefaction. *Fuel*, **2014**, 121, 141-148.

(158) Badami, M.; Mallamo, F.; Millo, F.; Rossi, E. E. Infulence of multiple injection strategies on emissions, combustion noise and BSFC of a DI common rail diesel engine. *SAE Tech. Pap*. **2002**, 2002-01-0503.

(159) Helmantel, A.; Somhorst, J.; Denbratt, I. Visualization of the effects of post injection and swirl on the combustion process of a passenger car common rail DI diesel engine. *Proceedings of ICE03*, **2003**, ICES2003-622.

(160) Chryssakis, C. A.; Hagena, J. R.; Knafl, A.; Hamosfakidis, V. D.; Filipi, Z. S.; Assanis, D. N. In-cylinder reduction of PM and NOx emissions from diesel combustion with advanced injection stragegies. *Int. J. Vehicle Des*. **2006**, 41, 83-102.

(161) Chartier, C.; Andersson, O.; Johansson, B.; Musculus, M.; Bobba, M. Effects of post-injection strategies on near-injector over-lean mixtures and unburned hydrocarbon emissions in a heavy duty optical diesel engine. *SAE Tech. Pap*. **2011**, 2011-01-1383.

(162) Yamamoto, K.; Takada, K.; Kusada, J.; Kanno, Y. Nagata, M. Influence of diesel post injection timing on HC emissions and catalytic oxidation performance. *SAE Tech. Pap*. **2006**, 2006-01-3442.

(163) Hardy, W. L.; Reitz, R. D. An experimental investigation of partially premixed combustion strategies using multiple injections in a heavy-duty diesel engine. *SAR Tech. Pap*. **2006**, 2006-01-0917.

(164) Yun, H.; Reitz, R. D. An experimental investigation on the effect of post-injection strategies on combustion and emissions in the low-temperature diesel combustion regime. *J. Eng. Gas turb. power*. **2007**, 129, 279-286.

(165) Konno, M.; Chikahisa, T.; Murayama, T. Reduction of smoke and NOx by strong turbulence generated during the combustion process in D. I. diesel engines. *SAE Tech. Pap*. **1992**, 920467.

(166) Poorghasemi, K.; Ommi, F.; Yaghmaei, H.; Namaki, A. An investigation on effect of high pressure post injection on soot and NO emissions in a DI diesel engine. *J. Mech. Sci. Technol*. **2012**, 26, 269-281.

(167) Ehleskog, R.; Ochoterena, R. L. Sot evolution in multiple injection diesel flames. *SAE Tech. Pap*. **2008**, 2008-01-2470.

(168) Nimodia, S.; Senthilkumar, K.; Halbe, V.; Ghodke, P. R.; Velusamy, R. Simultaneous reduction of NOx and soot using early post injection. *SAE Tech. Pap*. **2014**, 2013-01-0055.

(169) Bertoia, A.; Schubiger, R.; Kasper, A.; Matter, U.; Forss, A. M.; Mohr, M.; Boulouchos, K.; Lutz, T. Characterization of diesel particulate emissions in heavy-duty DI-diesel engines with common rail fuel injection influence of injection parameters and fuel composition. *SAE Tech. Pap*. **2001**, 2001-01-3573.

(170) Molina, S.; Desantes, J.; Garcia, A.; Pastor, J. A numerical investigation on combustion on characteristics with the use of post injection in DI diesel engines. *SAE Tech. Pap*. **2010**, 2010-01-1260.

(171) Arregle, J.; Pastor, J. V.; Lopez, J. J.; Garcia, A. Insights on postinjecion-associated soot emissions in direct injection diesel engines. *Combust. Flame*. **2008**, 154, 448-461.

(172) O'Connor, J.; Musculus, M. In-cylinder mechanisms of soot reduction by close-coupled post-injections as revealed by imaging of soot luminosity and planar laser-induced soot incandescence in heavy-duty diesel engine. *SAE Tech. Pap*. **2014**, 2014-01-1255.

(173) Dec, J.; Kelly-Zion, P. The effects of injection timing and diluents addition on late-combustion soot burnout in a DI diesel engine based on simultaneous 2-D imaging of OH and soot. *SAE Tech. Pap*. **2000**, 2000-01-0238.

(174) Yokomichi, H.; Hayashi, T.; Masuda, A. Changes in structure and nature of defects by annealing of fluorinated amorphous carbon thin films with low dielectric constant. *Appl. Phys. Lett*. **1998**, 72, 2704-2706.

(175) Estrade-Szwarckoph, H. XPS photoemissions in carbonaceous materials: A "defect" peak beside the graphitic asymmetric peak. *Carbon*. **2004**, 42, 1713-1721.

(176) Ruiz, M. P.; Callejas, A.; Millera, A.; Alzueta, M. U.; Bilbao, R. Soot formation from C2H2 and C2H4 pyrolysis at different temperatures. *J. Anal. Appl. Pyrol*. **2007**, 79, 244-251.

(177) Rodríguez-Fernandez, J.; Oliva, F.; Vazquez, R. A. Characterization of the diesel soot oxidation process through an optimized thermogravimetric method. *Energ. Fuel*. **2011**, 25, 2039-2048.

(178) Wang, C.; Xu, H.; Herreros, J. M.; Lattimore, T.; Shuai, S. Fuel effect on particulate matter composition and soot oxidation in a direct-injection spark ignition (DISI) engine. *Energ. Fuel*. **2014**, 28, 2003-2012.

(179) Guan, B.; Zhan, R. Lin, H.; Huang, Z. Review of the state-of-the-art of exhaust particulate filter technology in internal combustion engines. *J. Environ. Manage*. **2015**, 154, 225-258.

(180) Su, J.; Lin, W.; Sterniak, J.; Xu, M.; and Bohac, S. V. Particulate matter emission comparison of spark ignition direct injection (SIDI) and port fuel injection (PFI) operation of a boosted gasoline engine. *J. Eng. Gas Turb. Power*. **2014**, 136, 091513.

(181) Lee, K. O.; Seong, H.; Sakai, S.; Hageman, M.; Rothamer, D. Detailed morphological properties of nanoparticles from gasoline direct injection engine combustion of ethanol blends. *SAE Tech. Pap*. **2013**, 2013-24-0185.

(182) Buseck P.R., Bo-Jun H, Keller L.P. Electron microscope investigations of the structures of annealed carbons. *Energ. Fuel*. **1987**,1,105–110.

(183) Yeliu, K. Impacts of fuel formulation and engine operating parameters on the nanostructure and reactivity of diesel soot. Ph.D thesis. The Pennsylvania State University. **2010**.

(184) Simonsen, S.B.; Dahl, S.; Johnson, E.; Helveg, S. Ceria-catalyzed soot oxidation studied by environmental transmission electron microscopy. *J. Catal*. **2008**, 255, 1-5.

(185) Escribano, R.; Sloan, J. J.; Siddique, N.; Sze, N.; Dudev, T. Raman spectroscopy of carbon-containing particles. *Vib. Spectrosc*. **2011**, 26, 179-186.

(186) Patel, M.; Azanza Richardo, C. L.; Scardi, P.; Aswath, P. B. Morphology, structure and chemistry of extracted diesel soot — Part I: Transmission electron mictoscopy, Raman spectroscopy, X-ray photoelectron spectroscopy and synchrotron X-ray diffraction study. *Tribol. Int*. **2012**, 52, 29-39.

(187) Yehliu, K.; Vander Wal, R. L.; Boehman, A. L. Development of an HRTEM image analysis method to quantify carbon nanostructure. *Combust. Flame*. **2011**, 158, 1837-1851.